OF PICOLINIC ACID BASED SINGLE CRYSTALS



Thesis submitted to Bharathidasan University in partial fulfilment of the requirements for the award of the degree of DOCTOR OF PHILOSOPHY IN PHYSICS

*By*Ms. N. MANOPRADHA

(Ref. No. 08641/Ph.D.K2/Physics/PT/Apr. 2017)

Under the Guidance of

Dr. K. KIRUBAVATHI, M.Sc., M.Phil., PGDCA., Ph.D.,
Assistant Professor



PG & RESEARCH DEPARTMENT OF PHYSICS GOVERNMENT ARTS COLLEGE (GRADE - I)

(Affiliated to Bharathidasan University & Reaccredited with B+ by NAAC)

ARIYALUR - 621 713, TAMIL NADU, INDIA

MARCH 2022



P.G. & RESEARCH DEPARTMENT OF PHYSICS

GOVERNMENT ARTS COLLEGE

(Affiliated to Bharathidasan University & Reaccredited with B+ by NAAC)

ARIYALUR - 621 713, TAMIL NADU, INDIA

Email : kkirubaphysics@gmail.com Tel : (O) : +91 4329-222050

(M): +91 9489247668

Fax (O) : +91 4329-221260

Dr. K. KIRUBAVATHI,

M.Sc., M.Phil., PGDCA., Ph.D.,

Assistant Professor & Research Advisor

Date:

CERTIFICATE

This is to certify that the thesis entitled "EXPERIMENTAL AND THEORETICAL INVESTIGATIONS OF PICOLINIC ACID BASED SINGLE CRYSTALS" submitted to the Bharathidasan University in partial fulfilment of the requirements for the degree of DOCTOR OF PHILOSOPHY IN PHYSICS is a bonafide record of work done by Ms. N. MANOPRADHA, who carried out the research under my supervision. Certified further that to the best of my knowledge, the contents of this thesis have not been formed the basis for the award of any degree, associateship, diploma, fellowship or any other similar title of any University or Institution.

Ariyalur

(Dr. K. KIRUBAVATHI)

March 2022

Research supervisor

Ms. N. MANOPRADHA

Assistant Professor,
Department of Physics,
Cauvery College for Women (Autonomous),
Annamalai Nagar,
Tirchirappalli - 620 018.

Date:

DECLARATION

I hereby declare that the thesis entitled "EXPERIMENTAL AND THEORETICAL INVESTIGATIONS OF PICOLINIC ACID BASED SINGLE CRYSTALS" is a record of the work done by me, under the guidance and supervision of Dr. K. KIRUBAVATHI, Assistant Professor, P.G. & Research Department of Physics, Government Arts College, Ariyalur - 621 713.

I also declare that this work has not formed in part or fully the basis for the award of any degree or diploma at any University.

Ariyalur

(Ms. N. MANOPRADHA)

March 2022



PG & RESEARCH DEPARTMENT OF PHYSICS GOVERNMENT ARTS COLLEGE ARIYALUR – 621 713. TAMILNADU, INDIA

CERTIFICATE OF PLAGIARISM CHECK

1	Name of the Research Scholar	Ms. N. MANOPRADHA
2	Course of Study	Ph.D., Physics
3	Title of the Thesis / Dissertation	"EXPERIMENTAL AND THEORETICAL INVESTIGATIONS OF PICOLINIC ACID BASED SINGLE CRYSTALS"
4	Name of the Research Supervisor	Dr. K. KIRUBAVATHI
5	Department / Institution / Research Centre	PG & Research Department of Physics, Government Arts College, Ariyalur - 621 713.
6	Acceptable Maximum Limit for Preliminary Chapters	15%
7	Acceptable Maximum Limit for Remaining Chapters	10%
8	Percentage of Similarity of Content Identified for Preliminary Chapters	1%
9	Percentage of Similarity of Content Identified for Remaining Chapters	8%
10	Software Used	Ouriginal
11	Date of Verification	23.02.2022

Report on plagiarism check, item with % of similarity is attached.

Signature of the Research Supervisor

Signature of the Candidate



Document Information

Analyzed document Gacari_Manopradha_Introduction_230222.pdf (D128631551)

> Submitted 2022-02-23T08:32:00.0000000

Submitted by Saravanan

Submitter email gacariyalurlibrary@gmail.com

Similarity

Analysis address gacariya lurlibrary.bdu @analysis.urkund.com

Sources included in the report

 ${\tt URL: https://www.slideshare.net/manikanthaTumarada/advantages-and-applications-of-advantages-advantag$

computational-chemistry

Fetched: 2022-02-23T08:32:10.5600000



Document Information

Analyzed document Gacari_Manopradha_Result_230222.pdf (D128631566)

Submitted 2022-02-23T08:33:00.0000000

Submitted by Saravanan

Submitter email gacariyalurlibrary@gmail.com

Similarity 8%

Analysis address gacariyalurlibrary.bdu@analysis.urkund.com

Sources included in the report

W	URL: https://www.researchgate.net/publication/260431872_Synthesis_Crystal_Structure_and_Thermal_Decomposition_of_the_CobaltIl_Complex_with_2-Picolinic_Acid Fetched: 2022-02-23T08:32:53.4230000	88	4
W	URL: https://oap-journals.com/article/694/xml Fetched: 2022-02-23T08:32:48.2100000	88	2
W	URL: https://www.slideshare.net/govindarasukannan/1s20s0022286015000939main Fetched: 2022-02-08T11:44:30.0670000	88	2
W	URL: http://www.orientjchem.org/vol36no5/structural-vibrational-electronic-and-optical-properties-of-3-methoxy-245-trifluorobenzoic-acid-using-dft-calculations/Fetched: 2021-06-20T18:40:29.8070000	88	5
W	URL: http://www.rsc.org/suppdata/c7/cp/c7cp07854d/c7cp07854d1.pdf Fetched: 2021-05-18T10:10:51.9400000	88	5
W	URL: https://www.ias.ac.in/public/Volumes/boms/015/04/0333-0338.pdf Fetched: 2020-04-21T16:49:05.5130000	88	1
W	URL: https://arxiv.org/pdf/2002.06097 Fetched: 2021-09-24T13:08:49.8130000	88	1

ACKNOWLEDGEMENT

First and foremost, I submit my gratitude goes to the *DIVINE GUIDANCE* and *BLESSINGS OF GOD ALMIGHTY* towards completing this research work successfully.

I would like to express my deep felt gratitude to my Advisor, **Dr. K. KIRUBAVATHI**,

Assistant Professor, PG & Research Department of Physics, Government Arts College,

Ariyalur, for her prodigious patience, endless encouragement, immense knowledge,

motivation and ethical assistance to complete this research.

Besides my advisor, I wholeheartedly thank Doctoral Committee Members **Dr. K. SELVARAJU**, Assistant Professor, P.G. & Research Department of Physics, Government Arts College, Ariyalur and **Dr. S. GOWRI**, Associate Professor, PG & Research Department of Physics, Cauvery College for Women (Autonomous), Trichy for their constant support, encouragement and insightful suggestions in my research work.

I would like to express my sincere thanks to **THE DIRECTOR** of Collegiate Education, Chennai and **THE PRINCIPAL**, Government Arts College, Ariyalur, for permitting me to carry out this research work in the Department of Physics.

I acknowledge the support rendered and facilities provided by **Dr. K. KANDASAMY**, Head & Assistant Professor and all the faculty members of PG & Research Department of Physics, Government Arts College, Ariyalur.

I would like to express my deep sense of gratitude to **Dr. S. RAMA**, Department of Physics, St. Joseph's College of Engineering, Chennai, for her support and encouragement during the period of my research work.

I am grateful to **THE MANAGEMENT** and **Dr. V. SUJATHA**, Principal, Cauvery College for Women (Autonomous), Tiruchirappalli, for their valuable suggestions and encouragement and all the teaching and non-teaching staff members of the PG & Research Department of Physics, Cauvery College for Women (Autonomous), Tiruchirappalli, for their memorable support.

I gratefully acknowledge **Dr. V. CHARLES VINCENT**, **Dr. D. MANIMARAN**, **Ms. R. ILAVARASI**, **Ms. K. ASWANIYA**, **Dr. G. SIVA SANKARI**, **Ms. K. KANIMOZHI** and **Dr. V. CHITHIIKA RUBY**, for their timely help and encouragement to complete this research work.

My sincere thanks to the Sophisticated Analytical Instrumentation Facility (SAIF), IIT, Chennai, Sophisticated Test and Instrumentation Centre (STIC), Kerala, Archbishop Casimir Instrumentation Center (ACIC), St. Joseph's College, Tiruchirappalli, Heber Analytical Instrumentation Facility (HAIF), Bishop Heber College, Tiruchirappalli and DST-FIST-Level'0' (Ref.No.SR/FST/College-246/2015(c)) sponsored lab, Cauvery College for Women (Autonomous), Tiruchirappalli, for their kind cooperation and valuable help for the instrumentation facilities provided in this research work.

I gratuitously recognize the spiritual support and endless love shown by my **FAMILY MEMBERS** in completing this work.

N. Manopradha

CONTENTS

Chapter No.			Title	Page No.
	List of	Figures		
	List of	Tables		
	Preface	e		
I	METH		ON TO NUCLEATION, CRYSTAL GROWTH OMPUTATIONAL AND EXPERIMENTAL	1
	1.1	Introduc	ction	1
	1.2	Crystall	ization and Nucleation	2
	1.3	Nucleat	ion Kinetics	2
	1.4	Crystal	Growth Methods	5
	1.5	High Te	emperature Solution Growth	5
	1.6	Low Te	mperature Solution Growth	5
	1.7	The Slo	w Evaporation Method	7
	1.8	Solution	and Solubility	7
	1.9	Saturati	on and Supersaturation	8
	1.10	Comput	rational Studies	10
	1.11	Hirshfel	d Surface Analysis	17
	1.12	Charact	erization Techniques	18
	1.13	Scope o	f the Work	26
	Referen	nces		28
II			AL AND THEORETICAL INVESTIGATIONS R OPTICAL CRYSTAL 2-PICOLINIC ACID	32
	2.1	Introduc	etion	32
	2.2	Experin	nental Analysis	33
		2.2.1	Solubility Study	33
		2.2.2	Nucleation Kinetics and Metastable Zone Width (MZW)	34
		2.2.3	Growth of 2PA Crystal	36
		2.2.4	Powder XRD	36
		2.2.5	UV-vis-DRS Analysis	38
		2.2.6	Fluorescence Analysis	45
		2.2.7	Z-scan Analysis	45

Chapter No.			Title	Page No.
	2.3	Comput	tational Analysis	48
		2.3.1	Optimized Geometry	48
		2.3.2	Hyperpolarizability	50
		2.3.3	Natural Bond Orbital (NBO) Analysis	51
		2.3.4	Mulliken Population Analysis	53
		2.3.5	Molecular Electrostatic Potential (MEP) Analysis	55
		2.3.6	Frontier Molecular Orbital Analysis	56
		2.3.7	Vibrational Spectral Analysis	58
		2.3.8	Hirshfeld Surface Analysis	61
	2.4	Conclus	sions	64
	Refere	ences		66
III	OF	RIMENTA NONLINE HLORO A		72
	3.1	Introduc	ction	72
	3.2	Experin	nental Analysis	73
		3.2.1	Solubility Study	73
		3.2.2	Nucleation Kinetics and Metastable Zone Width (MZW)	74
		3.2.3	Growth of PTCA Crystal	76
		3.2.4	Powder XRD	77
		3.2.5	UV-vis-DRS Analysis	79
		3.2.6	Fluorescence Analysis	83
		3.2.7	Z-scan Analysis	84
		3.2.8	Microhardness Study	85
	3.3	Comput	tational Analysis	88
		3.3.1	Optimized Geometry	88
		3.3.2	Hyperpolarizability	91
		3.3.3	Natural Bond Orbital (NBO) Analysis	92
		3.3.4	Mulliken Population Analysis	93
		3.3.5	Molecular Electrostatic Potential (MEP) Analysis	96
		3.3.6	Frontier Molecular Orbital Analysis	97
		3.3.7	Vibrational Spectral Analysis	98
		3.3.8	Hirshfeld Surface Analysis	101
	3.4	Conclus	sions	103
	Refere	ences		105

Chapter No.			Title	Page No.
IV	OF	RIMENTA NONLINE ZOTRIAZO		110
	4.1	Introduc	etion	110
	4.2	Experin	nental Analysis	111
		4.2.1	Solubility Study	111
		4.2.2	Nucleation Kinetics and Metastable Zone Width (MZW)	112
		4.2.3	Growth of PBTA Crystal	114
		4.2.4	Powder XRD	114
		4.2.5	UV-vis-DRS Analysis	116
		4.2.6	Fluorescence Analysis	121
		4.2.7	Second Harmonic Generation (SHG) Test	121
		4.2.8	Microhardness Study	122
	4.3	Comput	ational Analysis	125
		4.3.1	Optimized Geometry	125
		4.3.2	Hyperpolarizability	128
		4.3.3	Natural Bond Orbital (NBO) Analysis	129
		4.3.4	Mulliken Population Analysis	130
		4.3.5	Molecular Electrostatic Potential (MEP) Analysis	133
		4.3.6	Frontier Molecular Orbital Analysis	134
		4.3.7	Vibrational Spectral Analysis	136
		4.3.8	Hirshfeld Surface Analysis	138
	4.4	Conclus	sions	140
	Refere	ences		142
V	OF	RIMENTA NONLINE ROCHLOI		146
	5.1	Introduc	etion	146
	5.2	Experin	nental Analysis	147
		5.2.1	Solubility Study	147
		5.2.2	Nucleation Kinetics and Metastable Zone Width (MZW)	148
		5.2.3	Growth of PHCL Crystal	150
		5.2.4	Powder XRD	150

Chapter No.			Title	Page No.
		5.2.5	UV-vis-DRS Analysis	152
		5.2.6	Fluorescence Analysis	156
		5.2.7	Z-scan Analysis	157
		5.2.8	Microhardness Study	158
	5.3	Comput	ational Analysis	161
		5.3.1	Optimized Geometry	161
		5.3.2	Hyperpolarizability	163
		5.3.3	Natural Bond Orbital (NBO) Analysis	164
		5.3.4	Mulliken Population Analysis	166
		5.3.5	Molecular Electrostatic Potential (MEP) Analysis	168
		5.3.6	Frontier Molecular Orbital Analysis	168
		5.3.7	Vibrational Spectral Analysis	170
		5.3.8	Hirshfeld Surface Analysis	173
	5.4	Conclus	sions	174
	Refere	ences		176
VI	SUMN	MARY AN	D SUGGESTIONS FOR FUTURE WORK	181
	6.1	Summa	ry	181
	6.2	Suggest	ions for Future Work	185
	ANNE	EXURES		
	*	List of Pu	blications	
	*	List of Pagand Work	per Presented/Participated in Seminar, Conference shop	

* Papers Published

LIST OF FIGURES

Figure No.	Title	Page No.
1.1	Solubility diagram	9
1.2	Schematic diagram of UV-vis-DRS	21
1.3	Block diagram of spectrofluorometer	22
1.4	Experimental Set Up for the Powder SHG Measurement	24
1.5	Experimental Setup for Z-Scan Analysis	26
2.1	Solubility curve for 2PA	33
2.2	Variation of Gibbs free energy with supersaturation and temperature for 2PA	35
2.3	Variation of radius of critical nucleus with temperature and supersaturation ratio of 2PA	35
2.4	As grown crystal of 2PA	36
2.5	Powder XRD pattern of 2PA crystal	37
2.6	Graph plotting βcosθ versus sinθ	38
2.7	Optical absorbance of 2PA	40
2.8	(a-d). Variation of optical constants as a function of photon energy	40
2.9	DASF plot for 2PA crystal	43
2.10	Curves of ln (A/ λ) vs ln (1/ λ - 1/ λ_g)	44
2.11	Urbach plot for 2PA	44
2.12	Fluorescence emission of 2PA crystal	45
2.13	(a) Self-focusing (closed aperture) Z-scan plot of 2PA crystal	48
	(b) Open aperture mode Z-scan plot of 2PA crystal	48
2.14	The optimized molecular structure of 2PA	49
2.15	Mulliken atomic charge distribution of 2PA	54
2.16	Mulliken atomic charges of all the atoms of 2PA	54
2.17	Molecular electrostatic potential of 2PA	55
2.18	HOMO-LUMO Plot of 2PA	58
2.19	(a) Simulated IR spectra of 2PA	59
	(b) FTIR spectra of 2PA	59
2.20	Hirshfeld surfaces for d _{norm} , d _i , d _e and curvedness for the 2PA molecule	62

Figure No.	Title	Page No.
2.21	2D fingerprint plots showing various intermolecular contacts in the 2PA	63
3.1	Solubility curve for PTCA	74
3.2	Variation of Gibbs free energy with supersaturation and temperature for PTCA	75
3.3	Variation of radius of critical nucleus with temperature and supersaturation ratio of PTCA	76
3.4	As grown crystal of PTCA	77
3.5	Powder XRD pattern of PTCA crystal	77
3.6	Graph plotting βcosθ versus sinθ	78
3.7	Optical absorbance of PTCA	80
3.8	(a-d) Variation of optical constants as a function of photon energy	80
3.9	DASF plot for PTCA crystal	81
3.10	Curves of ln (A/ λ) vs ln (1/ λ - 1/ λ_g)	82
3.11	Urbach plot for PTCA	82
3.12	Fluorescence emission of PTCA crystal	83
3.13	(a) Self-focusing (closed aperture) Z-scan plot of PTCA crystal	85
	(b) Open aperture mode Z-scan plot of PTCA crystal	85
3.14	(a) variation of H _v against applied load P	86
	(b) log P against log d	86
	(c) H _v against d	86
3.15	Load P against d ²	87
3.16	Load P against Elastic Stiffness Constant (C ₁₁)	88
3.17	The optimized molecular structure of PTCA	89
3.18	Mulliken atomic charge distribution of PTCA	95
3.19	Mulliken atomic charges of all atoms of PTCA	95
3.20	Molecular electrostatic potential of PTCA	96
3.21	HOMO-LUMO Plot of PTCA	98
3.22	(a) Computed IR spectra of PTCA	99
	(b) Experimental FTIR spectra of PTCA	99
3.23	Hirshfeld surfaces for $d_{\text{norm}},\ d_i,\ d_e$ and curvedness for the PTCA molecule	102

Figure No.	Title	Page No.
3.24	2D fingerprint plots showing various intermolecular contacts in the PTCA	103
4.1	Solubility curve for PBTA	111
4.2	Variation of Gibbs free energy with supersaturation and temperature for PBTA	113
4.3	Variation of radius of critical nucleus with temperature and supersaturation ratio of PBTA	113
4.4	As grown crystal of PBTA	114
4.5	Powder XRD pattern of PBTA crystal	115
4.6	Graph plotting βcosθ versus sinθ	116
4.7	Optical absorbance of PBTA	117
4.8	(a-d) Variation of optical constants as a function of photon energy	118
4.9	DASF plot for PBTA crystal	119
4.10	Curves of ln (A/ λ) vs ln (1/ λ - 1/ λ _g)	120
4.11	Urbach plot for PBTA	120
4.12	Fluorescence emission of PBTA crystal	121
4.13	(a) Variation of H _v against applied load P	123
	(b) log P against log d	123
	(c) H _v against d	123
4.14	Load P against d ²	124
4.15	Load P against Elastic Stiffness Constant (C ₁₁)	124
4.16	The optimized molecular structure of PBTA	126
4.17	Mulliken atomic charge distribution of PBTA	132
4.18	Mulliken atomic charges of all atoms of PBTA	132
4.19	Molecular electrostatic potential of PBTA	133
4.20	HOMO-LUMO Plot of PBTA	135
4.21	(a) FTIR spectra of PBTA	136
	(b) computed IR spectra of PBTA	136
4.22	Hirshfeld surfaces for d_{norm} , d_{i} , d_{e} and curvedness for the PBTA molecule	139
4.23	2D fingerprint plots showing various intermolecular contacts in the PBTA	140
5.1	Solubility curve for PHCL	147

Figure No.	Title	Page No.
5.2	Variation of Gibbs free energy with supersaturation and temperature for PHCL	149
5.3	Variation of radius of critical nucleus with temperature and supersaturation ratio of PHCL	149
5.4	As grown crystal of PHCL	150
5.5	Powder XRD pattern of PHCL crystal	151
5.6	Graph plotting $\beta\cos\theta$ versus $\sin\theta$	152
5.7	Optical absorbance of PHCL	153
5.8	(a-d) Variation of optical constants as a function of photon energy	153
5.9	DASF plot for PHCL crystal	155
5.10	Curves of ln (A/ λ) vs ln (1/ λ - 1/ λ _g)	155
5.11	Urbach plot for PHCL	156
5.12	Fluorescence emission of PHCL crystal	157
5.13	(a) Self-focusing (closed aperture) Z-scan plot of PHCL crystal	158
	(b) Open aperture mode Z-scan plot of PHCL crystal	158
5.14	(a) Variation of H _v against applied load P	159
	(b) log P against log d	159
	(c) H _v against d	159
5.15	Load P against d ²	160
5.16	Load P against Elastic Stiffness Constant (C ₁₁)	161
5.17	The optimized molecular structure of PHCL	162
5.18	Mulliken atomic charge distribution of PHCL	167
5.19	Mulliken atomic charges of all atoms of PHCL	167
5.20	Molecular electrostatic potential of PHCL	168
5.21	HOMO-LUMO Plot of PHCL	170
5.22	(a) Experimental FTIR spectra of PHCL	171
	(b) Computed IR spectra of PHCL	171
5.23	Hirshfeld surfaces for d_{norm} , d_{i} , d_{e} and curvedness for the PHCL molecule	173
5.24	2D fingerprint plots showing various intermolecular contacts in the PHCL	174

LIST OF TABLES

Table No.	Title	Page No.
2.1	Nucleation Table from 2PA for Supersaturation Ratio-1.1	35
2.2	Optical parameters of 2PA	43
2.3	Obtained nonlinear optical parameter from open- and closed-aperture Z-scan measurement data for 2PA crystal	47
2.4	Optimized parameters of 2PA by B3LYP level with 6-311++G(d,p) basis set	49
2.5	NLO properties of 2PA calculated using DFT at B3LYP/6-311++G (d,p) level	51
2.6	Second order perturbation theory analysis of Fock matrix in NBO basis including the stabilization energies using DFT at B3LYP/ $6\text{-}311\text{++}G(d,p)$ level	52
2.7	Natural population analysis (NPA) of 2PA calculated with DFT/B3LYP/6-311++G(d,p) method	53
2.8	Calculated quantum chemical molecular orbital properties for 2PA at DFT/B3LYP/6-311++G(d,p) method	57
2.9	Experimental and calculated vibrational wavenumbers and fundamental bands positions assignments of 2PA	61
3.1	Nucleation Table from PTCA for Supersaturation Ratio-1.1	75
3.2	Optical parameters of PTCA	81
3.3	Obtained nonlinear optical parameter from open- and closed-aperture Z-scan measurement data for PTCA crystal	84
3.4	Hardness parameters of PTCA	86
3.5	Optimized parameters of PTCA by B3LYP level with 6-311++G(d,p) basis set	90
3.6	NLO properties of PTCA calculated using DFT at B3LYP/ 6-311++G(d,p) level	91
3.7	Second order perturbation theory analysis of Fock matrix in NBO basis including the stabilization energies using DFT at B3LYP/ $6-311++G(d,p)$ level	93
3.8	Natural population analysis (NPA) of PTCA calculated with DFT/B3LYP/6-311++G(d,p) method	94
3.9	Calculated quantum chemical molecular orbital properties for PTCA	97
3.10	Experimental and calculated vibrational wavenumbers and fundamental bands positions assignments of PTCA	101

4.1	Nucleation Table from PBTA for Supersaturation Ratio-1.1	112
4.2	Optical parameters of PBTA	119
4.3	Hardness parameters of PBTA	123
4.4	Optimized parameters of PBTA by B3LYP level with 6-311++G(d,p) basis set	126
4.5	NLO properties of PBTA calculated using DFT at B3LYP/6-311++G(d,p) level	128
4.6	Second order perturbation theory analysis of Fock matrix in NBO basis including the stabilization energies using DFT at B3LYP/6-311++G(d,p) level	130
4.7	Natural population analysis (NPA) of PBTA calculated with DFT/B3LYP/6-311++G(d,p) method	131
4.8	Calculated quantum chemical molecular orbital properties for PBTA	135
4.9	Experimental and calculated vibrational wavenumbers and fundamental bands positions assignments of PBTA	138
5.1	Nucleation Table from PHCL for Super Saturation Ratio-1.1	149
5.2	Optical parameters of PHCL	154
5.3	Obtained nonlinear optical parameter from open- and closed-aperture Z-scan measurement data for PHCL crystal	158
5.4	Hardness parameters of PHCL	159
5.5	Optimized parameters of PHCL by B3LYP level with 6-311++G(d,p) basis set	163
5.6	NLO properties of PHCL calculated using DFT at B3LYP/6-311++G(d,p) level	164
5.7	Second order perturbation theory analysis of Fock matrix in NBO basis including the stabilization energies using DFT at B3LYP/6-311++G(d,p) level	165
5.8	Natural population analysis (NPA) of PHCL calculated with DFT/B3LYP/6-311++G(d,p) method	166
5.9	Calculated quantum chemical molecular orbital properties for PHCL at DFT/B3LYP/6-311++G (d, p) method	169
5.10	Experimental and calculated vibrational wavenumbers and fundamental bands positions assignments of PHCL	172
6.1	Summary of present work	185

PREFACE

a. Title of the thesis

OF PICOLINIC ACID BASED SINGLE CRYSTALS

b. State of the art of the research topic

Organic nonlinear optical materials have recently received a lot of attention due to their prospective uses in photonics, optical data storage devices, high-speed telecommunications, electro optical modulation, nonlinear optics, and detection. Despite the fact that various organic materials have been studied for these applications, 2-picolinic acid (also known as pyridine-2-carboxylic acid, 2-pyridine carboxylic acid and picolinic acid) based single crystals are being evaluated as an alternative due to their improved nonlinear optical (NLO) capabilities. Pyridine-2-Carboxylic acid possesses two strong carboxylic active groups. A carboxylic group and a pyridine nitrogen atom of carboxylic group tend to ionize the molecule, but cannot ionize completely due to its weak acidic property. As a result, picolinic acid functions as a base, forming the molecule via pyridine nitrogen atoms. Pyridine-2-Carboxylic acid compound has many biological, chemical and medical applications and has the tendency to form a stable compound. However, new materials are produced using organic and inorganic materials, which are referred to as semiorganic materials, in order to attain enhanced physical properties. These semiorganic materials have strong mechanical strength, thermal and nonlinear coefficient, and can be used for laser manufacturing, optical data processing, and optical limits. Owing to their suitability for optical limiting applications, picolinic acid based crystals may be worth investigating. These materials could be used to shield human eyes and delicate optical sensors from strong lasers.

c. Definition of the Problem

The current study focuses on the growth and characterization of organic and semiorganic nonlinear optical crystals based on pyridine-2-carboxylic acid. Since the first prediction of the nonlinear optical process, the field of molecular nonlinear optics has been growing, and Franken's experimental observation of nonlinear optical phenomena in 1961 gave it a big push. The invention of the modern laser provided

scientists with a source of high-intensity fields, which were required for nonlinear optical processes to work. Inorganic crystals were used to make the majority of early nonlinear optical materials. However, due to the much larger design flexibility in molecular compounds, which allows for careful adjustment of the microscopic characteristics and consequently the linear and nonlinear optical behavior of the materials, attention has recently switched to organic molecules. Generally the organic materials have high second order Nonlinear Optical (NLO) efficiency because the organic materials have more π -conjugation hydrogen bonded system. However, the mechanical and thermal stability of most organic nonlinear optical materials is low. Organic materials are mixed with inorganic compounds to improve mechanical strength and thermal stability. Hence, the goal of this research was to generate and characterize single crystals made of organic and semiorganic materials for NLO applications. The thesis summarizes the procedure and findings of organic and semiorganic based crystals. Single crystals of 2-Picolinic Acid (2PA), 2-Picolinic Trichloro Acetate (PTCA), 2-Picolinic Benzotriazole (PBTA), and 2-Picolinic Hydrochloride (PHCL) are studied.

Scope of the research work

The current research focused on:

- To grow the organic and semiorganic single crystals based on pyridine-2carboxylic acid
- Estimation of materials solubility and different nucleation kinetic parameters
- Using powder X-ray diffraction studies to determine the crystal structure
- Evaluate the average crystallite size of the grown crystal and its lattice strain using the Williamson–Hall technique
- FTIR, UV spectral analysis, energy band gap, optical constants, fluorescence, Second Harmonic Generation (SHG), Z-scan, and microhardness studies are used to characterize the grown crystals.
- Density Functional Theory (DFT) investigations to understand molecular behavior of the materials
- NBO analysis determines the inter- and intramolecular charge transfer interactions as well as the molecules stability.
- Hirshfeld surface analysis reveals the percentage of strong and weak intermolecular interactions in crystals.

d. Results and Discussion

Experimental Details

(i) Solubility studies and Nucleation kinetics

The solubility tests were carried out in a temperature bath that was kept at a constant temperature of 0.01°C. The solute was mixed with double distilled water until it achieved saturation. Gravimetric analysis was used to determine the solute's equilibrium concentration. The experiment was carried out at various temperatures. The solubility of formed crystals and the width of their metastable zone as a function of temperature are studied. The parameters of nucleation at various super saturation levels were calculated.

(ii) Synthesis and Crystal Growth

Slow evaporation was used to form single crystals of organic and semiorganic materials in an equimolar ratio. For additional purification, the crystallization process was repeated. At room temperature, perfect single crystals with optimum transparency were achieved.

(iii) Powder X-ray analysis

The powder X-ray diffraction technique was used to analyze the structural information of the grown crystals, such as lattice constants, space group, and crystal system.

(iv) FTIR analysis

To examine the various functional groups present, the molecular structure of the formed crystal was subjected to FTIR analysis using the KBr pellet method. This technique was used to identify the vibrational modes of the grown crystals.

(v) UV-DRS (Diffuse Reflectance Spectroscopy) analysis

UV spectrum analysis revealed the transparent nature of the grown crystals. The UV spectra were used to determine the absorption range of the synthesized crystals. The transparencies of the obtained crystals, as well as their different optical constants, were determined.

(vi) Analysis of fluorescence emission and Z-scan

Spectro Fluorophotometer was used to get the fluorescence spectrum. It gives growing crystals their emission color. The second order NLO characteristics of the grown crystals were investigated using the Kurtz powder SHG technique whereas the third order NLO characteristics were studied by means of the Z-scan technique.

(vii) Mechanical research

The mechanical stability of the grown crystal was assessed using a Vickers microhardness tester, and the work hardening coefficient was computed.

Computational Studies

All computational analyses in this thesis were carried out using the GAUSSIAN 09W DFT programme with the B3LYP method 6-311++G(d,p) as the basis set. The results of the molecules were viewed using the GAUSSVIEW 5.0 molecular visualization tool.

Original contribution

2-Picolinic Acid: The slow evaporation approach was used to grow single crystals of 2-Picolinic acid (2PA). The powder X-ray diffraction results reveal that the grown crystal is a monoclinic system with space group $C2_c$. Williamson–Hall approach indicates the minimum value of lattice strain on the grown crystal has lower dislocation density. The nucleation parameters was assessed at various supersaturation ratios (1.1-1.4) at 304, 308, 316 and 321K. The metastable zone width of crystal as a function of supersaturation is studied. The grown crystal shows good transmittance in the entire visible region. Optical band gap value is calculated to be 3.5 eV by using Tauc's method and 3.47 eV by Derivation of absorption spectrum fitting (DASF) method. Fluorescence emission analysis confirms the emission of 2PA is in the blue region. A computation of 2PA molecule calculated gives the optimized structure. Bond length and bond angle are calculated theoretically by DFT method. The functional groups in the 2PA molecule were identified using theoretical and experimental IR spectroscopy analysis. The molecular energy gap was found via HOMO-LUMO analysis. Apart from that, the DFT/B3LYP/6-311++G(d,p) basis set was used to calculate the NBO analysis and the first hyperpolarizability parameters. Intermolecular interactions were analyzed using three-dimensional Hirshfeld surfaces. It exhibits that

H···H/H···H interactions contribute 44.4% and the 28.1% contribution from the O···H/H···O interactions of the total Hirshfeld surface. All above results show that the 2-picolinic acid crystal has good quality with improved crystalline perfection and optical transparency.

2-Picolinic Trichloro Acetate: The slow evaporation solution growth technique was used to grow single crystals of 2-picolinic trichloro acetate (PTCA). Powder Xray diffraction revealed the monoclinic crystal structure with space group $P2_1$. The solubility curve exhibits positive solubility coefficient. The metastable zone width, interfacial surface energy, critical free energy, free energy change and critical radius have been estimated. From UV-Vis-DRS studies, it is witnessed that PTCA has minimum absorption, which is the key requirement for materials having Nonlinear Optical (NLO) applications. It shows the maximum absorption peak at 260 nm which corresponds to π – π * transition. The Z-scan technique points out the reverse saturated absorption optical process observed in the PTCA crystal. The fluorescence test shows PTCA has blue color emission. The mechanical behavior reveals that the PTCA crystal belongs to soft category. Density Functional Theory (DFT) computations of PTCA molecule calculated by DFT (B3LYP) level with 6-311++G(d,p) basis set gives the optimized structure. Bond lengths and bond angles determined experimentally are compared to those calculated theoretically. Theoretical and experimental IR spectroscopic analysis was carried out and the presence of functional groups in PTCA molecule was qualitatively analyzed. The NBO analysis reveals the possible intramolecular charge transfer interactions and stability in PTCA. The Molecular Electrostatic Potential (MEP) study confirms PTCA as an electron rich species and explains its electrophilic nature. The hardness value and negative chemical potential from HOMO-LUMO indicate that the PTCA molecule is stable. The Hirshfeld surface analysis of PTCA interprets the percentage of strong and weak intermolecular interactions in the crystalline state.

2-Picolinic benzotriazole: The defect free ideal crystal of 2-picolinic benzotriazole (PBTA) has been effectively grown up from the solvent evaporation technique using methanol as solvent at room temperature. Nucleation kinetics of PBTA crystal is analyzed. Powder XRD analysis was performed on the grown crystals, and the results revealed an orthorhombic crystal structure with the space group *Pna2*₁. From optical

absorption spectrum it is found that it has minimum absorption between 200-1100 nm. The optical band gap of the material is found as 3.49 eV by using Tauc's method and 3.46 eV by DASF method. The optical parameters of PBTA crystal is calculated and related with incident photon energy. The NLO efficiency of the grown crystal is analyzed by Kurtz-Perry method. From Vicker's test it inferred that hardness number H_v increases with the increasing load and the Meyer's value is determined as 1.6. Optimization of PBTA single crystal is performed by using DFT approach. The first order hyperpolarizability for this molecule is in suitable range to exhibit NLO behavior. Molecular energy gap of PBTA is found as 4 eV by HOMO-LUMO analysis. Theoretically calculated vibrational frequencies are compared with experimentally obtained FTIR frequencies. Spectral assignments are carried out for various vibrational frequencies. Hirshfeld surface analysis and 2-dimensional finger print plot quantify the interactions associated with PBTA molecule.

2-Picolinic hydochloride: The 2-picolinic hydochloride (PHCL) crystal was successfully grown by using the solvent evaporation method. Powder XRD confirmed PHCL single crystal belongs to orthorhombic system with space group *Pnma*. The optical absorption study reveals grown crystal has the wide transparency nature in the entire visible spectral range, which makes these crystals potentially active material for device applications. Third order nonlinearity of the PHCL compound is determined using Z-Scan technique. Mechanical studies reveal reverse indentation size effect (RISE) and the work hardening coefficient was found to be 2.8. The elastic stiffness constant (C₁₁) was calculated and it confirms the tightness of bonding between the neighboring atoms. The experimental FTIR assignments were compared to theoretically computed values using the 6-311++G(d,p) basis set. Theoretical and experimental values are in good accord. The NBO analysis discloses the possible inter- and intramolecular charge transfer interactions (ICT) and stability in PHCL. The computed HOMO-LUMO energy gap is 3.63 eV. First order hyperpolarizability of PHCL is calculated. Hirshfeld surface analysis of PHCL reveals intermolecular interactions in the crystalline state. Further, the fingerprint 2D plots confirm the percentage of interaction present in the PHCL molecule.

e. Conclusion

The work deals with analyzing the solubility of the 2PA, PTCA, PBTA and PHCL crystals at different temperatures. Nucleation parameter has been evaluated. Powder X-ray diffraction (XRD) studies establish the crystal structure. Williamson-Hall approach assesses the structural characteristics such as, average crystallite size of the grown crystals and its lattice strain. The structural and optical characterization of the crystals was analyzed experimentally by Fourier transform infrared, UV-DRS technique and theoretical studies, by density functional theory method. This study elucidates various physico-chemical behaviors of 2PA, PTCA, PBTA and PHCL crystals in both experimental and theoretical methods at the same time. The optical properties of the grown crystals and their band gap energy value are determined by both Tauc's and DASF (Derivation of absorption spectrum fitting) method. The emission characteristics of the grown crystal were verified by Fluorescence studies. Z-scan technique confirms the third order optical behavior of the 2PA, PTCA and PHCL crystals. Kurtz-Perry technique was used to determine the SHG efficiency of the grown PBTA crystal. The charge transfer interactions leading to nonlinear properties taking place in the molecule has been studied by highest energy occupied molecular orbital and lowest energy unoccupied molecular orbital analysis and natural bond orbital analysis. Hirshfeld surface maps and fingerprint graphs gives the various types of intermolecular interactions in the molecular crystal package. From the above studies, it could be proved that above selected crystals are very suitable for optical device applications.

Chapter-I

Introduction to Nucleation, Crystal Growth Methods, Computational and Experimental Techniques

CHAPTER - I

INTRODUCTION TO NUCLEATION, CRYSTAL GROWTH METHODS, COMPUTATIONAL AND EXPERIMENTAL TECHNIQUES

1.1. INTRODUCTION

In the creation of contemporary materials such as semiconductors for electrical devices, solar cells, and lasers, crystalline materials play a significant role in both science and industry [1]. A vast range of modern materials may now be manufactured or grown as crystals artificially. There has been a growing interest in crystal formation technologies in recent decades, to readily meet out the requirements of basic research and technological applications. Single crystals of appropriate size and quality are required for the above criteria. Many physical features of solids are veiled or confounded by the effect of grain boundaries, which is why single crystals are grown. Single crystals can have unique mechanical, optical, and electrical properties because to the lack of flaws associated with grain boundaries, which can also be anisotropic depending on the type of crystallographic structure. As a result, new fields of application necessitate the use of high-quality single crystals. [2]

Crystal growth processes, in general, are complicated systems of motion, temperature regulation, heat transmission, and fluid dynamics. Heat and mass transfer mechanisms, as well as convection effects, are all involved in crystal growth. The quality of the developing crystals is heavily influenced by the temperature and concentration fields. As a result, proper fluid dynamics management and a thorough grasp of convection phenomena are important for the formation of high-quality single crystals.

1.2. CRYSTALLIZATION AND NUCLEATION

The process of crystallization entails the production of a seed crystal and the subsequent expansion of the nucleus. Condensation and evaporation are two types of processes that occur at the crystal—solution interface during the development of a seed crystal. The change in Gibbs free energy between the supersaturated/supercooled mother phase (liquid phase) and the newly created phase (solid phase) is influenced by these two processes, and the change in Gibbs free energy acts as a driving factor to promote the crystallization process [3,4]. Crystal nucleation and growth theory, in which atoms or molecules are assumed to assemble directly from solution, is commonly used to describe the development of crystalline materials from solution.

1.3. NUCLEATION KINETICS

Nucleation studies are helpful in interpreting correct supersaturation in order to achieve a controlled nucleation rate and high-quality single crystals [5]. Gibbs was the first to establish the concept of nucleation kinetics. Nucleation is the first step in the development of a crystal from a solution, in which a limited number of ions form a pattern and serve as a location for additional particles to be deposited as the grown crystals. The nucleation process must overcome the potential barrier in order to develop a new nucleus from the parent phase. It is accomplished by the process of super saturation, which results in the production of seed nuclei. The nucleation rate parameter, which is important in the development of new phases, regulates the process of nucleation. The interfacial energy, which is an important parameter in the theories of nucleation and crystal growth, is formed at the solution–solid interface. However, in the nucleation tests, certain challenges were encountered, such as the demand for a solution devoid of foreign particles, the volume of the solution, and so on. Several researchers have made

theoretical attempts to determine the interfacial energy using solubility data [6,7]. The nucleation process is influenced by the interfacial energy of the solid-liquid interface. Bennema and Sohnel [8] have obtained an expression that describes the linear relationship of interfacial energy (σ) on solubility based on solution kinetics theory:

$$\sigma = \left(\frac{kT}{d^2}\right) [0.173 - 0.248 \ln \chi_m] \qquad ... (1.1)$$

 σ - interfacial energy (J/m²); K - Boltzmann constant (J K¹¹); T-Temperature in (K); d - mean molar ionic diameter in crystal = {(6/\pi)v}¹¹³; χ_m - mole fraction of solute in solution.

The relationship between the solubility and enthalpy of a real solution is given as [9]:

$$\ln \chi_{\rm m} = \left(-\Delta H_{\rm S} / RT\right) + \left(\Delta S_{\rm E} / R\right) \qquad \dots (1.2)$$

where ΔH_s is the Enthalpy of fusion (J mol⁻¹); R - Gas constant (J K⁻¹mol); ΔS_E - Excess entropy of mixing.

From Eqs. (1.1) and (1.2), it is clear that plotting of $\ln \chi_m$ vs 1/T yields a straight line with a slope equal to $\left(\Delta H_s\right)_R$ and an intercept equal to $\left(\Delta S_E\right)_R$, allowing the value of ΔH_s to be calculated from the solubility curve. The creation of microscopic clusters of molecules known as embryos can be caused by fluctuations in the supersaturated solution [10]. The change in entropy per unit volume is expressed by

$$\Delta G_{v} = -\left(\frac{KT \ln S}{V}\right) \qquad \dots (1.3)$$

where V, stands for the solute molecules specific volume.

A change in Gibbs free energy for the production of nuclei (spherical) involves two terms, namely the volume free energy term and the surface free energy term. According to classical nucleation theory [11], it may be derived by Eq. (1.4)

$$\Delta G = 4\pi r^2 \sigma + \left(\frac{4}{3}\right) \pi r^3 \Delta G_v \qquad \dots (1.4)$$

The free energy of formation obeys the condition $\left(\frac{d\left(\Delta G\right)}{dr}\right)=0$ at the critical state.

As a result, the critical radius (r^*) and critical free energy barrier (ΔG^*) for nucleation [11] can be written as

$$\mathbf{r}^* = -\frac{2\sigma}{\Delta G_{v}} \qquad \dots (1.5)$$

$$\Delta G^* = \frac{16\pi\sigma^3}{3\Delta G_v^2} \qquad \dots (1.6)$$

The number of molecules in the critical nucleus is represented as

$$i^* = \frac{4\pi [r]^*}{3V}$$
 ... (1.7)

The rate of nucleation (J) is computed using,

$$J = A \exp\left(\frac{-\Delta G^*}{KT}\right) \qquad \dots (1.8)$$

where J is the nucleation rate (nuclei/m 3 /s), ΔG^* is the critical free energy barrier (J) and A is a slow-changing pre-exponential component compared to the exponential term:

$$A = \frac{Zv}{d^2} exp\left(\frac{-\Delta G_{diff}}{KT}\right) 4\pi r^{*2} C(i) \qquad \dots (1.9)$$

$$Z = 0.01, \, v = 10^{12} \; Hz, \, C(i) = 1, \; \Delta G_{\rm diff} = \frac{-\Delta G^*}{KT}$$

where Z is the Zeldowhich factor, v is the attachment frequency, and C(i) is the equilibrium concentration. The nucleation parameters of crystals are computed using equations (1.1) to (1.8) at varying temperatures with constant supersaturation ratio and vice versa.

1.4. CRYSTAL GROWTH METHODS

Solid-to-solid, liquid-to-solid, and vapor-to-solid phase changes culminate in crystal development. In general, crystal growth processes are divided into two categories: solution growth and melt growth [12]. The kind of crystallization is used to classify the crystal growth procedures, and one of them is solution growth. Low temperature solution growth and high temperature solution growth are two types of growth process.

1.5. HIGH TEMPERATURE SOLUTION GROWTH

The elements of the material to be crystallized are dissolved in a suitable solvent in high-temperature solutions, and crystallization occurs when the solution becomes critically supersaturated. There are two major categories of high-temperature crystal growth:

- Growth from single component system.
- Growth from multi component system.

For the development of oxide crystals, the above approach is commonly utilized. The technique entails heating the flux and solute container to a temperature where all of the solute materials dissolve. The temperature is maintained for a 'soak' period of several hours, after which it is gradually reduced.

1.6. LOW TEMPERATURE SOLUTION GROWTH

One of the oldest ways of crystal formation is the generation of crystals from aqueous solution. In the synthesis of many technologically essential crystals, the process of crystal growth from low temperature aqueous solutions is particularly popular. When the starting materials are unstable at high temperature and also undergo phase changes below melting point, it is the most extensively employed approach for the

growth of single crystals. Crystal growth through low temperature solution growth might take long period of duration. Though the technology for growing crystals from solutions has been refined, it still requires meticulous effort and a lot of time. Months of work can be ruined by a power outage or a tainted batch of raw material. Lowtemperature solution technique may produce materials with moderate to high solubility in the temperature range of ambient to 100°C at atmospheric pressure. The interaction of ions or molecules of the solute and the solvent, which is based on the solubility of the substance on the thermodynamical parameters of the process; temperature, pressure, and solvent concentration which governs the mechanism of crystallization from solutions. The advantages of crystal growth from a low-temperature solution closer to the ambient temperature result in a simple and straight forward equipment design that provides a fair degree of control with a temperature accuracy of ± 0.01°C. Supersaturation may be precisely managed owing to the exact temperature control. In addition, effective solution stirring decreases variations to a minimum level. The crystals proximity to ambient temperature decreases the risk of significant thermal shock during growth and removal from the apparatus.

The main drawbacks of low-temperature solution growth include the slow pace of development in many circumstances and the ease with which solvent can be incorporated into the forming crystal. Solvent inclusion may be avoided under regulated growth circumstances, and the high quality of the grown crystal can compensate for the drawback of significantly longer development times. The three types of low-temperature solution growth include slow cooling, slow evaporation, and temperature gradient methods. A full grasp of these distinct crystal growth mechanisms is required for the

formation of single crystals. In the present work, single crystals were grown using the slow evaporation solution growth technique.

1.7. THE SLOW EVAPORATION METHOD

One of the simple and effective methods of crystallizing organic and semiorganic compounds is slow evaporation. The difference between the rate of evaporation of the solvent and the solute is used to determine an excess of a certain solute in this technique. The vapour pressure of the solvent above the solution is higher than the solute vapour pressure. As a result, the solvent evaporates faster, causing the solution to become supersaturated. For materials with a very low temperature coefficient of solubility, this approach can be used.

1.8. SOLUTION AND SOLUBILITY

The term "solution" is most usually used to refer to the liquid that results from dissolving a specific amount of a chemical in a pure liquid. Solute is the component in a solution that is present in a lower quantity. The amount of material accessible for growth is determined by the solubility of the substance in a solvent, which limits the total size limit. There may be several solvents for a given solute. The growth technique is dictated by the solubility gradient, which is a crucial parameter. It will be seen that the saturation of a given solvent by a solid (the solute) is represented by a series of values that may be plotted on a curve with temperatures as ordinates and solute concentrations as abscissae. For every given solvent, a series of points can be plotted for any chemical soluble in it; these curves are known as solubility curves or saturation curves. A flat or steep solubility curve will not allow the growth of bulk crystals from solution, and the level of supersaturation in the former cannot be changed by lowering the temperature.

In both circumstances, even a little change in temperature will impact the supersaturation required to grow good quality bulk crystals. In order to calculate the amount of supersaturation, solubility data at various temperatures is required. As a result, before beginning the growth process, the solutes solubility in the chosen solvent must be determined. When the solubility gradient is very small, slow evaporation of the solvent provides an alternative for crystal formation to keep the solution supersaturated. If the solubility of a substance increases with increasing temperature, it is referred to as positive temperature coefficient material; if it decreases with increasing temperature, it is stated as negative temperature coefficient material. The vast majority of the materials have a positive temperature coefficient.

1.9. SATURATION AND SUPERSATURATION

A solution is considered to be saturated with regard to the solid phase if it is in equilibrium with it. A supersaturated solution is one that contains more dissolved solids than the saturation state represents. Uncontaminated solutions in clean containers can easily be made to exhibit substantial degrees of supersaturation when cooled slowly and without disturbance in a dust-free environment. For the solution growth process, supersaturation is a crucial characteristic. As a degree of supersaturation is maintained, the crystal grows by the addition of the solute in the solution. To calculate the amount of supersaturation, solubility data at various temperatures is required. As a result, before beginning the growth process, the solutes solubility in the chosen solvent must be determined [13]. Fig. 1.1 depicts a typical solubility diagram.

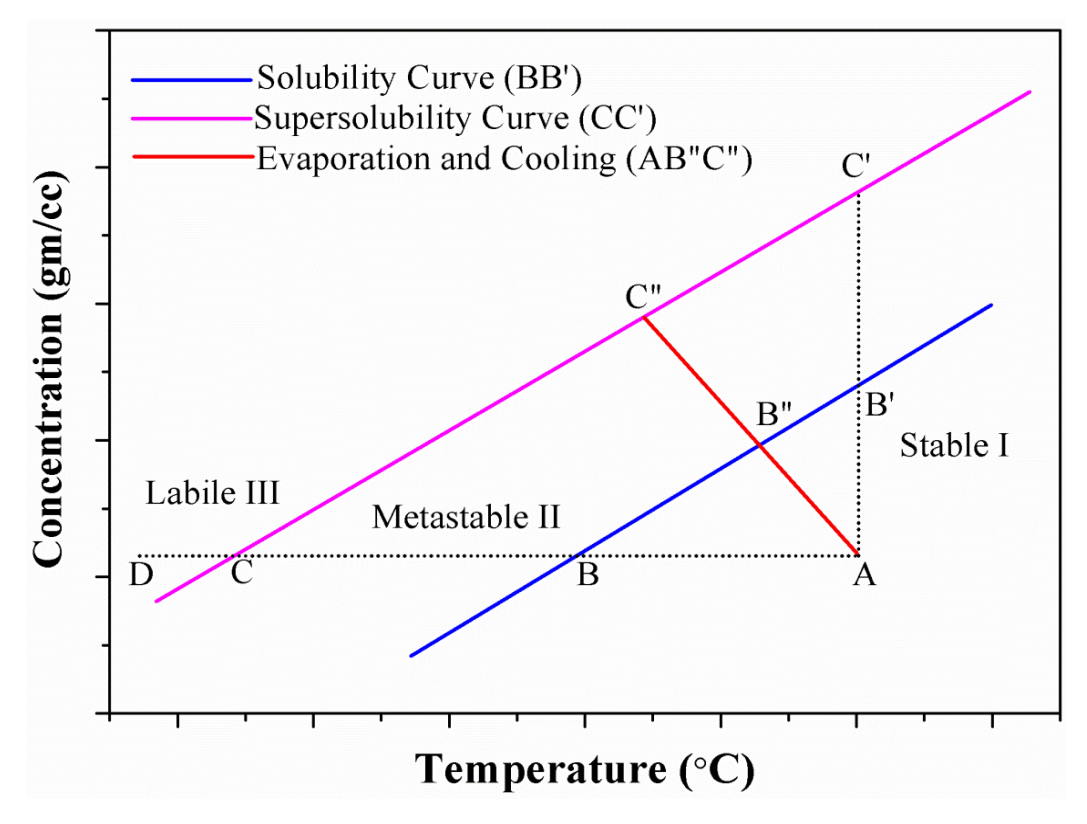


Fig. 1.1. Solubility diagram

The normal solubility curve for the substance in question is the lower continuous line. The upper curve, also known as the supersolubility curve, depicts the temperatures and concentrations at which spontaneous crystallization occurs. The curve is not as well defined as the solubility curve, and its location in the diagram is dependent on other factors like the degree of agitation of the solution. In the supersaturated zone above the solubility curve, there is a region of metastability. As a result, the diagram is separated into three zones:

- i. Region I corresponds to the stable (unsaturated) zone, which is incapable of crystallization. Thermodynamically, this zone is stable.
- ii. The metastable (supersaturated) zone, which lies between the supersolubility and solubility curves, is where spontaneous crystallization is unlikely. A crystal seed, on the other hand, would grow if placed in such a metastable solution.

iii. Region III refers to the unstable or labile (supersaturated) zone where spontaneous crystallization is possible.

The solution must be supersaturated in order to grow crystals; the concentration of the solute in the solvent must be greater than the equilibrium concentration. A system supersaturation can be expressed in a variety of ways. The following is the relationship between the concentration driving force (Δc), the supersaturation ratio (S), and relative supersaturation:

Concentration driving force
$$\Delta c = c - c_0$$
 ... (1.10)

Supersaturation ratio
$$S = c / c_0$$
 ... (1.11)

Relative supersaturation =
$$(c - c_0) / c_0$$
 ... (1.12)

Relative supersaturation
$$= S - 1$$
 ... (1.13)

1.10. COMPUTATIONAL STUDIES

Computational chemistry uses the results of theoretical chemistry to calculate the structure and characteristics of molecules using an efficient computer programme. It calculates the structure, relative energy, charge distribution, dipole moment, vibrational frequency, reactivity, and other spectroscopic quantities of a molecule. Quantum chemical calculations are today performed on a wide range of molecules using advanced computer programs. Ionization energy (HOMO energy), electron affinity (LUMO energy), proton affinity, electronic excitation energy (UV-Vis spectra), NMR chemical shifts and coupling constants, reaction path, and reaction rate are all calculated using computational chemistry. Computational models based on molecular or quantum mechanics are the most common one. Both approaches result in a total energy equation for the structure. Energy minimization, identifying stable conformations, energy calculation for specific conformations, researching molecule motion, and

investigating diverse conformations are all possible using molecular mechanics. Quantum mechanics may be used to calculate molecular orbital energies, heat formation for certain conformations, dipole moments, bond dissociation energies, and transition-state geometries and energies.

There are three types of quantum mechanics methods:

- 1. Molecular mechanics
- 2. Semiemperical method
- 3. *Ab inito* method

1.10.1. Ab initio Methods

Normal mode harmonic force constants and frequencies can be predicted using ab initio orbital molecular techniques. Ab initio approaches optimize the molecule geometry first, then use analytical derivatives to evaluate the second derivative at the equilibrium points. For somewhat large molecules, such approaches yield credible results for harmonic vibrational frequencies. Furthermore, such computations can be utilized to estimate internal rotational barriers as well as relative conformer stabilities. Structure characteristics, conformational stabilities, force constants, vibrational frequencies, and infrared and Raman band intensities all contribute to the field of vibrational spectroscopy in significant ways. Ab initio computations can be used to generate harmonic force constants in Cartesian coordinates. These force constants can be converted to internal or symmetry coordinates force constants. Making reliable vibrational assignments requires ab initio calculations followed by normal coordinate analysis. Another key outcome is band intensities from ab initio studies. This type of band intensity data can also help with vibrational assignments. The Hartree-Fock technique and Density Functional Theory (DFT) are two fundamentally distinct quantum mechanical strategies for addressing vibrational problems.

The technique makes no concessions to the theoretical quantum mechanical framework that is utilized to precisely describe molecular systems. In calculating the integrals that arise during the complex computations, no compromises are made. The following are the different *ab intio* techniques in use:

- Hartree Fock or MO theory
- Configuration Interaction (CI) method
- Perturbation theory (PT)
- Density Functional theory (DFT)

1.10.2. Density Functional Techniques in ab initio Methods

In recent years, the utilization of density functional theory computations has grown in importance. The accurate prediction of numerous observables in chemical systems has prompted continuous research in other fields to determine the accuracy of calculating methods, with unexpectedly good findings. The current research focuses mostly on the spectral analysis of pesticide chemicals, where DFT calculations have proven to be an invaluable tool in pesticide research. Because of its efficiency and accuracy in evaluating a variety of molecular properties, spectroscopic studies using DFT methods have proven to be a crucial tool for interpreting and estimating the numerous molecular features of pesticide materials. The introduction of lasers and the widespread availability of fast computers, as well as sophisticated computational approaches, have simplified the task of resolving different structural chemistry difficulties in pesticide samples.

DFT calculations have lately proven to be an effective method for predicting molecular structure, harmonic force fields, vibrational wavenumbers, absorption wavelengths, chemical shift, and IR and Raman activities of pharmaceutically significant

compounds. In recent years, DFT calculations have emerged as a viable alternative to the classical Hartree-Fock approach. DFT approaches, particularly hybrid functional methods, have evolved as a potent quantum chemical tool for determining a molecules electronic structure [14]. Different exchange and correlation functional are frequently utilized in the DFT framework. The Becke-3-Lee-Yang-Parr (B3LYP) combination is the most often utilized since it has proven to be capable of recreating a variety of molecular features, such as vibrational spectra, electronic transitions, nonlinear optical activity (NLO), and molecule electrostatic potential [15].

For large and medium-sized molecules, the combination of B3LYP functional and various standard basis sets provides an excellent compromise between accuracy and computational efficiency of molecular properties, vibrational spectra, electronic transitions, NLO properties, and natural bond orbital analysis (NBO). The vibrational frequencies calculated using DFT methods are typically 2-5 percent higher than experimental results on average. Electron correlation, anharmonicities, and incomplete basis sets are all factors that contribute to this overestimation. This overestimation can be reduced by using empirical scaling corrections, with empirical scaling factors ranging from 0.8 to 1.0. The scaling factors are dependent on both the method and the basis sets, and they help to compensate for systematic errors in frequency calculation. The Gaussian 09 software suite [16] could be used to do *ab initio* calculations.

1.10.3. Gaussian Software - Overview

Gaussian is a computational software programme created by John Pople and his Carnegie-Mellon University research group in 1970 [16]. Since then, it has been updated on a regular basis. The name comes from the word Gaussian function or orbital, which was chosen to boost the computational power of current software that

employed the Slatter type function or orbital. In statistics, Gaussian functions are commonly employed to characterise normal distributions. It depicts the wave function of a harmonic oscillator ground state in this Quantum computation. A Gaussian orbital is a linear combination of such Gaussian functions for a molecular orbital. Physicists, chemists, chemical engineers, biochemists, and others utilize the Gaussian software package for study in established and emerging areas of molecular physics and chemistry. Gaussian predicts the energies, molecular structures, vibrational frequencies, and other molecular characteristics resulting from these basic quantities using quantum mechanics basic equations. It may be used to investigate molecules and processes in a variety of environments, including both stable and short-lived intermediate compounds.

Ab initio methods, semi-empirical methods, and molecular mechanics are the three types of computational techniques. Molecular mechanics uses classical physics to solve massive systems of molecules and is the least accurate since electron behaviour is not taken into account. Because quantum physics is used to account for some of the electron behaviour, semi-empirical approaches are more precise, but their reach is still limited because they rely on extensive approximations and empirical parameters. Ab initio methods explain the electronic structure of a molecule very accurately using only quantum physics and no approximations from classical physics. The disadvantage of employing ab initio methods is that the computations are incredibly time consuming, hence they are limited to much smaller systems like single molecules. Ab initio approaches, on the other hand, provide a wealth of information on the electrical structure of a molecule without requiring the molecule to be synthesized experimentally. The basic idea underlying ab initio calculations is to use a set of mathematical functions called a basis set to solve Schrodinger's equation.

1.10.4. Capabilities of the Software

Gaussian Software has the following technical capabilities.

- Energy calculations utilizing various approaches such as Molecular mechanics, semi-empirical calculations, Self-Consistent Field calculations, correlation energy calculations using CI CID, CISD techniques, and Density functional theory.
- RHF, DFT, MP2, and other analytical computations of force constants, polarizabilities, hyperpolarizabilities, and dipole moment derivatives.
- Thermochemistry and harmonic vibrational analysis employing arbitrary isotopes, temperature, and pressure.
- Internal coordinates analysis of normal modes.
- Determination of IR and Raman Intensities for vibrational transitions,
 pre-resonance Raman intensities.
- To find the constants of harmonic vibration-rotation coupling.
- To determine the constants of Anharmonic vibration and vibration-rotation coupling.
- Mulliken population analysis, APT analysis, electrostatic potentials and electro-static derived charges.
- Static and frequency dependent polarizabilities and hyperpolarizabilites for HF and DFT.
- SCF, DFT, and MP2 methods for calculating NMR shielding tensors and molecule susceptibilities.
- Calculation of spin-spin coupling constants at HF and DFT level.
- Intensities of vibrational circular dichroism.
- The HOMO-LUMO analysis.

1.10.5. Gauss View Software - Overview

Gauss View is a graphical user interface for preparing input for Gaussian and examining the result that Gaussian produces graphically [17]. Gauss View is a front-end-back-end processor that aids in the use of Gaussian. It is not integrated with the computational module of Gaussian. Gaussian users gain from Gauss View in three ways. To begin, Gauss View powerful visualization feature allow users to quickly sketch in even very large molecules, then rotate, move, and zoom in on them using simple mouse motions. It can also read PDB files, which are common molecular file formats. Second, Gauss View makes it simple to set up a variety of Gaussian calculations. It simplifies the preparation of complex input for both common and advanced task types, including ONIOM, STQN transition structure optimizations, CASSCF computations, periodic boundary conditions (PBC) calculations, and more. Finally, to speed up the job setup process, run default and named calculation templates called as schemes. Finally, Gauss View is used to use a range of graphical ways to analyze the results of Gaussian calculations. The following are some examples of Gaussian outcomes that can be seen graphically:

- Optimized molecular structures.
- Molecular orbitals.
- Electron density surfaces from any computed density.
- Electrostatic potential surfaces.
- Surfaces for magnetic properties.
- Surfaces can be perceived as contours as well.
- Dipole moments and atomic charges.
- Animation of the normal modes corresponding to vibrational frequencies.

- Spectra such as infrared, Raman, NMR, VCD, and others.
- Information on molecular stereochemistry..
- Animation of geometry optimizations, IRC reaction path following, potential energy surface scans, and ADMP and BOMD trajectories. Two variable scans can also be displayed as 3D plots.
- Plots of total energy and other data from the same job kinds as before.

All computational analyses in this paper were carried out using the GAUSSIAN 09W [16] DFT programme with the B3LYP method 6-311++G(d,p) as the basis set [18]. The results of the molecules were viewed using the GAUSSVIEW 5.0 molecular visualization tool [17].

1.11. HIRSHFELD SURFACE ANALYSIS

Hirshfeld surface analysis is a useful tool for determining how different functions (such as molecular shape, some chemical information, and some features of the crystal environment) influence crystal packing behavior [19]. It uses three-dimensional (3D) surface and two-dimensional (2D) fingerprint plots to visualize intermolecular interactions within a crystal structure. Initially, it was utilized to determine the molecular dipole, quadruple moments in molecular crystals, and examine small molecule polymorphs [20]. The partitioning of space within a crystal where the ratio of promolecule to procrystal electron densities is W(r) = 0.5, which covers the 0.002 a.u. electron density isosurface, is known as Hirshfeld surfaces. The weight function for a particular molecule can be defined as [21]:

$$W(r) = \sum_{\text{asmolecule}} \frac{\rho_a(r)}{\sum_{\text{ascrustal}} \rho_a(r)} \dots (1.14)$$

$$= \frac{\rho_{\text{promolecule}}(\mathbf{r})}{\rho_{\text{procrystal}}(\mathbf{r})} \qquad \dots (1.15)$$

where $\rho_{\scriptscriptstyle a}(r)$ is spherical atomic electron distribution located at the a^{th} nucleus.

The following equation represents the normalized contact distance d_{norm} based on d_i (nearest nucleus internal to the surface) and d_e (nearest nucleus external to the surface).

$$d_{\text{norm}} = (d_{i} - r_{i}^{\text{vdW}}) / r_{i}^{\text{vdW}} + d_{e} - r_{e}^{\text{vdW}}) / r_{e}^{\text{vdW}} \qquad \dots (1.16)$$

where r_i^{vdW} and r_e^{vdW} are the van der Waals radii of two atoms internal and external to the molecular surface Crystal Explorer 3.1 [22] was used to identify the Hirshfeld surface and its two-dimensional fingerprint plots using crystallographic data.

1.12. CHARACTERIZATION TECHNIQUES

1.12.1. Powder X-ray Diffraction Analysis

The technique of X-ray diffraction is commonly used to characterize crystals. It is also utilized to identify crystalline phases qualitatively and confirm the production of the intended compound. The crystals are powdered and exposed to monochromatic radiations for irradiation. The unlimited number of small crystals in the powder sample gives a large number of diffraction planes, which favors the Bragg reflection. First and higher order reflections are caused by all of these parallel planes that make distinct angles to the incident X-ray beam. Bragg diffraction occurs at the crystal plane for monochromatic X-rays. The intensity of the diffracted beam that results depends on the nature of crystals and their atomic arrangements. The entire structure of the molecule can be determined by analyzing the recorded data in conjunction with diffracted light intensities from a full set of planes. In addition, X-ray diffraction may be used to determine unit cell characteristics, space groups, molecular structure of crystalline solids, and miller indexing of the different faces of the crystal. An X-ray

generator with an X-ray diffractometer emitting monochromatic X-rays is used in the powder XRD experiment. The setup also includes a proportionate scintillator or a Geiger counter, which is coupled to a chart recorder or a digital output.

In the present work, the powder XRD data was collected using a BRUKER X-ray diffractometer with CuK α radiation (λ =1.5406 Å) and a step size of 0.0130 and a scanning step time of 23.97s. To ensure phase purity, the process was carried out at room temperature. Fullprof Suite software was used to calculate the lattice parameters of the crystal [23].

1.12.2. Infrared Spectroscopy

The infrared (IR) spectrum is created by the absorption of light waves with frequencies similar to molecular bond vibrations. Through IR analysis, the internal structure of the molecule, the nature of the chemical bonds, and the functional units present in the molecule may be understood. This is why IR spectra are often referred to as a compounds fingerprint. The compounds are identified from the IR spectra by comparing the spectral data to the existing data [24].

The IR absorption bands in a polyatomic molecule correspond to the movement of individual atoms. By adjusting the frequency of the incident radiation, the experiment can be repeated. The samples absorbance and transmittance are measured. The resonance happens when the frequency of incident radiation and the vibration frequency of some part of the molecule coincide. As a result, there is energy absorption. Energy is released when a molecule returns to its natural ground state from an excited state. Peaks in the IR spectrum can be used to detect this energy release. This is how the sample molecules unique fingerprint is discovered. The

rotation, vibration, bending, and twisting actions of a molecule are all recorded by IR spectroscopy.

A scanning interferometer is used in the Fourier Transform Infrared (FTIR) spectrometer to analyze IR radiation. Radiations with an IR wavelength divide into two beams, which combine after reflection at the beam splitter. Depending on the optical path traced by the interference, it can be constructive or destructive for a wavelength. The acquired interferogram is reconstructed into spectral form using the Fourier Transformation.

1.12.3. UV-Visible Spectroscopy

Absorption or reflectance spectroscopy in the ultraviolet-visible spectral band is referred to as ultraviolet-visible spectrophotometry (UV-vis). The colour of the substances involved is directly affected by their absorption or reflectance in the visual spectrum. Electronic transitions occur in this region of the electromagnetic spectrum. In contrast to fluorescence spectroscopy, which measures transitions from the excited state to the ground state, absorption spectroscopy measures transitions from the ground state to the excited state. In general, there are two basic measuring techniques: determining the amount of analyte in the sample (quantitative analysis) and determining which analyte is in the sample (qualitative analysis). According to the Beer-Lambert law, a solutions absorbance is proportional to the concentration of the absorbing species in the solution and the route length. UV-vis spectroscopy can thus be used to determine the concentration of a substance in a solution for a particular route length. It is a crucial to understand how quickly absorbance varies with concentration. References (tables of molar extinction coefficients) or, more precisely, a calibration curve can be used to determine this. The quantitative determination of

diverse analytes, such as transition metal ions, highly conjugated organic compounds, and biological macromolecules, is frequently done using UV-vis spectroscopy in analytical chemistry.

1.12.4. UV-Visible Diffuse Reflectance Spectroscopy (UV-VIS-DRS)

DRS spectroscopy is a spectroscopic technique that uses a powdered sample to reflect light in the ultraviolet (UV), visible (VIS), and near-infrared (NIR) regions. The ratio of scattered light from an infinitely thick layer to scattered light from an ideal non-absorbing reference sample is measured as a function of wavelength in a DRS spectrum [25]. When incoming radiation illuminates powdered samples, the result is diffuse lighting. The incident light is absorbed in part and dispersed in part. The dispersed radiation emitted by the sample is collected and monitored in an integration sphere and is seen schematically in Fig. 1.2.

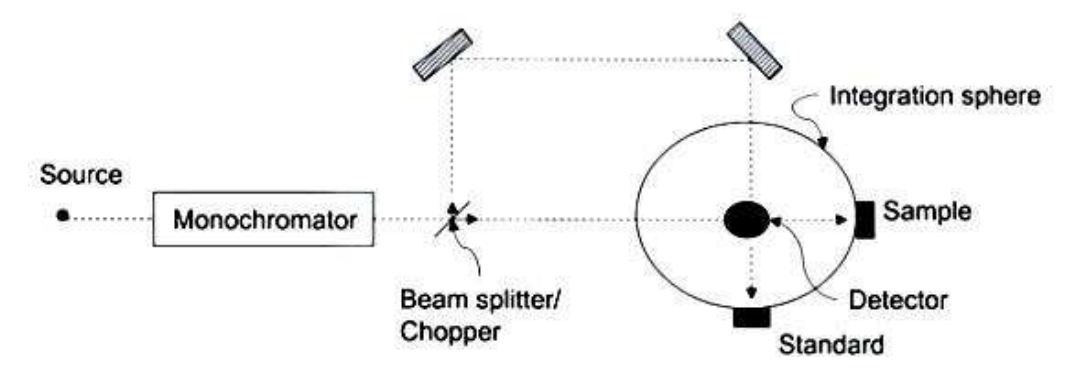


Fig. 1.2. Schematic diagram of UV-vis-DRS

1.12.5. Fluorescence Spectroscopy

Fluorescence spectroscopy, often known as fluorometry or spectrofluorometry, is a type of electromagnetic spectroscopy that examines samples fluorescence. Typically, ultraviolet light is employed as a beam of light that excites the electrons in molecules of specific substances and causes them to release light in this process. Absorption spectroscopy is another complementary technique. In single molecule fluorescence

spectroscopy, intensity fluctuations from emitted light are investigated using either single fluorophores or pairs of fluorophores. Fluorometers are instruments that are used to measure fluorescence.

Light from an excitation source travels through a filter or monochromator before striking the sample. The sample absorbs a fraction of the incident light, and some of the molecules in the sample glow. The fluorescent light that was emitted spread out in all directions. Some of this fluorescent light travels through a second filter or monochromator before reaching a detector, which is normally positioned at 90 degrees to the incident light beam to reduce the chance of incident light being transmitted or reflected. Fig. 1.3 shows a block diagram of spectrofluorometry.

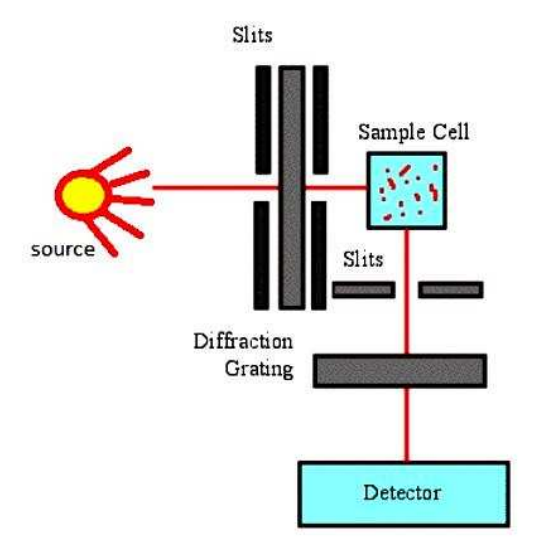


Fig.1.3. Block diagram of spectrofluorometer

The wavelength of the excitation light is kept constant when measuring fluorescence spectra, preferably at a wavelength with strong absorption, and the emission monochromator scans the spectrum. When measuring excitation spectra and excitation monochromator, the wavelength of light travelling through the emission filter or monochromator is kept constant. Because fluorescence intensity is proportional to absorption, the excitation spectrum is usually similar to the absorption spectrum [26,27].

1.12.6. Microhardness Test

The hardness of a substance is a measure of that materials ability to tolerate local deformation. It is the mathematical ratio of the applied load to the indentation surface area. The hardness test is an important tool in the broad study of plastic deformations of a material. Hardness is also related to mechanical qualities like yield stress, elastic constants, and so on. A crystals hardness is influenced by a variety of parameters such as dislocations, impurities, composition, temperature, and vacancies. The measurement of hardness can be classified as Macro, Micro, or Nano scale depending on the applied force and the resulting displacement. Microhardness is the hardness measured by indentation with a load between 15g and 1000g. This type of indentation is always microscopic. It can be defined by either the average contact pressure or the average specific work of deformation. As a result, substantial associated research between the shape of the indenter and that of the indentation is required. Hardness testing can be done by cutting, scratching, abration, or indenting, depending on the sample.

The measurement of hardness can be done in a variety of ways [28]. The static indentation test is the most common among them because it is the most basic. A constant load is applied to an indenter, which can be a diamond cone, diamond pyramid, or a ball, in the Static Indentation test. Hardness is calculated by measuring the area of indentation or the depth of indentation. The static indentation test is performed by pressing the indenter against the samples surface perpendicularly. The indentation depth is determined by the applied load. When calculating the empirical hardness number, two elements are taken into account. They are the cross sectional area or indentation depth, as well as the applied load. This is the basis of Vicker's test.

Vicker's test, a type of static indentation test in which a diamond pyramidal indenter is used for the indentation, is considered the most effective method for the hardness test. The pyramid indenter opposite faces are at an angle of 136° . The contact pressure is independent of incident size since the indenter is pyramidal. It also decreases elastic deformation. The Vicker's Harness number H_v of the diamond pyramid is defined as, $H_v=1.8544P/d^2$ kg/mm², Where P is the applied load in gram and d is the diagonal length of indentation in mm [29].

1.12.7. SHG Measurement

A crystal with no visible absorption is a suitable option for second harmonic generation, especially in the blue, violet, and near-infrared regions. Nonlinearity of a crystal is measured by Kurtz and Perry [30] powder SHG technique (Fig.3.1). In this process the Q-switched Nd:YAG laser is passed through the crystal which are powdered and filled in the micro capillaries of same diameter. By keeping the laser energy constant, the monochromated output is compared to that of the KDP.

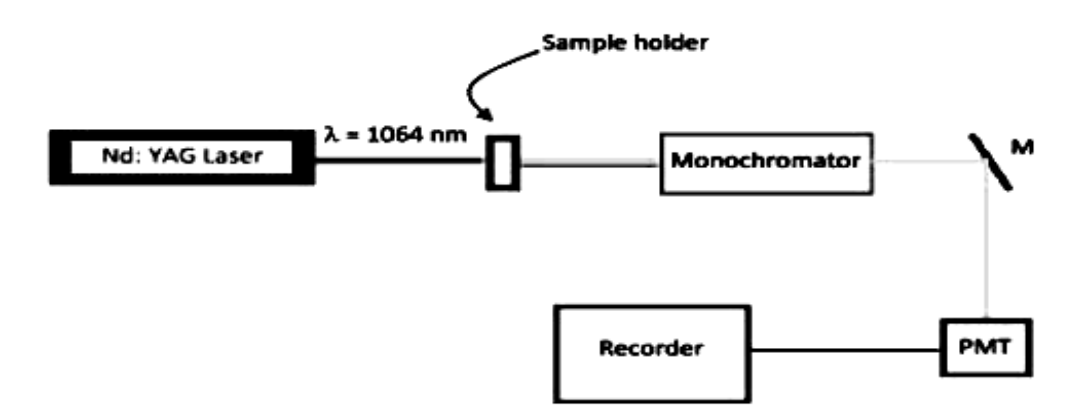


Fig. 1.4. Experimental Set Up for the Powder SHG Measurement

1.12.8. Z-Scan Analysis

The single beam Z-Scan technology operates on the principle of spatial beam distortion. This method is utilized to identify the sign as well as the magnitude of the

nonlinear refractive index n_2 , which may be extracted easily [31]. Z-scan examinations provide practically all of the information about material nonlinear properties. Nonlinear refraction and nonlinear absorption can be studied individually using open aperture Z-Scan and closed aperture Z-Scan when they coexist.

The sample is permitted to move along a narrowly focused Gaussian beam in this method. Because the samples beam intensity is dependent on its position in relation to the focus, movement of the sample causes the laser beam intensity to fluctuate. The induced self-phase modulation causes the incident beam to defocus or re-collimate, and this is dependent on the Z position of the sample relative to the focal plane. The change in transmittance is seen through a circular aperture of smaller diameter kept at a distant location at the field position to determine the nonlinear refractive index. The nonlinear absorption can be observed by replacing the aperture with a lens, which is known as open aperture Z-Scan. The development of high-power laser resources has aided the study of optical limiting behavior and nonlinear optical properties of materials [32]. For the most efficient utilization of the crystal, it is essential to evaluate the NLO characteristics. The nonlinear refraction and nonlinear absorption of the NLO materials may have an impact on the functionality of laser systems in which they are used. Due to self-focusing of the radiation, changes in the spatial distribution of the laser field can even cause the device to fail. It limits the amount of laser intensity and output power that can be used. When a laser beam passes through a nonlinear medium, its amplitude and phase change. Closed aperture Z-Scan refers to the measuring of transmitted light through an aperture kept at a distant plane from the focal region, which can measure both nonlinear absorption and nonlinear refraction. Open aperture Z-Scan is the measurement mode when it is done without an aperture.

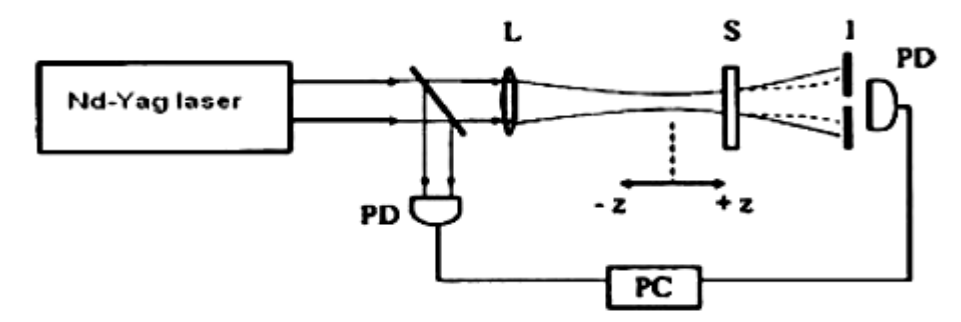


Fig. 1.5. Experimental Setup for Z-Scan Analysis

The third order NLO properties were studied utilizing a He–Ne laser (5mW) with a wavelength of 632.8 nm and a beam diameter of 0.5 mm as a source. To convert the input laser beam into Gaussian form, a Gaussian filter was employed to focus the beam. A convex lens with a focal length of 30 mm was used to pass the Gaussian beam TEM₀₀ mode. The incident Gaussian beam determines the focal length entirely. The Gaussian beam waist ω_0 measured 12.05 μ m in diameter at the focal length. The incidence intensity falling on the crystal surface was varied by translating the sample in the +Z to -Z axial direction with the help of a stepper motor. A digital power meter (Field master GS-coherent) was used to measure the far field transmittance intensity fluctuations through the closed aperture.

1.13. SCOPE OF THE WORK

The current research focused on:

- To grow 2-picolinic acid (also known as pyridine-2-carboxylic acid, 2-pyridine carboxylic acid and picolinic acid) based organic and semiorganic single crystals such as:
 - o Organic:
 - 2-Picolinic Acid (2PA)
 - 2-Picolinic Trichloro Acetate (PTCA)
 - 2-Picolinic Benzotriazole (PBTA)

- o Semiorganic:
 - 2-Picolinic Hydrochloride (PHCL)
- > To evaluate the materials solubility and nucleation kinetic parameters.
- ➤ Using powder X-ray diffraction studies to determine the crystal structure and system.
- > To evaluate the average crystallite size of the grown crystal and its lattice strain using the Williamson–Hall technique.
- > FTIR, UV spectral analysis, energy band gap, optical constants, fluorescence, SHG, Z-scan, and microhardness studies are used to characterize the grown crystals.
- > DFT investigations to understand molecular behavior of the materials.
- ➤ NBO analysis determines the inter- and intramolecular charge transfer interactions as well as the molecules stability.
- ➤ Hirshfeld surface analysis reveals the percentage of strong and weak intermolecular interactions in crystals.

REFERENCES

- Willem J. P. Van Enckevort, Introduction to crystal growth and characterization, Crystallogr. Rev., 22 (2016) 288-292.
- Wolfgang Neumann, Klaus-Werner Benz, Anna Mogilatenko, Introduction to Crystal Growth and Characterization, Wiley, Germany, 2014
- 3. P. Hartman (Ed.), Crystal Growth: An Introduction, North-Holland series in crystal growth Vol. 1, North Holland Publishing Co., Amsterdam, 1973
- K. Sangwal, On the estimation of surface entropy factor, interfacial tension, dissolution enthalpy and metastable zone-width for substances crystallizing from solution, J. Cryst. Growth 97 (1989) 393–405
- Gibbs J. Willard, Collected works of J. Willard Gibbs, Longmans and Green, New York, 1928.
- 6. O. Sohnel, Electrolyte crystal-aqueous solution interfacial tensions from crystallization data, J. Cryst. Growth, 57 (1982) 101-108.
- A. Mersmann, Calculation of interfacial tensions, J. Cryst. Growth, 102 (1990)
 841-847.
- 8. P. Bennema, O. Sohnel, Interfacial surface tension for crystallization and precipitation from aqueous solutions, J. Cryst. Growth 102 (1990) 547–556.
- 9. Chen Changkang, Physico-chemical investigations on crystal growth of oxide superconductors, Prog. Cryst. Growth Charact. Mater., 24 (1992) 213-267.
- A.E. Nielsen, S. Sarig, Homogeneous nucleation of droplets and interfacial tension in the liquid system methanol-water-tribromomethane, J. Cryst. Growth 8 (1971) 1–7.

- S. Boomadevi, R. Dhanasekaran, P. Ramasamy, Investigations on Nucleation and Growth Kinetics of Urea Crystals from Methanol, Cryst. Res. Technol. 37 (2002) 159-168.
- Alexander A. Chernov, Modern Crystallography III Crystal Growth, Springer-Verlag, New York, 1984.
- H. A. Meirs, F. Isaac: The spontaneous crystallization, Proc. Roy. Soc. London A, 79 (1987) 322-325.
- Nathan Argaman, Guy Makov, Density functional theory: An introduction,
 Am. J. Phys., 68 (2000) 69-79.
- 15. Axel D. Becke, A new mixing of Hartree–Fock and local density functional theories, J. Chem. Phys., 98 (1993) 1372-1377.
- M.J. Frisch, G.W. Trucks, H.B. Schlegel, G.E. Scuseria, M.A. Robb, J.R.
 Cheeseman et al 2009 Gaussian 09 revision A. Wallingford, CT: 02 Gaussian Inc.
- R. Dennington, T. Keith, J. Millam 2009 GaussView Version 5 Semichem
 Inc., Shawnee Mission
- 18. H. Bernhard Schlegel, Optimization of equilibrium geometries and transition structures, J. Comp. Chem., 3 (1982) 214-218
- M.A. Spackman, S.P. Thomas, D. Jayatilaka, High Throughput Profiling of Molecular Shapes in Crystals, Sci. Rep., 6 (2016) 22204.
- M.A. Spackman, P.G. Byrom, A novel definition of a molecule in a crystal,
 Chem. Phys. Lett., 267 (1997) 215-220.
- J.J. McKinnon, M.A. Spackman, A.S. Mitchell, Novel tools for visualizing and exploring intermolecular interactions in molecular crystals, Acta. Crystallogr.
 B. Struct. Sci. Cryst. Eng. Mater., 60 (2004) 627-668.

- S.K. Wolff, D.J. Grimwood, J.J. McKinnon, M.J. Turner, D. Jayatilaka, M.A.
 Spackman, 2012, Crystal Explorer.
- 23. Senthilkumar Chandran, Rajesh Paulraj, P.Ramasamy, Nucleation kinetics, crystal growth and optical studies on lithium hydrogen oxalate monohydrate single crystal, J. Cryst. Growth 468 (2016) 68-72.
- 24. H.H. Willard, L.L. Merritt Jr, J.A. Dean, F.A. Settle Jr, Instrumental methods of analysis, 7th edition, Wadsworth Publishing Company; Florence, United States, 1988.
- 25. Minoo Tasbihi, Urška Lavrenčič Štangar, Urh Černigoj, Jaromir Jirkovsky, Snejana Bakardjieva, Nataša Novak Tušar, Photocatalytic oxidation of gaseous toluene on titania/mesoporous silica powders in a fluidized-bed reactor, Catal. Today, 161 (2011) 181-188.
- Valeur, Bernard, Mario Nuno Berberan-Santos, Molecular Fluorescence:
 Principles and Applications, John Wiley & Sons, 2012
- 27. Daniel R Stabley, Carol Jurchenko, Stephen S Marshall, Khalid S Salaita, Visualizing mechanical tension across membrane receptors with a fluorescent sensor, Nat. Methods, 9 (2012) 64–67.
- 28. Anton F. Mohrnheim, Microhardness testing and Hardness numbers,
 Interpretive Techniques for Microstructural Analysis, Springer, Boston, 1977.
- J. Gubicza, A. Juhasz, P. Tasnadi, P. Arato, G. Voros, Determination of the hardness and elastic modulus from continuous vickers indentation testing,
 J. Mater. Sci., 31 (1996) 3109-3114.
- S.K. Kurtz, T.T. Perry, A Powder Technique for the Evaluation of Nonlinear Optical Materials, J. App. Physics., 39 (1968) 3798.

- 31. K. Senthil, S. Kalainathan, A. Ruban Kumar, P.G. Aravindan, Investigation of synthesis, crystal structure and third-order NLO properties of a new stilbazolium derivative crystal: a promising material for nonlinear optical devices, RSC Adv., 4 (2014) 56112-56127.
- 32. K. Nivetha, S. Kalainathan, Manabu Yamada, Yoshihiko Kondo, Fumio Hamada, Investigation on the growth, structural, HOMO–LUMO and optical studies of 1-ethyl-2-[2-(4-hydroxy-phenyl)-vinyl]-pyridinium iodide (HSPI) a new stilbazolium derivative for third-order NLO applications, RSC Adv., 6 (2016) 35977-35990.

Chapter-II

Experimental and Theoretical Investigations of Nonlinear Optical Crystal 2-Picolinic acid

CHAPTER - II

EXPERIMENTAL AND THEORETICAL INVESTIGATIONS OF NONLINEAR OPTICAL CRYSTAL 2-PICOLINIC ACID

2.1. INTRODUCTION

A large number of organic molecules have now been found as effective materials in the field of NLO, such as frequency doubling, which has a wide range of optical applications [1]. 2-Picolinic Acid (2PA) (also known as pyridine-2-carboxylic acid, 2-pyridine carboxylic acid and picolinic acid), is an organic molecule utilized in crystal engineering and several coordination polymers as a building block.2-picolinic acid is beneficial compound for human organism and are also involved in several essential biochemical processes. 2PA has been used as a valuable chelating agent [1]. It is not only a potential proton acceptor but also a proton donor depending on the deprotonated groups [2]. The structural analysis of 2-picolinic acid crystal is solved and reported [3-5], but there are no reports on the nucleation kinetics and DFT study of this organic material. In the present work, the nucleation parameters such as interfacial energy (σ), volume free energy (ΔG_v), critical energy barrier for nucleation (ΔG^*) , radius of the critical nucleus (r^*) and nucleation rate (J) were evaluated. X-ray diffraction investigating the structural aspects establishes the crystal structure belonging to crystal system as monoclinic nature. Williamson–Hall approach assesses the structural characteristics of the grown crystal such as average crystallite size along with lattice strain. DFT method was performed to acquire the vibrational information on the optimized geometry, molecular structure, hydrogen bonding, hyperpolarizability, and nonlinear response of the 2PA compound was obtained. This can be used to support the effort towards the discovery of new efficient materials for technological applications by the design strategy for engineering of crystals with predesigned architecture,

especially, in the field of optics [6]. The optical transparency of the crystal is detected by UV-Vis–DRS spectrum and the optical properties of the grown crystal are discussed. The emission characteristic of the grown crystal was verified by fluorescence spectra. Open-aperture Z-scan results on evaluating the nonlinear optical properties experimentally; confirm these materials as good optical limiters.

2.2. EXPERIMENTAL ANALYSIS

2.2.1. Solubility Study

The solubility study of 2PA was carried out in a constant temperature bath with temperature accuracy \pm 0.01°C. The solute was added to double distilled water until the saturation condition was reached. The equilibrium concentration of the solute was analyzed gravimetrically. The experiment was repeated at different temperatures. The solubility and metastable zone width of 2PA crystal as the function of temperature is shown in Fig. 2.1. The solubility and nucleation curve linearly increase with increasing temperature, resulting in a positive coefficient of solubility.

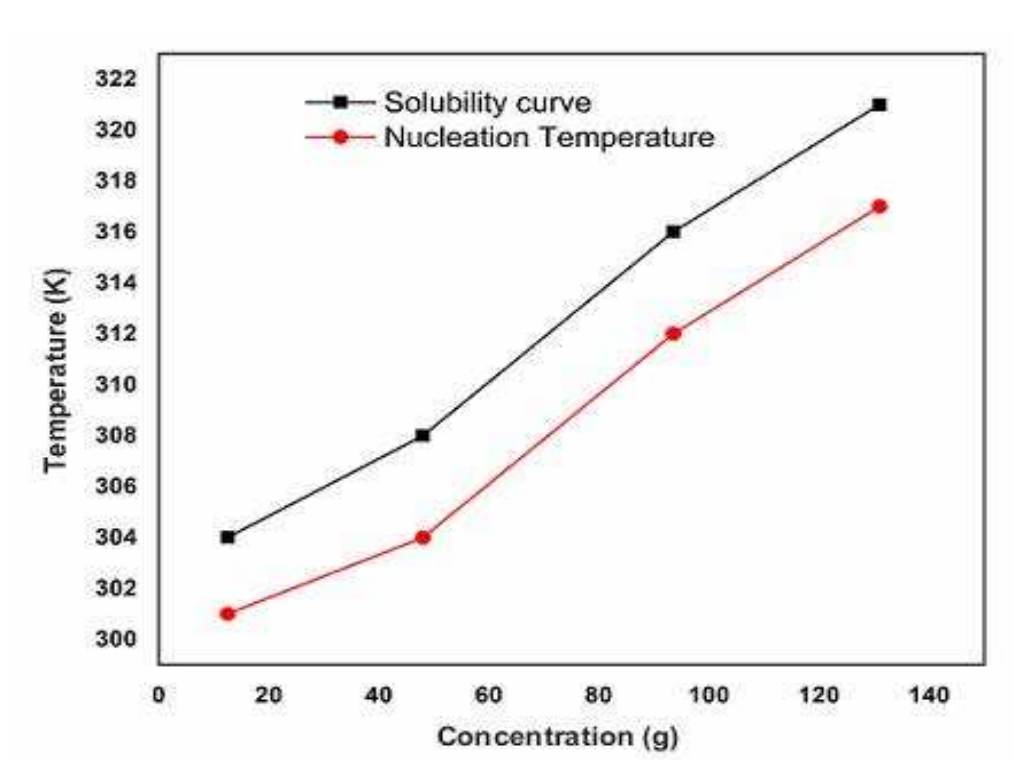


Fig. 2.1. Solubility curve for 2PA

2.2.2. Nucleation kinetics and Metastable Zone Width (MZW)

The estimated nucleation parameters of 2PA crystal at various supersaturation values from the formulas given in chapter-I, eqn. no. (1.1 to 1.8) are tabulated in Table 2.1. The change in free energy per unit volume (ΔG_v) decreases with increasing the supersaturation which drives the crystallization process. Fig. 2.2 shows the variation in energy barrier (ΔG^*) with respect to temperature. Fig. 2.3 shows the change in critical radius (r^*) as a function of temperature as well as the supersaturation. A decrease in interfacial energy (σ) (as shown in Table 2.1) with higher value of temperature leads to decrease in radius of critical nuclei, causing the diminished free energy in the system. The classical nucleation theory diagram implies that when volume free energy decreases and surface free energy increases the crystal growth initiates.

The knowledge of MZW will help in the selection of optimum rate of supersaturation generation to avoid the exercise of secondary nucleation. MZW (ΔT_{max}) for each saturation temperature is obtained from the relation

$$\Delta T_{\text{max}} = \frac{RT^2}{\Delta H_S} (S-1) \qquad ... (2.1)$$

where, the value of enthalpy is obtained from eqn. no. (1.2) in chapter-I, by plotting $\ln\chi_m$ vs 1/T which gives a straight line, the slope of which is equal to $\Delta H_s/R$. Nucleation temperature for each saturation temperature can be calculated from Fig. 2.1. The present study involves reporting theoretically calculated values of metastable zone width for the crystallization temperatures of crystals by slow evaporation method. From the results it is observed that zone width is narrow at lower temperatures and broader at higher temperatures.

T (K)	$\Delta G_{\rm v} ({\rm J/m}^3)$	$\sigma (J/m^2)$	$\Delta \mathbf{G}^*(\mathbf{J})$	r* (m)	i [*]	J (nuclei/m³/sec)
304	-2543049.7	0.006923	8.59E-19	5.44E-09	4.30E+03	8.30E+12
308	-2576510.9	0.003852	1.44E-19	2.99E-09	7.12E+02	2.50E+12
316	-2643433.2	0.002345	3.09E-20	1.77E-09	1.49E+02	8.81E+11
321	-2685259.7	0.001556	8.75E-21	1.16E-09	4.15E+01	3.76E+11

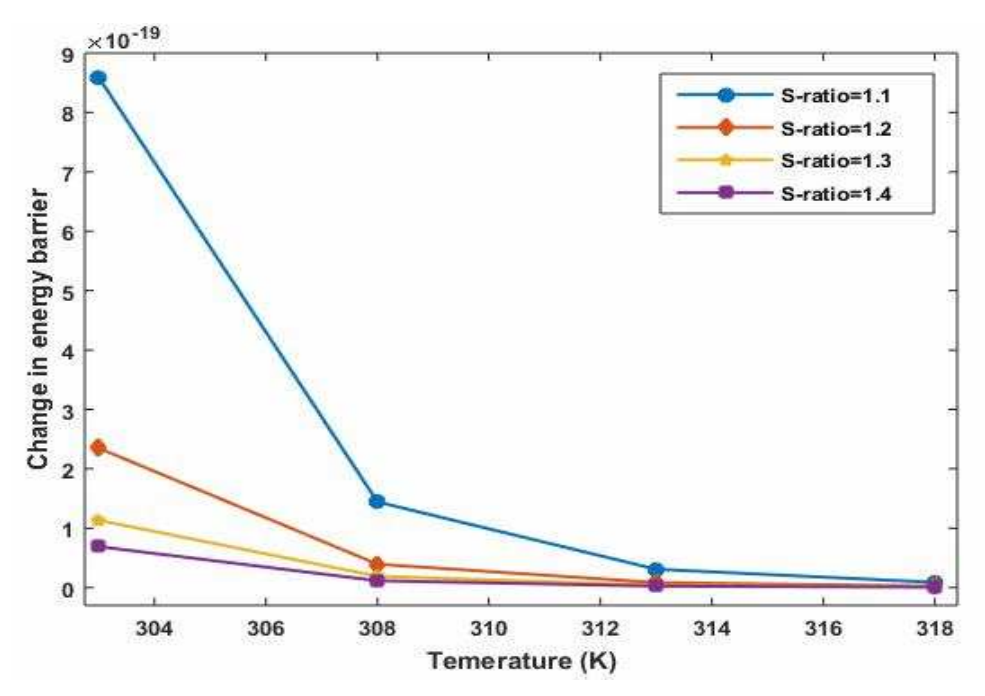


Fig. 2.2. Variation of Gibbs free energy with supersaturation and temperature for 2PA

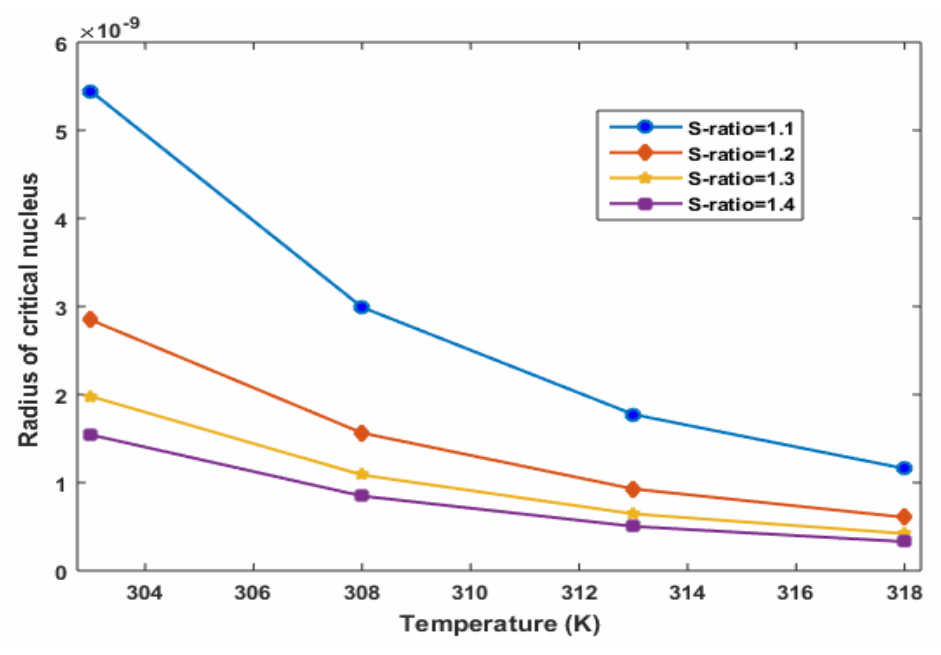


Fig. 2.3. Variation of radius of critical nucleus with temperature and supersaturation ratio of 2PA

2.2.3. Growth of 2PA Crystal

The chemical used in this experiment was an analytical reagent as received from the commercial sources without further purification. Pyridine-2-carboxylic acid was purchased from Alfa Aesar and dissolved in double distilled water. The solution is stirred well using a temperature controlled magnetic stirrer to yield a homogeneous mixture. Then as a result of evaporation of the filtered solution at room temperature, transparent crystals have been harvested in three weeks. Successive re-crystallization and filtration account for the purity of the crystal is shown in Fig. 2.4.

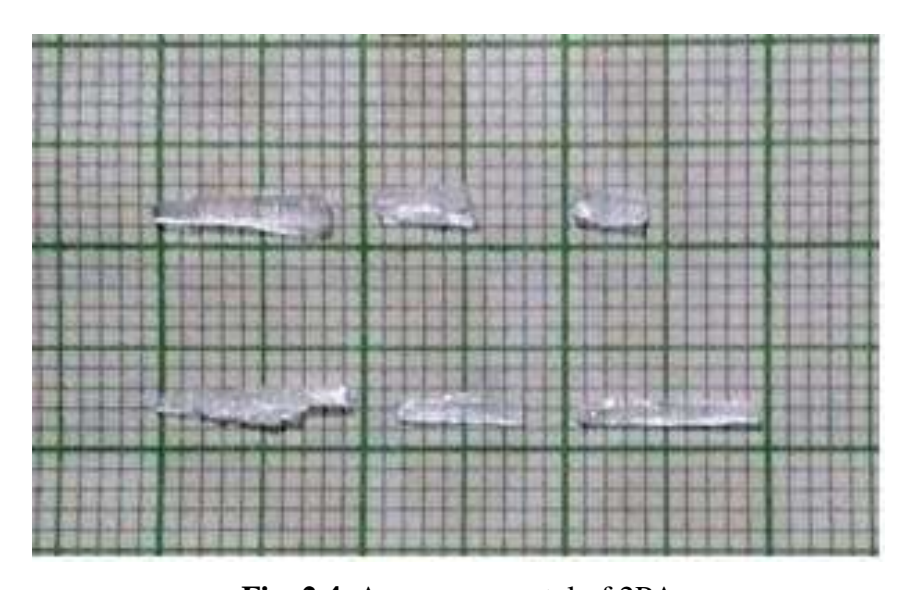


Fig. 2.4. As grown crystal of 2PA

2.2.4. Powder XRD

The powder XRD data of 2PA crystal is obtained from BRUKER X-ray diffractometer with CuK α radiation (λ =1.5406 Å) and a step size of 0.0130 and a scanning step time of 23.97s. The powder XRD pattern of 2PA crystal is shown in Fig.2.5. The lattice parameters of the 2PA crystal obtained from Fullprof Suite software are a= 21.251 (18) (Å), b = 3.839 (1) (Å), c = 13.962 (5) (Å), α = γ =90°, β = 107.95° (6) and volume = 1083.8 (1) (ų), monoclinic system with space group $C2_c$. It agrees well with the reported values [3].

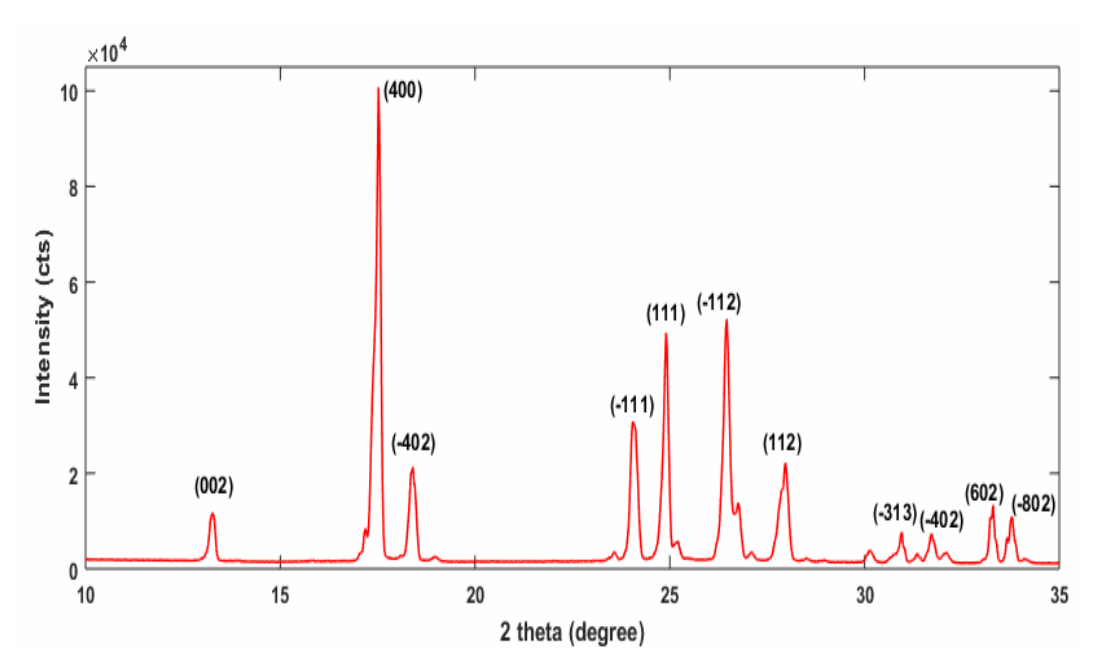


Fig. 2.5. Powder XRD pattern of 2PA crystal

Further, using Williamson–Hall equation the strain present in the grown crystal is evaluated [7]:

$$\beta \cos\theta = \frac{K\lambda}{\tau} + \eta \sin\theta \qquad \dots (2.2)$$

where, β - FWHM of the diffraction peak (rad); θ - Bragg's diffraction angle (rad); $K \text{ - Scherrer constant; } \lambda \text{ - wavelength of the X-rays} \left(\overset{\circ}{A} \right); \tau \text{ - crystallite size } (\mu m) \text{ and } \\ \eta \text{ - lattice strain.}$

Plotting the $\beta\cos\theta$ versus $\sin\theta$ [Fig. 2.5] and fitting the data linearly, the crystallite size (τ) is obtained by Williamson-Hall method [7]

$$\tau = \frac{k\lambda}{y - axis intercept} \qquad \dots (2.3)$$

whose value is $\sim 0.4 \mu m$. A graph is plotted between $\beta \cos\theta$ versus $\sin\theta$ (Fig.2.6) whose slope of the fitted line gives lattice strain, $\eta = 0.006$ which points 2PA crystal has less lattice strain.

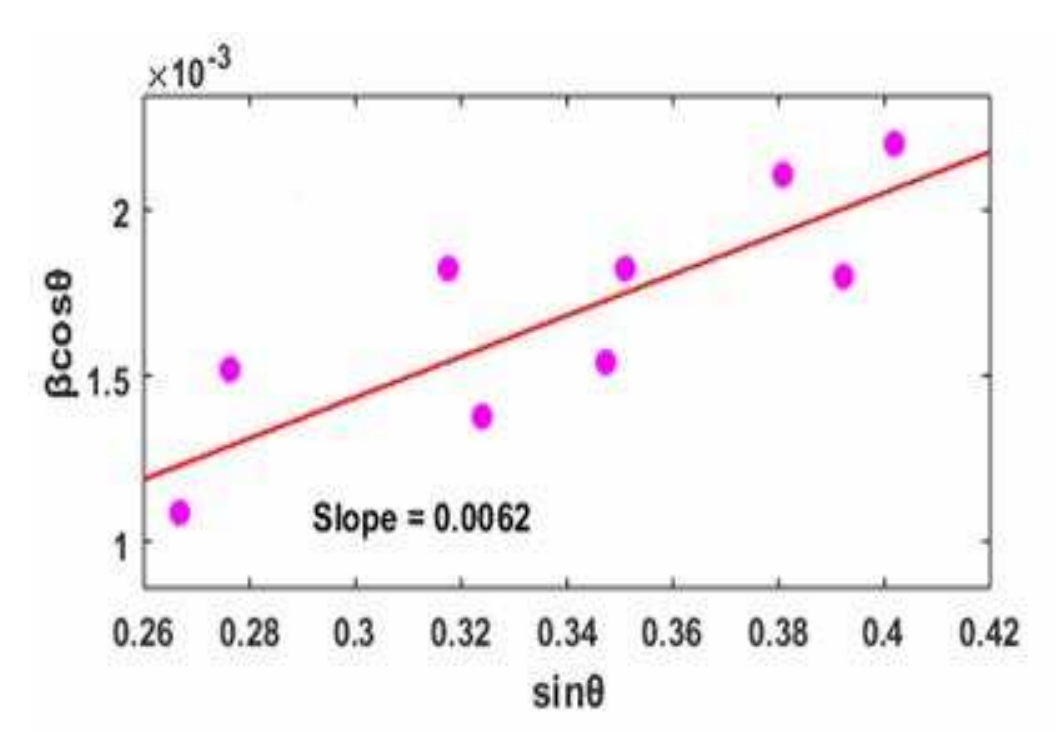


Fig. 2.6. Graph plotting $\beta\cos\theta$ versus $\sin\theta$

2.2.5. UV-vis-DRS Analysis

(a) By Tauc's Plot

The optical absorption spectrum of 2PA crystal is evaluated using SHIMADZU/UV 2600 Spectrophotometer in the range 220 -1100 nm and is shown in Fig. 2.7. It displays intense absorption peak at 263 nm and the crystal shows good transmittance in the entire visible region and this property enables the material holds good for NLO application [8]. Using the absorption spectra, the linear optical constants of 2PA are calculated and the variation in optical constants as a function of photon energy is plotted (Fig. 2.8 (a-d)).

The optical constants such as band gap energy, extinction coefficient and refractive index are crucial to analyze the optical material for the fabrication of optical devices [8]. The band gap energy can be calculated using the Tauc's plot relation [9]

$$\alpha hv = A \left(hv - E_g \right)^{\frac{1}{2}}$$
 ... (2.4)

$$\alpha = \frac{2.3026}{t} \log_{10} \left(\frac{100}{t} \right)$$
 ... (2.5)

where T is the transmittance, t is the thickness of the crystal. The energy band gap was obtained via intercept of the extrapolated linear part of the Fig. 2.8a. The band gap value (E_g) is obtained as 3.5eV.

The refractive index (n) can be determined from reflectance data using the following relation [10]

$$n = \frac{-(R+1) \pm 2\sqrt{R}}{R-1} \qquad ... (2.6)$$

From the optical constants, the electric susceptibility (χ_C) can be calculated using the following relation [11]

$$\varepsilon_{\rm r} = \varepsilon_0 + 4\pi\chi_{\rm C} = n^2 - k^2 \qquad \dots (2.7)$$

Hence,

$$\chi_{\rm C} = \frac{n^2 - k^2 - \epsilon_0}{4\pi} \qquad ... (2.8)$$

where ε_0 is the dielectric constant in the absence of any contribution from free carriers.

The real part of dielectric constant ε_r and imaginary part of dielectric constant ε_i can be calculated following the relation [12]

$$\varepsilon_{\rm r} = n^2 - k^2$$
 and $\varepsilon_{\rm i} = 2nk$... (2.9)

The calculated values of refractive index (n), electric susceptibility (χ_C), real (ϵ_r) and imaginary (ϵ_i) dielectric constants at $\lambda=800$ nm, are 1.08, 0.094, 1.179 and 2.354 \times 10⁻⁶, respectively. These values suggest that the 2PA material has potential optoelectronic devices [13].

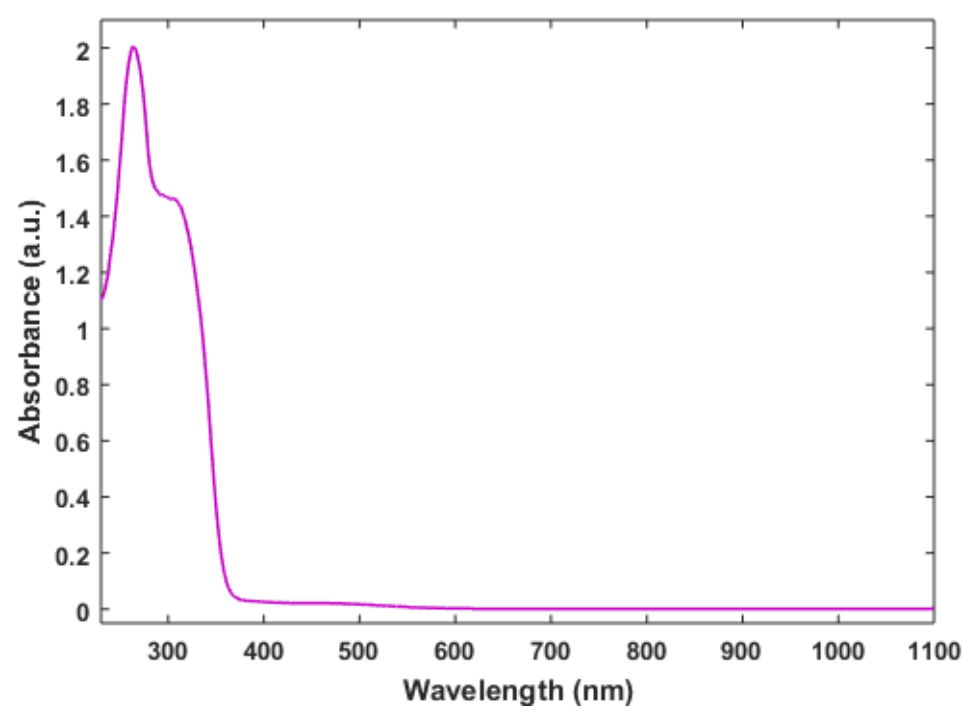


Fig. 2.7 Optical absorbance of 2PA

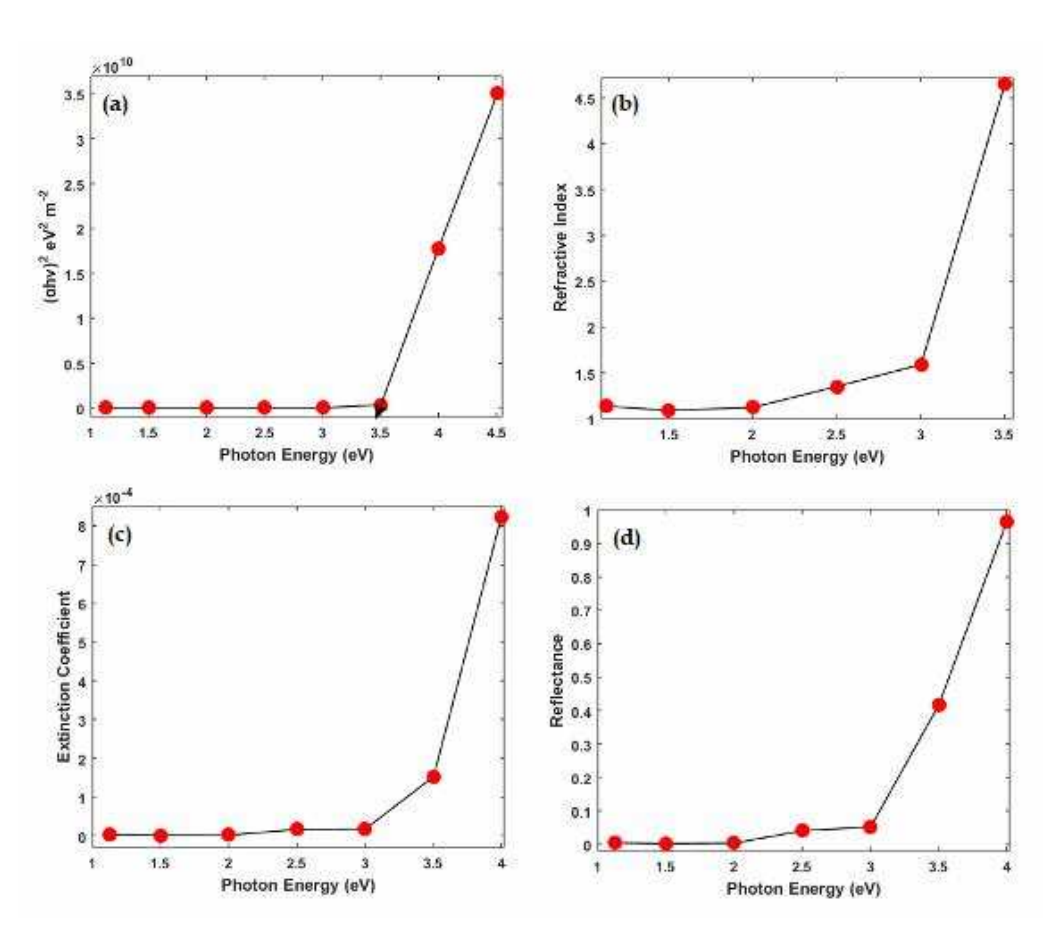


Fig. 2.8 (a-d). Variation of optical constants as a function of photon energy

(b) By Derivation of absorption spectrum fitting (DASF) method

The optical band gap and other optical parameters were also estimated by using Derivation of absorption spectrum fitting (DASF) method [14]. This method determines the type of optical transition more precisely and more directly in contrast to Tauc's method [15].

The absorption spectra of the 2PA crystal are depicted in Fig.2.7. In the current work, precise DASF method is made use of to find the band gap energy. The ratio of the optical absorbance (A) and the wavelength of the radiation (λ) is given by [14,16].

$$\frac{d\left(\frac{\ln A}{\lambda}\right)}{d\left(\frac{1}{\lambda}\right)} = \frac{m}{\frac{1}{\lambda} - \frac{1}{\lambda_g}} \qquad \dots (2.10)$$

In the above equation,

 λ_g - wavelength attributed to the energy gap, m - optical transition index of charge carriers. From Fig. 2.9, optical energy band gap is acquired by using λ_g ,

$$E_g^{DASF} = \frac{1239.83}{\lambda_g} (eV) \qquad ... (2.11)$$

This is done devoid of any assumption about the nature of charge carrier transition.

From the slope of Fig. 2.10, the value of optical transition (m) is acquired. Present analysis expose the value of m near to 1/2, which indicates 2PA has the direct band gap and direct allowed transition of charge carriers [17].

An exponential part called Urbach tail is present near the optical band edge in the absorption coefficient curve. This exponential tail appears to be more for poor crystalline materials which are disordered in lattices and for amorphous materials. If this tail appears to be minimum, this indicates good crystalline nature and also good perfection in lattice sites [18]. Urbach equation is expressed as,

$$A(\lambda) = kexp\left(\frac{hc}{E_{Tail}\lambda}\right) \qquad ... (2.12)$$

where h - Planck's constant, c - light speed, k - constant, E_{Tail} - width of the tail of the localized states adjacent to bands.

The Urbach energy value is obtained from equation $E_{Tail} = \frac{1239.83}{Slope} (eV)$, where the slope is acquire from linear fit established in the straight-line segment of the graph of ln (A) in terms of λ^{-1} (Fig. 2.11) [19]. The obtained value of E_{Tail} is 0.01 eV. The minimal value of E_{Tail} , imparts the 2PA crystal has less disorder in near band edge in addition to perfect crystalline quality [20,21].

Steepness parameter σ , whose value is used to estimate the temperature dependence of the indirect energy gap is derived from the equation:

$$\sigma = \frac{K_B T}{E_{Total}} \qquad \dots (2.13)$$

where, K_B is 8.6173 x 10^{-5} eV/K which is Boltzmann constant and T is 273.16 K (Absolute temperature).

The energy exchange between the electrons and lattice, electron-phonon interaction $(E_{\text{e-p}})$ is measured through the relation:

$$E_{e-p} = \frac{2}{3\sigma}$$
 ... (2.14)

Apart from these, refractive index (n) and dielectric constant (ϵ_d) at the absorption edge were estimated by applying the disclosed energy gap values in the equation below [22]:

$$\frac{n^2 - 1}{n^2 + 1} = \left(1 - \frac{E_g^{DASF}}{20}\right)^{\frac{1}{2}} \qquad \dots (2.15)$$

$$\varepsilon_{\rm d} = n^2 \qquad \qquad \dots (2.16)$$

The results obtained (Table 2.2) from the optical studies reveal that the 2PA crystal holds good optical behavior for NLO applications [13].

Table 2.2. Optical parameters of 2PA

Optical parameters (DASF method)	Values
λ_g (wavelength of energy gap)	357 nm
$1/\lambda_{\rm g}$	0.0028
E _g (optical energy band gap)	3.47 eV
E _{Tail} (Urbach energy)	0.01 eV
σ (steepness parameter)	0.21
E _{e-p} (electron-phonon interaction)	3.17
n (refractive index)	2.22
ϵ_d (dielectric constant)	1.93

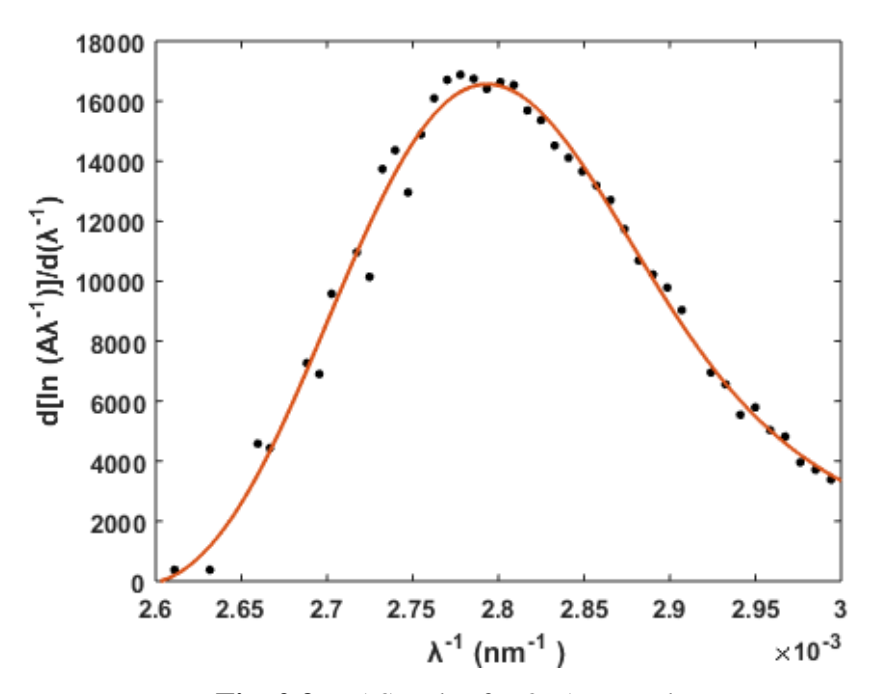


Fig. 2.9. DASF plot for 2PA crystal

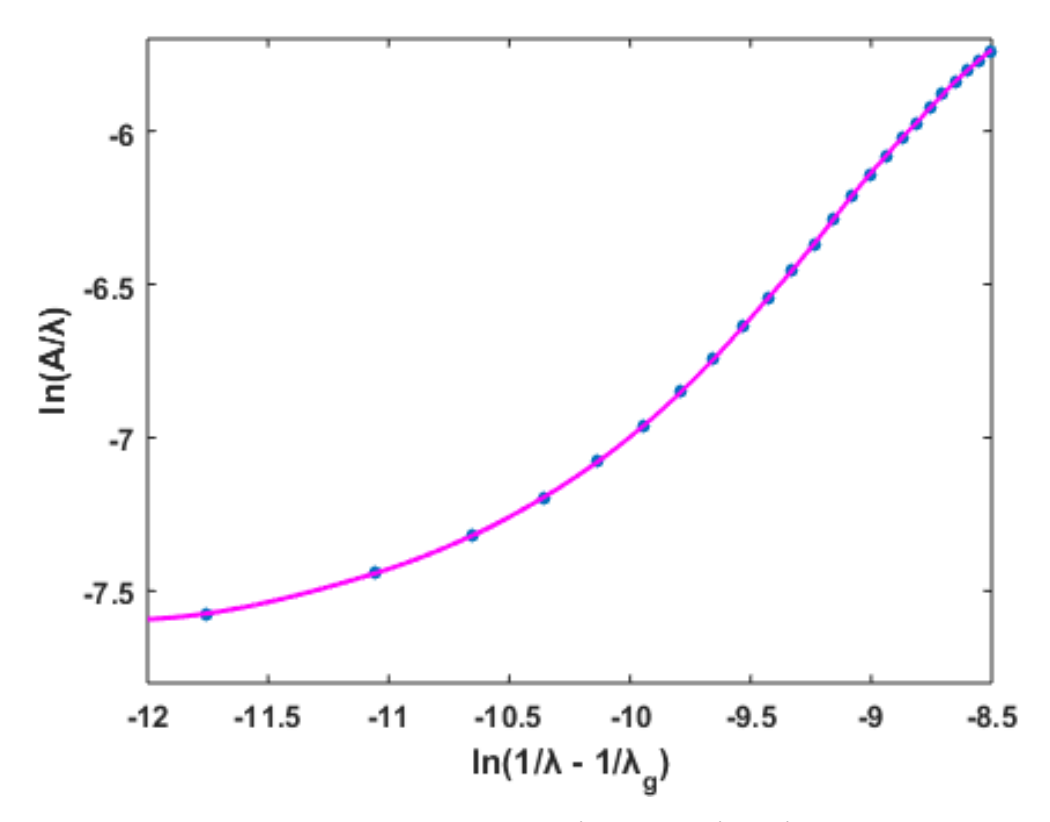


Fig. 2.10. Curves of ln (A/λ) vs ln $(1/\lambda - 1/\lambda_g)$

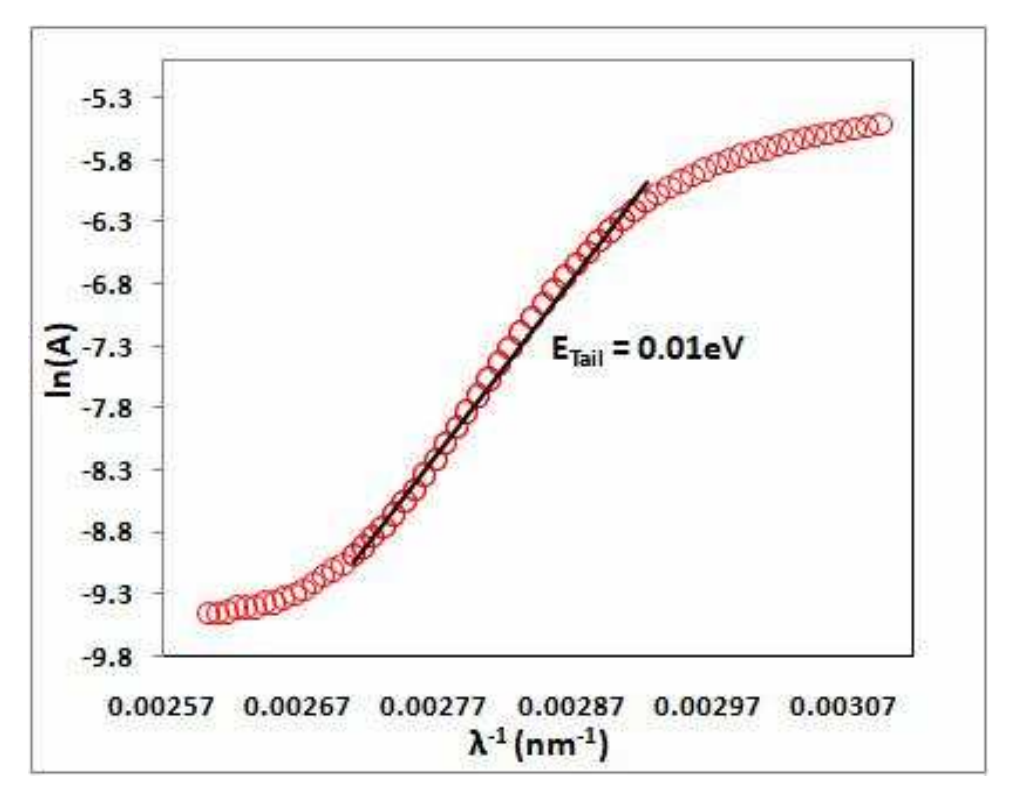


Fig. 2.11. Urbach plot for 2PA

2.2.6. Fluorescence Analysis

A fluorescence spectrum of the 2PA crystals are obtained using SHIMADZU/RF 6000 Spectro Fluorophotometer and are displayed in Fig. 2.12. The crystal was excited with the energy wavelength of 250 nm and the emission spectrum is recorded. The spectrum exhibits an intense fluorescence peak at 481 nm and a hump at 451 nm, implying that 2PA crystals have a blue fluorescence emission and could be a potential candidate for an OLED of wide emission spectrum [13].

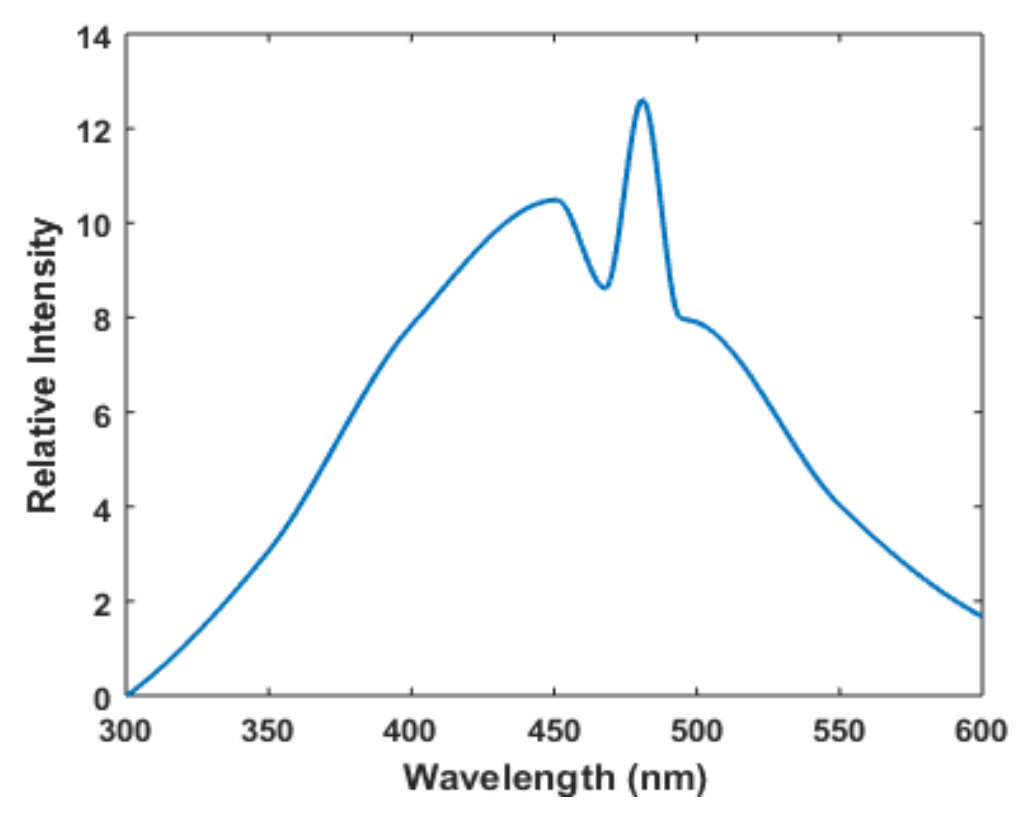


Fig. 2.12. Fluorescence emission of 2PA crystal

2.2.7. Z-scan Analysis

The Z-scan measurements determine the magnitude and sign of third order nonlinear optical parameters for the grown 2PA crystals such as nonlinear optical absorption coefficient, nonlinear optical refractive index and nonlinear optical third order susceptibility. The calculation details for the position of the peak and valley,

relative to the z-axis, depends on the sign of the non linear phase shift $\Delta \phi$. The magnitude of the phase shift can be determined from the change in normalized transmittance between peak and valley.

$$\Delta T_{p-y} = 0.406(1-S)^{0.25} |\varphi|$$
 ... (2.17)

where S is the aperture linear transmittance and is calculated using the following equation

$$S = 1 - \exp\left(-\frac{2r_a^2}{\omega_a^2}\right)$$
 ... (2.18)

where r_a is the radius of the aperture and ω_a is the beam radius at the aperture, the nonlinear refractive index is given by the relation

$$n_2 = \frac{\varphi}{KI_0L_{\text{eff}}} \qquad \dots (2.19)$$

where, $K = \frac{2\pi}{\lambda}$ (where, λ is the laser wavelength)

 I_0 is the input intensity, Z=0, L_{eff} = [1-exp(- α L)]/ α is the effective thickness of the sample and α is the linear absorption co-efficient of the 2PA crystal. From the open aperture Z – scan data, the nonlinear absorption co-efficient is estimated as

$$\beta = \frac{2\sqrt{2\Delta T}}{I_0 L_{\text{off}}} \qquad \dots (2.20)$$

where, ΔT is the one valley at the open aperture Z-scan curve.

The value of β will be negative for saturable absorption and positive for two photon absorption. The real and imaginary parts of the third order nonlinear optical susceptibility χ^3 are defined as equation

$$\operatorname{Re}\chi^{3}\left(\operatorname{esu}\right) = 10^{-4} \frac{\varepsilon_{0} C^{2} n_{0}^{2} n_{2}}{\pi} \left(\frac{\operatorname{cm}^{2}}{\operatorname{W}}\right) \qquad \dots (2.21)$$

Im
$$\chi^{3}$$
 (esu) = $10^{-2} \frac{\varepsilon_{0} C^{2} n_{0}^{2} \lambda \beta}{4\pi^{2}} \left(\frac{cm}{W}\right)$... (2.22)

where ϵ_0 is the vacuum permittivity, n_0 is the linear refractive index of the 2PA & c is the velocity of the light in vacuum. For 2PA crystal the value of nonlinear refractive index $n_2 = 2.15 \times 10^{-09}$ (cm²/W). The absorption co-efficient β calculated from open aperture normalized transmittance was obtained as 2.07×10^{-04} (cm/W). According to equations 2.21 and 2.22, the values of n_2 & β are used to calculate third order susceptibility (χ^3). The third order nonlinear optical susceptibility $\chi^3 = 2.95 \times 10^{-06}$ esu. The open and closed aperture Z-scan results obtained for 2PA are shown in the Fig. 2.13a and 2.13b. The peak-valley configuration in which transmittance increase in the pre-focal region and decrease in the post-focal region shows negative nonlinearity [23,24]. Figure 2.13b exhibits reverse saturable absorption (RSA) with a positive nonlinear absorption coefficient [25-27]. Table 2.3 tabularizes the experimental details and the results of the Z- scan technique for 2PA crystal.

Table 2.3. Obtained nonlinear optical parameter from open- and closed-aperture Z-scan measurement data for 2PA crystal

Parameters	Measured values for 2PA crystal
Nonlinear refractive index (n ₂)	$2.15 \times 10^{-09} (\text{cm}^2/\text{W})$
Nonlinear absorption coefficient (β)	$2.07 \times 10^{-04} (\text{cm/W})$
Real part of the third order susceptibility [$Re(\chi^3)$]	$2.92 \times 10^{-06} (\text{cm}^2/\text{W})$
Imaginary part of the third order susceptibility[Im(χ^3)]	$3.63 \times 10^{-07} (\text{cm/W})$
Third order nonlinear optical susceptibility (χ^3)	$2.95 \times 10^{-06} (esu)$

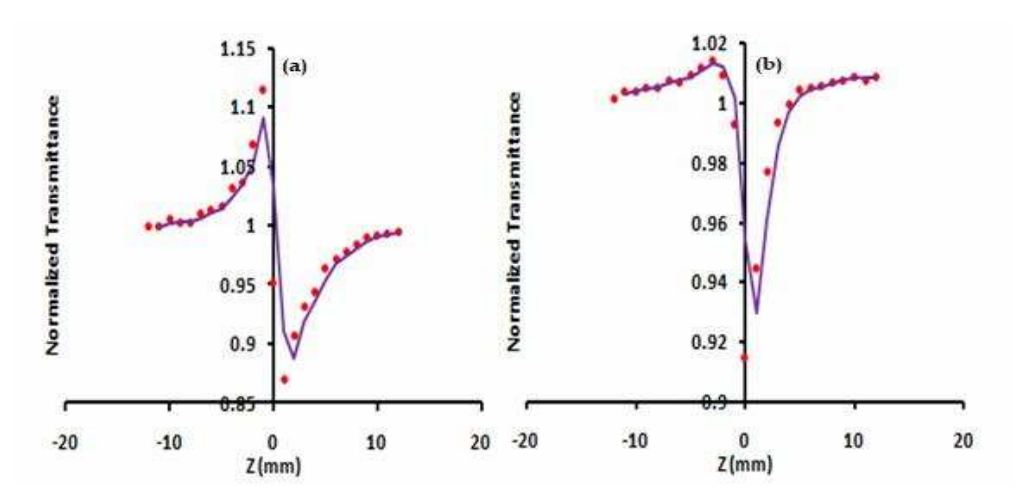


Fig. 2.13(a) Self-focusing (closed aperture) Z-scan plot of 2PA crystal **(b)** Open aperture mode Z-scan plot of 2PA crystal

2.3. COMPUTATIONAL ANALYSIS

2.3.1. Optimized Geometry

The optimized geometries of 2PA with symbols and numbering scheme for the atoms are shown in Fig. 2.14. Table 2.4 lists their main structural parameters maximized at DFT/B3LYP/6-311++G(d,p) level. The global minimum energy value measured by the DFT structure optimization method is -1.147 × 10⁶ kJ/mol. The computed bond lengths show slightly different than the experimental data, as the theoretical values correspond to the isolated molecules in gas-phase whereas the experimental results are correlated with the molecules in solid state [28]. The optimized structure reveals the C-C bond lengths in pyridine ring are close to the values found in pyridine [3], except for the C(4)-C(5) bond length. The value of C-N-C bond angle in a pyridine ring is intermediate between that of non protonated pyridine derivatives and that of some protonated pyridine derivatives [4]. This implies existence of the N-H-N inter molecular hydrogen bond. The small deviations dihedral angles are due to strong charge delocalization. In spite of these differences, the calculated geometric parameters show a good agreement with X-ray data hence can be used to calculate other parameters reported below.

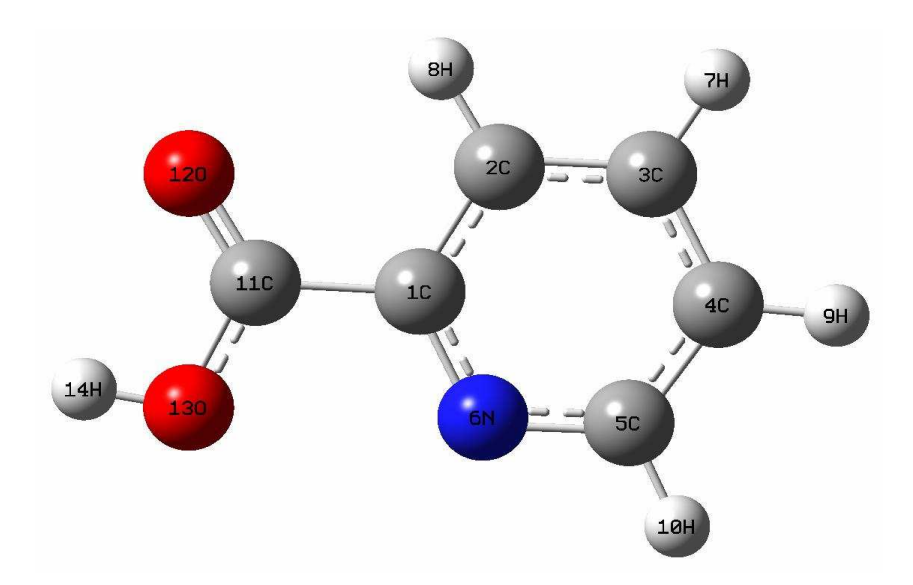


Fig. 2.14. The optimized molecular structure of 2PA

Table 2.4. Optimized parameters of 2PA by B3LYP level with 6-311++G(d,p) basis set

Bond	Value	es (Å)	Bond Angle	Value		Dihedral	Valu	es (°)
Length	Calc.	Exp.[3]	Dona Angle	Calc.	Exp.[3]	Angle	Calc.	Exp. ^[3]
O1-C4	1.210	1.213	C5-N3-C9	117.5	119.9	H9-C9-N3-C5	179.99	179.89
O2-C4	1.344	1.279	O1-C4-O2	122.9	126.8	C8-C9-N3-C5	0.0009	0.2
N3-C5	1.336	1.348	O1-C4-C5	123.2	118.7	Н6-С6-С7-Н7	0.0013	0.4139
N3-C9	1.332	1.338	O2-C4-C5	113.7	114.5	H7-C5-C6-C7	-179.99	-179.60
C4-C5	1.501	1.512	N3-C5-C4	118.5	119.1	N3-C9-C8-H8	179.99	179.70
C5-C6	1.390	1.373	N3-C5-C6	123.4	120.4	N3-C9-C8-C7	-0.0014	-0.2
C6-C7	1.397	1.380	C4-C5-C6	118.6	120.5	C9-N3-C5-C4	179.99	179.42
C7-C8	1.391	1.373	C5-C6-C7	118.5	119.9	C9-N3-C5-C6	0.0003	0.0188
C8-C9	1.395	1.375	C6-C7-C8	118.3	119.3	O1-C4-C5-N3	-179.99	175.30
O2-H2	0.968	0.803	C7-C8-C9	117.8	118.7	O1-C4-C5-C6	-0.0009	-5.2830
С6-Н6	1.083	0.961	N3-C9-C8	123.5	121.9	O2-C4-C5-N3	0.0026	-4.0034
С7-Н7	1.083	0.960	C4-O2-H2	106.4	114.6	O2-C4-C5-C6	-179.99	175.40
C8-H8	1.086	0.963	С5-С6-Н6	120.1	120.1	O1-C4-O2-H2	0.0011	8.5228
С9-Н9	1.082	0.959	С7-С6-Н6	122.2	120.0	C5-C4-O2-H2	179.99	-172.22
			C6-C7-H7	120.4	120.4	C6-C7-C8-C9	0.0005	0.1
			C8-C7-H7	120.5	120.4	С6-С7-С8-Н8	-179.99	179.99
			С7-С8-Н8	120.8	120.7	H7-C7-C8-C9	-179.99	179.86
			С9-С8-Н8	121.2	120.6	Н7-С7-С8-Н8	0.0004	0.018
			N3-C9-H9	116.0	119.0	N3-C5-C6-C7	-0.0010	-0.3231
			C8-C9-H9	119.4	119.1	N3-C5-C6-H6	179.99	179.66
						C4-C5-C6-C7	-179.99	-179.72
						С4-С5-С6-Н6	0.0009	0.2608
						C5-C6-C7-C8	0.0006	0.4
						C5-C6-C7-H7	-179.99	-179.60
						H6-C6-C7-C8	-179.99	-179.62
						Н8-С8-С9-Н9	0.0003	-0.2

2.3.2. Hyperpolarizability

To understand the microscopic origin of nonlinear behavior of the molecule (2PA), polarizability (α) and first-order hyperpolarizability (β) tensor [29] have been executed by B3LYP/6-311++G(d,p) basis set using Gaussian 09 program. The total linear polarizability (α ₀) can be calculated by the following equation,

$$\alpha = (\alpha_{xx} + \alpha_{yy} + \alpha_{zz})/3 \qquad \dots (2.23)$$

where, α_{xx} , α_{yy} and αzz are the diagonal components of polarizability tensor.

The first order hyper-polarizability is a third rank tensor which can be depicted by a $3 \times 3 \times 3$ matrix. Due to the Kleinmann symmetry [30], the 27 components of the 3D matrix can be minimized to ten components. Using the DFT calculations, ten components of this matrix such as β_{xxx} , β_{xxy} , β_{xyy} , β_{yyy} , β_{xxz} , β_{xyz} , β_{yyz} , β_{yzz} and β_{zzz} have been obtained. Using the x, y and z components, one can calculate the magnitude of the total first-order hyperpolarizability (β) tensor by the following equation,

$$\beta = [(\beta_{xxx} + \beta_{xyy} + \beta_{xzz})^2 + (\beta_{yyy} + \beta_{yzz} + \beta_{yxx})^2 + (\beta_{zzz} + \beta_{zxx} + \beta_{zyy})^2]^{\frac{1}{2}} \qquad \dots (2.24)$$

The calculated values of α and β components are listed in Table 2.5.

The polarizability(α) and first hyperpolarizability(β) of 2PA are $1.316x10^{-23}esu$ and 8.730×10^{-30} esu, respectively. The first hyperpolarizability of the 2PA compound is greater than those of urea (β of urea is 0.3728×10^{-30} esu obtained by HF/6-311G(d,p) method) [6].

Table 2.5. NLO properties of 2PA calculated using DFT at B3LYP/6-311++G(d,p) level

Polarizability		First hyperpolarizability	
α_{xx}	83.57	β_{xxx}	-12.18
α_{xy}	-3.15	β_{xxy}	-74.23
$\alpha_{ m yy}$	62.64	β_{xyy}	-14.80
α_{xz}	3.30	$eta_{ m yyy}$	-142.77
$\alpha_{ m yz}$	30.63	β_{xxz}	-160.80
α_{zz}	120.34	eta_{xyz}	-13.44
		$eta_{ m yyz}$	95.94
		β_{xzz}	-31.75
		β_{yzz}	603.83
		β_{zzz}	996.65

2.3.3. Natural Bond Orbital (NBO) Analysis

In order to elucidate the inter and intramolecular charge transfer interactions and electron delocalization within the molecule, the NBO analysis is performed on 2PA at DFT/B3LYP with 6-311++G(d,p) basis set. The second order perturbation theory analysis of Fock matrix in the NBO shows those strong intramolecular hyperconjugative interactions, which are presented in Table 2.6. The NBO analysis shows hydrogen bond interaction between $\sigma(C\text{-H})$ bonding and (C-N) and (C-C) σ^* anti-bonding orbitals. The most energetic donor - acceptor NBO interactions are those involving the $\pi^*(C_5\text{-N}_6)$ with $\pi^*(C_3\text{-C}_4)$ and $\pi^*(C_1\text{-C}_2)$ antibonds having energy contribution 224.43 and 171.59 kJ/mol respectively. These interactions are observed as an increase in electron density (ED) in C-C antibonding orbital that weakens the respective bonds and thereby causing stabilization to the structure. These intramolecular hyper conjugative interactions results in intramolecular charge transfer (ICT) causing stabilization of 2PA pyridine ring. The interaction between $n_2(O_{12})$ and $\sigma^*(C_{11}\text{-}O_{13})$ results in a low stabilization of 31.13 kJ/mol with low occupancy (0.08931e) of

antibonding orbital, whereas the charge transfer from $n_2(O_{13})$ to $\pi^*(C_{11}\text{-}O_{12})$ causes low stabilization of 46.96 kJ/mol. The hyperconjugative interactions between $n_2(O_{12})$ and $\sigma^*(C_1\text{-}C_{11})$ increases the C-C=O bond angles. These $(n_2$ to $\sigma^*)$ interactions are related to the resonance in the molecule, i.e., the negative charge resonates between the two oxygen atoms, because of the electron donation from the atom of the electron-donating orbital to the anti-bonding acceptor orbital [6].

Table 2.6. Second order perturbation theory analysis of Fock matrix in NBO basis including the stabilization energies using DFT at B3LYP/6-311++G(d,p) level

C						
Donor (i)	ED (i)	Acceptor (j)	ED (j)	^a E(2) Kcal/mol	^b E(j)-E(i) a.u.	°F(i,j) a.u.
$\pi(C_1-C_2)$		$\pi^*(C_3-C_4)$	0.30223	20.26	0.28	0.069
	1.61277	$\pi^*(C_5-N_6)$	0.35249	18.80	0.27	0.064
		$\pi^*(C_{11}-O_{12})$	0.24353	17.44	0.27	0.064
$\sigma(C_1-C_{11})$	1.97510	$\sigma^*(C_5-N_6)$	0.01484	3.25	1.20	0.056
(C. H.)	1.07700	$\sigma^*(C_1-N_6)$	0.02287	5.38	1.05	0.067
$\sigma(C_2-H_8)$	1.97790	$\sigma^*(C_3-C_4)$	0.01591	3.36	1.09	0.054
- (C, C)	1 62560	$\pi^*(C_1-C_2)$	0.32954	19.50	0.28	0.067
$\pi(C_3-C_4)$	1.63569	$\pi^*(C_5-N_6)$	0.35249	26.26	0.27	0.075
	1.98151	$\sigma^*(C_1-C_2)$	0.03062	3.25	1.09	0.053
$\sigma(C_3-H_7)$		$\sigma^*(C_4-C_5)$	0.02583	3.26	1.09	0.053
-(C II)	1.00045	$\sigma^*(C_2-C_3)$	0.01496	3.38	1.10	0.055
$\sigma(C_4-H_9)$	1.98045	$\sigma^*(C_5-N_6)$	0.01484	4.33	1.07	0.061
$\sigma(C_5-N_6)$	1.98635	$\sigma^*(C_1-C_{11})$	0.07737	3.01	1.23	0.055
$\pi(C_5-N_6)$ 1.71083	1 71002	$\pi^*(C_1-C_2)$	0.32954	25.08	0.32	0.081
	$\pi^*(C_3-C_4)$	0.30223	14.17	0.32	0.060	
5 (C II)	1.00102	$\sigma^*(C_1-N_6)$	0.02281	4.77	1.05	0.063
$\sigma(C_5-H_{10})$ 1.98193	1.96193	σ*(C ₃ -C ₄)	0.01591	3.54	1.09	0.055
n ₂ (O ₁₂)	1.85622	$\sigma^*(C_1-C_{11})$	0.07937	17.49	0.67	0.098
		$\sigma^*(C_{11}-O_{13})$	0.08931	31.13	0.62	0.126
n ₂ (O ₁₃)	1.81064	$\pi^*(C_{11}-O_{12})$	0.24353	46.96	0.34	0.114
π*(C N)	0.35249	$\pi^*(C_1-C_2)$	0.32954	171.59	0.02	0.079
$\pi^*(C_5-N_6)$	0.33249	$\pi^*(C_3-C_4)$	0.30223	224.43	0.01	0.084
$\pi^*(C_{11}-O_{12})$	0.24353	$\pi^*(C_1-C_2)$	0.32954	161.41	0.01	0.072

^aE(2) means the energy of hyper conjugative interactions.

^bEnergy difference between donor and acceptor i and j NBO orbitals.

^cF(i,j) is the Fock matrix element between i and j NBO orbitals.

2.3.4. Mulliken population analysis

The total atomic charges of 2PA molecule are obtained from the Mulliken charge population using DFT method. Atomic charges play an important role in quantum chemistry. Mulliken atomic charge population is one of the simplest pictures of charge distribution and it predicts the net atomic charges in the molecule [31]. The strong negative and positive charges on the atoms of 2PA molecule demonstrate the electrostatic attraction or repulsion between the atoms (Table 2.7). The Mulliken atomic charge distribution and plots of Mulliken atomic charges of all the atoms are shown in Fig. 2.15 and Fig. 2.16, respectively. The charges of the molecule are ranging from 1 to -0.8 (Fig. 2.16). The highest value is observed in C_{11} (+0.77237) and C_{13} (-0.65255), whereas the lowest value is observed in C_{2} (-0.19245) and C_{3} (-0.16797) atom. All the hydrogen atoms exhibit positive charge and all the oxygen atoms exhibit negative charge. The carbon atoms possess both positive and negative charges and the nitrogen atom exhibits negative charge. The sum of Mulliken atomic charges for 2PA molecule becomes zero and thus maintains the charge neutrality.

Table 2.7. Natural population analysis (NPA) of 2PA calculated with DFT/B3LYP/6-311++G(d,p) method

Atoms	Natural Charge	Atomic Charge
C_1	0.08733	-0.285942
C_2	-0.19245	0.533298
C_3	-0.16797	-0.662069
C_4	-0.22029	0.131323
C_5	0.05534	-0.234784
N ₆	-0.41543	0.023066
H_7	0.21332	0.184306
H ₈	0.23848	0.249154
H ₉	0.21497	0.186442
H_{10}	0.19094	0.202031
C ₁₁	0.77237	-0.161785
O ₁₂	-0.60557	-0.306514
O ₁₃	-0.65255	-0.157673
H ₁₄	0.48151	0.299147
Total	0.00000	0.000000

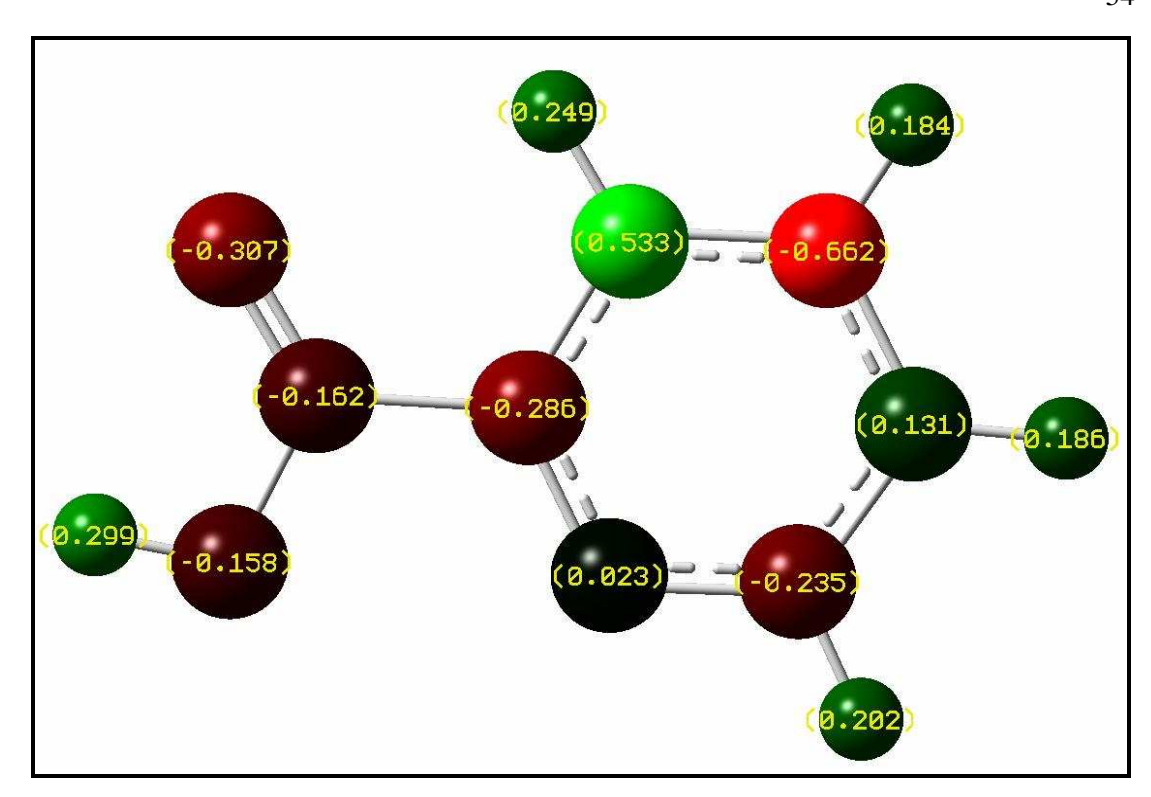


Fig. 2.15. Mulliken atomic charge distribution of 2PA

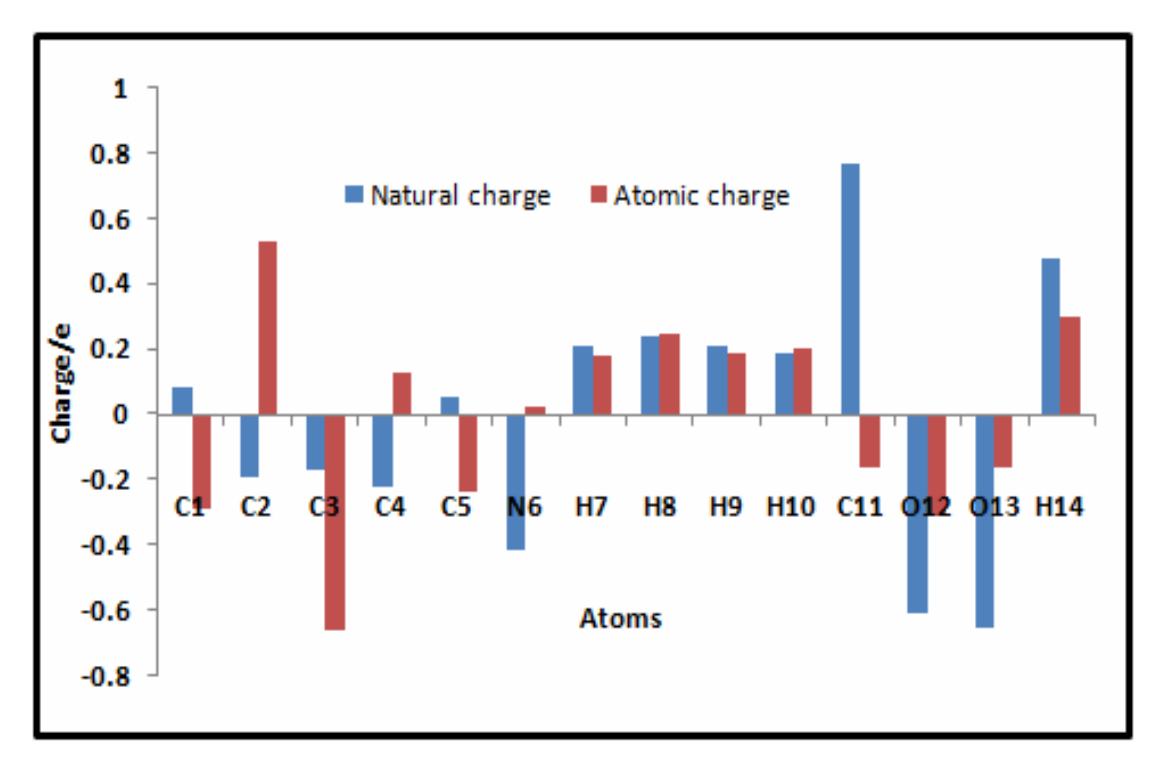


Fig. 2.16. Mulliken atomic charges of all the atoms of 2PA

2.3.5. Molecular Electrostatic Potential (MEP) analysis

Molecular Electrostatic Potential (MEP) is the three dimensional representation of the charge distributions of molecules. MEP is primarily used to find out the reactive sites of molecules which empower to anticipate how one molecule can interact with other molecules [32]. The electrostatic potential values at the surface are represented in different colors. The color code of these maps ranges between -5.706e-2 (deepest red) and +5.706e-2 (deepest blue) (Fig. 2.17). The light blue indicates the slight electron deficient region while the yellow portion shows the slight electron rich region. As depicted in Fig. 2.17, the regions having negative charges are around the Cl1, Ol2, Ol3 and N6 atoms. The absence of maximum negative potential region in MEP plot confirms the low chemical reactivity of the molecule and the presence of partial negative potential region (yellow colour) indicates the electron rich region which is the favourable site for electrophilic reactivity.

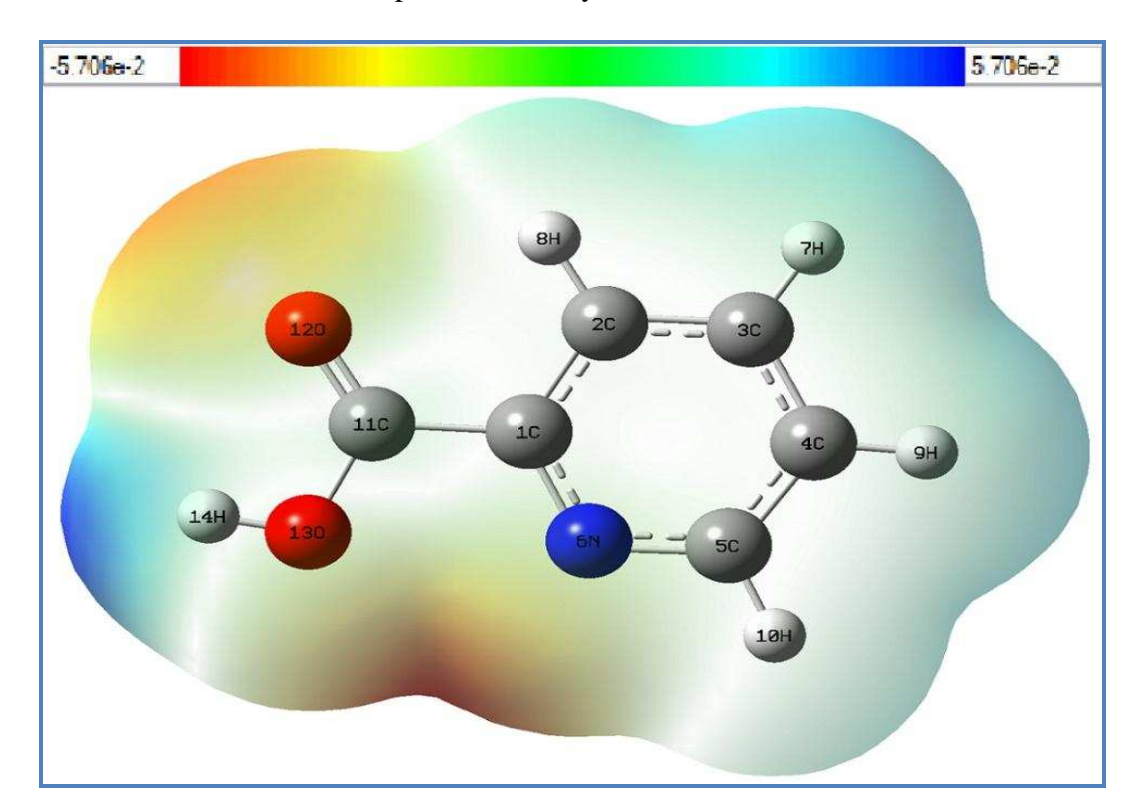


Fig. 2.17. Molecular electrostatic potential of 2PA

2.3.6. Frontier Molecular Orbital Analysis

The energy gap of HOMO-LUMO explains the charge transfer interactions within the conformers. The HOMO and LUMO energies of 2PA, as calculated by DFT/B3LYP/6-311++G(d,p) method, are as follows: HOMO energy, $E_{HOMO}=-7.47 eV$; LUMO energy, $E_{LUMO}=-2.09 eV$; HOMO-LUMO energy gap, $\Delta E_{GAP}=E_{LUMO}-E_{HOMO}=5.38 eV$.

The plots of HOMO and LUMO are shown in Fig. 2.18. The computed larger value of the HOMO-LUMO energy gap (5.38eV) in 2PA confirms higher kinetic stability and lower chemical reactivity of the molecule. The 5.38 eV gap falls within the UV region, so the molecule is colorless.

The energy gap between HOMO and LUMO is a critical parameter to determine molecular electrical transport properties. The global chemical reactivity descriptors of molecules such as hardness (η) , chemical potential (μ) , softness (S) and electronegativity (χ) can be calculated using the following equations [33]:

$$\eta = \frac{I - A}{2}; \mu = \frac{-(I + A)}{2}; S = \frac{1}{2\eta} \text{ and } \chi = \frac{I + A}{2}$$
 ... (2.25)

where I and A are the ionization potential and electron affinity of the molecules respectively. The ionization energy (I = - E_{HOMO}) and electron affinity (A = - E_{LUMO}) can be expressed through HOMO and LUMO orbital. It is widely known that the chemical hardness and softness are useful properties to measure the molecular stability and reactivity. The electrophilicity index (ω) is a measure of energy lowering due to the maximum electron flow between donor and acceptor [34]. It has been obtained from the following equation:

$$\omega = \frac{\mu^2}{2\eta} \qquad \dots (2.26)$$

The total energy change is defined as, $\Delta E_T = \frac{\eta}{4}$. The overall energy balance (ΔE) which determines the energy gain or lost, in an electron donor–acceptor transfer [35] is given as, $\Delta E = (A - I)$. The calculated reactivity descriptors are presented in Table 2.8. The hardness value and negative chemical potential indicate that the molecule is stable [36].

Table 2.8. Calculated quantum chemical molecular orbital properties for 2PA at DFT/B3LYP/6-311++G (d, p) method

Parameters	B3LYP/6-311++G(d,p)
HOMO energy, E _{HOMO}	-7.47 eV
LUMO energy, E _{LUMO}	-2.09 eV
HOMO–LUMO energy gap, ΔE _{GAP}	5.38 eV
Ionization potential (I)	7.47 eV
Electron affinity (A)	2.09 eV
Total energy change, ΔE_T	-0.67 eV
Overall energy balance, ΔE	-5.38 eV
Electronegativity, χ	4.78 eV
Chemical hardness (η)	2.69 eV
Chemical potential (µ)	-4.78 eV
Electrophilicity index (ω)	4.24 eV
Softness (S)	0.37 eV ⁻¹
SCF energy	$1.15 \times 10^6 \text{ kJ mol}^{-1}$

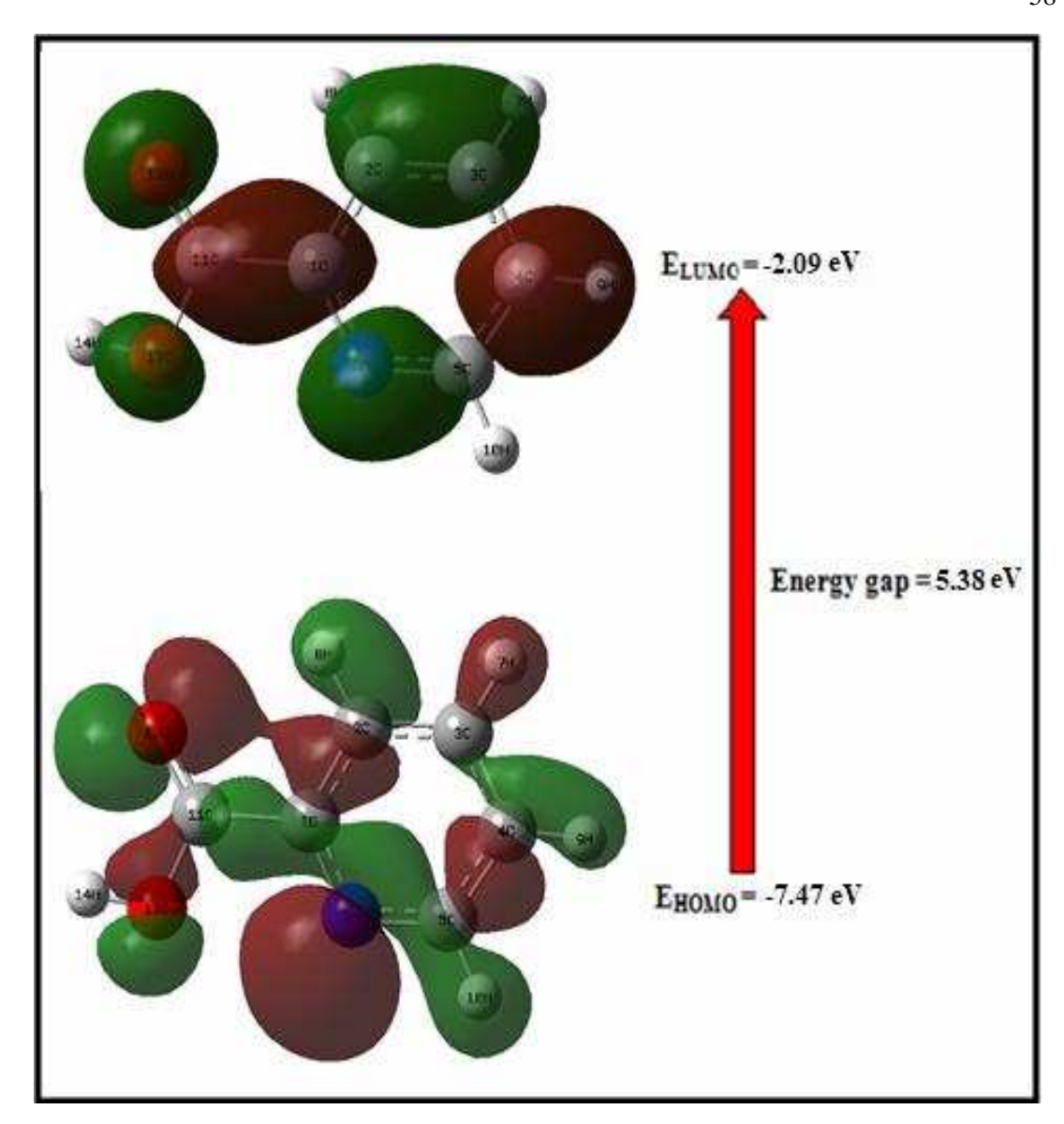


Fig. 2.18. HOMO-LUMO Plot of 2PA

2.3.7. Vibrational Spectral Analysis

The various vibrations with assignments of 2PA crystal is carried out on the DFT with B3LYP/6-311++G(d,p) basis set. The FTIR spectrum was recorded using a Perkin Elmer Spectrum II FTIR spectrometer in the scan range 4000–400 cm⁻¹. The experimental frequencies of FTIR intensities and their different assignments were compared with theoretically computed assignments and are shown in Table 2.9 and spectra in Fig. 2.19.

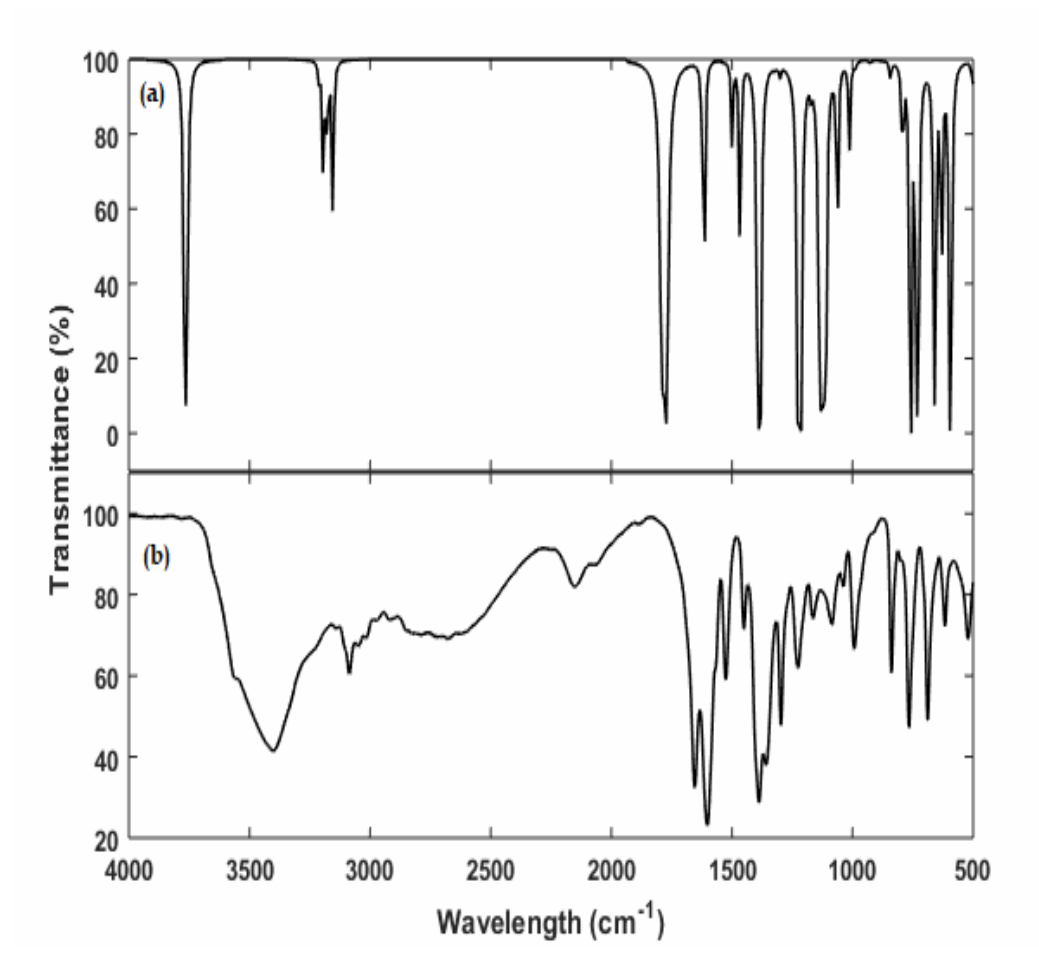


Fig. 2.19(a). Simulated IR spectra of 2PA (b) FTIR spectra of 2PA

O-H Vibrations

The O-H stretching vibrations of water molecule are expected in the wavenumber region have 3600–3400 cm⁻¹ [1]. In 2PA, broad IR band is observed at 3400 cm⁻¹ have been assigned to the stretching vibrations of water molecules. The medium weak bands are observed at 838, 688 and 616 cm⁻¹ in IR are attributed to the out-of-plane O-H bending mode. The computed O-H vibrations show good agreement with the experimental results.

Pyridine Ring Vibrations

The C-H stretching wavenumber of pyridine ring are expected in the spectral region 3100–3010 cm⁻¹ [1]. In 2PA, the IR medium band observed at 3040 cm⁻¹ corresponds

to the pyridine ring C-H stretching mode. The C-H in-plane bending modes can be expected in the region 1300 –1000 cm⁻¹ and the absorption bands arising from C-H out-of-plane bending vibrations are usually observed in the region at 1000–675 cm⁻¹. The observed C-H bending bands are sharp but are weak to medium intensity. The C-H in-plane bending vibrations are observed in IR at 1164 and 1085 cm⁻¹. The C-H out-of-plane bending vibration observed at 992 and 765 cm⁻¹, which is close to computed vibration at 983 and 759 cm⁻¹. The aromatic ring C-C stretching vibrations occur in the region 1625–1430 cm⁻¹. In 2PA, the IR bands at 1601, 1525 and 1450 cm⁻¹ are assigned to the C-C stretching modes; it shows good agreement with computed results. Simultaneous activation of the C-C stretching mode of the pyridine ring in IR spectra provides evidence for the charge transfer (ICT) interaction between the donor and acceptor groups through the π system, which enhances the NLO activity.

Carboxyl Group Vibrations

Carbonyl stretching vibrations are generally appeared in the region 1715–1680 cm⁻¹ [1]. In 2PA, the C=O stretching is observed in IR band at 1653 cm⁻¹. The lowering of C=O stretching mode is owing to the hydrogen bonding of carbonyl group with water molecule. The COO in-plane bending mode appears as very strong band at 1387cm⁻¹ in both experimental and calculated vibration.

Table 2.9. Experimental and calculated vibrational wavenumbers and fundamental bands positions assignments of 2PA

Calculated wavenumber (cm ⁻¹)	Experimental wavenumber (cm ⁻¹)	Vibrational Assignments
-	3400	O-H stretching vibration
3154	3040	C-H stretching
-	2152	N-H stretching vibrations
-	1653	C=O stretching vibration
1613	1601	aromatic ring C-C stretching vibrations
-	1525	aromatic ring C-C stretching vibrations
1465	1450	aromatic ring C-C stretching vibrations
1387	1387	COO in-plane bending
1292	1296	C-O stretching vibration
1219	1226	C-O stretching vibration
1129	1164	C-H in-plane bending
-	1085	C-H in-plane bending
983	992	C-H out-of-plane bending
-	838	out-of-plane O-H bending
759	765	C-H out-of-plane bending
658	688	out-of-plane O-H bending
-	616	out-of-plane O-H bending

2.3.8. Hirshfeld surface analysis

The 3D picture in Hirshfield surface analysis depicts internuclear distances and angles whereas the 2D fingerprint plot shows the existence of different types of intermolecular interactions [37,38]. The Hirshfield surfaces of the 2PA are given in Fig. 2.20 and it explains the surfaces that have been mapped over dnorm, de, di, and curvedness. The surface, representing the deep red colored circular depressions indicates

hydrogen bonding contacts (Fig.2.21). The most major H···H/H···H interactions contribute 44.4% to the overall crystal packing and the 28.1% contribution from the O···H/H···O contacts are represented by a pair of sharp spikes characteristic of a strong hydrogen-bond interaction. This is evidence that van der Waals forces exert an important influence on the stabilization of the packing in the system [39,40]. Weak interactions are identified as C-C (8.3%), C-H (7.2%), O-C (6.1%), N-C (3.8%), N-H (1.3%), O-O (0.3%), O-N (0.2%) and N-N (0.1%). The strong interactions occupy more space and weak ones occupy less space in the finger print region.

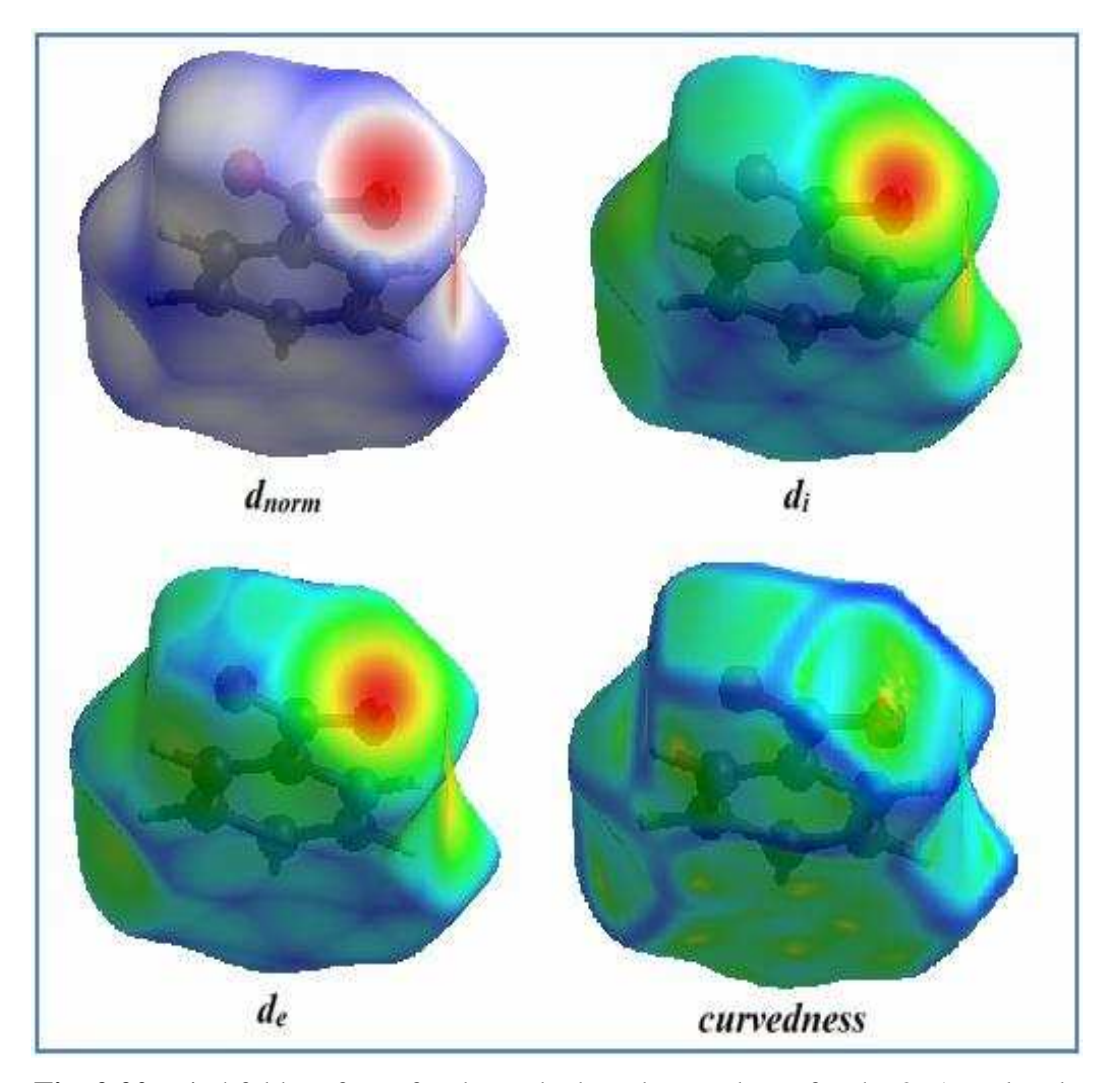


Fig. 2.20. Hirshfeld surfaces for d_{norm} , d_i , d_e and curvedness for the 2PA molecule

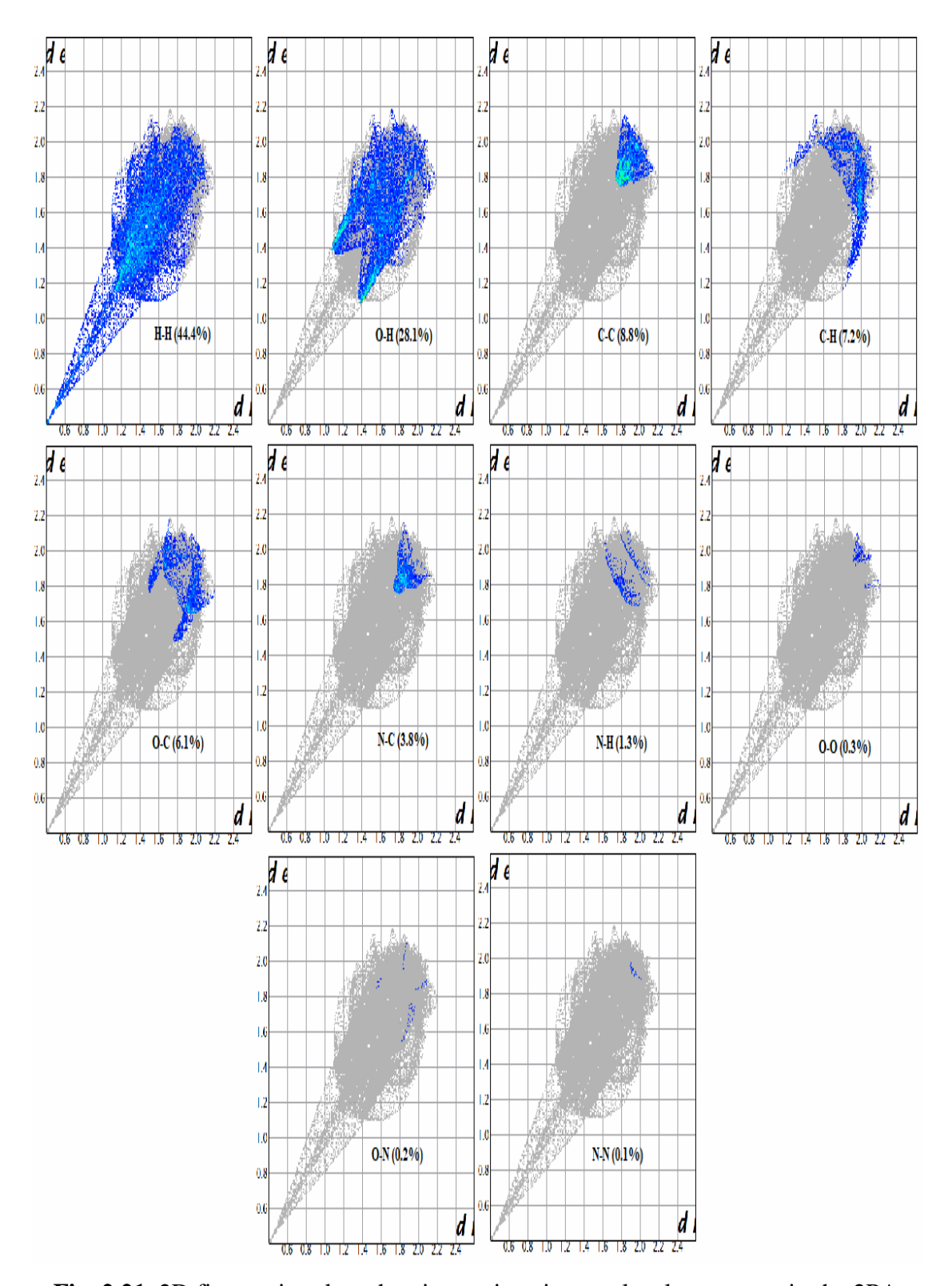


Fig. 2.21. 2D fingerprint plots showing various intermolecular contacts in the 2PA

2.4. CONCLUSIONS

Solubility studies of 2-picolinic acid (2PA) revealed positive coefficient of solubility. Nucleation parameters of crystallization process of the 2PA crystals are determined by the classical nucleation theory and density functional theory. The 2-picolinic acid single crystals have been successfully grown by slow evaporation solution technique (SEST). The powder X-ray diffraction analysis was carried out to confirm the crystallinity nature and also to ascertain the purity of the grown crystal. Williamson-Hall approach is found to be good for the calculation of the crystallite size and lattice strain. UV studies show that the 2PA crystal is transparent in the entire visible region. From the optical studies, optical constants like refractive index (n=1.08), reflectance, extinction coefficient, real and imaginary dielectric constants are evaluated. The band gap energy for the grown crystal is found to be 3.5 eV, whereas optical band gap by DASF method is equal to 3.47 eV. The fluorescence emission analysis confirms the emission of 2PA is in the blue region. The Z-scan analysis of 2PA shows that it can be used in optical limiting devices applications. Molecular structure optimization is accomplished perfectly by using DFT computation. The first-order hyperpolarizability and polarizability of 2PA are computed at the DFT level and the results are discussed. The NBO analysis reveals hyper conjugative interaction, ICT and stabilization of the molecule. Mulliken charges and molecular electrostatic potential and are computed to know about the potential and charge distribution within molecule. Furthermore, the HOMO-LUMO energy gap value reflects the stability of 2PA molecule. The DFT based quantum mechanical approach provides the most reliable theoretical information on the vibrational properties of 2PA. The theoretical results were compared with the experimental vibrations. The assignments of most of the fundamentals provided in the

present work are believed to be unambiguous. The Hirshfeld surface analysis of 2PA interprets the percentage of strong and weak intermolecular interactions in the crystalline state. The vibrational, UV, NBO and Z-scan studies suggest 2PA as an attractive material for optical applications.

REFERENCES

- S. Gowri, T. Uma Devi, D. Sajan, C. Surendra Dilip, A. Chandramohan, N. Lawrence,
 Crystal growth, spectral, optical and thermal properties of semiorganic nonlinear optical material: Picolinic acid hydrochloride, Spectrochim. Acta A Mol. Biomol. Spectrosc., 110 (2013) 28–35.
- Di Li, Guo-Qing Zhong, Synthesis, Crystal Structure, and Thermal Decomposition
 of the Cobalt(II) Complex with 2-Picolinic Acid, Sci. World J., 2014 (2014)
 641608.
- 3. H. Hamazaki, H. Hosomi, S. Takeda, H. Kataoka, S. Ohba, 2 Pyridinecarboxylic Acid, Acta Cryst. C54 (1998) IUC9800049.
- Fusao Takusagawa, Akira Shimada, The Crystal Structure of Picolinic Acid,
 Chem. Lett., 2 (1973) 1089-1090.
- C. Tamura, H. Kuwano, Y. Sasada, Crystallographic data of carboxylic acids and carboxyamides of picoline and pyrazine derivatives, Acta Cryst. 14 (1961) 693.
- V. Sasikala, D. Sajan, N. Vijayan, K. Chaitanya, M. S. Babu Raj, B.H. Selin Joy, Growth, molecular structure, NBO analysis and vibrational spectral analysis of 1-tartaric acid single crystal, Spectrochim. Acta A Mol. Biomol. Spectrosc., 123 (2014) 127-141.
- 7. Sonia, N. Vijayan, Medha Bhushan, Kanika Thukral, Rishabh Raj, K. K. Maurya, D. Haranath, S. A. Martin Britto Dhas, Growth of a bulk-size single crystal of sulphamic acid by an in-house developed seed rotation solution growth technique and its characterization, J. Appl. Cryst., 50 (2017) 763–768.

- 8. Jyoti Dalal, Binay Kumar, Bulk crystal growth, optical, mechanical and ferroelectric properties of new semiorganic nonlinear optical and piezoelectric Lithium nitrate monohydrate oxalate single crystal, Opt. Mater., 51 (2016) 139-147.
- J. Tauc, Amorpus and liquid semiconductors, Plenum press, London and New York, 1974.
- M.A. Omar, Elementary Solid State Physics, Addison-Wesley Publishing Company, 1987.
- 11. V. Gupta, A. Mansingh, Influence of post deposition annealing on the structural and optical properties of sputtered zinc oxide film, J. Appl. Phys., 80 (1996) 1063–1073.
- M.A. Gaffar, A. Abu El-Fadl, S. Bin Anooz, Influence of strontium doping on the indirect band gap and optical constants of ammonium zinc chloride crystals, Phys. B: Condens. Matter, 327 (2003) 43–54.
- 13. Rejeena V. Rajan, S. Gowri, N. Manopradha, D.R. Leenaraj, Lija K. Joy, D. Sajan, Growth, structural, third order nonlinear optical properties, dielectric properties, conductivity mechanisms and spectroscopic characterization of a luminescent material trans-diaqua-bis(pyridine-2-carboxylato)-cobalt(ii) dihydrate for optoelectronic applications, Opt. Laser Technol. 119 (2019) 105664.
- Dariush Souri, Zahra Esmaeili Tahan, A new method for the determination of optical band gap and the nature of optical transitions in semiconductors, Appl. Phys. B 119 (2015) 273–279.
- S. Terny, M.A. Frechero, Understanding how the mixed alkaline-earth effect tunes transition metal oxides-tellurite glasses properties, Phys. B: Condens. Matter, 583 (2020) 412054.

- 16. D. Souri, A.R. Khezripour, M. Molaei, M. Karimipour, ZnSe and copper-doped ZnSe nanocrystals (NCs): Optical absorbance and precise determination of energy band gap beside their exact optical transition type and Urbach energy, Curr. Appl. Phys. 17 (2017) 41–46.
- 17. Yazdan Shahmoradi, Dariush Souri, Growth of silver nanoparticles within the tellurovanadate amorphous matrix: Optical band gap and band tailing properties, beside the Williamson-Hall estimation of crystallite size and lattice strain, Ceram. Int. 45 (2019) 7857-7864.
- 18. G. Iyappan, Rajesh Paulraj, Ramasamy Perumalsamy, Kamalesh Kumar Maurya, Soma Venugopal Rao, An investigation on the growth and propitiates of KDP admixtured ADP single crystals, Ferroelectrics, 550 (2019) 151-172.
- D.S. Arteev, A.V. Sakharov, E.E. Zavarin, W.V. Lundin, A.N. Smirnov, V. Yu
 Davydov, M. A. Yagovkina, S.O. Usov, A.F. Tsatsulnikov, Investigation of
 Statistical Broadening in InGaN Alloys, J. Phys. Conf. Ser. 1135 (2018) 012050.
- 20. F. Urbach, The long-wavelength edge of photographic sensitivity and of the electronic absorption of solids, Phys. Rev. 92 (1953) 1324.
- 21. S.J. Ikhmayies, R.N. Ahmad-Bitar, A study of the optical bandgap energy and Urbach tail of spray-deposited CdS: In thin films, J. Mater. Res. Technol. 2 (2013) 221–227.
- 22. V. Dimitrov, S. Sakka, Electronic oxide polarizability and optical basicity of simple oxides. I, J. Appl. Phys. 79 (1996) 1736–1740.
- 23. R. Ravisankar, P. Jayaprakash, P. Eswaran, K. Mohanraj, G. Vinitha, Moorthi Pichumani, Synthesis, growth, optical and third-order nonlinear optical properties of glycine sodium nitrate singlecrystal for photonic device applications, J Mater Sci: Mater Electron, 31 (2020) 17320–17331.

- 24. J.H. Joshi, S. Kalainathan, M.J. Joshi, K.D. Parikh, Influence of L-serine on microstructural, spectroscopic, electrical and nonlinear optical performance of ammonium dihydrogen phosphate single crystal, J Mater Sci: Mater Electron, 30 (2019) 14243–14255.
- J. Wang, W.J. Blau, Inorganic and hybrid nanostructures for optical limiting,J. Opt. A: Pure Appl. Opt. 11 (2009) 024001.
- 26. F.Z. Henari, W.J. Balu, L.R. Milgrom, G. Yahyoglu, D. Philips, J.A. Lacey, Third-order optical non-linearity in Zn(II) complexes of 5,10,15,20-tetraarylethynyl-substituted porphyrins, Chem. Phys. Lett. 267 (1977) 229-233.
- 27. F.Z. Henari, Optical switching in organometallic phthalocyanin, J. Opt. A: Pure Appl. Opt. 3 (2001) 188-190.
- N. Matsuzawa, M. Ata, D.A. Dixon, Density functional theory prediction of the second-order hyperpolarizability of metalloporphines, J. Phys. Chem., 99 (1995) 7698–7706.
- 29. R. Rahmani, N. Boukabcha, A. Chouaih, F. Hamzaoui, S. Goumri–Said, On the molecular structure, vibrational spectra, HOMO-LUMO, molecular electrostatic potential, UV–Vis, first order hyperpolarizability, and thermodynamic investigations of 3-(4-chlorophenyl)-1-(1yridine-3-yl) prop-2-en-1-one by quantum chemistry calculations, J. Mol. Struct., 1155 (2018) 484–495.
- 30. D.R. Kanis, M.A. Ratner, T.J. Marks, Design and construction of molecular assemblies with large second-order optical nonlinearities. Quantum chemical aspects, Chem. Rev., 94 (1994) 195–242.

- 31. M. Arivazhagan, S. Manivel, S. Jeyavijayan, R. Meenakshi, Vibrational spectroscopic (FTIR and FT-Raman), first-order hyperpolarizablity, HOMO, LUMO, NBO, Mulliken charge analyses of 2-ethylimidazole based on Hartree–Fock and DFT calculations, Spectrochim. Acta A Mol. Biomol. Spectrosc., 134 (2015) 493-501.
- 32. R.S. Mulliken, Electronic Population Analysis on LCAOMO Molecular Wave Functions. I, J. Chem. Phys., 23 (1955) 1833–1840.
- 33. Vishnu A. Adole, Bapu S. Jagdale, Thansing B. Pawar, Arun B. Sawant, Experimental and theoretical exploration on single crystal, structural, and quantum chemical parameters of (E)-7-(arylidene)-1,2,6,7-tetrahydro-8H-indeno[5,4-b]furan-8-one derivatives: A comparative study, J Chin Chem Soc., 67 (2020) 1763-1777.
- 34. J. Gilman, Chemical and physical "hardness", Mater. Res. Innov., 1 (1977) 71-76.
- 35. V. Balachandran, A. Lakshmi, A. Janaki, Conformational stability, vibrational spectral studies, HOMO–LUMO and NBO analyses of 2-hydroxy-4-methyl-3-nitropyridine and 2-hydroxy-4-methyl-5-nitropyridine based on density functional theory, J. Mol. Struct., 1013 (2012) 75–85.
- 36. M.V.S. Prasad, Kadali Chaitanya, N. Udaya Sri, V. Veeraiah, Vibrational and electronic absorption spectral studies of 5-amino-1-(4-bromophenyl)-3-phenyl -1 -H-pyrazole, Spectrochim. Acta A Mol. Biomol. Spectrosc., 99 (2012) 379–389.
- 37. S. Chitrambalam, D. Manimaran, I. Hubert Joe, V.K. Rastogi, IsrarUl Hassan, Synthesis, Hirshfeld surface analysis, laser damage threshold, third-order nonlinear optical property and DFT computation studies of Dichlorobis(DL-valine) zinc(II): A spectroscopic approach, Opt. Mater., 75 (2018) 285-296.

- 38. S. Goel, H. Yadav, N. Sinha, B. Singh, I. Bdikin, D. C. Rao, K. Gopalaiah, B. Kumar, An insight into the synthesis, crystal structure, geometrical modelling of crystal morphology, Hirshfeld surface analysis and characterization of N-(4-methyl-benzyl)-benzamide single crystal, J. Appl. Cryst. 50 (2017) 1498-1511.
- 39. M.A. Spackman, J.J. McKinnon, Fingerprinting intermolecular interactions in molecular crystals, Cryst.Eng.Comm., 4 (2002) 378-392.
- 40. Madan Kumar Shankar, Basavapattana C. Manjunath, Koravangala Shivakumar Vinay Kumar, Kudigana J. Pampa, Marilinganadoddi P. Sadashiva, Neartur K. Lokanath, Crystal Structure, Spectral Studies, and Hirshfeld Surfaces Analysis of 5-Methyl-5H-dibenzo[b,f]azepine and 5-(4-Methylbenzyl)-5H-dibenzo[b,f] azepine, J. Crystallogr., 2014 (2014) 862067.

Chapter-III

Experimental and Theoretical Investigations of Nonlinear Optical Crystal 2-Picolinic Trichloro Acetate

CHAPTER – III

EXPERIMENTAL AND THEORETICAL INVESTIGATIONS OF NONLINEAR OPTICAL CRYSTAL 2-PICOLINIC TRICHLORO ACETATE

3.1. INTRODUCTION

Growing organic single crystals has recently attracted a lot of attention from researchers because of their potential use in optical communication and image process [1,2]. The organic materials enable calibration of their optical properties through molecular engineering and chemical synthesis [3,4]. Carboxylic acids are the fascinating organic materials in the optical applications because of their potential to form hydrogen bonding interactions. The 2-carboxypyridine (also known as pyridine-2-carboxylic acid, 2-pyridine carboxylic acid and picolinic acid) is one such carboxylic acid that likely creates stable compound.Pyridine-1-ium-2-carboxylatehydrogenbromide [5], picolinic acid hydrochloride [6], 2-Carboxypyridinium hydrogen chloranilate [7], phosphoric acid pyridine-1-ium-2-carboxylate [8], and 2-Carboxypyridin-1-ium trichloroacetate (also known as 2-picolinic trichloro acetate) [9] are all examples of stable carboxylic acids that have been reported previously.

The present investigation is a novel one for reporting the nucleation kinetics, third order nonlinearity and spectroscopic studies of 2-Picolinic Trichloro Acetate (2PTCA) crystal. X-ray diffraction investigating the structural aspects establishes the crystal structure belonging to crystal system as monoclinic nature. Williamson–Hall approach assesses the structural characteristics of the grown crystal such as average crystallite size along with lattice strain. Optical and Mechanical studies of PTCA have

also been carried out alongside, and its results are discussed. The study also focuses on experimental study and quantum chemical calculations of PTCA crystal. The study elucidates the correlation between the molecular structure and the NLO property together with the theoretical spectral simulations using the density functional theoretical (DFT) computations. The natural bond orbital (NBO) analysis explores the interaction between inter- and intra-molecular charge transfers. The quantum chemical molecular orbital parameters have been evaluated from Frontier molecular orbital analysis. Hirshfeld surface maps and fingerprint graphs are plotted to understand the various types of intermolecular interactions in the molecular crystal package.

3.2. EXPERIMENTAL ANALYSIS

3.2.1. Solubility Study

The solubility of 2-picolinic trichloro acetate was determined gravimetrically for four temperatures (303 K to 318 K). Fine powder of PTCA compound was dissolved in 100 ml of deionized water at 303 K until an equilibrium concentration of the solution was obtained. The similar procedure was followed for 308 K to 318 K with step increase of 5 K. The solubility of 2-picolinic trichloro acetate was found to be 11 g/100 ml at 303 K. The concentration vs temperature of PTCA crystal is shown in Fig. 3.4. It is observed that the solubility of material increases with an increase in temperature and nucleation temperature increases with the increase in concentration. Thus the grown PTCA crystal has a positive temperature coefficient of solubility.

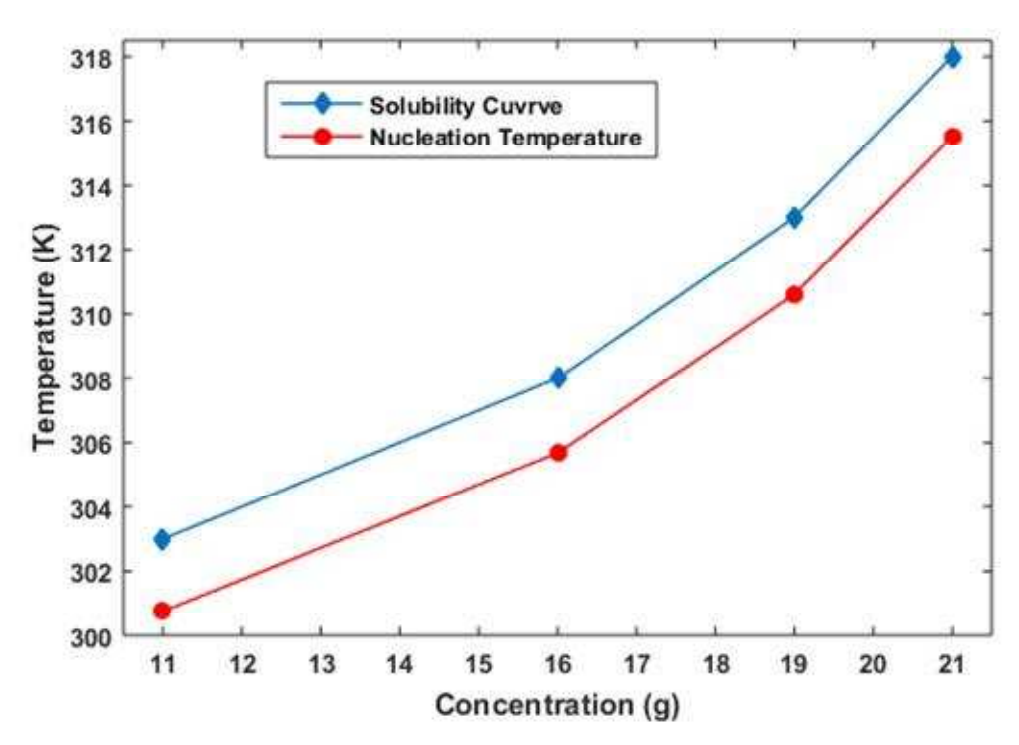


Fig. 3.1. Solubility curve for PTCA

3.2.2. Nucleation Kinetics and Metastable Zone Width (MZW)

The value of radius of critical nucleus (r^*) , Gibbs free energy per unit volume (ΔG_v) , critical free energy barrier (ΔG^*) and the number of molecules present in the critical nucleus (i^*) are calculated as per eqn.no. (1.1 to 1.8) in chapter-I and are given in Table 3.1. The critical free energy barrier (ΔG^*) decreases with increasing the supersaturation and temperature and is shown in Fig. 3.2. The change in critical radius (r^*) as a function of temperature, as well as the supersaturation are shown in Fig. 3.3. At low supersaturation the formation of critical nucleus requires more free energy change. Hence, radius of critical nucleus and number of molecules (i^*) present in the critical nucleus requires low free energy change. Thus, the critical radius of the nucleus, the critical free energy barrier and the number of molecules present in the critical nucleus were decreased with increasing supersaturation.

A real control of nucleation and growth rate scan only be realized by the knowledge of the actual width of the metastable zone and control of the actual operating point within the metastable zone throughout the crystallization process. Nucleation temperature for each saturation temperature can be calculated from Fig. 3.1. The present study involves reporting theoretically calculated values of metastable zone width for the crystallization temperatures of crystals by slow evaporation method. The metastable zone width of grown crystal very slightly broadens with the increasing of temperature, which is the essential aspect for bulk size crystal growth.

 \mathbf{i}^* **T**(**K**) $\Delta Gv(J/m^3)$ $\sigma (J/m^2)$ $\Delta \mathbf{G}^* (\mathbf{J})$ r* (m) J (nuclei/m³/sec) 303 -1466231.2 0.006351 1.99E-18 8.66E-09 10015.636 1.45898E+13 308 -1490426.4 0.005845 1.51E-18 7.84E-09 7431.595 1.19578E+13 0.005655 1.32E-18 313 -1514621.6 7.47E-09 6412.663 1.08382E+13 -1538816.9 0.005577 1.23E-18 7.25E-09 5864.569 1.02114E+13 318

Table 3.1. Nucleation Table from PTCA for Supersaturation Ratio-1.1

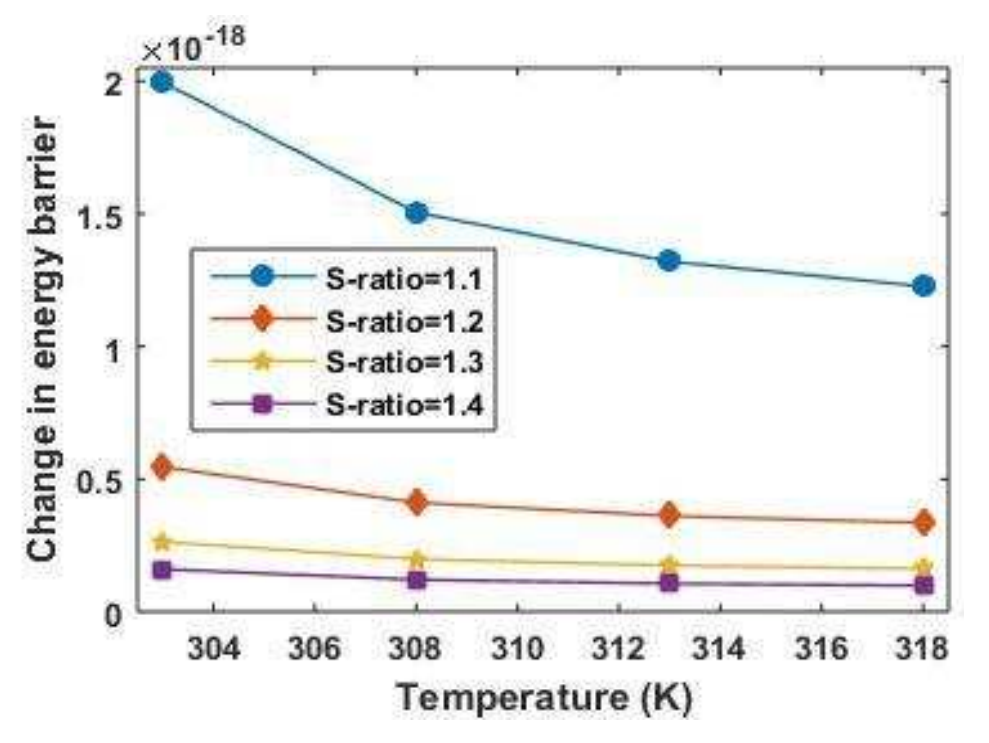


Fig. 3.2. Variation of Gibbs free energy with supersaturation and temperature for PTCA

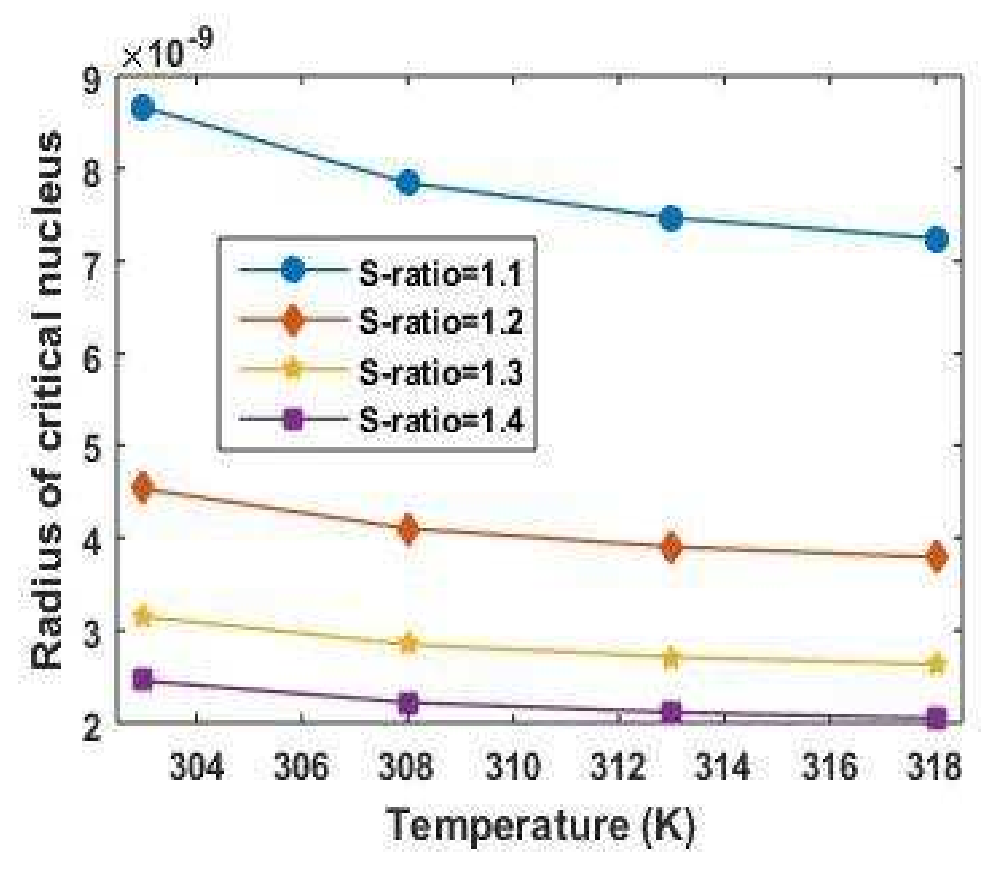


Fig. 3.3. Variation of radius of critical nucleus with temperature and supersaturation ratio of PTCA

3.2.3. Growth of PTCA Crystal

The commercially available 2-carboxypyridine and tricholoroacetic acid (AR grade) was taken as raw materials in equimolar ratio for growth of crystal and dissolved in double distilled water. The saturated solution was prepared after attempting the stirring process continuously for a period of six hours using a temperature controlled magnetic stirrer. Then the saturated solution was filtered using Whatman filter paper and poured in a well cleaned Petri dish for synthesizing process. The synthesized salts were purified by repeated recrystallization and at last good transparent colorless single crystals were harvested after three weeks and are shown in Fig. 3.4.

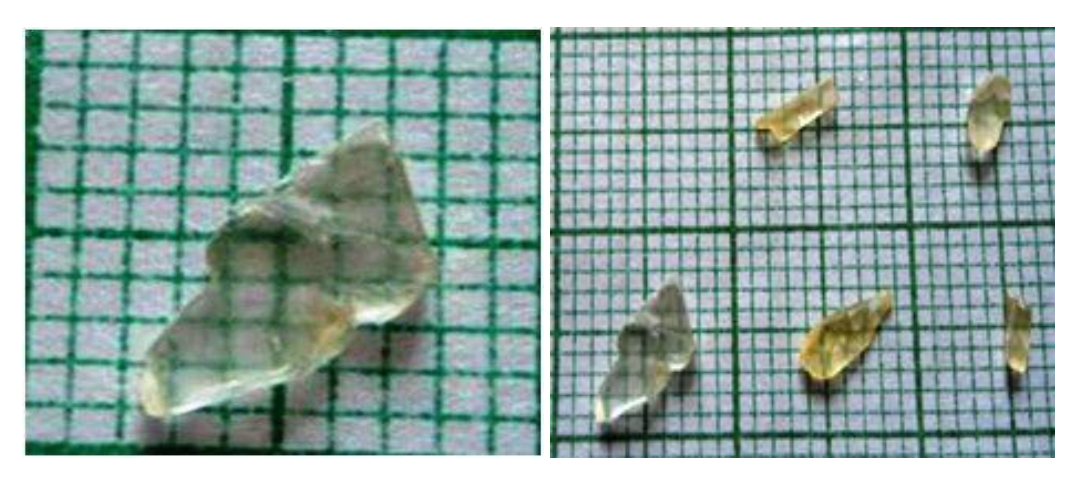


Fig. 3.4. As grown crystal of PTCA

3.2.4. Powder XRD

The powdered sample of the grown crystal was subjected to powder crystal X-ray diffraction using BRUKER X-ray diffractometer with CuK α radiation (λ = 1.5406 Å) and a step size of 0.0130 and a scanning step time of 23.97s, to confirm the crystalline nature of the grown crystal and it is evident from the sharp peaks as in Fig. 3.5. From the Fullprof Suite software, it is confirmed that PTCA crystal belongs to monoclinic system with space group $P2_I$ and unit cell parameters are a = 6.134 (7) (Å), b = 22.140 (30) (Å), c = 8.049 (9) (Å), α = γ =90°, β = 95.755 (8) and volume = 1087.8 (2) (Å³). These values are in good agreement with the reported values [9].

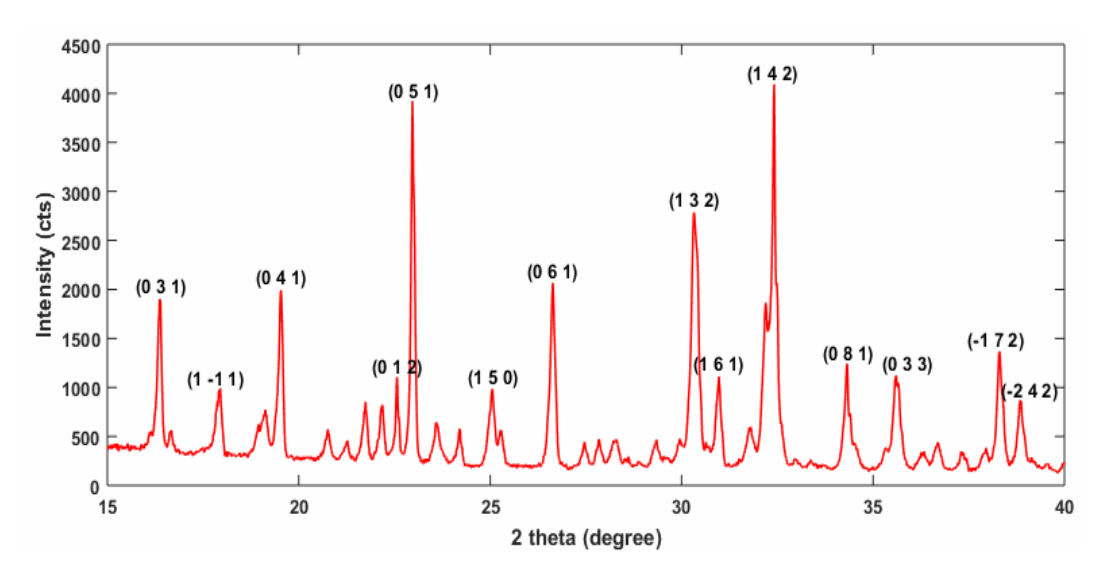


Fig. 3.5. Powder XRD pattern of PTCA crystal

The size of crystal and its characteristics are important in determining their semiconducting nature, physical and optical properties, and so Williamson-Hall (W-H) approach has been proposed to estimate them. In the W-H method, the XRD peak broadness is due to the grain size and the lattice strain (measuring the distribution of lattice constants and crystalline imperfections, such as lattice dislocations). It is possible to estimate the crystallite size and the strain via the more precise Williamson-Hall approach considering all of the diffraction peaks.

Upon using equations 2.3 and 2.4 from chapter-II, crystallite size (τ) and lattice strain (η) is calculated from the slope and y-axis intercept of the $\beta\cos\theta$ versus $\sin\theta$ plot, respectively. Fig. 3.6 shows the Williamson-Hall plot for PTCA crystal. The value of τ is ~0.1 μ m and η , is 0.006 which indicates PTCA crystal has less lattice strain, which suggests larger elastic stiffness constant, and is discussed in microhardness section [10].

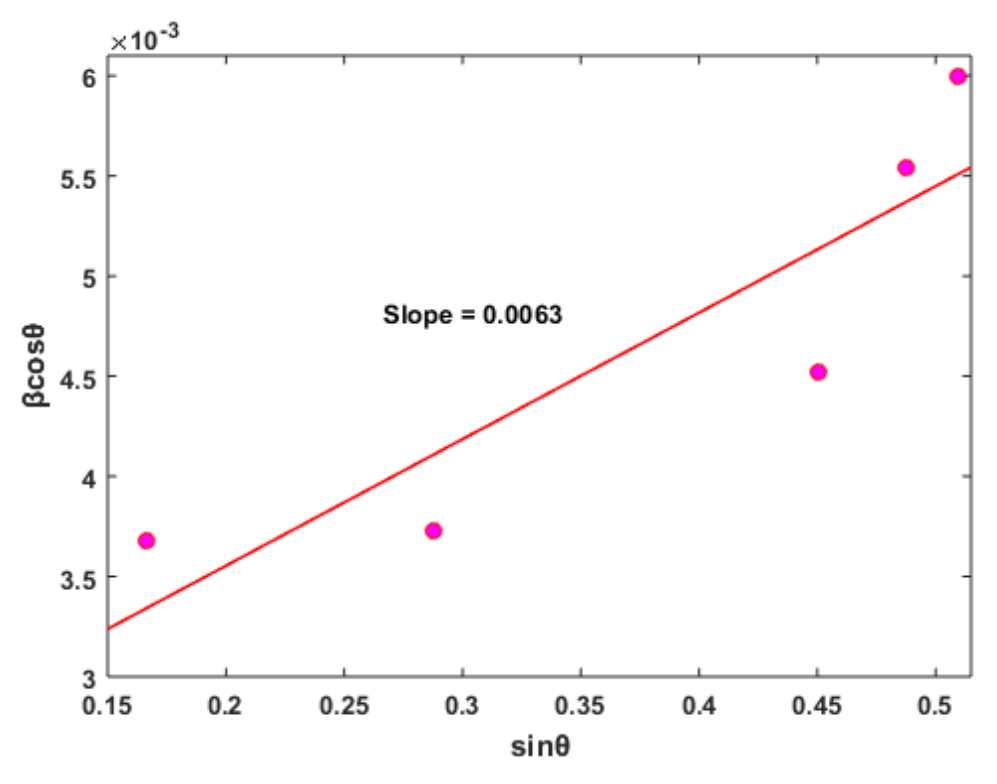


Fig. 3.6. Graph plotting $\beta\cos\theta$ versus $\sin\theta$

3.2.5. UV-vis-DRS Analysis

(a) By Tauc's Plot

Optical transmission and absorption spectra are essential in determining material optical characteristics. The optical behavior of materials is tightly related to localized states, atomic structures, and optical transitions [11]. For optical applications, the crystal must have a high degree of transparency and minimal absorption over a wide wavelength range. The lower cut-off wavelength of the grown crystal is 260 nm, which corresponds to π - π * transition. The absorbance spectrum of the PTCA crystal recorded using SHIMADZU/ UV 2600 Spectrophotometer in the range 220 -1100 nm presented in Fig. 3.7, shows high transmittance, indicating good crystal quality.

Using the absorption spectra, the linear optical constants of PTCA are calculated and the variation in optical constants as a function of photon energy is plotted (Fig. 3.8(a-d)). From Fig. 3.8a the bandgap of PTCA crystal is jotted down to be 4.25 eV, which indicates the grown crystal possessing large transmittance and permits it to be a suitable candidate for optoelectronic applications. Refractive index (n), electric susceptibility (χ_C), real (ϵ_r) and imaginary (ϵ_i) dielectric constants are calculated via equations 2.5 to 2.8 from chapter-II, and obtained values at $\lambda=800$ nm, are n = 1.48, $\chi_C=0.175$, $\epsilon_r=2.198$ and $\epsilon_i=7.275\times 10^{-6}$. These values suggest that the PTCA material has profound NLO efficiency.

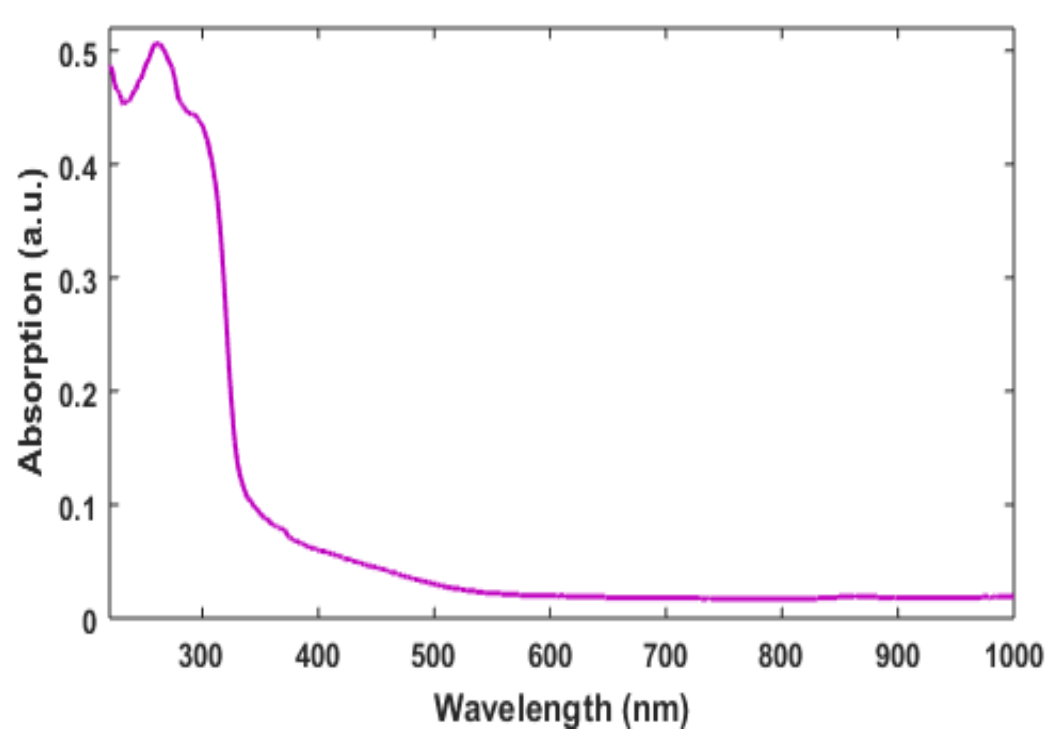


Fig. 3.7. Optical absorbance of PTCA

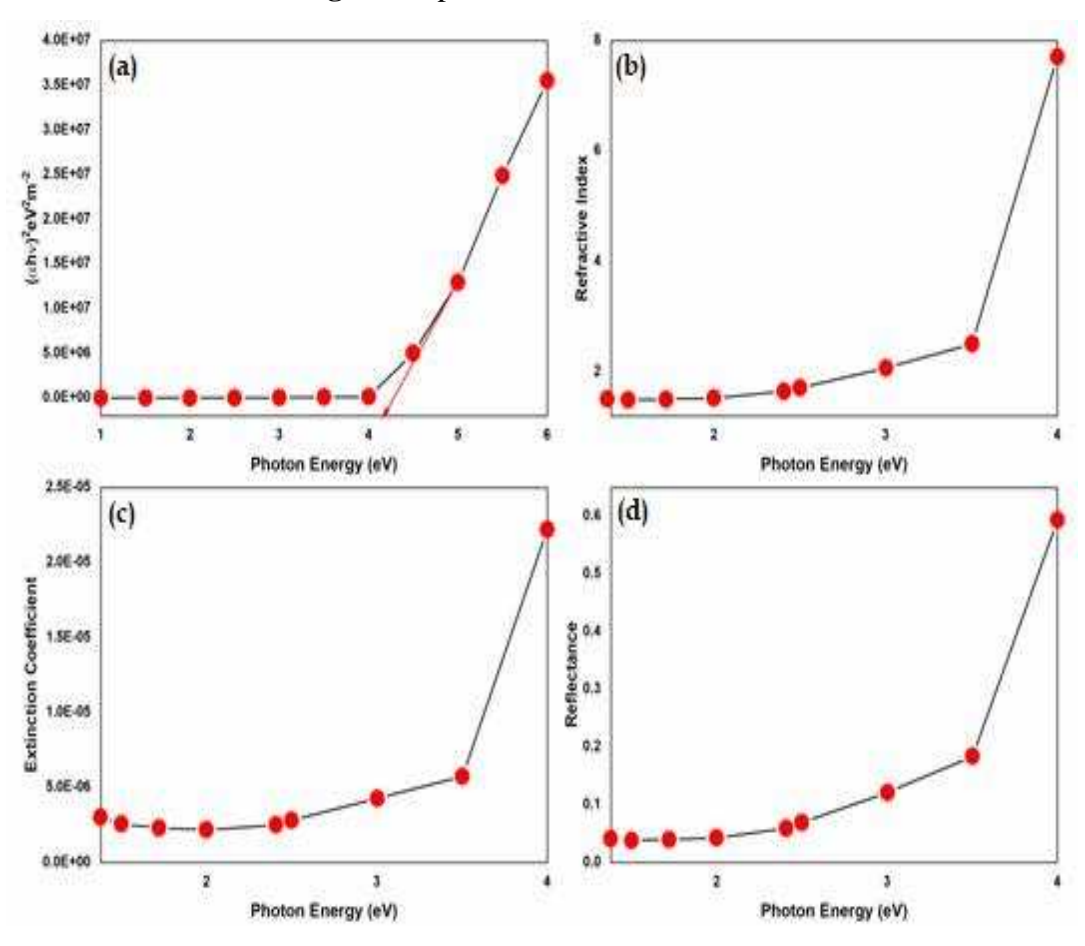


Fig. 3.8(a-d). Variation of optical constants as a function of photon energy

(b) By DASF method

Optical parameters of PTCA are calculated as per method given in section 2.2.5 (b) of chapter-II. From Fig. 3.9 the obtained value of energy band gap is 3.83 eV. The slope of Fig. 3.10, gives the value of m, the value of m near to 1/2, which indicates PTCA has the direct band gap and direct allowed transition of charge carriers. The Urbach energy value is obtained from linear slope of Fig. 3.11. The results obtained (Table 3.2) from the optical studies reveal that the PTCA crystal holds good optical behavior for NLO applications [12].

Table 3.2. Optical parameters of PTCA

Optical Parameters (DASF method)	Values
λ_g (wavelength of energy gap)	323 nm
$1/\lambda_{ m g}$	0.0031
E _g (optical energy band gap)	3.83 eV
E _{Tail} (Urbach energy)	0.19 eV
σ (steepness parameter)	0.12
E _{e-p} (electron-phonon interaction)	5.56
n (refractive index)	1.88
$\varepsilon_{\rm d}$ (dielectric constant)	3.56

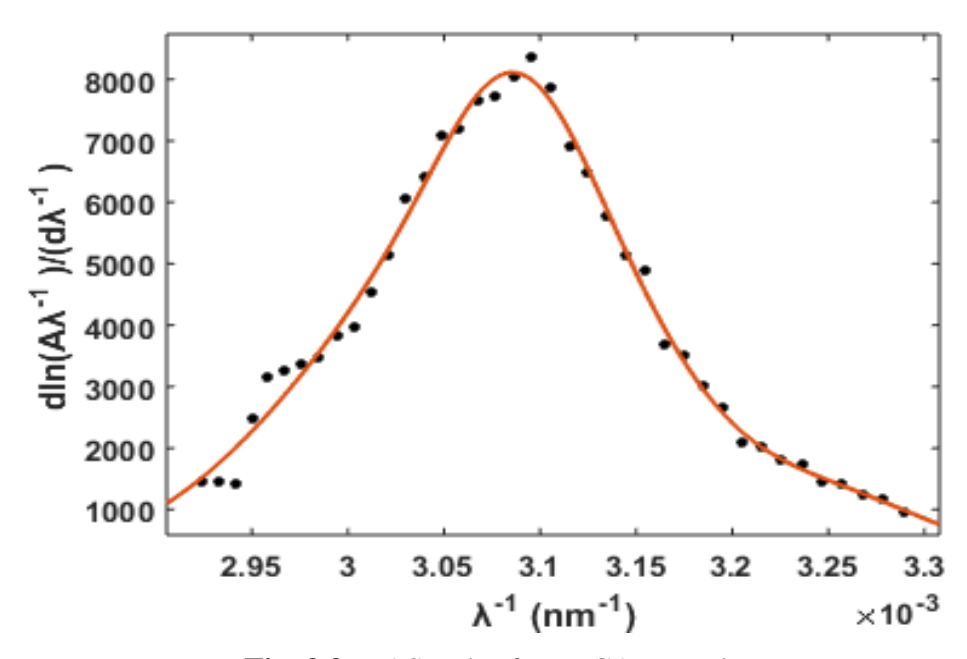


Fig. 3.9. DASF plot for PTCA crystal

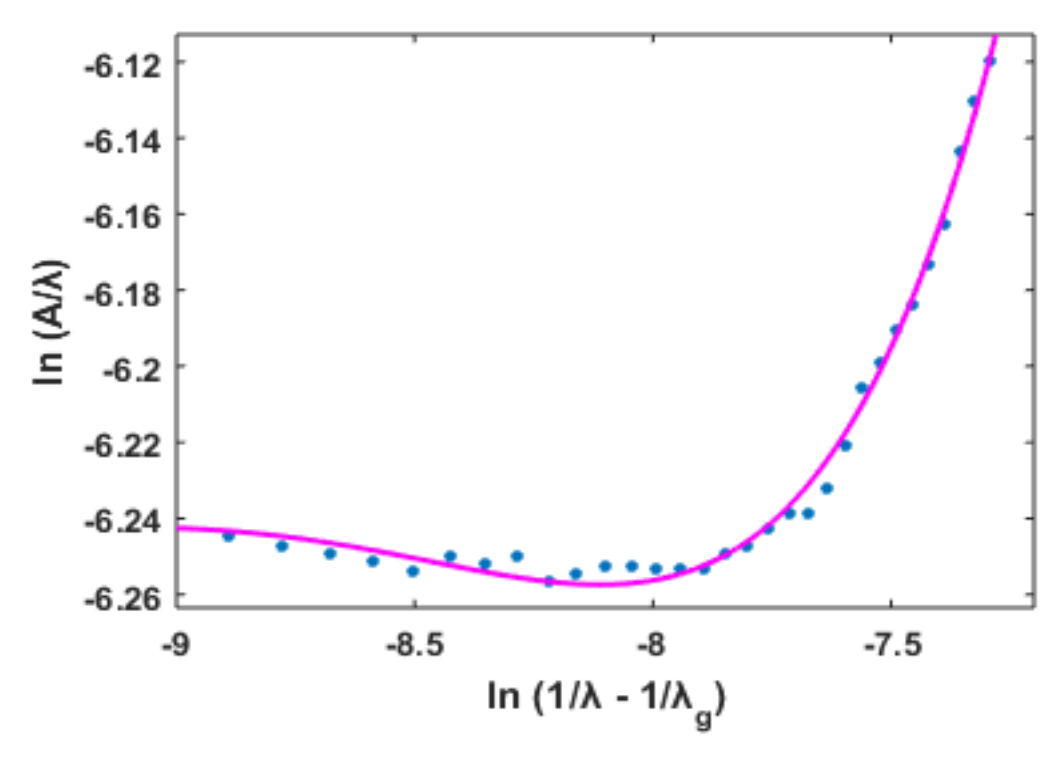


Fig. 3.10. Curves of ln (A/ λ) vs ln (1/ λ - 1/ λ_g)

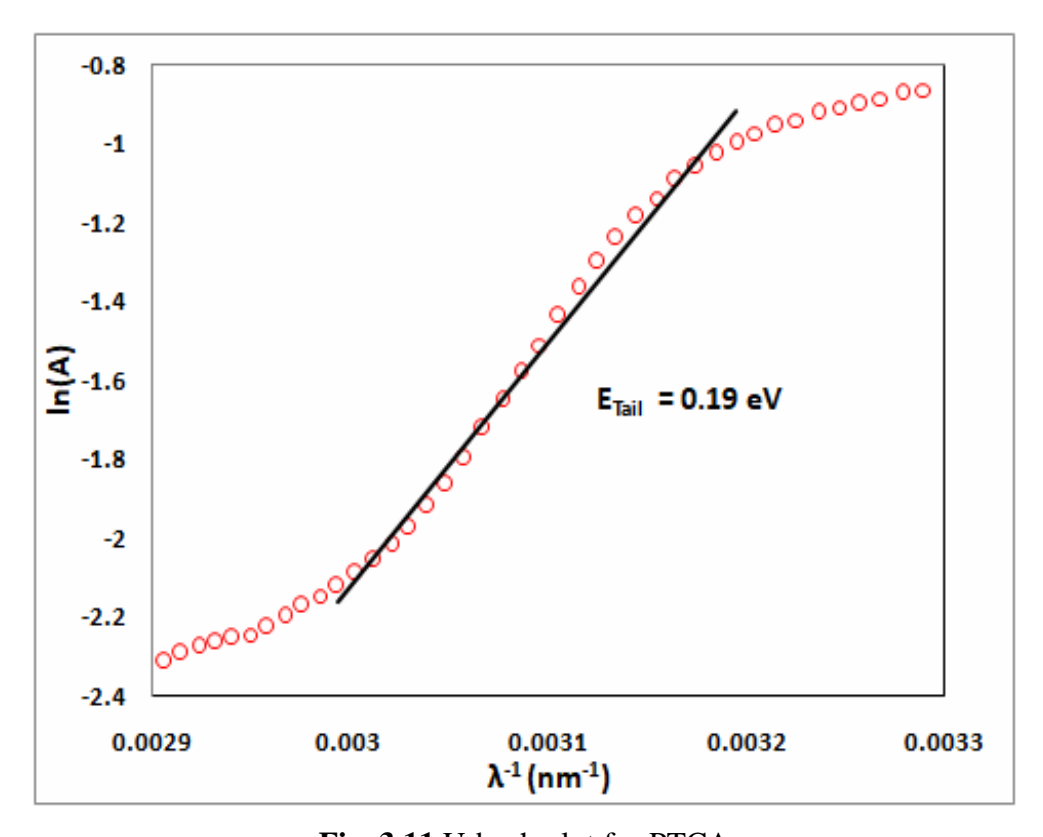


Fig. 3.11. Urbach plot for PTCA

3.2.6. Fluorescence analysis

Fluorescence is an optical property of a substance that develops as a result of stimulated electron relaxation. It furnishes the quality information regarding the electronic states of the material, influence of intrinsic impurities on the material emission spectra [11]. A fluorescence spectrum of the grown crystal is obtained using SHIMADZU/ RF 6000 Spectro Fluorophotometer and is given in Fig. 3.12. The photoluminescence reveals only a significant emission peak at 513 nm across the entire range between 300 and 900 nm. PTCA crystals have a blue fluorescence emission owing to π - π * transition. The high acuity of the emission wavelength of these grown crystals has high potential application in luminescent probes [12].

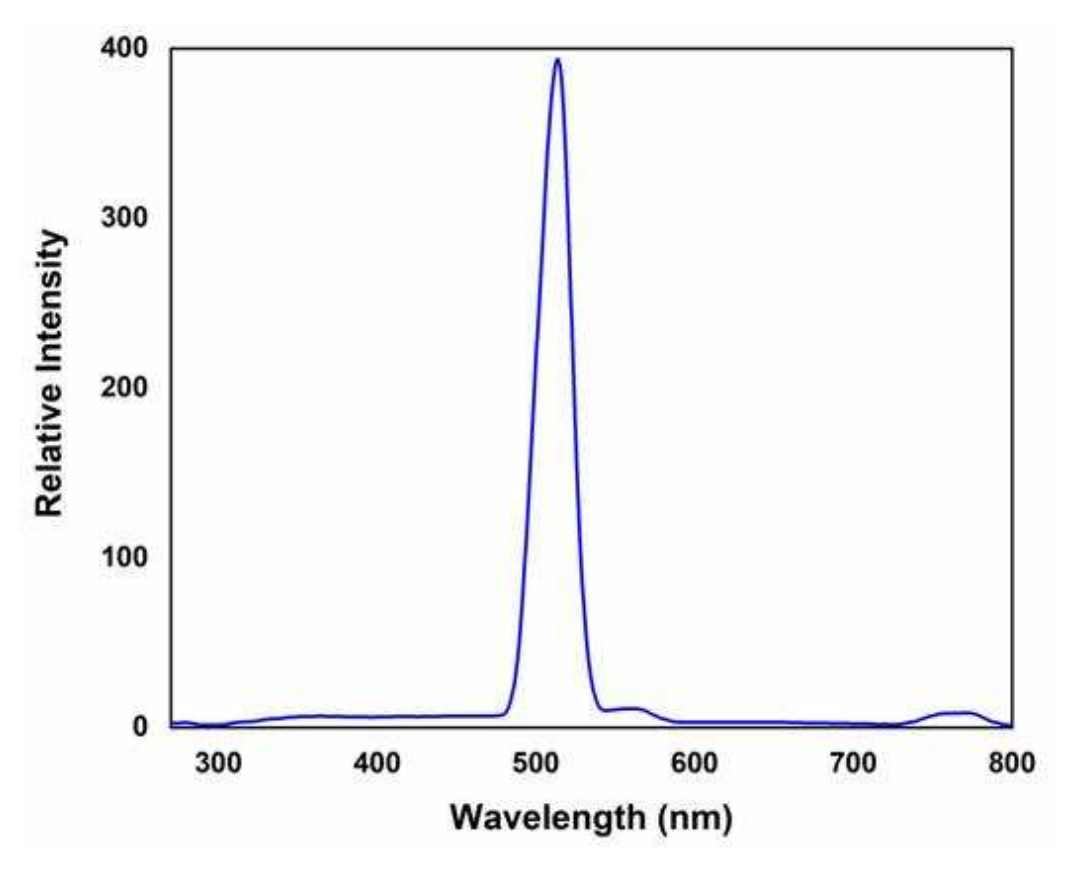


Fig. 3.12. Fluorescence emission of PTCA crystal

3.2.7. Z-scan Analysis

The Z-scan is a widely accepted technique for the characterization of nonlinear optics by the scientific community. It is a very simple and highly sensitive but relatively the most accurate method to determine the nonlinear index of refraction (n_0) , nonlinear absorption coefficient (β), and third order nonlinear optical susceptibility ($\chi^{(3)}$) by closed and open aperture mode respectively [13]. All these values are obtained as per equations 2.16 to 2.21 given in chapter-II. The closed aperture and open aperture normalized transmittance as a function of sample position Z have been measured for PTCA crystal and are exemplified in Fig. 3.13a and 3.13b. In a closed aperture pattern (Fig. 3.13a) the peak followed by the valley intensity is vividly visible, signifying that the sign of the refraction nonlinearity is negative, i.e., the feasibility of self-defocusing effect [14]. Fig. 3.13b exhibits a decrease in transmission with an increase in the input intensity illustrative of the presence of reverse saturable absorption (RSA) (excited state absorption) with a positive nonlinear absorption coefficient enabling the material for optical limiting applications [15-17]. Table 3.3 tabularizes the experimental details and the results of the Z-scan technique for PTCA crystal. The excellent nonlinear optical properties of the grown crystal testify it as a promising material for optical limiting applications.

Table 3.3. Obtained nonlinear optical parameter from open- and closed-aperture Z-scan measurement data for PTCA crystal

Parameters	Measured values for PTCA crystal
Nonlinear refractive index (n ₂)	$3.03 \times 10^{-10} (\text{cm}^2/\text{W})$
Nonlinear absorption coefficient (β)	$8.47 \times 10^{-06} (\text{cm/W})$
Real part of the third order susceptibility [$Re(\chi^3)$]	$6.05 \times 10^{-08} (\text{cm}^2/\text{W})$
Imaginary part of the third order susceptibility[Im(χ^3)]	$5.03 \times 10^{-07} \text{ (cm/W)}$
Third order nonlinear optical susceptibility (χ^3)	$5.06275 \times 10^{-07} \text{ (esu)}$

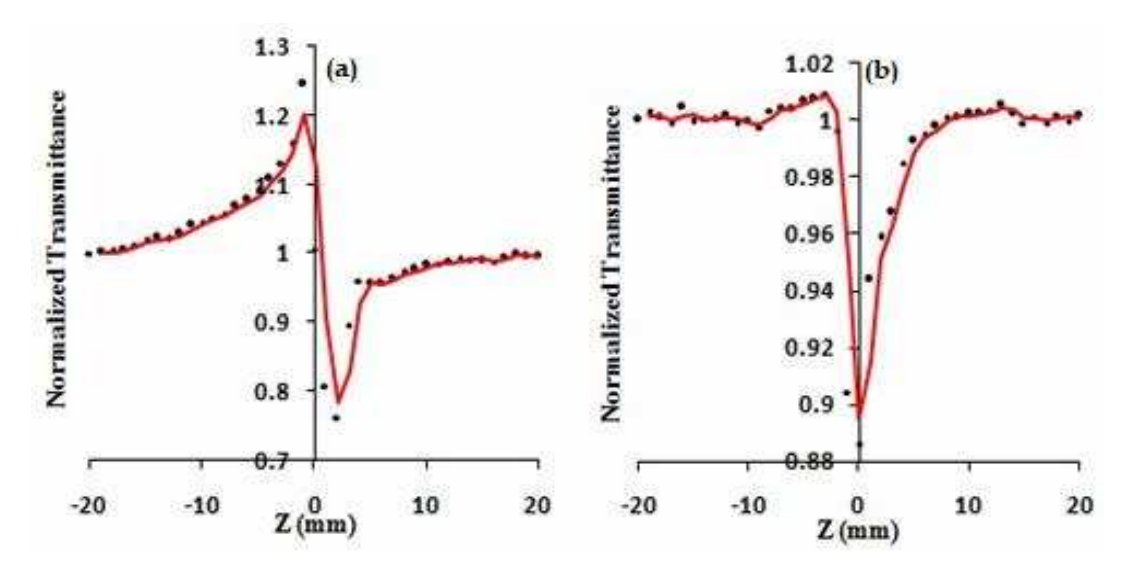


Fig. 3.13 (a). Self-focusing (closed aperture) Z-scan plot of PTCA crystal **(b)** Open aperture mode Z-scan plot of PTCA crystal

3.2.8. Microhardness Study

The indentation of PTCA crystal is measured for various loads from 2g to 100g using a SHIMADZU - HMV-G MicroVickers Hardness Tester. The hardness parameters are calculated and listed in Table 3.4, using the relation [18]

$$H_v = 1.854 \text{ P/d}^2 \text{ kg/mm}^2$$
 ... (3.1)

where, H_v - Vickers micro hardness number (kg/mm²), P- applied load (kg) and d - average diagonal length of the impression (mm).

Fig. 3.14a graphs the increase in hardness number for increase in load. The Meyer's index number [19] is determined from the relation $P = kd^n$ where k is the material constant and n, the "Meyer's index". By linear square fitting (Fig. 3.14b) the value of n is obtained as 3.8. According to Hanneman [20], the values of n read 1 to 1.6 for hard materials and more than 1.6 for the softer ones ascertaining PTCA categorized under soft material group. Fig. 3.14c reveals the PTCA crystal to exhibit reverse indentation size effect (RISE) indicative of plastic deformation predominance.

Table 3.4. Hardness parameters of PTCA

Load P (g)	H _v (kg/mm ²)	d (µm)	$C_{11} \times 10^{15} (Pa)$	σ _v (MPa)
2	3.65	31.88	0.016	0.006
5	4.46	45.61	0.024	0.007
10	8.09	47.87	0.067	0.013
25	18.1	50.62	0.273	0.029
50	33.8	52.38	0.814	0.054
100	50.1	60.82	1.622	0.080

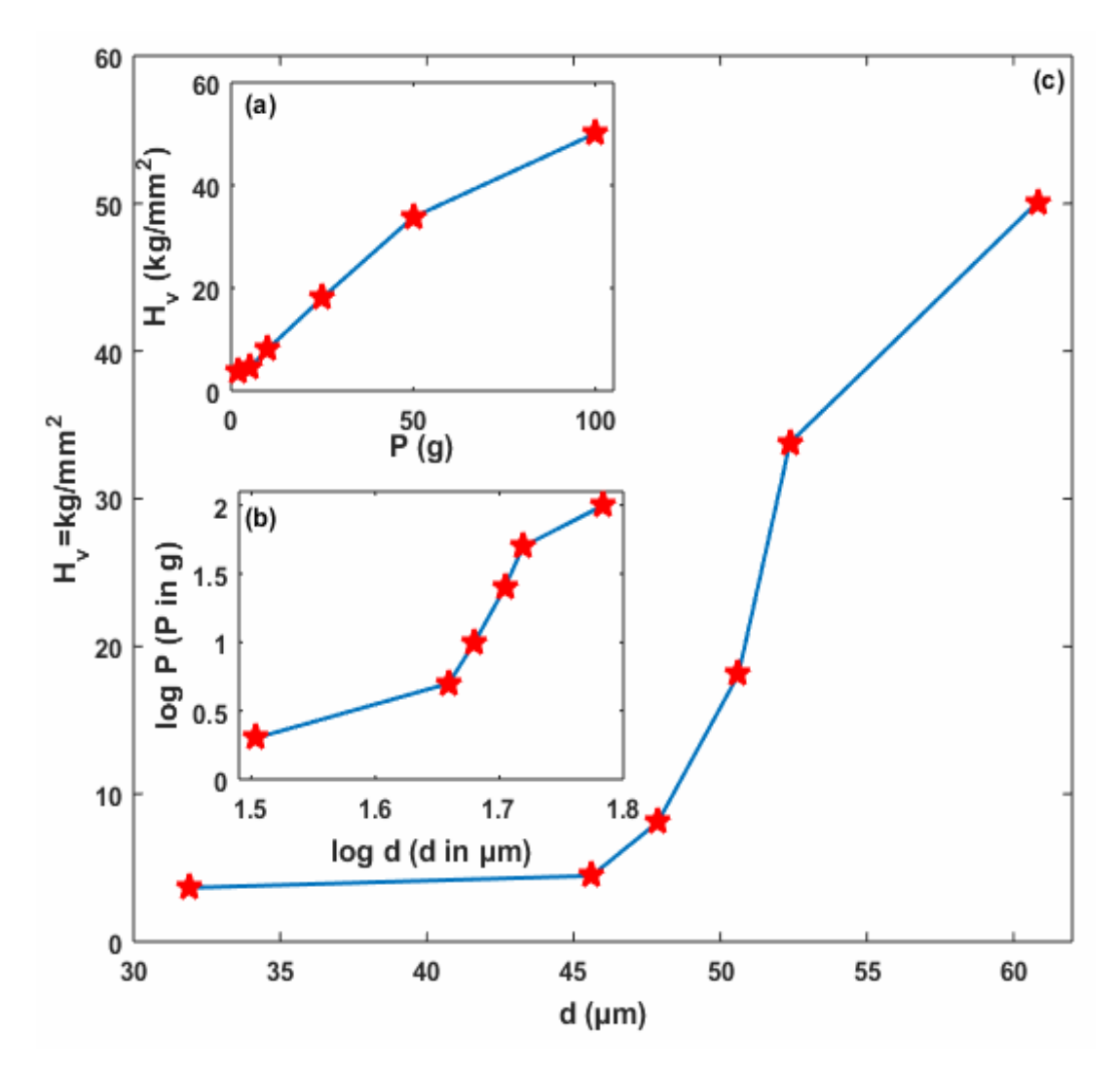
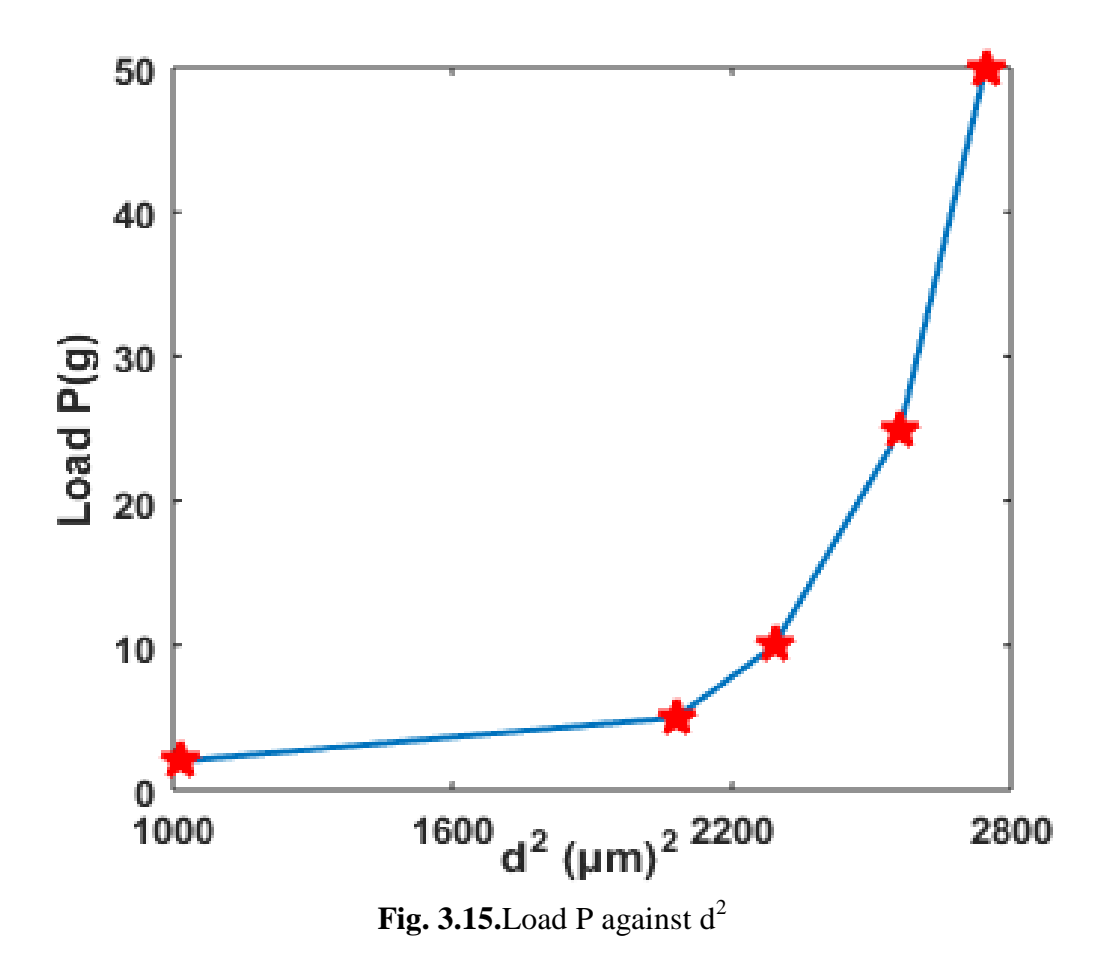


Fig. 3.14. (a) Variation of H_v against applied load P (b) log P against log d (c) H_v against d

According to Hays-Kendall's approach, load dependent hardness may be expressed by [21]:

$$P = W + A_1 d^2$$
 ... (3.2)

where 'W' is the minimum load initiate plastic deformation and A_1 is the load independent constant. The value of W and A_1 can be calculated by plotting the experimental P against d^2 . These two values estimated from the plot drawn between P and d^2 (Fig. 3.15) are -135.7g and $0.065(g/\mu m^2)$ respectively. The corrected hardness (H_o) calculated using the relation H_o = 1854.4 × A₁ is 97.08 (kg/mm²).



Elastic stiffness constant (C_{11}) is estimated by Wooster's empirical relation [22]. From Fig. 3.16 it is evident that the elastic stiffness constant increases with increase in load, which authenticates the tightness of bonding between the neighboring atoms [23].

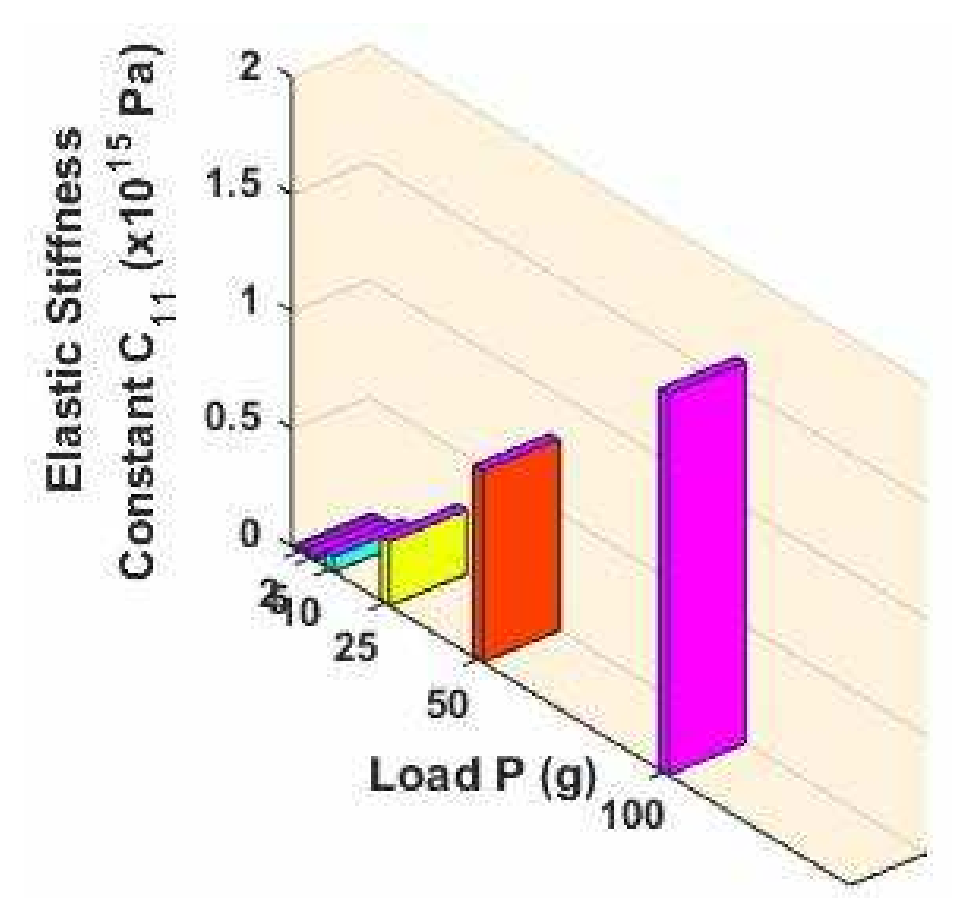


Fig. 3.16. Load P against Elastic Stiffness Constant (C_{11})

3.3. COMPUTATIONAL ANALYSIS

3.3.1. Optimized geometry

The optimized geometries of PTCA with symbols and numbering scheme for the atoms are shown in Fig. 3.17. Table 3.5 lists their main structural parameters maximized at DFT/B3LYP/6-311++G(d,p) level. The global minimum energy value measured by the DFT structure optimization method is -5.372×10^6 kJ/mol. The computed bond lengths show slightly higher readings than the X-ray data, as the theoretical values correspond to the isolated molecules in gas-phase whereas the experimental results are taken from crystal structures [24]. The optimized structure reveals intermolecular hydrogen bonding of the type N10-H22...O4, which is caused

by cations and anions forming ion pairs via the N10-H22 atom. Protonation effected between COO- atoms and NH+ group of hydrogen bonding are confirmed by the increase in C11-N10 (1.361Å) and N10-C15 (1.340Å) and C11-N10-C15 (123.0°) bond angle. The increase in N10-H22 (1.017Å) reveals strong intramolecular hydrogen bonding N10-H22...O5. Despite the differences, calculated geometric parameters show a good approximation and hence can be used to calculate other parameters reported below.

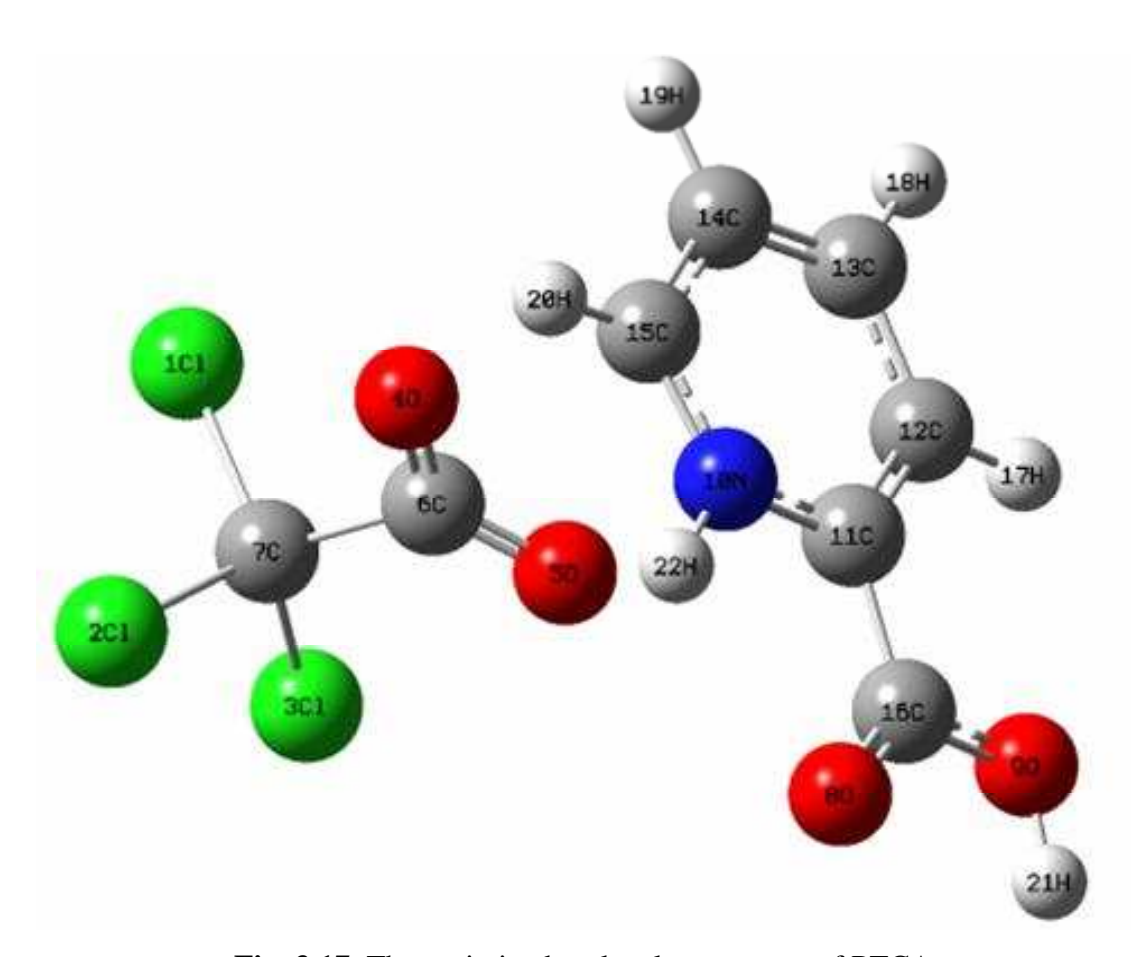


Fig. 3.17. The optimized molecular structure of PTCA

Table 3.5. Optimized parameters of PTCA by B3LYP level with 6-311++G(d,p) basis set

Bond	Value	es (Å)	Dand Anala	Value	es (°)	Dibadual Amala	Valu	es (°)
Length	Calc.	Exp.9	Bond Angle	Calc.	Exp.9	Dihedral Angle	Calc.	Exp.9
H17-C12	1.079	0.975	C6-C7-CL3	112.2	112.8	H17-C12-C13-H18	-1.938	0.269
CL3-C7	1.791	1.752	C6-C7-CL2	109.1	111.3	H17-C12-C13-C14	176.618	-179.755
C12-C13	1.408	1.383	C6-C7-CL1	108.7	108.8	C11-C12-C13-H18	179.184	-178.432
C12-C11	1.369	1.373	CL1-C7-CL3	108.7	108.3	C11-C12-C13-C14	-2.258	1.542
C13-C14	1.376	1.379	CL3-C7-C13	112.2	112.8	H17-C12-C11-C16	0.0205	-0.410
O9-H21	0.969	0.953	CL2-C7-CL3	108.7	108.8	H17-C12-C11-N10	179.675	-179.458
O9-C16	1.338	1.306	CL1-C7-CL2	109.1	108.7	C13-C12-C11-C16	179.923	178.335
CL1-C7	1.808	1.775	CL2-C7-C13	109.1	108.6	C13-C12-C11-N10	-1.4212	-0.713
C7-C6	1.594	1.564	C16-O9-H21	108.04	111.2	H18-C13-C14-H19	1.3026	-1.695
CL2-C7	1.807	1.770	C11-N10-C15	123.0	109.5	H18-C13-C14-C15	178.302	179.113
C14-C15	1.405	1.371	C11-N10-H22	115.8	122.8	C12-C13-C14-H19	-177.246	178.329
C11-C16	1.488	1.500	C15-N10-H22	120.2	117.3	C12-C13-C14-C15	-0.246	-0.863
C11-N10	1.361	1.348	C12-C11-C16	126.4	119.5	H21-O9-C16-C11	-177.871	179.196
O4-C6	1.258	1.249	N10-C11-C12	119.8	125.7	H21-O9-C16-O8	2.590	-1.614
C16-O8	1.207	1.203	N10-C11-C16	113.7	119.3	CL3-C7-C13-O5	1.466	20.121
N10-C15	1.340	1.328	C13-C12-H17	121.8	114.9	CL3-C7-C13-O9	-178.751	-162.33
N10-H22	1.017	0.855	C13-C12-H17	119.6	122.1	CL1-C7-C13-O5	-118.885	-98.759
C15-H20	1.076	0.937	C11-C12-C13	118.5	118.9	CL1-C7-C13-O9	60.896	78.793
O5-C6	1.231	1.226	C12-C13-H18	119.5	188.8	CL2-C7-C13-O5	122.1532	142.836
			C14-C13-H18	120.1	120.8	CL2-C7-C13-O9	-58.0648	-39.612
			C12-C13-C14	120.2	117.9	C13-C14-C15-N10	6.4420	-0.667
			C13-C14-H19	121.8	120.1	C13-C14-C15-H20	-174.588	178.278
			C13-C14-C15	119.4	119.3	H19-C14-C15-N10	-176.459	-179.841
			C15-C14-H19	118.6	119.1	H19-C14-C15-H20	-8.3128	-0.897
			N10-C15-C14	118.2	121.4	C12-C11-C16-O9	-2.0120	0.316
			C14-C15-H20	123.3	119.6	C12-C11-C16-O8	177.540	-178.930
			N10-C15-H20	117.3	124.2	N10-C11-C16-O9	178.314	-179.400
			O9-C16-C11	112.8	116.0	N10-C11-C16-O8	-2.1331	0.155
			O8-C16-O9	124.8	112.1	C12-C11-N10-C15	8.1167	-0.849
			O8-C16-C11	122.2	126.9	C12-C11-N10-H22	177.2117	173.046
					120.8	C16-C11-N10-C15	-172.186	-179.997
						C16-C11-N10-H22	-3.0913	-6.102
						C11-N10-C15-C14	-10.5471	1.553
						C11-N10-C15-H20	-179.416	-177.475
						H22-N10-C15-C14	-179.175	-172.220
						H22-N10-C15-H20	11.9549	8.751

3.3.2. Hyperpolarizability

Quantum mechanical calculations are used for predicting the molecular NLO properties of molecules. The total linear polarizability (α) can be calculated by the following equation,

$$\alpha = (\alpha_{xx} + \alpha_{yy} + \alpha_{zz})/3 \qquad ... (3.3)$$

where, $\alpha_{xx},\,\alpha_{yy}$ and αzz are the diagonal components of polarizability tensor.

The total first-order hyperpolarizability (β) is given by the following equation,

$$\beta = [(\beta_{xxx} + \beta_{xyy} + \beta_{xzz})^2 + (\beta_{yyy} + \beta_{yzz} + \beta_{yxx})^2 + (\beta_{zzz} + \beta_{zxx} + \beta_{zyy})^2]^{1/2} \qquad ... (3.4)$$

where, β_{xxx} , β_{xxy} , β_{xyy} , β_{yyy} , β_{xxz} , β_{xyz} , β_{yyz} , β_{xzz} , β_{yzz} and β_{zzz} are the 10 components of the 3D matrix.

The calculated values of α and β components are listed in Table 3.6. The polarizability (α) and first hyperpolarizability (β) of the PTCA are 3.759×10^{-25} esu and 2.7965×10^{-28} esu, respectively. The β value of PTCA is greater than that of urea [25], which confirms PTCA as the best material for NLO applications.

Table 3.6.NLO properties of PTCA calculated using DFT at B3LYP/6-311++G(d,p) level

Polar	rizability	First hyper	polarizability
α_{xx}	262.29	eta_{xxx}	1098.15
α_{xy}	-64.15	eta_{xxy}	-1025.61
$\alpha_{ m yy}$	159.44	β_{xyy}	828.98
α_{xz}	150.12	β_{yyy}	-336.05
$\alpha_{ m yz}$	-70.61	β_{xxz}	2074.21
α_{zz}	339.41	$eta_{ ext{xyz}}$	-1245.02
		$eta_{ m yyz}$	877.74
		eta_{xzz}	3772.29
		$eta_{ ext{yzz}}$	-1554.82
		eta_{zzz}	6753.71

3.3.3. Natural Bond Orbital (NBO) Analysis

In order to elucidate the inter and intramolecular charge transfer interactions and electron delocalization within the molecule, the NBO analysis is performed on PTCA at DFT/B3LYP with 6-311++G(d,p) basis set. The second order perturbation theory analysis of Fock matrix in the NBO is presented in Table 3.7. The NBO analysis shows hydrogen bond interaction between oxygen lone pairs and (C-H) and (N-H) σ^* anti-bonding orbitals. The stabilization energies coupled with the hyper conjugative interactions for $n_2(O_4)$ to $\sigma^*(C_{15}-H_{20})$, $n_2(O_8)$ to $\sigma^*(N_{10}-H_{22})$, are obtained as 0.63 and 0.99 kcal/mol, respectively (Table 3.7), which quantify the extent of intramolecular N-H...O and intermolecular C-H...O hydrogen bonding. The most important intramolecular interaction $(n-\pi^*)$ energy related to the resonance in the molecules are electron donating from $n_2(O_4)$ atom to anti-bonding acceptor $\pi^*(O_5-C_6)$ atom whose energy is 95.01 kcal/mol resulting in hyperconjugation interactions from n(O) to O-C bond. The second-order perturbation energies of $\pi^*(O_8-C_{16})$ to $\pi^*(C_{11}-C_{12})$, $\pi^*(N_{10}-C_{15})$ to $\pi^*(C_{11}-C_{12})$ and $\pi^*(N_{10}-C_{15})$ to $\pi^*(C_{13}-C_{14})$ are 85.48, 29.55 and 50.45 kcal/mol, respectively. These interactions make the pyridine ring of PTCA stable [26].

Table 3.7. Second order perturbation theory analysis of Fock matrix in NBO basis including the stabilization energies using DFT at B3LYP/6-311++G(d,p) level

Donor (i)	ED (i)	Acceptor (j)	ED (j)	^a E(2)Kcal/mol	bE(j)-E(i)a.u.	°F(i,j)a.u.
		$\sigma^*(C_6-C_7)$	0.16071	20.79	0.56	0.018
$n_2(O_4)$	1.76589	$\sigma^*(C_{15}-H_{20})$	0.01245	0.63	0.68	0.020
		$\pi^*(N_{10}-C_{15})$	1.76589	27.15	0.19	0.069
n ₃ (O ₄)	1.63936	$\pi^*(O_5-C_6)$	0.35315	95.01	0.27	0.144
T (O)	1 92100	$\sigma^*(O_4-C_6)$	0.05485	18.56	0.79	0.111
$n_2(O_5)$	1.82100	$\sigma^*(C_6-C_7)$	0.35315	26.43	0.52	0.105
$\pi(N_{10}\text{-}C_{15})$	1.83345	$\pi^*(C_{11}-C_{12})$	0.25128	20.44	0.39	0.081
		$\pi^*(O_8-C_{16})$	0.24683	18.05	0.28	0.065
$\pi(C_{11}-C_{12})$	1.67927	$\pi^*(N_{10}-C_{15})$	0.46254	11.72	0.24	0.049
		$\pi^*(C_{11}-C_{12})$	0.25128	17.28	0.31	0.067
-(C, C,)	1 (5961	$\sigma^*(O_9-C_{16})$	0.08837	33.97	0.23	0.081
$\pi(C_{13}-C_{14})$	1.65861	$\sigma^*(C_{11}-C_{16})$	0.07068	16.56	0.29	0.063
		$\sigma^*(O_9-C_{16})$	0.08837	31.53	0.63	0.128
$n_2(O_8)$	1.84616	$\sigma^*(N_{10}\text{-}H_{22})$	0.02342	0.99	0.66	0.024
		$\sigma^*(C_{11}-C_{16})$	0.07068	18.31	0.68	0.101
$n_2(O_9)$	1.81254	$\pi^*(O_8-C_{16})$	0.24683	49.92	0.34	0.115
$\pi^*(O_8-C_{16})$	0.24683	$\pi^*(C_{11}-C_{12})$	0.25128	85.48	0.02	0.073
~*(N C)	0.46254	$\pi^*(C_{11}-C_{12})$	0.25128	29.55	0.06	0.062
$\pi^*(N_{10}-C_{15})$	0.46254	$\pi^*(C_{13}-C_{14})$	0.20932	50.45	0.06	0.088

^aE(2) means the energy of hyper conjugative interactions.

3.3.4. Mulliken Population Analysis

Mulliken atomic charges are calculated at the DFT/B3LYP/6-311++G(d,p) method. All oxygen atoms of PTCA molecule have negative charges and all hydrogen atoms have positive charges. Natural population analysis for PTCA is presented in Table 3.8. The natural charge distribution on each atom is evaluated in terms of natural atomic orbital occupancies. The strong negative charges on all the oxygen atoms and

^bEnergy difference between donor and acceptor i and j NBO orbitals.

^cF(i,j) is the Fock matrix element between i and j NBO orbitals.

strong positive charges on the remaining atoms of PTCA molecule demonstrates the electrostatic attraction or repulsion between the atoms that can result significant contribution to the intramolecular charge transfer interactions leading to the stabilization of the molecule. The Mulliken atomic charge distribution and plots of Mulliken atomic charges of all the atoms are shown in Figs. 3.18 and 3.19, respectively.

Table 3.8. Natural population analysis (NPA) of PTCA calculated with DFT/B3LYP/6-311++G(d,p) method

Atoms	Natural Charge	Atomic Charge
Cl ₁	0.01743	-0.21914
Cl ₂	0.01981	-0.22891
Cl ₃	0.03812	0.207285
O ₄	-0.70406	-0.40746
O_5	-0.70172	-0.31059
C ₆	0.74571	-0.24939
C ₇	-0.23762	0.371943
O_8	-0.58049	-0.26106
O ₉	-0.65983	-0.14551
N ₁₀	-0.45967	0.003785
C ₁₁	0.14429	-0.08669
C ₁₂	-0.17075	0.386243
C ₁₃	-0.11541	-0.15483
C ₁₄	-0.19154	0.002402
C ₁₅	0.18254	-0.12328
C ₁₆	0.77685	-0.2187
H ₁₇	0.24599	0.264346
H ₁₈	0.22463	0.160484
H ₁₉	0.23760	0.159076
H ₂₀	0.24721	0.19246
H ₂₁	0.49777	0.319722
H ₂₂	0.44314	0.33782
Total	0.00000	0.00000

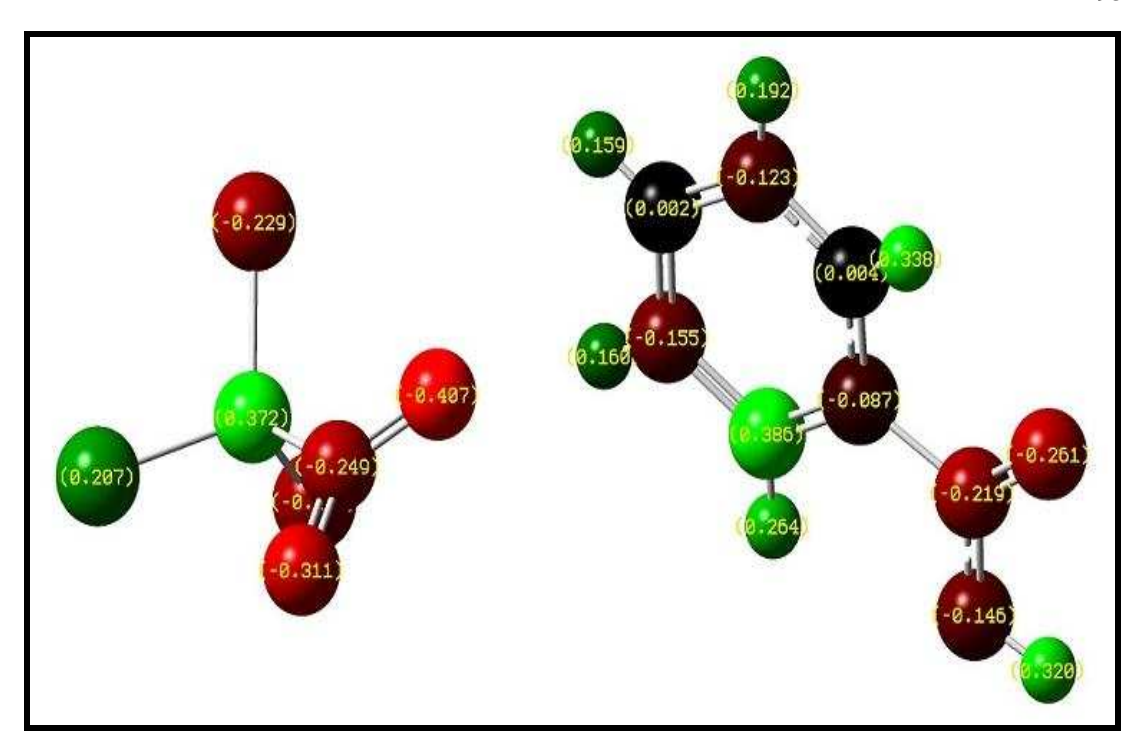


Fig. 3.18. Mulliken atomic charge distribution of PTCA

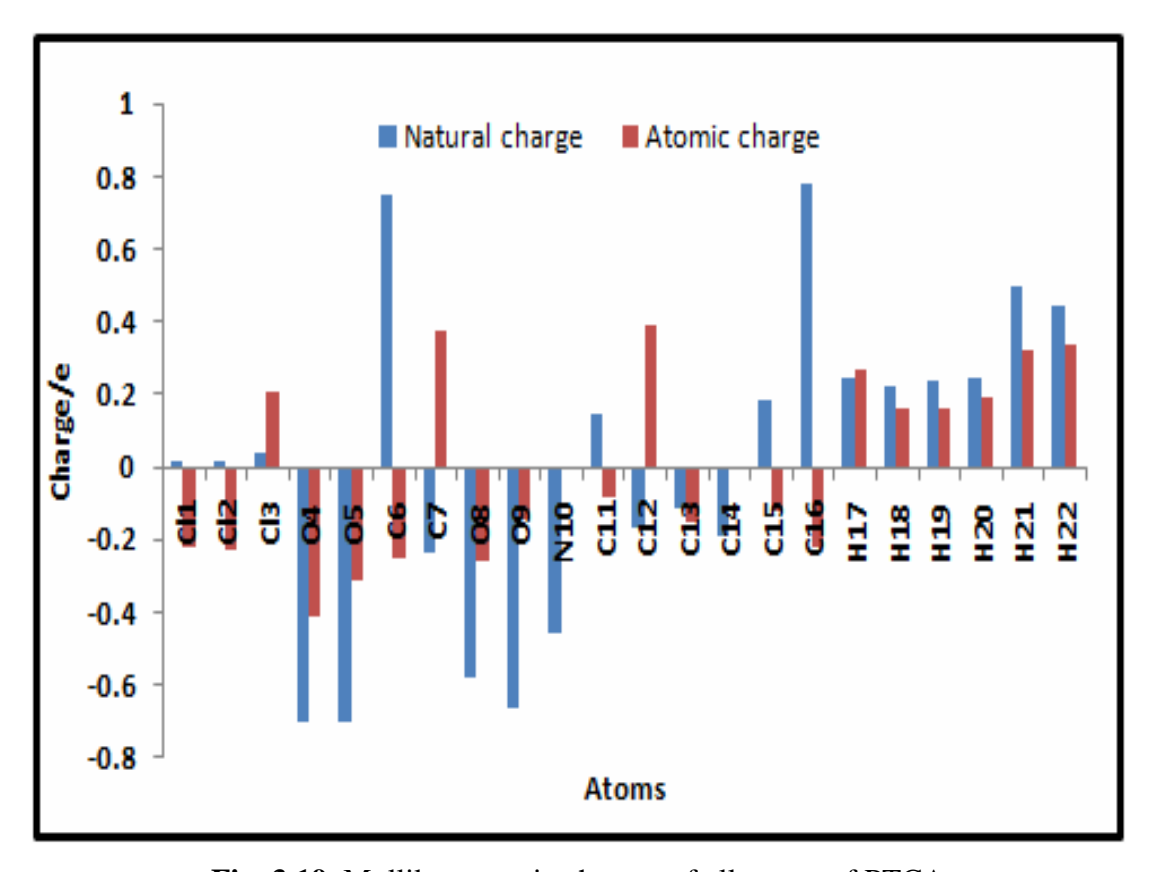


Fig. 3.19. Mulliken atomic charges of all atoms of PTCA

3.3.5. Molecular Electrostatic Potential (MEP) Analysis

Molecular electrostatic potential (MEP) mapping is extremely effective in studying molecular structure and its physiochemical property relations [27]. Figure 3.20 shows the total Self-consistent field (SCF) electron density surface mapped with the molecular electrostatic potential of PTCA obtained by the B3LYP/6-311++G(d,p) technique. The color pattern for the MEP surface is as follows: red- electron rich or partially negative charge; blue-electron deficient or partially positive charge; light blue-slightly electron deficient zone; and yellow-slightly electron rich region. The electron density found in PTCA has extreme limits of -8.081e-2 (red) and +8.081e-2 (blue). The electron-rich sites of C11, C12, C13, O4, and O5 atoms are vividly indicated by the MEP of PTCA.

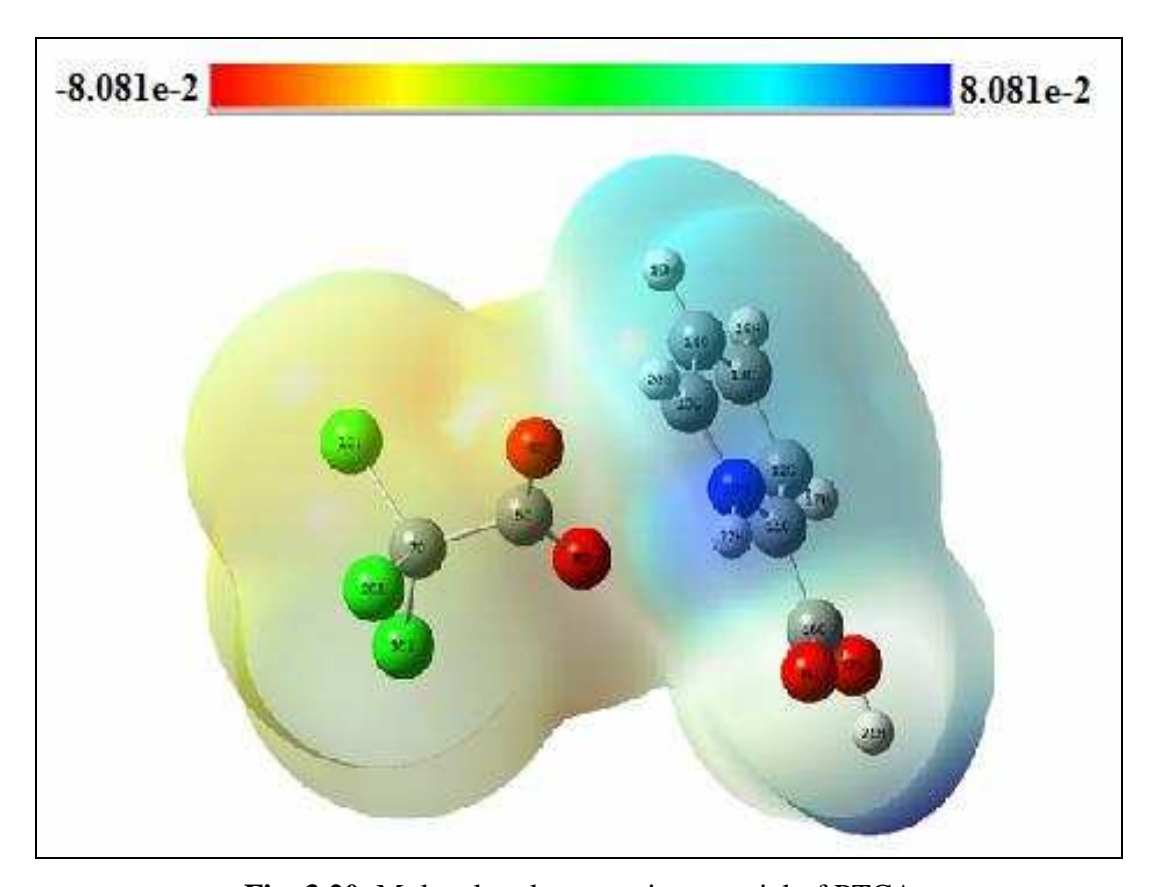


Fig. 3.20. Molecular electrostatic potential of PTCA

3.3.6. Frontier Molecular Orbital Analysis

The HOMO represents the ability to donate an electron and LUMO as an electron acceptor represents the ability to obtain an electron. The HOMO-LUMO energy gaps are calculated directly as the difference in HOMO and LUMO energy values, obtained from the density functional theory [28]: HOMO energy, $E_{HOMO} = -6.59$ eV; LUMO energy, $E_{LUMO} = -3.45$ eV; HOMO-LUMO energy gap, $\Delta E_{GAP} = E_{LUMO} - E_{HOMO} = 3.14$ eV.

The plots of HOMO and LUMO are shown in Fig. 3.21. The computed larger value of the HOMO-LUMO energy gap (3.14 eV) in PTCA confirms higher kinetic stability and lower chemical reactivity of the molecule. The 3.14 eV gap falls within the UV region, so the molecule is colorless. The global reactivity descriptors, such as ionization potential (I), electron affinity (A), electrophilicity index (ω), chemical hardness (η), softness (S), chemical potential (μ) and charge transfer (Δ Nmax), have been calculated using the energy of HOMO and LUMO. The calculated values are listed in the Table 3.9. The hardness value and negative chemical potential indicate that the molecule is stable [29].

Table 3.9. Calculated quantum chemical molecular orbital properties for PTCA

Parameters	B3LYP/6-311++G(d,p)
HOMO energy, E _{HOMO}	- 6.59 eV
LUMO energy, E _{LUMO}	-3.45 eV
HOMO–LUMO energy gap, ΔE_{GAP}	3.14 eV
Ionization potential (I)	6.59 eV
Electron affinity (A)	3.45 eV
Total energy change, ΔE_T	-0.39 eV
Overall energy balance, ΔE	-3.04 eV
Electronegativity, χ	4.55 eV
Chemical hardness (η)	1.57 eV
Chemical potential (µ)	-5.02 eV
Electrophilicity index (ω)	8.02 eV
Softness (S)	0.64 eV ⁻¹
SCF energy	-5.37 x 10 ⁶ kJ mol ⁻¹

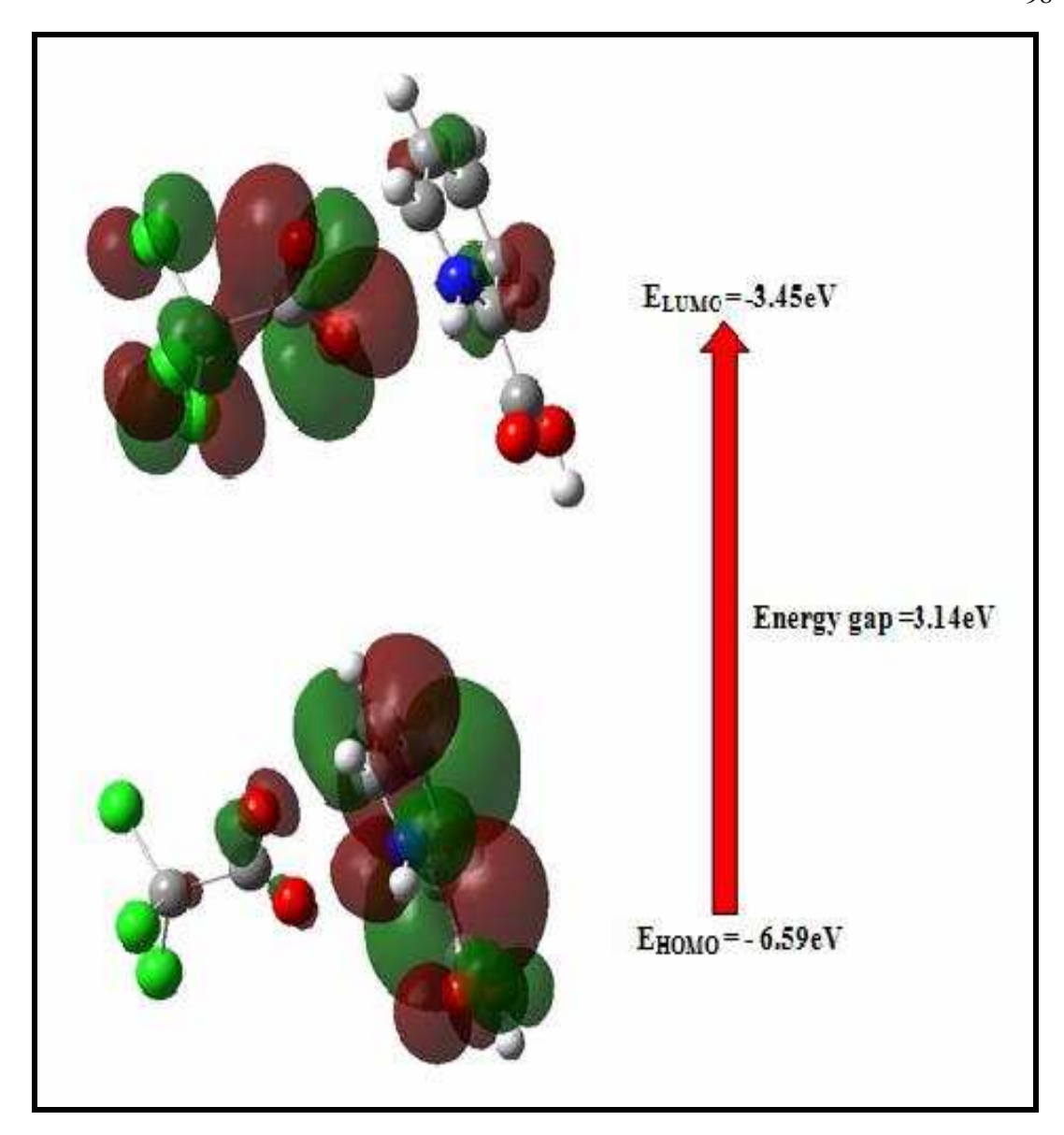


Fig. 3.21. HOMO-LUMO Plot of PTCA

3.3.7. Vibrational Spectral Analysis

The various assignments of PTCA crystal is performed using DFT/B3LYP/6-311++G(d,p) basis set. The FT-IR spectrum was recorded using a Perkin Elmer Spectrum II FT-IR spectrometer in the scan range 4000–400 cm⁻¹. The experimental frequencies and their different assignments were compared with theoretically computed assignments and are shown in Table 3.10 and the computed and experimental FTIR spectra are presented in Fig. 3.22.

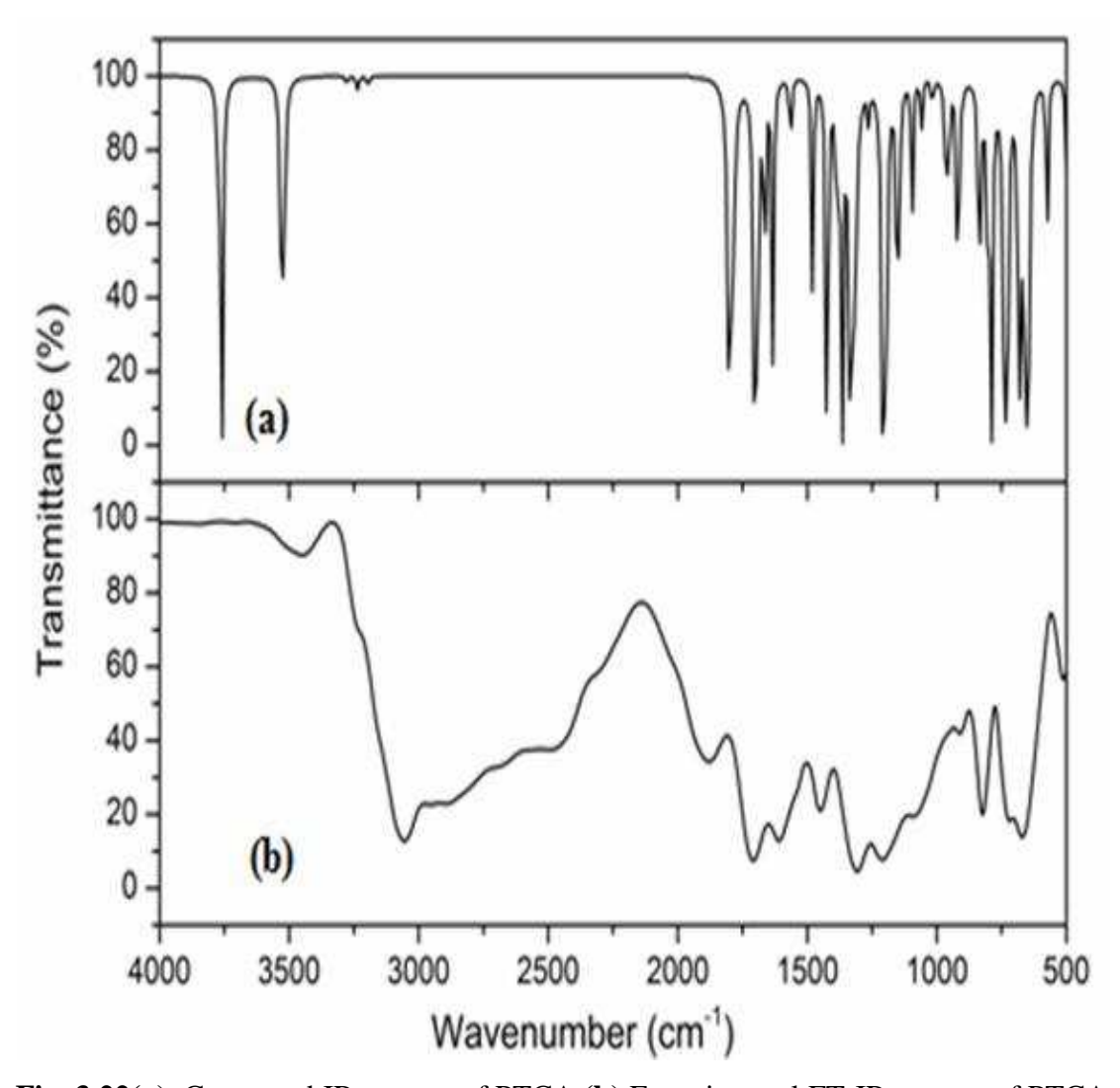


Fig. 3.22(a). Computed IR spectra of PTCA (b) Experimental FT-IR spectra of PTCA

C-H vibrations

The hetero aromatic structure shows the presence of C–H stretching vibration in the region 3100–3000 cm⁻¹ which is the characteristic region for C–H stretching vibration [9]. The aromatic C–H stretching of PTCA gives band at 3055cm⁻¹ in IR with strong bands which is close to the calculated wavenumber 3195 cm⁻¹. In general in-plane aromatic C–H deformations occur in the region 1300–1000 cm⁻¹. In PTCA, two strong infrared bands at 1232 and 1154 cm⁻¹ assigned to C–H in-plane bending vibrations are in good agreement with calculated wavenumbers 1203 and 1150 cm⁻¹.

Bands involving the out-of-plane C–H vibrations appear in the range 1000–600 cm⁻¹. The bands at 900, 748 cm⁻¹ in IR spectrum and 919, 733 cm⁻¹ in calculated spectra correspond to C–H out-of-plane bending vibrations.

N-H vibrations

The vibrational bands due to the N-H stretching are sharp and weak than those of O–H stretching vibration by virtue of which they can be easily identified. The N–H stretching modes are observed as a broad band in the FT–IR spectrum at 3441 cm⁻¹ and simulated spectra at 3525 cm⁻¹. The N–H out-of-plane bending mode can be observed as a weak band in the IR spectrum at 672 cm⁻¹ is in good agreement with calculated wavnumber 680 cm⁻¹.

O-H vibrations

The in-plane bending O–H deformation vibration usually appears as a strong band in the region 1400–1260 cm⁻¹ in the IR spectrum [9], which gets shifted to higher wavenumbers in the presence of hydrogen bonding. The O–H in-plane bending vibration is observed at 1295 cm⁻¹ in IR spectrum and at 1326 cm⁻¹ at computed spectra.

Pyridine ring vibrations

The carbon–carbon stretching modes of the benzene ring are expected in the range from 1610 to 1200 cm⁻¹ [9]. The bands at 1610 and 1458 cm⁻¹ in infrared spectrum of PTCA owe to C-C stretching are in good agreement with computed wavenumbers 1632 and 1423 cm⁻¹.

Table 3.10. Experimental and calculated vibrational wavenumbers and fundamental bands positions assignments of PTCA

Calculated wavenumber (cm ⁻¹)	Experimental wavenumber ^[9] (cm ⁻¹)	Experimental wavenumber (cm ⁻¹) Present work	Vibrational Assignments
3525	3449	3441	N-H stretching vibration
3195	3056	3055	C-H stretching vibration
1698	1709	1672	C=O stretching vibration
1632	1610	1610	Ring stretching vibration
1423	1449	1458	Ring stretching vibration
1326	1307	1295	O-H in-plane bending
1203	1209	1232	C-H in-plane bending
1150	1130	1154	C-H in-plane bending
919	911	900	C-H out-of-plane bending
836	823	811	C-H out-of-plane bending
733	725	748	C-H out-of-plane bending
680	670	672	N-H out-of-plane bending
501	512	511	C-C-C bending

3.3.8. Hirshfeld Surface Analysis

The Hirshfeld surface analysis made an attempt to define the space occupied, by a molecule in a crystal for the purpose of partitioning the crystal electron density into molecular fragments [30,31]. Fig. 3.23 shows the dnorm, shape index and curvedness of molecular Hirshfeld surface analysis for PTCA crystal. Close-contact interactions are primarily responsible for the major intermolecular hydrogen bonding interactions,

as shown by the deep red spots on the dnorm Hirshfeld surfaces. Fig. 3.24 shows the percentage contribution of chosen interatomic contacts to the Hirshfeld surface region as well as a 2D fingerprint map of PTCA. The O...H/H...O intermolecular interactions (30.4%) is represented by a two sharp spike in the 2D fingerprint plot region. The O...H interactions represented by the left long sharp spike in the donor region (16.5%) shows the hydrogen atom interacting with carboxylate groups of two compounds. The H...O interactions are indicated by a right long spike (13.9%) in the acceptor region. It specifies carboxyl oxygen atom acts as an acceptor to the hydrogen atom of the NH⁺ group [32,33]. The relative contributions of the H...H, C...H, H...Cl, Cl...Cl, and C...C contacts are 5, 3.8, 25, 13, and 1%, respectively.

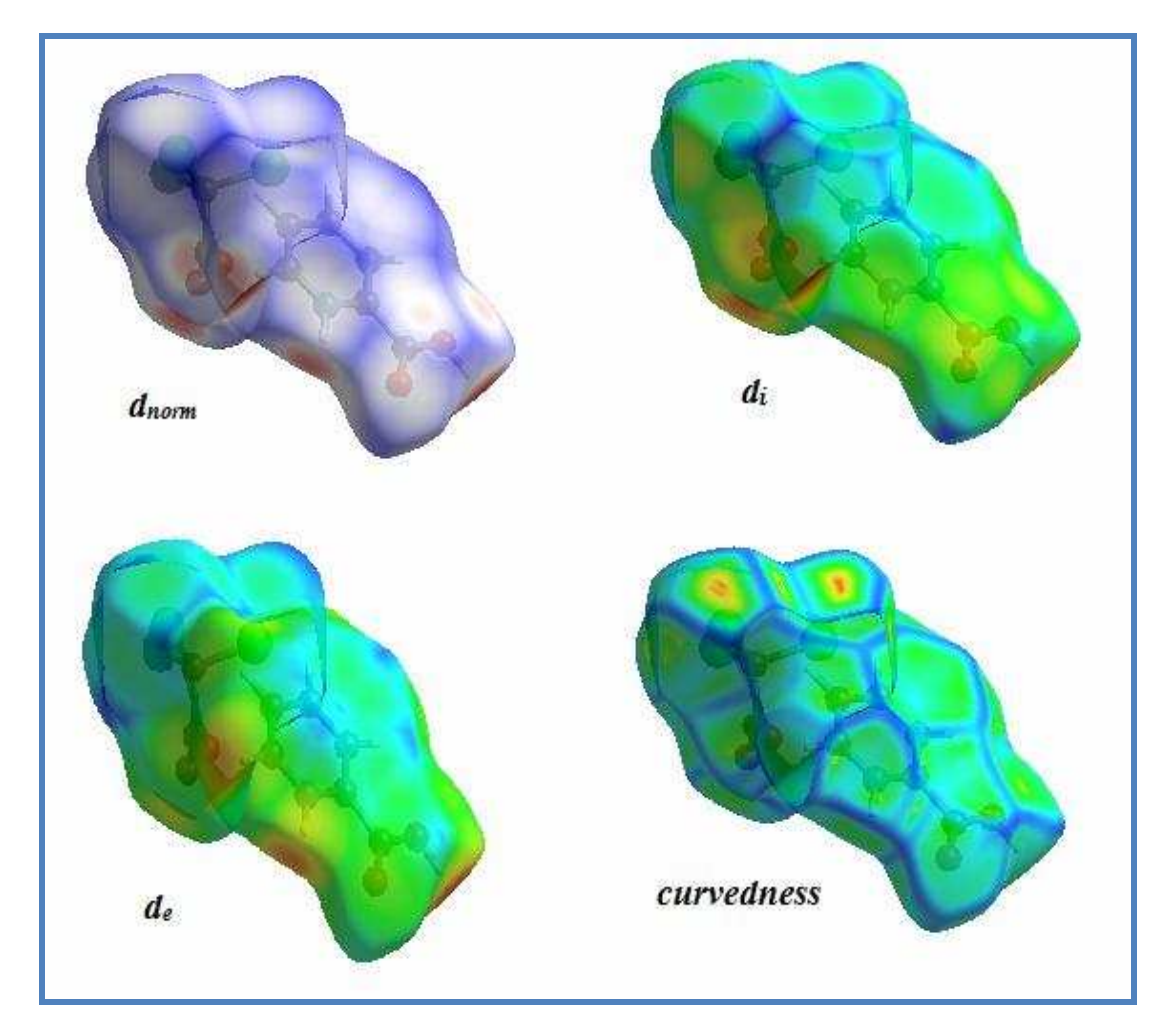


Fig. 3.23. Hirshfeld surfaces for d_{norm}, d_i, d_e and curvedness for the PTCA molecule

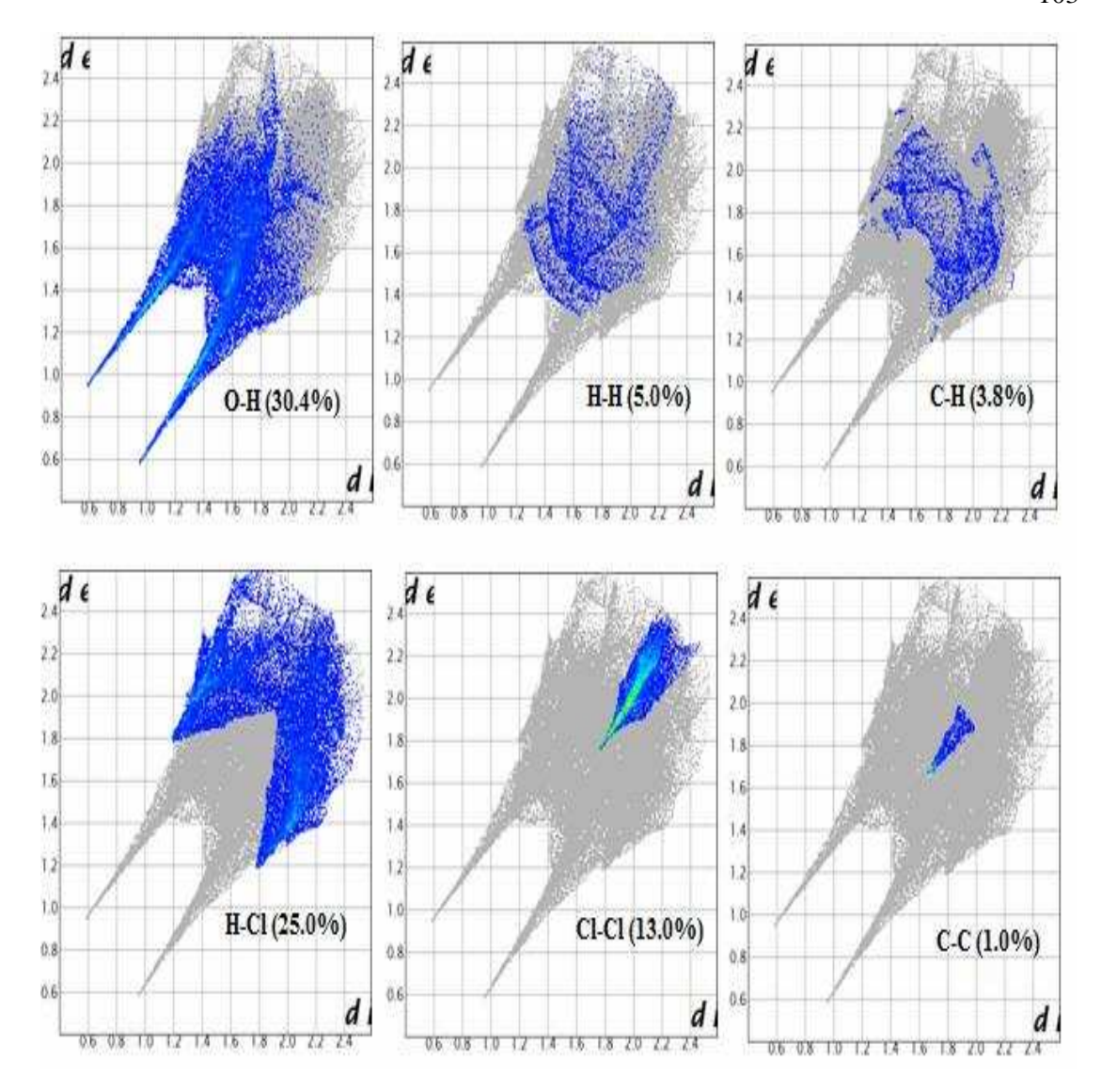


Fig. 3.24. 2D fingerprint plots showing various intermolecular contacts in the PTCA

3.4. CONCLUSIONS

Solubility studies of 2-picolinic trichloro acetate (PTCA) have been undergone and the nucleation kinetics of grown crystal is studied. The values of kinetic parameters obtained by the application of different equations are in good agreement with each other. This confirms that the evaluated nucleation parameters are possible for the growth of PTCA crystals. Single crystal of PTCA has been grown by slow evaporation technique. The powder XRD studies have been carried out on grown crystal. Also,

average crystallite size and lattice strain analyzed using Williamson-Hall approach indicate the minimum value of lattice strain on the grown crystal has lower dislocation density. UV-Vis studies disclose that the PTCA compound is transparent in the entire visible region. Also, optical constants like bandgap (Eg=4.25 eV), refractive index (n=1.48), reflectance, and extinction coefficient are evaluated. DASF method used to acquire the optical band gap and other optical parameters interpret the optical band gap of PTCA crystal equal to 3.83 eV. The fluorescence emission analysis confirms the emission of PTCA is in the blue region. The Z-scan technique points out the reverse saturated absorption optical process observed in the PTCA crystal. The mechanical behavior reveals that the PTCA crystal belongs to soft category. The computed spectroscopic parameters are in good agreement with the experimental data results. The NBO analysis reveals the possible intramolecular charge transfer interactions and stability in PTCA. The MEP study confirms PTCA as an electron rich species and explains its electrophilic nature. The hardness value and negative chemical potential from HOMO-LUMO indicate that the PTCA molecule is stable. The Hirshfeld surface analysis of PTCA interprets the percentage of strong and weak intermolecular interactions in the crystalline state. UV studies, NBO, and Z-scan studies suggest PTCA as an attractive material for optical limiting applications.

REFERENCES

- 1. S.Yari Kivshar, Nonlinear optics: The next decade, Opt. Express, 16 (2008) 22126-22128.
- Xu. Mao-Liang, Ming.-Tao. Li, Zi.-Ruo. Hong, Wen.-Lian. Li, Zhong.-Wei.
 An, Qun. Zhou, Highly efficient red electrophosphorescent device based on a new iridium complex with trifluoromethyl-substituted 2-benzo[b]thiophen-2-yl-pyridine ligand, Opt. Mater., 28 (2006) 1025–1028.
- 3. T. Jayanalina, G. Rajarajan, K. Boopathi, Synthesis, Growth, Structural, Spectral, Thermal And Dielectric Studies of a New Organic Salt Crystal: 2- amino 5-chloropyridinium pyridine- 2- carboxylate monohydrate, Dig. J. Nanomater. Biostructures, 10(4) (2015), 1139 1151.
- 4. T. Chen, Z. Sun, L. Li, S. Wang, Y. Wang, J. Luo, M. Hong, Growth and characterization of a nonlinear optical crystal—2,6-diaminopyridinium 4-nitrophenolate 4-nitrophenol (DAPNP), J. Cryst. Growth, 338 (2012) 157–161.
- S. Gowri, T. Uma Devi, S. Priya, C. Surendra Dilip, S. Selvanayagam, N. Lawrence, Growth, structure, spectral and optical properties of semiorganic crystal: Pyridine-1-ium-2-carboxylatehydrogenbromide, Spectrochim. Acta A Mol. Biomol. Spectrosc., 143 (2015) 192-199.
- M.R.J. Elsegood, D.A. Hussain, N.M. Sanchez-Ballester, Redetermination of picolinic acid hydro-chloride at 150 K, Acta Cryst., E63 (2007) o4044.
- 7. Y. Tabuchi, A. Takahashi, K. Gotoh, H. Akashi, H. Ishida, 2-Carboxy-pyridinium hydrogen chloranilate, Acta Cryst., E61 (2005) o4215-o4217.

- 8. S. Gowri, T. Uma Devi, S. Alen, D. Sajan, C. Surendra Dilip, G. Vinitha, Synthesis, crystal structure, optical and third order nonlinear optical properties of phosphoric acid pyridine-1-ium-2-carboxylate, J. Mater. Sci. Mater. Electron., 29 (2018) 19710–19723.
- 9. S. Gowri, K. Anitha, A. Suresh, T. Uma Devi, S. Selvanayagam, D. Sajan, A. Chandramohan, N. Lawrence, Synthesis, growth, spectral and thermal properties of a new organic crystal: 2-Carboxypyridin-1-ium trichloroacetate, Spectrochim. Acta A Mol. Biomol. Spectrosc., 95 (2012) 73-79.
- H.Wang, P.D.Wu, C.N.Tomé, J.Wang, Study of lattice strains in magnesium alloy AZ31 based on a large strain elastic-viscoplastic self-consistent polycrystal model, Int J Solids Struct, 49 (2012) 2155-2167
- 11. Senthil Kumar Chandran, Rajesh Paulraj, P. Ramasamy, Structural, optical, thermal, photoconductivity, laser damage threshold and fluorescence analysis of an organic material: b-P-amino benzoic acid single crystal, Opt. Mater., 52 (2016) 49-55.
- 12. G.Peramaiyan, P.Pandia, B.M.Sornamurthy, G.Bhagavannarayana, R.Mohan Kumar, Growth, structural, thermal, linear and nonlinear optical and laser damage threshold studies of Picolinium tartrate monohydrate single crystals, Spectrochim. Acta A Mol. Biomol. Spectrosc., 95 (2012) 310-316
- A. Saranraj, J. Thirupathy, S. Sahaya Jude Dhas, M. Jose, G. Vinitha, S. A.
 Martin Britto Dhas, Growth and characterization of unidirectional benzil single crystal for photonic applications, Appl. Phys. B 124 (2018) 97.
- 14. P.S. Latha Mageshwari, R. Priya, S. Krishnan, V. Joseph, S. Jerome Das, Growth, optical, thermal, mechanical and dielectric studies of sodium succinate hexahydrate (β phase) single crystal: A promising third order NLO material, Opt. Laser Technol., 85 (2016) 66-74

- 15. B. Thirumalaiselvama, R. Kanagadurai, V. Natarajan, D. Jayaramana, Growth, dielectric, thermal and Z-scan studies of isatin admixtured 4-methyl benzene sulfonamide crystal, Optik, 158 (2018) 1194-1202
- Jesby George, D. Sajan, Experimental and theoretical investigations on nonlinear optical properties of L-alanine crystal: Z-scan & hyperpolarizability studies, AIP Conf Proc, 2115 (2019) 030415
- C. Torres-Torres, B.A. Can-Uc, R. Rangel-Rojo, L. Castañeda, R. Torres-Martínez,
 C.I. García-Gil, A.V. Khomenko, Optical Kerr phase shift in a nanostructured
 nickel-doped zinc oxide thin solid film, Opt. Express 21 (2013) 21357-21364
- T. Pal, T. Kar, Studies of microhardness anisotropy and Young's modulus of nonlinear optical crystal l-arginine hydrochlorobromo monohydrate, Mater.
 Lett. 59 (2005) 1400-1404.
- 19. Min Jin, Jiayue Xu, Xinhua Li, Hui Shen, Qingbo He, Microhardness and fracture toughness of 〈1 1 1〉 -oriented Pb(Zn1/3Nb2/3)O3–PbTiO3 single crystal, Mater. Sci. Eng. A, 472 (2008) 353-357.
- 20. P. Karuppasamy, Muthu Senthil Pandian, P. Ramasamy, S.K. Das, Growth and characterization of semi-organic nonlinear optical (NLO) Guanidinium trichloroacetate (GTCA) single crystal, Optik, 156 (2018) 707-719.
- J. Mary Linet, S. Dinakaran, S. Jerome Das, Optical and microhardness studies on unidirectional grown triaqua glycine sulfato zinc (II): A semiorganic NLO crystal, J. Alloys Compd., 509 (2011) 3832–3836.
- W.A. Wooster, Physical properties and atomic arrangements in crystals, Rep. Prog. Phys. 16 (1953) 62-82.

- 23. P. Nisha Santha kumari, S. Kalainathan, N. Arunai Nambi Raj, Vickers microhardness studies on cadmium mercury thiocyanate (CMTC) single crystals grown in silica gel, Mater. Lett. 62 (2008) 305–308.
- 24. Ghiasuddin, Muhammad Akram, Muhammad Adeel, Muhammad Khalid, Muhammad Nawaz, Tahir Muhamma, Usman Khan, Muhammad Adnan Asghar, Malik Aman Ullah, Muhammad Iqbal, A combined experimental and computational study of 3-bromo-5-(2,5-difluorophenyl) pyridine and 3,5-bis(naphthalen-1-yl)pyridine: Insight into the synthesis, spectroscopic, single crystal XRD, electronic, nonlinear optical and biological properties, J. Mol. Struct., 1160 (2018) 129-141.
- V. Sasikala, D. Sajan, N. Vijayan, K. Chaitanya, M.S. Babu Raj, B.H. Selin Joy, Growth, molecular structure, NBO analysis and vibrational spectral analysis of l-tartaric acid single crystal, Spectrochim. Acta A Mol. Biomol. Spectrosc., 123 (2014) 127-141.
- V. Balachandran, S. Lalitha, S. Rajeswari, Rotational isomers, density functional theory, vibrational spectroscopic studies, thermodynamic functions, NBO and HOMO–LUMO analyses of 2,6-Bis(chloromethyl)pyridine, Spectrochim. Acta A Mol. Biomol. Spectrosc., 97 (2012) 1023-1032.
- I. Fleming, Frontier Orbitals and Organic Chemical Reactions, John Wiley and Sons, New York, 1976
- S. Prabu, R. Nagalakshmi, P. Srinivasan, Investigations on the physico chemical properties of 4-bromochalcone single crystals for nonlinear optical applications, Spectrochim. Acta A Mol. Biomol. Spectrosc., 103 (2013) 45-52

- 29. V. Charles Vincent, K. Kirubavathi, G. Bakiyaraj, K. Selvaraju, Experimental and theoretical investigations of 4-hydroxy L-proline cadmium chloride nonlinear optical crystal, Spectrochim. Acta A Mol. Biomol. Spectrosc., 212 (2019) 61-70.
- 30. H. Yadav, N. Sinha, S. Goel, B. Singh, I. Bdikin, A. Saini, K. Gopalaiah, B. Kumar, Growth, crystal structure, Hirshfeld surface, optical, piezoelectric, dielectric and mechanical properties of bis-(L-asparaginium hydrogensquarate) single crystal, Acta Cryst. B73 (2017) 347-359
- 31. P. Muthuraja, M. Sethuram, T. Shanmugavadivu, M. Dhandapani, Single crystal X-ray diffraction and Hirshfeld surface analyses of supramolecular assemblies in certain hydrogen bonded heterocyclic organic crystals, J. Mol. Struct., 1122 (2016) 146-156.
- 32. F.L. Hirshfeld, Bonded-atom fragments for describing molecular charge densities, Theoret. Chim. Acta, 44 (1977) 129–138.
- M.A. Spackman, D. Jayatilaka, Hirshfeld surface analysis, Cryst. Eng. Comm.,
 11 (2009) 19-32.

Chapter-IV

Experimental and Theoretical Investigations of Nonlinear Optical Crystal 2-Picolinic Benzotriazole

CHAPTER - IV

EXPERIMENTAL AND THEORETICAL INVESTIGATIONS OF NONLINEAR OPTICAL CRYSTAL 2-PICOLINIC BENZOTRIAZOLE

4.1. INTRODUCTION

Nonlinear optical materials are gaining a lot of attention because they're used in data storage, optical switching, picture reconstruction, and holography recording [1,2]. Material scientists have focused their attention on the creation of innovative nonlinear optical single crystals with high nonlinear optical coefficients due to day-to-day technological requirements [3]. In this view, organic nonlinear optical materials may be far superior owing to their relatively high and faster nonlinearities [4,5]. Among the various organic compounds reported for their NLO properties, a series of studies on organic benzotriazole compounds such benzotriazole p-hydroxy benzoic acid [6], benzotrizolium picrate [7], benzotriazole pyridine-2-carboxylic acid [8] etc., having good NLO properties and crystallizability. Despite the fact that the 2-picolinic benzotriazole (PBTA) compound has previously been reported [8], this is the first study to focus on DFT calculations in addition to structural, optical and hardness properties. The growth of a possible nonlinear optical single crystal of 2-picolinicbenzotriazole (PBTA) using slow evaporation solution growth process by methanol as the solvent is described in this paper. The heterocyclic molecule benzotiazole has three nitrogen atoms. It is a type of organic compound that has flexible ligands. Because picolinic acid (also known as pyridine-2-carboxylic acid, 2-pyridine carboxylic acid and 2picolinic acid) is a chelating agent, it creates coordination bonds with the ligand, which is required for non-centrosymmetric space group crystal formation [9]. PBTA crystallizes into a non-centrosymmetric crystal structure, which is a need for nonlinear optical materials. The different molecular properties of PBTA molecule is computed

quantum-chemical calculations, including the optimized geometry, bond lengths, bond angles, charge transfers, hyperpolarizability, and the energies and characteristics of the HOMO and LUMO. The behavior of the PBTA crystal is discussed using both experimental and theoretical methods.

4.2. EXPERIMENTAL ANALYSIS

4.2.1. Solubility Study

The solubility of grown PBTA crystals was tested using methanol in the temperature range between 303 K and 318 K with intervals of 5 K. Initially, the constant temperature bath was kept at 303 K, and stirring was continued. The re-crystallized material was added step by step to 100 mL of methanol in an airtight container until equilibrium concentration of the solution was achieved. The similar procedure was followed to find out the solubility for other temperatures. Fig.4.1 shows the solubility of PBTA crystal. It has been discovered that as the temperature rises, so does the solubility of the material, and the nucleation temperature rises with the concentration. As a result, the PBTA compound exhibits positive solubility gradient.

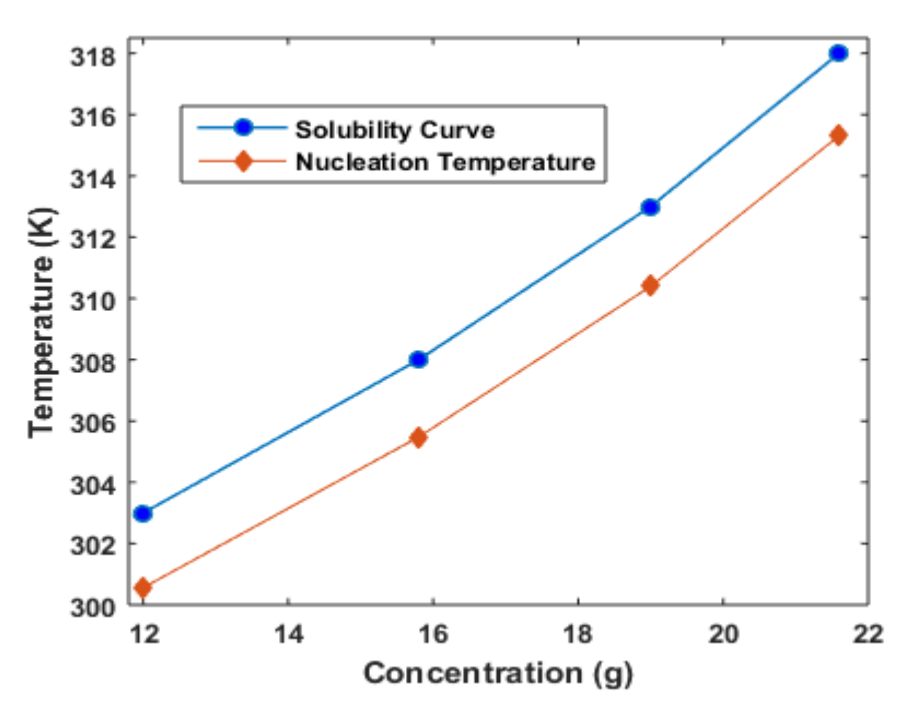


Fig. 4.1. Solubility curve for PBTA

4.2.2. Nucleation kinetics and Metastable zone width (MZW)

The different nucleation characteristics such as critical free energy of the nucleus (ΔG^*), radius of the critical nucleus (r^*), nucleation rate (J), and number of molecules in the critical nucleus (i*) have been estimated using the interfacial tension values. Table 4.1 lists the nucleation characteristics of PBTA crystals at various supersaturation levels. With increasing supersaturation and temperature, the radius of critical nuclei shrinks. With rising supersaturation, the change in free energy per unit volume (ΔG_v) diminishes. Fig. 4.2 illustrates the calculated change in energy barrier (ΔG^*) as a function of supersaturation ratio. The ΔG^* will decrease as the supersaturation ratio rises. The radius of the critical nucleus as a function of supersaturation ratio is shown in Fig.4.3. At different supersaturation values (1.1 - 1.4) for 303 K, the critical free energy barrier and critical radius of PBTA were determined to be (ΔG^*) 1.63×10⁻¹⁸ J to 1.31×10^{-19} J and (r^{*}) 8.22 nm to 2.33 nm, respectively. The width of the metastable zone is crucial for bulk size crystal formation. The goal of this study is to suggest theoretically calculated metastable zone width values for crystallization temperatures using the slow evaporation method. The results show that when the temperature drops, the zone width of the formed crystal narrows.

Table 4.1. Nucleation Table from PBTA for Supersaturation Ratio-1.1

T (K)	$\Delta G_{\rm v}(~{ m J/m}^3)$	$\sigma (J/m^2)$	$\Delta \mathbf{G}^{*}(\mathbf{J})$	r* (m)	i*	J (nuclei/m³/sec)
303	-1407072.1	0.005781	1.63E-18	8.22E-09	8203.02	1.27716E+13
308	-1430291.1	0.00544	1.32E-18	7.61E-09	6507.057	1.09443E+13
313	-1453510.1	0.005231	1.13E-18	7.2E-09	5512.157	9.79815E+12
318	-1476729.1	0.005104	1.02E-18	6.91E-09	4883.708	9.03849E+12

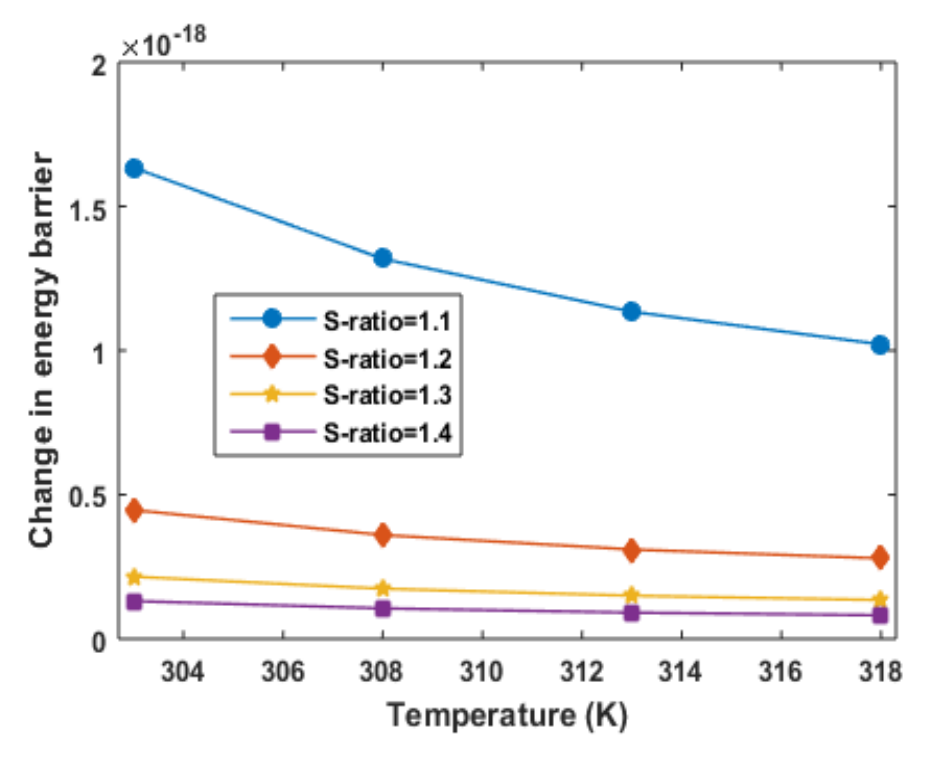


Fig. 4.2. Variation of Gibbs free energy with supersaturation and temperature for PBTA

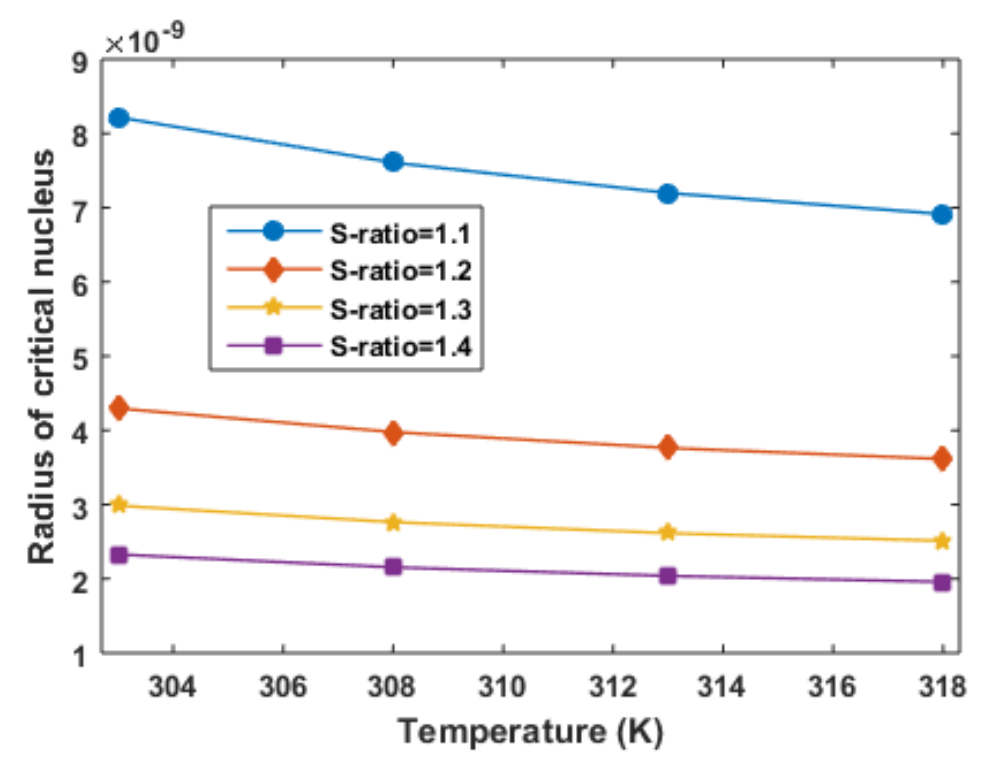


Fig. 4.3. Variation of radius of critical nucleus with temperature and supersaturation ratio of PBTA

4.2.3. Growth of PBTA Crystal

The growth of 2-picolinic benzotriazole single crystals, by using 2-carboxypyridine and 1H-1,2,3 benzotriazole (AR grade), both commercially available, are combined in an equimolar ratio and dissolved in methanol. The solution is then stirred continuously for six hours at room temperature to maintain homogeneity. The solution is filtered using Whatmann filter paper to eliminate impurities before being transferred to a crystal growth vessel and allowed to grow by slow evaporation at room temperature. To control the rate of evaporation, the opening of the vessel is covered with a porous polythene sheet. Slow evaporation solution growth method yields optically good quality PBTA crystals after two weeks, as illustrated in Fig. 4.4.

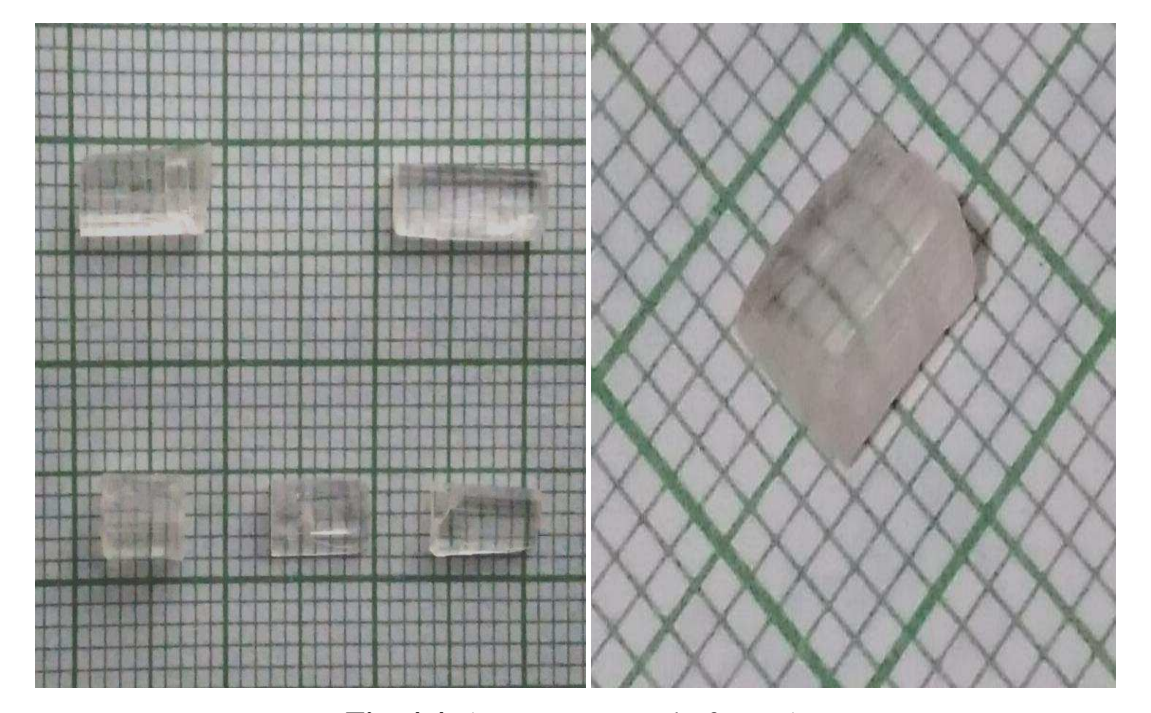


Fig. 4.4. As grown crystal of PBTA

4.2.4. Powder XRD

The powder XRD pattern of the PBTA crystal using BRUKER X-ray diffractometer with CuK α radiation ($\lambda = 1.5406$ Å) and a step size of 0.0130 and a

scanning step time of 23.97s, given in Fig.4.5 displays the (hkl) values corresponding to each diffraction plane. The crystalline nature of the sample is revealed by the razor sharp and well defined peaks at certain 2θ values, which are a characteristic property of the XRD spectrum. The following are the lattice properties of the PBTA crystal as determined by Fullprof Suite software: a = 22.671 (20) (Å), b = 3.898 (1) (Å), c = 12.717 (5) (Å), $\alpha = \beta = \gamma = 90^{\circ}$ and volume = 1123.9 (1) (Å³), orthorhombic system with space group $Pna2_1$. It closely matches the reported value [8].

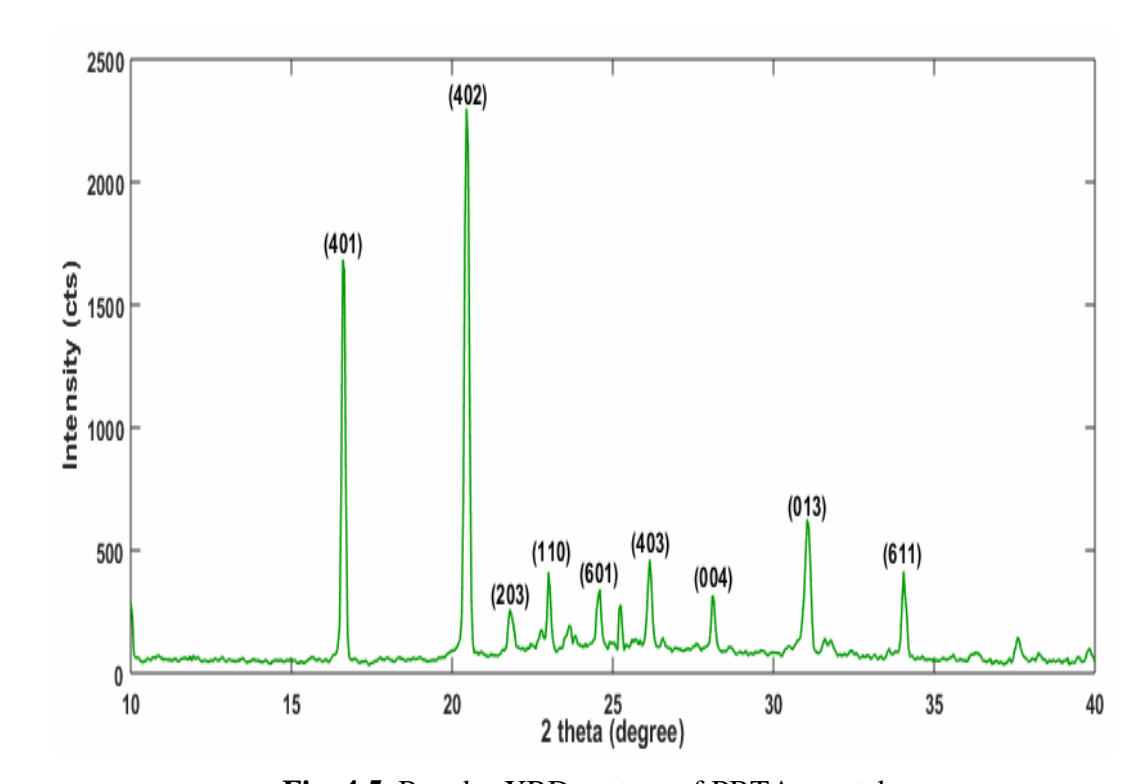


Fig. 4.5. Powder XRD pattern of PBTA crystal

The diffraction peaks suggest two main components are crystallite size and strain. Fig.4.6 exhibits the Williamson-Hall analysis to estimate crystallite size τ and induced strain in PBTA sample. Lattice strain is generally measured from the lattice parameter arising from crystal imperfection such as crystal dislocation and grain boundary point [10]. The size and strain broadening is evaluated by W-H analysis using the relation [11]:

$$\beta \cos\theta = \frac{K\lambda}{\tau} + \eta \sin\theta \qquad ... (4.1)$$

where, β - FWHM of the diffraction peak (rad); θ - Bragg's diffraction angle (rad); $K \text{ - Scherrer constant; } \lambda \text{ - wavelength of the X-rays } \begin{pmatrix} \mathring{A} \end{pmatrix}; \tau \text{ - crystallite size } (\mu m);$ $\eta \text{ - lattice strain.}$

The size and strain of PBTA is evaluated from intercept and slope of straight line respectively by linear fit. The crystallite size (τ) value is ~0.2 μ m and lattice strain, $\eta = 0.003$. Because the value of η is small, the PBTA crystal has less lattice strain, implying a larger elastic stiffness constant. [12].

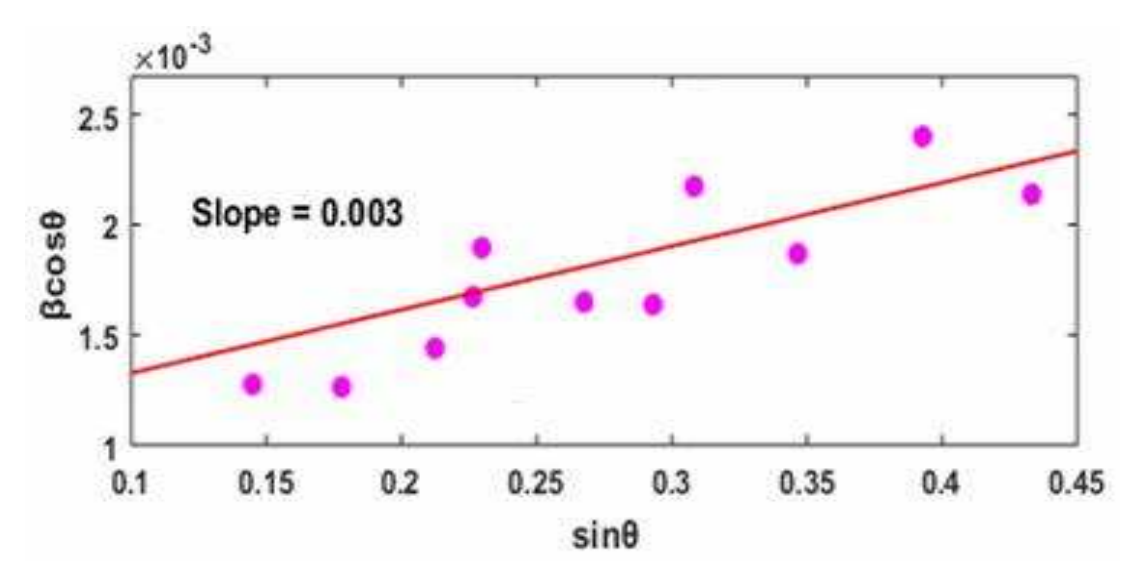


Fig. 4.6. Graph plotting $\beta \cos \theta$ versus $\sin \theta$

4.2.5. UV-vis-DRS Analysis

(a) By Tauc's Plot

The most specific optical parameters of materials are transmittance, absorption, reflectance, absorption coefficient, optical energy gap and refractive index were calculated from the transmittance spectrum. The optical absorption spectrum was recorded in the range of 220-1100 nm using SHIMADZU/ UV 2600 Spectrophotometer and is

depicted in Fig. 4.7. The crystal is highly transparent if it has a low absorption region. It is found that the crystal is transparent from 450 nm to 1100 nm. Hence the crystal can be used for frequency doubling process [13]. The linear optical constants of PBTA are determined using the absorption spectra, and the variation in optical constants as a function of photon energy is displayed (Fig. 4.8(a-d)). Fig. 4.8a shows that the bandgap of the PBTA crystal is 3.49 eV, which was obtained by extrapolating the linear part of the curve to the hv axis. The refractive index increases with increase in photon energy and is depicted in Fig. 4.8b. Fig. 4.8c and 4.8d illustrates the extinction coefficient and reflectance varies linear with respect to photon energy. The calculated values of refractive index (n), electric susceptibility (χ_C), real (ε_r) and imaginary (ε_i) dielectric constants derived from the optical constants at $\lambda = 800$ nm, are 1.05, 0.088, 1.111 and 9.131 × 10⁻⁸, respectively.

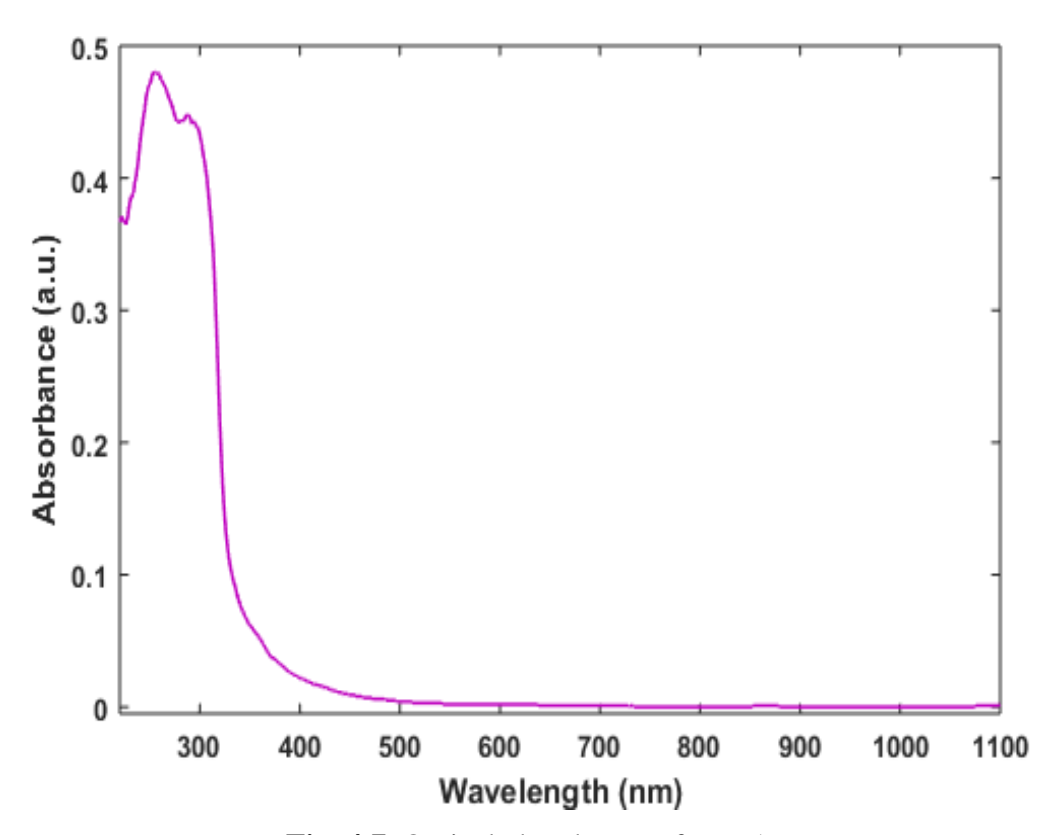


Fig. 4.7. Optical absorbance of PBTA

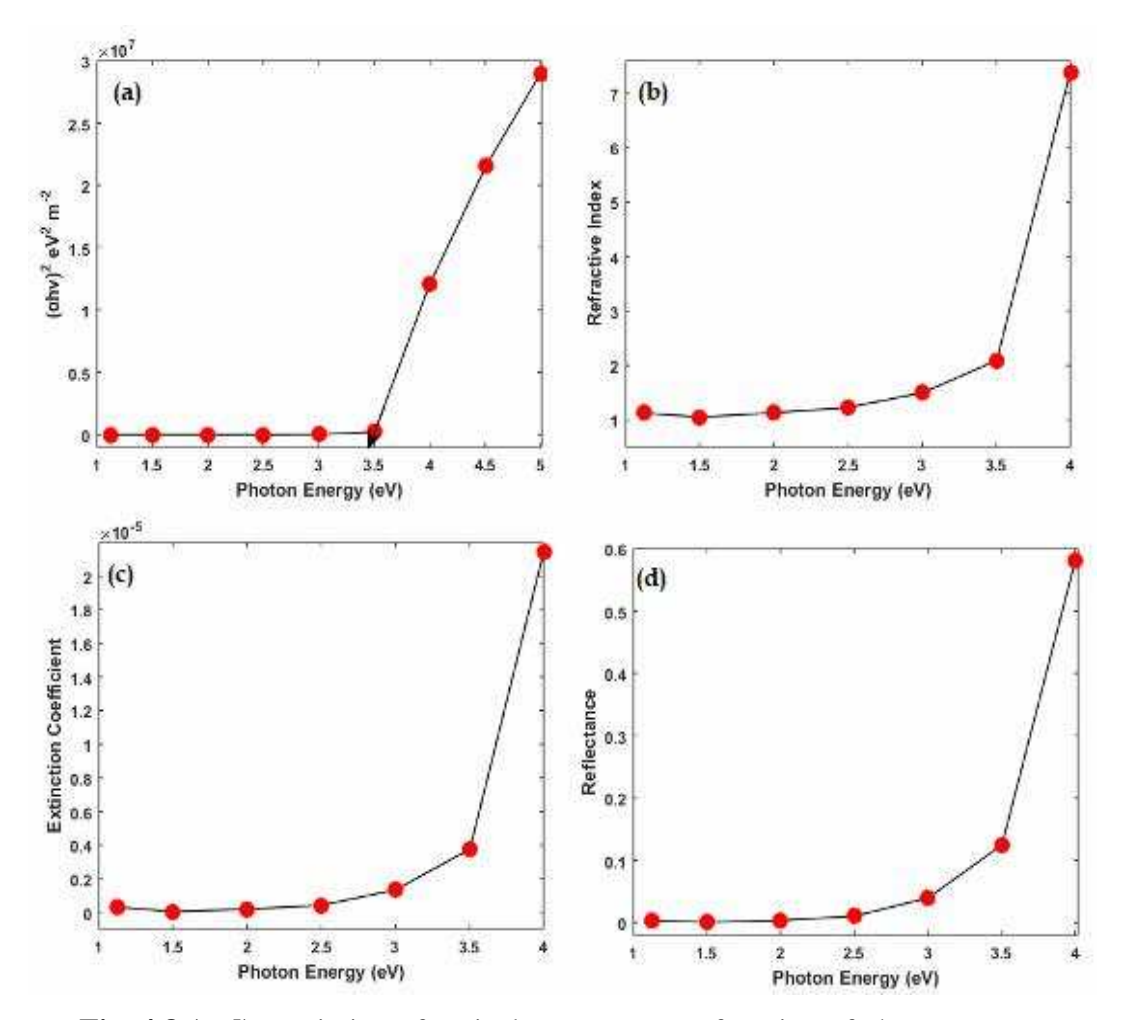


Fig. 4.8 (a-d). Variation of optical constants as a function of photon energy

(b) By Derivation of absorption spectrum fitting (DASF) method

This method is already described in section 2.2.5(b) of chapter-II is used to calculate the optical properties of PBTA. The energy band gap is calculated as 3.46 eV from Fig. 4.9. The value of m is obtained from the slope of Fig. 4.10 to study the band structure and the type of transition of electron of grown crystals. For different kinds of transitions m has different values they are m = 1/2: Direct allowed transition; m = 1: non metallic materials; m = 3/2: Direct forbidden transition; m = 2: Indirect allowed transition; m = 3: Indirect forbidden transition [14]. The current research reveals a value of m close to 1/2, indicating that PBTA possesses a direct band gap and the optical transition is direct allowed transition. The crystalline nature of grown crystal

was measured by the Urbach relation $E_{Tail} = \frac{1239.83}{Slope} (eV)$ and Fig. 4.11 gives us the

Urbach energy value. In addition, the grown crystals are found to be defects-free from the Urbach energy of 0.11 eV obtained from linear fit in Fig. 4.11. The optical study findings (Table 4.2) imply that PBTA crystals are suitable for opto-electronic device manufacturing [15].

Table 4.2. Optical parameters of PBTA

Optical Parameters (DASF method)	Values		
λ_g (wavelength of energy gap)	358 nm		
$1/\lambda_{\rm g}$	0.00279		
E _g (optical energy band gap)	3.46 eV		
E _{Tail} (Urbach energy)	0.11 eV		
σ(steepness parameter)	2.35		
E _{e-p} (electron-phonon interaction)	0.28		
n (refractive index)	2.24		
$\varepsilon_{\rm d}$ (dielectric constant)	1.93		

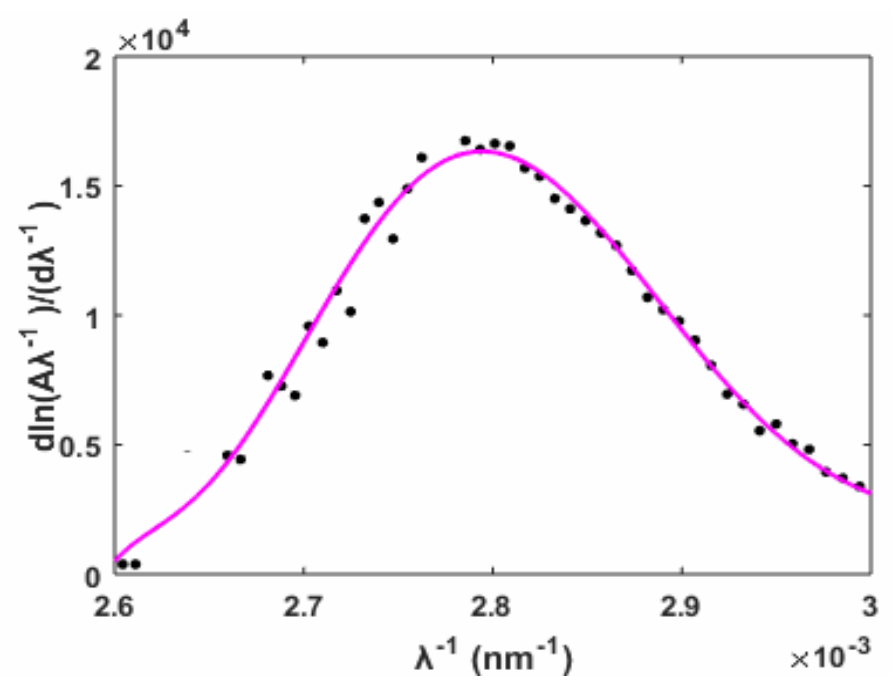


Fig. 4.9. DASF plot for PBTA crystal

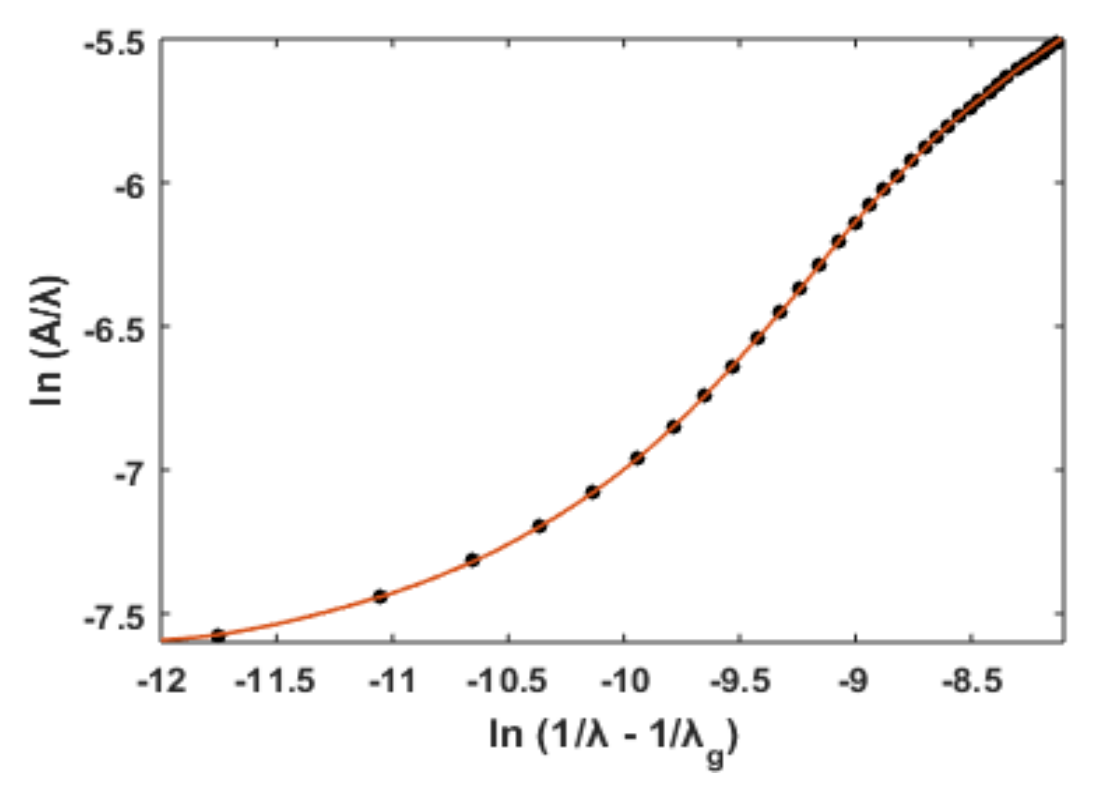


Fig. 4.10. Curves of ln (A/ λ) vs ln (1/ λ - 1/ λ_g)

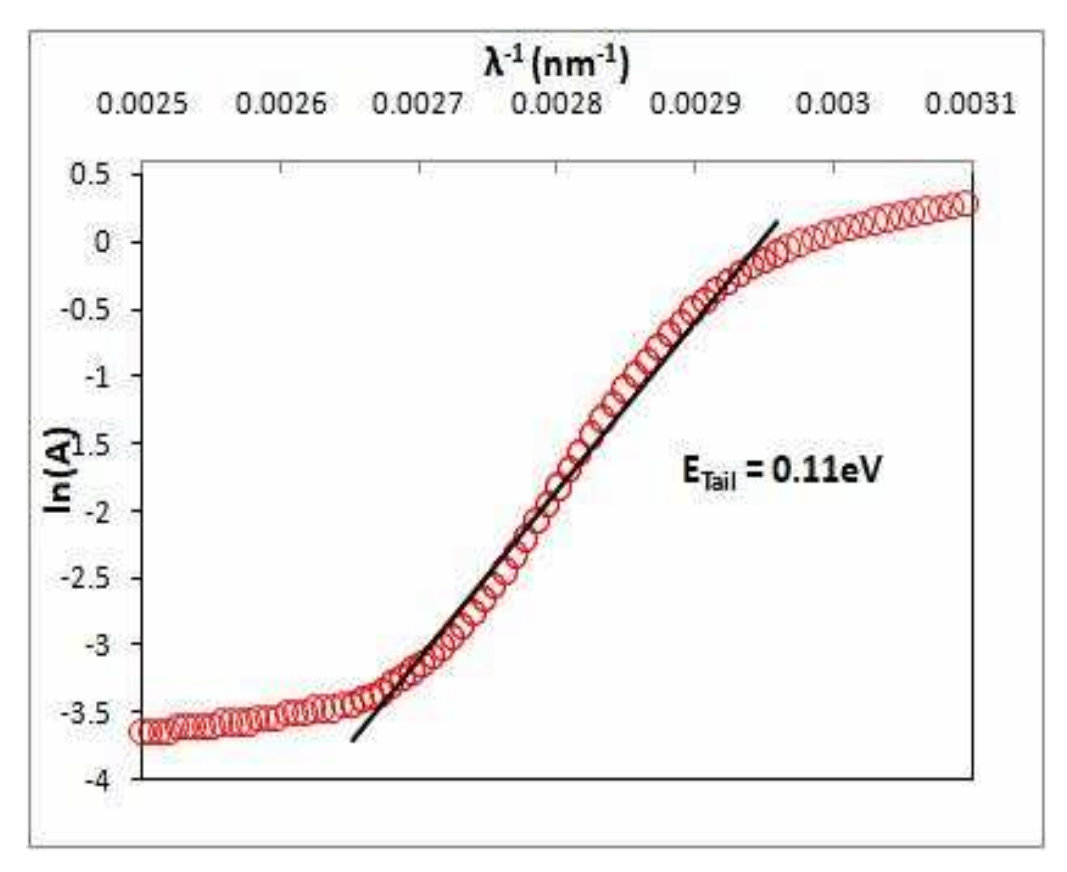


Fig. 4.11. Urbach plot for PBTA

4.2.6. Fluorescence analysis

Fluorescence is one of the optical properties of the material which exist owing to the relaxation of excited electrons. The fluorescence spectrum of PBTA is shown in Fig. 4.12 and it was recorded by using a SHIMADZU/ RF 6000 Spectro Fluorophotometer. The molecule emits a peak centered at 480 nm after being excited at 250 nm. As a result of this, the PBTA crystal has the blue emission spectrum. The absence of new peaks can be attributed to the crystals enhanced purity and lower defect levels.

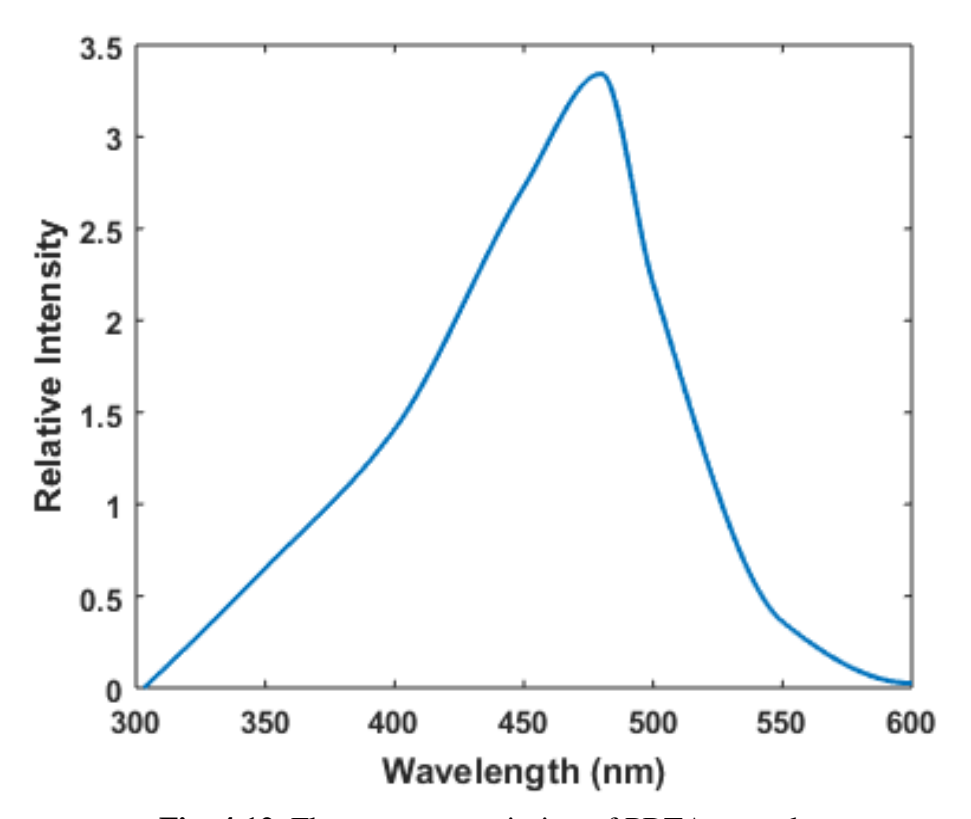


Fig. 4.12. Fluorescence emission of PBTA crystal

4.2.7. Second Harmonic Generation (SHG) Test

Using a Q-switched Nd:YAG laser operating at a fundamental wavelength of 1064 nm, the second harmonic output power of the PBTA crystal was measured using the Kurtz power technique. The capillary tube, which has an inner diameter of around 600 m, was filled with well-ground powder of PBTA crystal sample. The emission of

green radiation ($\lambda = 532$ nm) from the PBTA sample confirmed the second harmonic signal generated in the crystalline sample. The SHG output power of the grown crystal was measured with an input energy of 1.1 mJ/pulse and a pulse width of 8 ns. With KDP and Urea as reference materials, the relative SHG output power of grown crystal was investigated. PBTA, KDP, and Urea had second harmonic signals of 82 mV/pulse, 32 mV/pulse, and 120 mV/pulse, respectively. The second harmonic output power of the PBTA crystal is 2.2 times that of the KDP crystal.

4.2.8. Microhardness Study

The mechanical behavior of a crystal is of paramount importance in technological applications [16]. The hardness measurement is treated as an efficient technique for providing information about the elastic, plastic, viscous andfracture properties. To assess such behavior, the grown crystal was subjected to Vicker's hardness test by considering the loading range from 25 to 100 g using a SHIMADZU-HMV-G MicroVickers Hardness Tester. The micro hardness was measured using the relation (3.2) in chapter-III. The variation of hardness with load is shown in Fig.4.13a. The Meyer's formula P = kdⁿ gives the relation between applied load (P) and the diagonal length (d) of indentation. The Work Hardening Coefficient (WHC), n is calculated as 2.4 from the linear fit of log P against log d shown in Fig. 4.13b. According to Hanneman [17], the values of n are 1 to 1.6 for hard materials and more than 1.6 for softer materials, putting PBTA in the soft material category. Fig. 4.13c shows that the PBTA chemical has a reverse indentation size effect (RISE) effect, indicating that plastic deformation is the dominant mode of deformation.

Load P (g)	H _v (kg/mm ²)	d (µm)	C ₁₁ (Pa)	σ _v (MPa)
25	15	57.62	1.96E+14	1.86
50	30.8	45.82	6.92E+14	3.83
100	43.3	34.43	1.25E+15	5.38

Table 4.3. Hardness parameters of PBTA

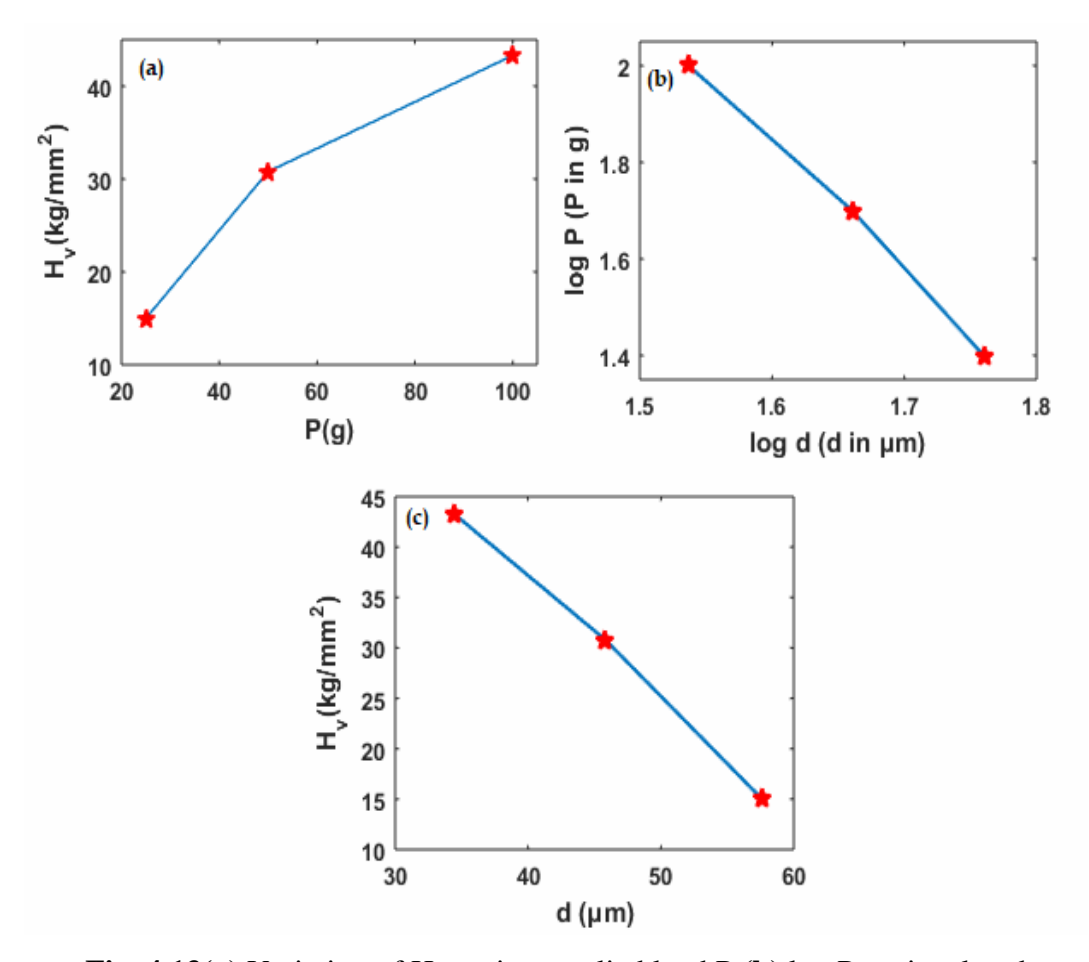


Fig. 4.13(a). Variation of H_v against applied load P (b) log P against log d (c) H_v against d

Load dependent hardness [18] is calculated using equation 3.3 and by graphing the experimental P against d^2 [Fig.4.14], the values of W and A_1 are found to be 58 g and 0.03 (g/m²), respectively. The corrected hardness (H_o) is 58.63 (kg/mm²) when computed using the formula $H_0 = 1854.4 \times A_1$.

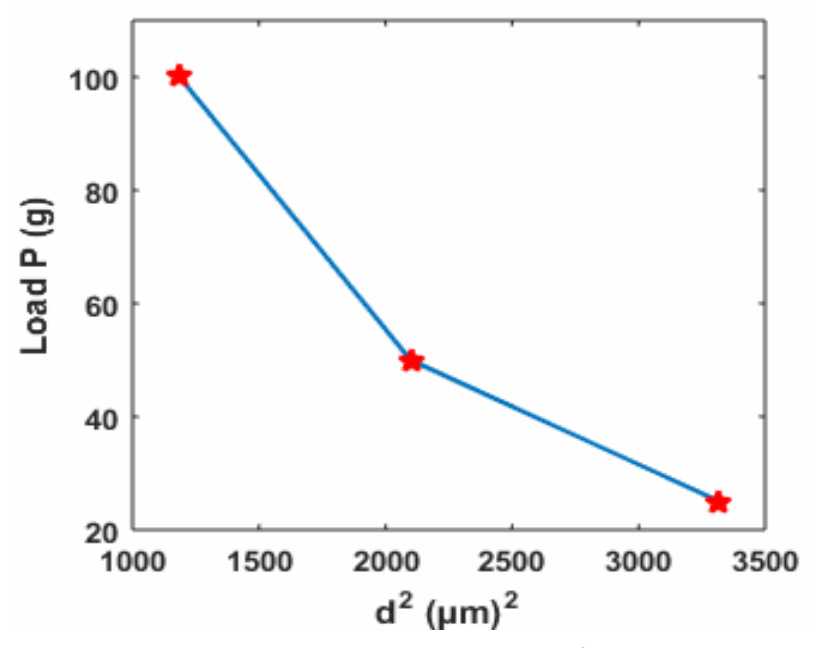


Fig. 4.14. Load P against d²

Wooster's empirical relation [19] is used to get the elastic stiffness constant (C₁₁). Table 4.3 shows the computed stiffness constants for various loads. The material is discovered to be suitable for device fabrications since it has a moderately higher hardness number [20].

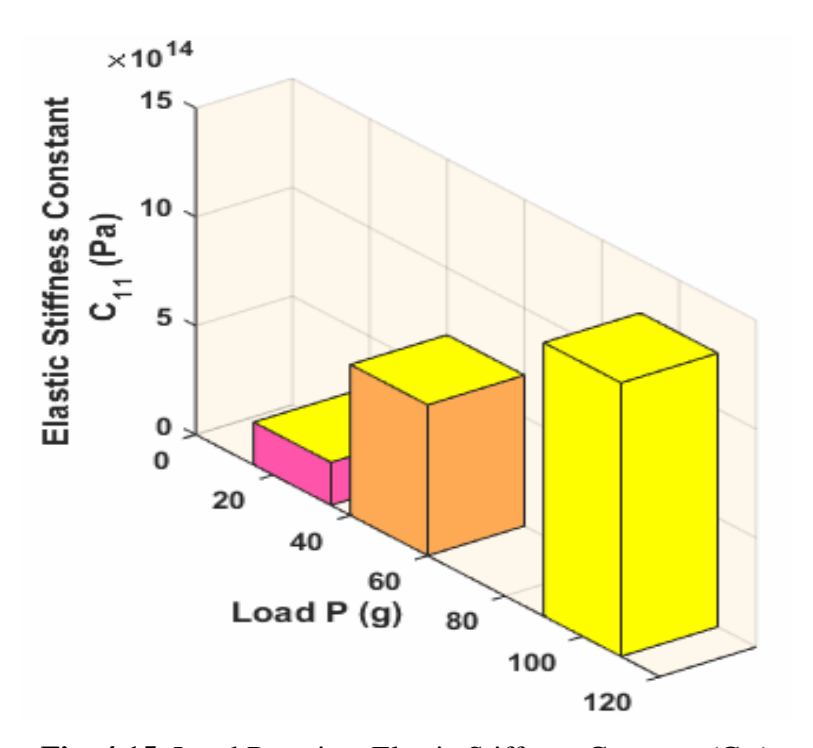


Fig. 4.15. Load P against Elastic Stiffness Constant (C₁₁)

4.3. COMPUTATIONAL ANALYSIS

4.3.1. Optimized Geometry

The optimized geometries of PBTA with symbols and a numbering scheme for the atoms are shown in Fig. 4.16. At the DFT/B3LYP/6-311++G(d,p) level, Table 4.4 summarizes their main structural parameters that were maximized. The DFT structure optimization method yielded a global minimum energy value of -2.185×10^6 kJ/mol. Because the calculations were done in the gaseous phase whereas the experimental results were for the crystalline state, the theoretical bond length and angles differed somewhat from the crystal characteristics [21]. The C-H bonds were shorter in all experimental results than those calculated by DFT. The bond lengths of C1-C2, C3-C4, C5-C6, C7-C8, C9-C10, and C11-C12 in the benzene rings calculated using the DFT approach were in close agreement with the experimental lengths with a minor difference (±0.035). This research demonstrates that electron delocalization occurs between the carbon atoms in the aromatic ring, resulting in a more stable structure [22]. Furthermore, the observed divergence could be attributable to the fact that the X-ray structure was solved in a crystalline form, whereas the optimal structures computations were for isolated molecules [23]. The N-N bonds within the triazole ring (N1-N2=1.292Å, N2-N3=1.356Å) are in good agreement with experimental results (N1-N2=1.304 Å, N3-N2=1.346 Å). The O-H···N, N-H···O and N-H···N hydrogen bonds connect the molecules, making a two-dimensional zig-zag chain. The benzotriazole ring is generally planar because the corresponding dihedral angles H4-C5-C4-C3 and C6-C1-C2-H1 are 180°. When compared to experimental results [8], the overall dihedral angles predicted using the DFT/B3LYP/6-311++G(d,p) approach correlated well.

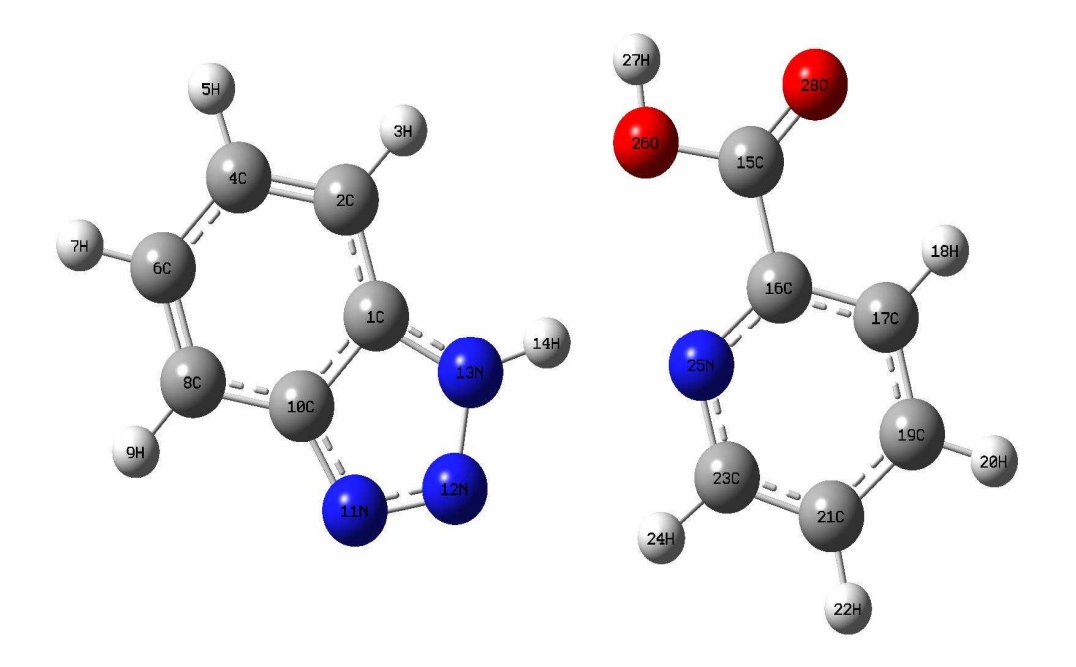


Fig. 4.16. The optimized molecular structure of PBTA

Table 4.4. Optimized parameters of PBTA by B3LYP level with 6-311++G(d,p) basis set

			•					
Bond	Values (Å)		Dand Anala	Values (°)		Dihadual Anala	Valu	es (°)
Length	Calc.	Exp. ^[8]	Bond Angle	Calc.	Exp. ^[8]	Dihedral Angle	Calc.	Exp. ^[8]
H7-C11	1.083	0.930	C6-C1-N3	103.5	104.2	Н7-С11-С12-Н8	0.0009	-0.022
H8-C12	1.085	0.930	C2-C1-C6	121.9	122.5	H7-C11-C12-N4	-179.9	-179.9
C11-C12	1.395	1.379	C2-C1-N3	134.5	133.2	С10-С11-С12-Н8	-179.9	179.9
C11-C10	1.391	1.356	C1-C2-C3	116.5	115.9	C10-C11-C12-N4	0.0012	0.046
N1-N2	1.292	1.304	C1-C2-H1	121.8	122.0	Н7-С11-С10-Н6	-0.0016	0.027
N1-C6	1.377	1.369	H1-C2-C3	121.7	122.0	H7-C11-C10-C9	179.9	-179.9
N2-N3	1.356	1.346	C2-C3-C4	121.9	122.4	С12-С11-С10-Н6	179.9	-179.9
C12-N4	1.336	1.323	H2-C3-C4	118.8	118.8	C12-C11-C10-C9	-0.0009	0.039
H6-C10	1.083	0.931	C2-C3-H2	119.2	118.7	C6-N1-N2-N3	-0.0007	0.505
C10-C9	1.391	1.370	H3-C4-C5	119.7	119.1	N2-N1-C6-C5	179.9	-179.9
H4-C5	1.083	0.929	C3-C4-C5	121.4	121.7	N2-N1-C6-C1	-0.0001	-0.367
C6-C5	1.403	1.397	C3-C4-H3	118.9	119.1	N1-N2-N3-H10	179.9	178.5
C6-C1	1.409	1.385	H4-C5-C6	120.1	121.8	N1-N2-N3-C1	0.0013	-0.468
N3-H10	1.026	0.959	C4-C5-H4	121.9	121.8	H8-C12-N4-C8	-179.9	179.5
N3-C1	1.382	1.354	C4-C5-C6	117.4	116.4	C11-C12-N4-C8	0.0003	-0.561
N4-C8	1.338	1.339	C5-C6-N1	130.8	130.9	C11-C10-C9-C8	-0.0008	0.390
C5-C4	1.382	1.365	C1-C6-N1	108.4	108.2	C11-C10-C9-H5	179.9	-179.7
C1-C2	1.402	1.387	C1-C6-C5	120.8	120.9	H6-C10-C9-C8	179.9	-179.6
C9-C8	1.394	1.373	C8-C7-O1	113.4	113.5	Н6-С10-С9-Н5	0.0003	0.368
С9-Н5	1.081	0.931	C8-C7-O2	123.8	121.8	N1-C6-C5-H4	0.0021	0.2947
C8-C7	1.498	1.492	O1-C7-O2	122.8	124.7	N1-C6-C5-C4	-179.9	-179.7

Bond	Value	es (Å)	D 14 1	Value	es (°)	D1 1 1 1 1	Valu	es (°)
Length	Calc.	Exp. ^[8]	Bond Angle	Calc.	Exp. ^[8]	Dihedral Angle	Calc.	Exp. ^[8]
С4-Н3	1.083	0.930	C9-C8-N4	123.2	122.2	C1-C6-C5-H4	179.9	-179.2
C4-C3	1.416	1.404	C7-C8-N4	118.4	117.7	C1-C6-C5-C4	-0.0005	0.774
C2-C3	1.384	1.357	C7-C8-C9	118.4	120.1	N1-C6-C1-N3	0.0008	0.079
C2-H1	1.082	0.929	C8-C9-C10	118.2	119.2	N1-C6-C1-C2	179.9	179.7
С3-Н2	1.084	0.930	H5-C9-C10	122.2	120.4	C5-C6-C1-N3	-179.9	179.7
C7-O1	1.351	1.308	C8-C9-H5	119.5	120.4	C5-C6-C1-C2	0.0010	-0.709
C7-O2	1.207	1.200	H6-C10-C11	120.7	120.5	N2-N3-C1-C6	-0.0013	0.230
О1-Н9	0.969	0.819	C9-C10-C11	118.8	119.1	N2-N3-C1-C2	-179.9	-179.3
			С9-С10-Н6	120.4	120.4	H10-N3-C1-C6	-179.9	-178.5
			H7-C11-C12	119.9	120.7	H10-N3-C1-C2	0.0076	1.969
			C10-C11-H7	121.3	120.7	C12-N4-C8-C9	-0.0021	1.012
			C10-C11-C12	118.8	118.6	C12-N4-C8-C7	179.9	-179.6
			С11-С12-Н8	121.5	118.4	H4-C5-C4-H3	0.0004	-0.565
			H8-C12-N4	115.8	118.3	H4-C5-C4-C3	180.0	179.4
			C11-C12-N4	122.7	123.3	С6-С5-С4-Н3	-179.9	179.4
			C6-N1-N2	108.2	108.7	C6-C5-C4-C3	-0.0003	-0.572
			N1-N2-N3	109.6	108.1	C6-C1-C2-C3	-0.0007	0.378
			N2-N3-H10	117.7	117.1	C6-C1-C2-H1	-180.0	-179.6
			C1-N3-N2	110.2	110.8	N3-C1-C2-C3	179.9	179.8
			C1-N3-H10	132.0	132.1	N3-C1-C2-H1	-0.0029	-0.129
			C8-N4-C12	118.2	117.5	C10-C9-C8-N4	0.0023	-0.946
			C7-O1-H9	106.4	109.5	C10-C9-C8-C7	-179.9	179.7
						H5-C9-C8-N4	-179.9	179.1
						H5-C9-C8-C7	0.0036	-0.286
						N4-C8-C7-O1	-0.0005	-1.812
						N4-C8-C7-O2	179.9	177.9
						C9-C8-C7-O1	179.9	177.6
						C9-C8-C7-O2	-0.0032	-2.651
						C5-C4-C3-C2	0.0006	0.288
						С5-С4-С3-Н2	-179.9	-179.7
						H3-C4-C3-C2	-179.9	-179.7
						Н3-С4-С3-Н2	0.0009	0.286
						C1-C2-C3-C4	-0.0001	-0.166
						C1-C2-C3-H2	179.9	179.8
			_			H1-C2-C3-C4	179.9	179.8
						Н1-С2-С3-Н2	-0.0015	-0.202
						С8-С7-О1-Н9	-179.9	-179.9
						О2-С7-О1-Н9	0.0082	0.362

4.3.2. Hyperpolarizability

NLO is at the forefront of current research as it provides the key functions of frequency shifting, optical modulation, optical switching, optical logic, and optical memory for developing technologies such as telecommunications, signal processing, and optical interconnections [24]. The complete equations for calculating the mean polarizability α and the mean first order hyperpolarizability β , using the x, y, z components are defined as follow:

$$\alpha = (\alpha_{xx} + \alpha_{yy} + \alpha_{zz})/3 \qquad \dots (4.3)$$

$$\beta = [(\beta_{xxx} + \beta_{xyy} + \beta_{xzz})^2 + (\beta_{yyy} + \beta_{yzz} + \beta_{yxx})^2 + (\beta_{zzz} + \beta_{zxx} + \beta_{zyy})^2]^{1/2} \ \dots \ (4.4)$$

where, α_{xx} , α_{yy} and α_{zz} are the diagonal components of polarizability tensor and β_{xxx} , β_{xxy} , β_{xyy} , β_{yyy} , β_{xxz} , β_{xyz} , β_{yyz} , β_{xzz} , β_{yzz} and β_{zzz} are the 10 components of the 3D matrix.

The components of polarizability and the first order hyperpolarizability of the PBTA compound can be seen in Table 4.5. Polarizability of PBTA is 2.58×10^{-23} esu. The first order hyperpolarizability of PBTA is 1.77×10^{-30} esu, which is greater than those of urea (β of urea 0.3728×10^{-30}) [25]. The calculated value shows that PBTA might have good NLO properties.

Table 4.5. NLO properties of PBTA calculated using DFT at B3LYP/6-311++G(d,p) level

Polarizability		First hyper	rpolarizability
α_{xx}	228.48	β_{xxx}	8.07
α_{xy}	-16.01	eta_{xxy}	0.33
$\alpha_{ m yy}$	203.25	eta_{xyy}	-84.21
α_{xz}	-0.0011	$eta_{ m yyy}$	155.59
$\alpha_{ m yz}$	0.0026	eta_{xxz}	-0.0037
α_{zz}	90.77	$eta_{ ext{xyz}}$	0.016
		$eta_{ m yyz}$	-0.032
		eta_{xzz}	-44.57
		$eta_{ m yzz}$	10.13
		eta_{zzz}	0.035

4.3.3. Natural Bond Orbital (NBO) Analysis

The NBO analysis is performed on PBTA at DFT/B3LYP with 6-311++G(d,p)basis set to elucidate the inter and intramolecular charge transfer interactions and electron delocalization inside the molecule. The second order perturbation theory analysis of Fock matrix in the NBO is presented in Table 4.6. The orbital overlap between $\pi(C-C)$ and $\pi^*(C-C)$ and (N-N) bond orbitals creates intramolecular hyperconjugative interactions, resulting in intramolecular charge transfer (ICT) and system stabilization. These interactions cause an increase in electron density (ED) in the C-C antibonding orbital, weakening the bonds. The benzene and triazole rings are stabilized. The stabilization energy for $n_1(N_{25})$ to $\sigma^*(N_{13}-H_{14})$ are calculated to be 12.87 kcal/mol, indicating that the intermolecular N-H•••N hydrogen bonding is quantified. The most critical interaction energies are 273.73, 158.28, 137.74 and 151.39 kcal/mol for $\pi^*(C_1-C_{10})$ to $\pi^*(C_6-C_8)$, $\pi^*(C_{15}-O_{28})$ to $\pi^*(C_{16}-C_{17})$, $\pi^*(C_{23}-N_{25})$ to $\pi^*(C_{16}-C_{17})$ and $\pi^*(C_{19}-C_{21})$, respectively. The pyridine ring of PBTA is stabilized as a result of these interactions. The molecule strong ICT interactions are revealed by the higher E(2) value.

Table 4.6. Second order perturbation theory analysis of Fock matrix in NBO basis including the stabilization energies using DFT at B3LYP/6-311++G(d,p) level

Donor (i)	ED (i)	Acceptor (j)	ED (j)	^a E(2) Kcal/mol	^b E(j)-E(i)	°F(i,j)
			0.20210		a.u.	a.u.
		$\pi^*(C_2-C_4)$	0.29210	16.48	0.28	0.063
$\pi(C_1-C_{10})$	1.57736	$\pi^*(C_6-C_8)$	0.27286	17.97	0.29	0.067
		$\pi^*(N_{11}-N_{12})$	0.42736	27.33	0.22	0.070
$\pi(C_2-C_4)$	1.74883	$\pi^*(C_1-C_{10})$	0.47605	18.95	0.28	0.070
$n(C_2-C_4)$	1.74003	$\pi^*(C_6-C_8)$	0.27286	16.25	0.30	0.062
T (C, C)	1.73646	$\pi^*(C_1-C_{10})$	0.47605	16.83	0.28	0.065
$\pi(C_6-C_8)$	1./3040	$\pi^*(C_2-C_4)$	0.29210	19.69	0.28	0.067
. (N.)	1 5 4 4 1 1	$\pi^*(C_1-C_{10})$	0.47605	40.15	0.29	0.097
$n_1(N_{13})$	1.54411	$\pi^*(N_{11}-N_{12})$	0.42736	48.57	0.23	0.096
$\pi^*(C_1-C_{10})$	0.47605	$\pi^*(C_6-C_8)$	0.27286	273.73	0.01	0.080
$\pi^*(N_{11}-N_{12})$	0.42736	$\pi^*(C_1-C_{10})$	0.47605	43.69	0.06	0.066
n ₁ (N ₂₅)	1.89783	$\sigma^*(N_{13}-H_{14})$	0.04604	12.87	0.79	0.092
		$\pi^*(C_{15}-O_{28})$	0.23379	17.33	0.27	0.064
$\pi(C_{16}-C_{17})$	1.61642	$\pi^*(C_{19}-C_{21})$	0.28970	19.83	0.29	0.069
		$\pi^*(C_{23}-N_{25})$	0.35871	18.39	0.27	0.063
(C. N.)	1.72204	$\pi^*(C_{16}-C_{17})$	0.32474	24.99	0.33	0.082
$\pi(C_{23}-N_{25})$	1.72394	$\pi^*(C_{19}-C_{21})$	0.28970	13.01	0.33	0.058
n ₂ (O ₂₆)	1.82224	$\pi * (C_{15}-O_{28})$	0.23379	44.28	0.35	0.112
n (O)	1 94074	$\sigma^*(C_{15}-C_{16})$	0.07667	18.05	0.67	0.100
$n_2(O_{28})$	1.84974	$\sigma^*(C_{15}-C_{26})$	0.09467	32.91	0.61	0.129
$\pi^*(C_{15}-O_{28})$	0.23379	$\pi^*(C_{16}-C_{17})$	0.32474	158.28	0.01	0.072
#(C N)	0.25971	$\pi^*(C_{16}-C_{17})$	0.32474	137.74	0.02	0.078
$\pi^*(C_{23}-N_{25})$	0.35871	$\pi^*(C_{19}-C_{21})$	0.28970	151.39	0.02	0.086

^aE(2) means the energy of hyper conjugative interactions.

4.3.4. Mulliken Population Analysis

The Mulliken atomic charges of PBTA is calculated by the electron population of each atom by using the DFT method with 6-311++G (d,p) basis set. It has a significant influence on dipole moment, polarizability, electronic structure and vibrational modes. In

^bEnergy difference between donor and acceptor i and j NBO orbitals.

^cF(i,j) is the Fock matrix element between i and j NBO orbitals.

the present work, the calculated Mulliken atomic charges of PBTA are plotted in Fig. 4.18. All H atoms are positive, H_{14} and H_{27} atom possesses more positive charge as it takes part in intermolecular hydrogen bonding in the crystal structure. Oxygen atoms O_{26} and O_{28} are highly electronegative. The presence of large amounts of negative charge on oxygen and net positive charge on hydrogen atoms confirms the intermolecular hydrogen bonding takes place in the crystalline solid state. Natural population analysis for PBTA is presented in Table 4.7.

Table 4.7. Natural population analysis (NPA) of PBTA calculated with DFT/B3LYP/6-311++G(d,p) method

Atoms	Natural Charge	Atomic Charge
C_1	0.11826	-0.26621
C_2	-0.22590	-0.22384
H_3	0.20851	0.097723
C_4	-0.19085	-0.21486
H_5	0.20452	0.186879
C_6	-0.22154	-0.17782
H_7	0.20619	0.161255
C_8	-0.18019	0.123996
H_9	0.21825	0.190318
C ₁₀	0.07094	-0.17516
N_{11}	-0.25605	0.195383
N ₁₂	-0.05886	-0.18854
N_{13}	-0.37487	-0.31453
H_{14}	0.45342	0.713181
C_{15}	0.77516	-0.07787
C_{16}	0.09663	-0.27079
C ₁₇	-0.18855	0.292855
H_{18}	0.23966	0.245938
C_{19}	-0.15851	-0.63813
H_{20}	0.21601	0.190762
C_{21}	-0.21056	0.070576
H_{22}	0.21998	0.202108
C_{23}	0.06684	-0.32135
H_{24}	0.21921	0.256696
N ₂₅	-0.47227	0.074478
O_{26}	-0.67535	-0.18814
H ₂₇	0.48694	0.332094
O_{28}	-0.58701	-0.27701
Total	0.00000	0.00000

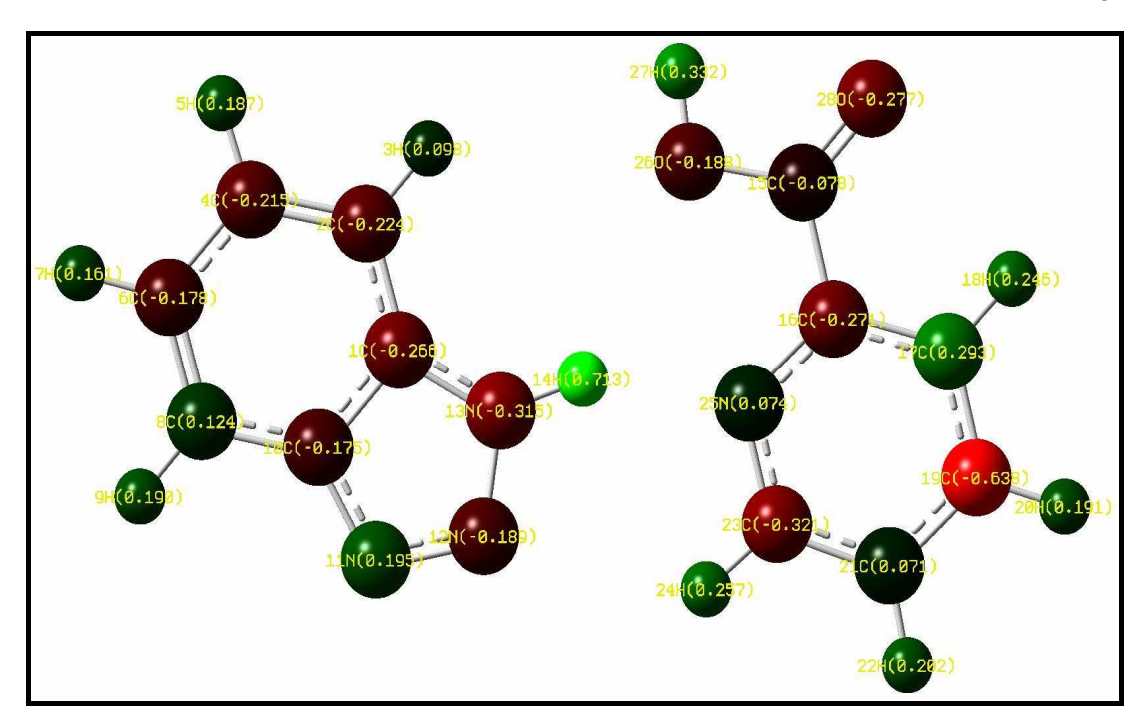


Fig. 4.17. Mulliken atomic charge distribution of PBTA

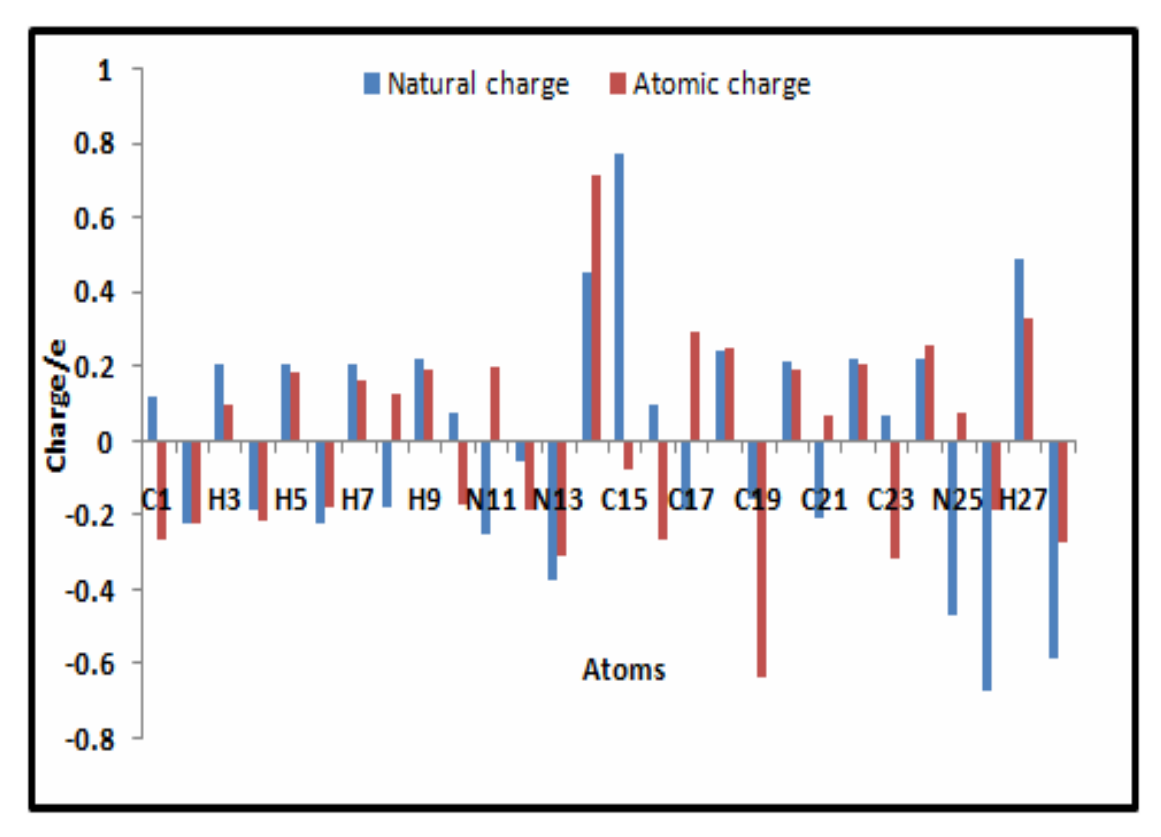


Fig. 4.18. Mulliken atomic charges of all atoms of PBTA

4.3.5. Molecular Electrostatic Potential (MEP)

The electrostatic potential values at the surface are represented in different colors. Fig. 4.19 shows the color code for these maps, which varies from -8.582e-2 (deepest red) to +8.582e-2 (deepest blue). The light blue area depicts an electron deficient zone, whereas the yellow portion depicts an electron rich region. Negatively charged areas are seen surrounding the Cl5 and N12 atoms, as shown in Fig. 4.19 on PBTA. The lack of a maximal negative potential zone in the MEP plot confirms the molecules low chemical reactivity, whereas the existence of a partial negative potential region (yellow color) shows an electron-rich region that is favorable for electrophilic reactivity.

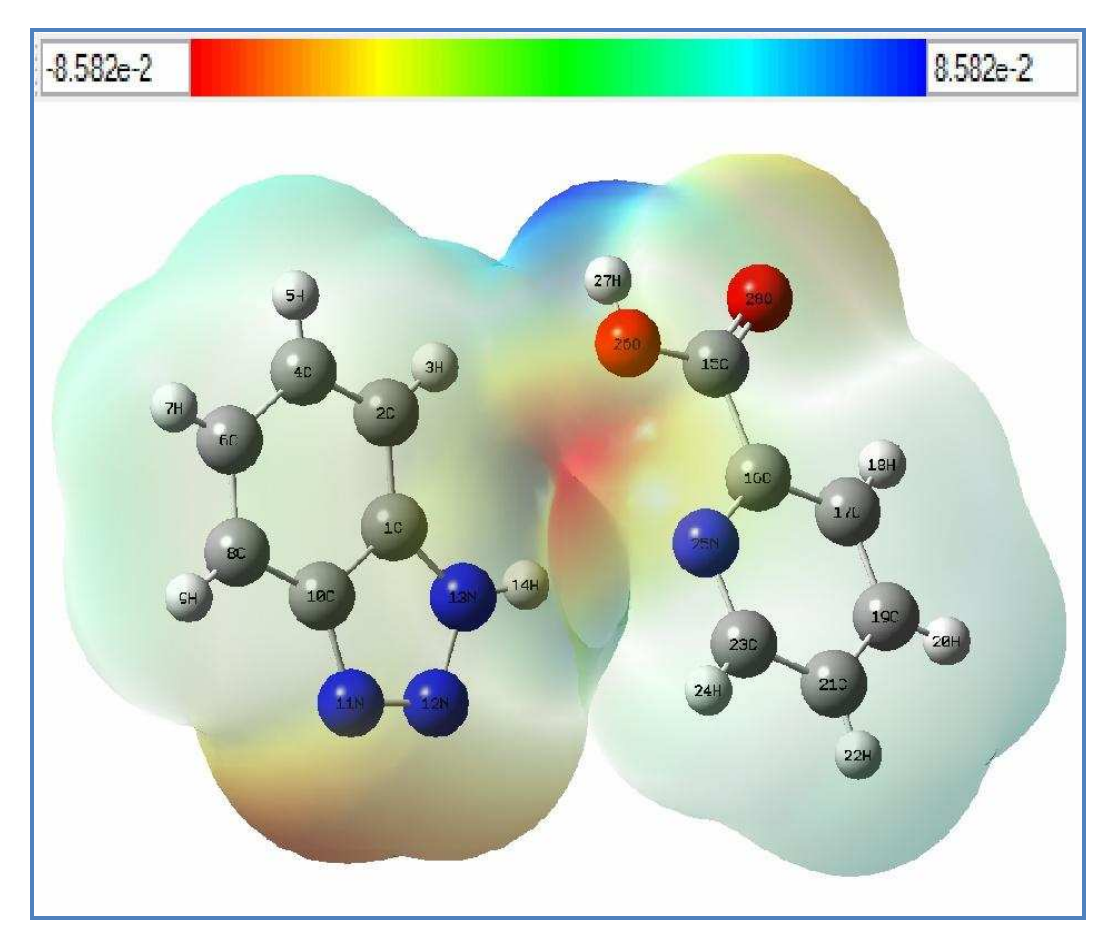


Fig. 4.19. Molecular electrostatic potential of PBTA

4.3.6. Frontier Molecular Orbital Analysis

Frontier molecular orbitals (FMO) are the highest occupied molecular orbitals (HOMOs) and the lowest-lying unoccupied molecular orbitals (LUMOs). FMOs have an important role in optical and electric properties, quantum chemistry, and UV-Vis spectra [26]. The HOMO and LUMO orbitals are the main orbitals involved in chemical reactions. The ability to give an electron is represented by the HOMO, while the ability to gain an electron is embodied by the LUMO as an electron acceptor. The kinetic stability, chemical reactivity, optical polarizability, and chemical hardnesssoftness of a molecule are all regulated by the energy gap between HOMO and LUMO [27]. Using B3LYP/6-311++G, the highest occupied MOs (HOMO) and the lowest unoccupied MOs (LUMO) were estimated (d,p). Figure 4.20 shows 3D plots of the HOMO and LUMO orbitals for the PBTA molecule. The positive phase is represented by red, whereas the negative phase is represented by green. The HOMO is localized on almost the whole benzotriazole, but the LUMO is localized on the2carboxypyridine, as shown in the figure. The HOMO and LUMO have energy separations of -6.55 eV and -2.55eV, respectively. The charge transfer interaction within the molecule is ensured by the HOMO-LUMO energy gap. Table 4.8 shows the results of calculating global reactivity descriptors such as ionization potential (I), electron affinity (A), electrophilicity index (ω), chemical hardness (η), softness (S), chemical potential (μ) and charge transfer (ΔNmax) using the energy of HOMO and LUMO. The estimated chemical potential value is negative (-3.55 eV) and is smaller than the electrophilicity index, which indicates the electron promotes from the nucleophile (HOMO) to the electrophile (LUMO), which provides the chemical reactivity, stability of the molecule [28].

Table 4.8. Calculated quantum chemical molecular orbital properties for PBTA

Parameters	B3LYP/6-311++G(d,p)
HOMO energy, E _{HOMO}	-6.55 eV
LUMO energy, E _{LUMO}	-2.55 eV
HOMO-LUMO energy gap, ΔE _{GAP}	4.00 eV
Ionization potential (I)	6.55 eV
Electron affinity (A)	2.55 eV
Total energy change, ΔE_T	-0.50 eV
Overall energy balance, ΔE	-4.00 eV
Electronegativity, χ	4.55 eV
Chemical hardness (η)	2.00 eV
Chemical potential (µ)	-3.55 eV
Electrophilicityindex (ω)	3.15 eV
Softness (S)	0.50 eV^{-1}
SCF energy	$-2.19 \times 10^6 \text{kJ mol}^{-1}$

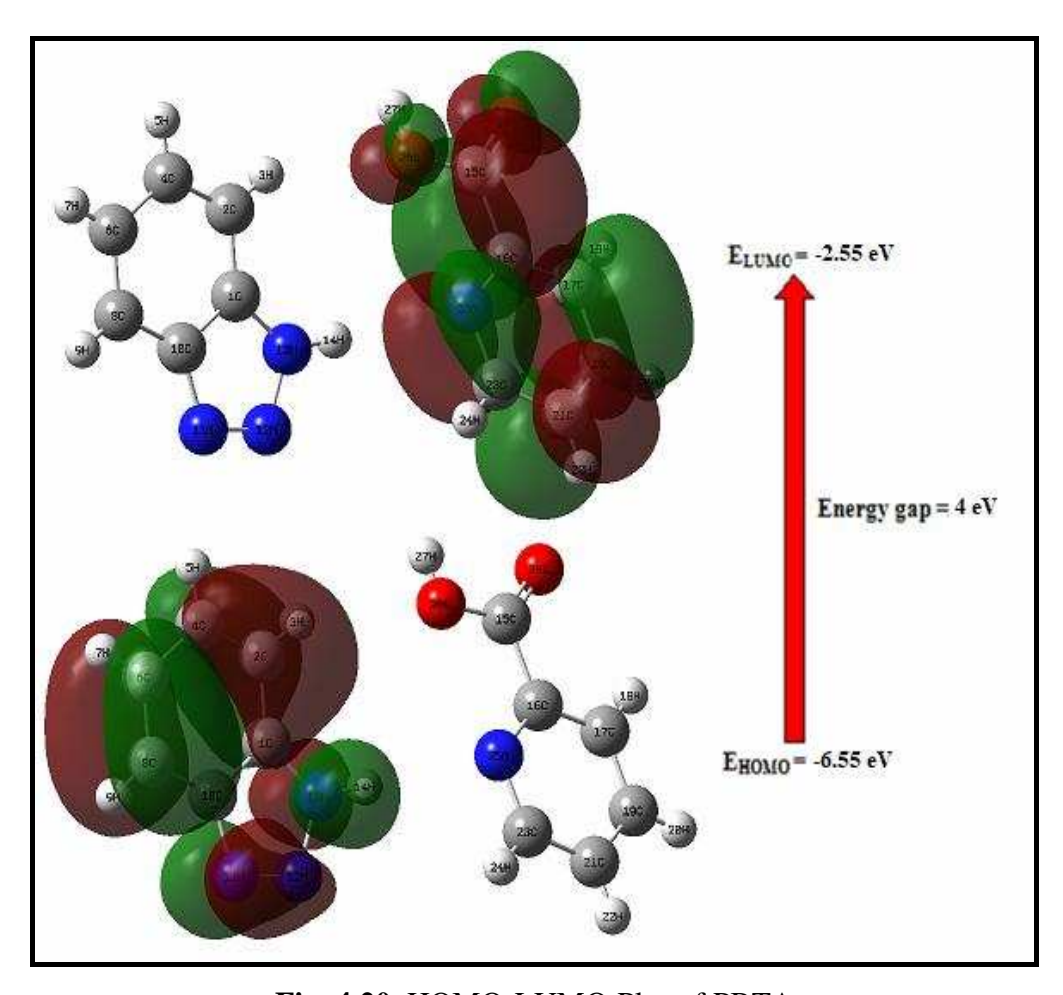


Fig. 4.20. HOMO-LUMO Plot of PBTA

4.3.7. Vibrational Spectral Analysis

The DFT/B3LYP/6-311++G(d,p) basis set was used to carry out the various PBTA crystal assignments. The FTIR spectrum was recorded using a Perkin Elmer Spectrum II FTIR spectrometer in the scan range 4000–400 cm⁻¹. Table 4.9 shows the experimental frequencies and their related assignments, which were compared to theoretically computed assignments, and Fig. 4.21 shows the computed and experimental FTIR spectra.

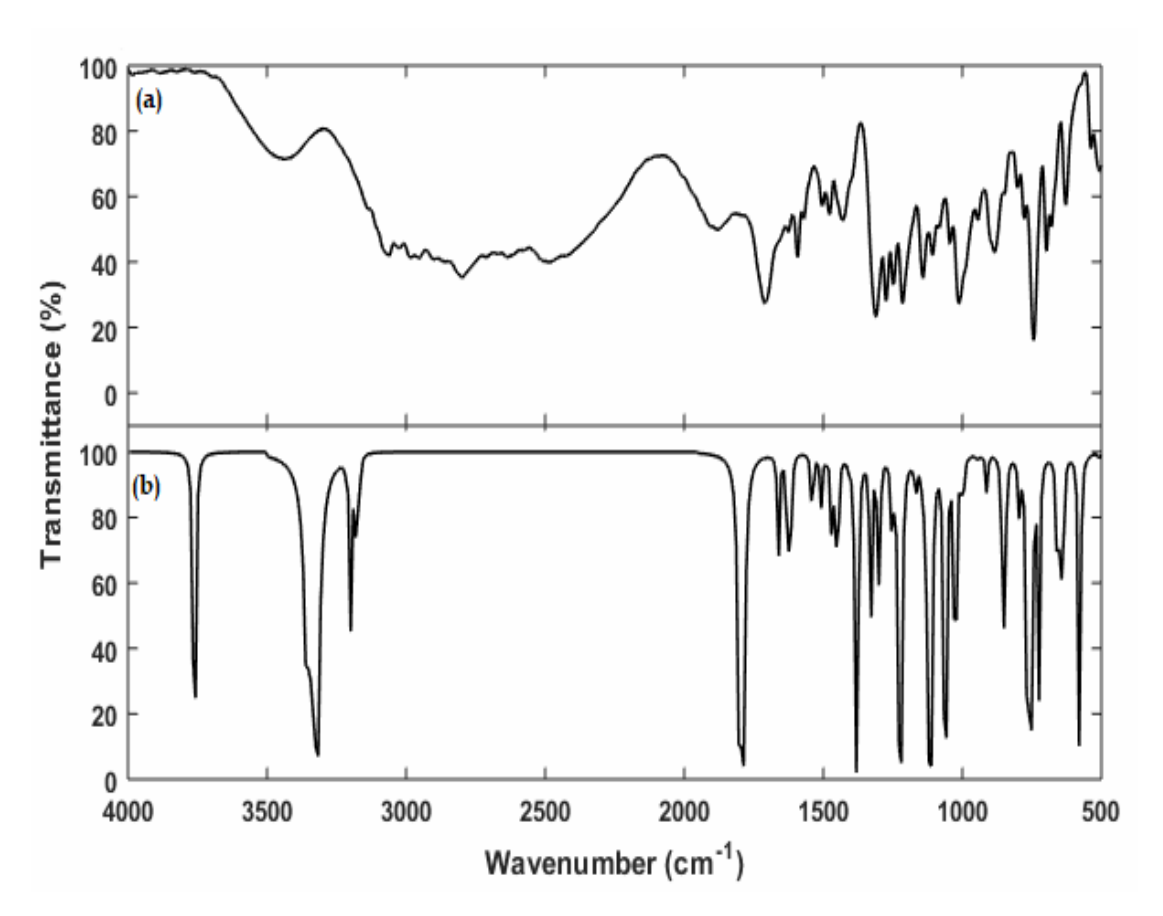


Fig. 4.21(a). FTIR spectra of PBTA (b) computed IR spectra of PBTA

C-H vibrations

The aromatic C-H stretching vibrations are observed at 3061 and 2983cm⁻¹. C-H deformation is observed at 1274 cm⁻¹. The absorption bands coming from C-H out of plane bending vibrations are detected in the region at 743, and 697 cm⁻¹, while its calculated wavenumber is observed in the region at 751 cm⁻¹.

N-H Vibrations

The broad frequency at 3437 cm⁻¹ is due to the N-H asymmetric stretching vibrations, while it's computed wavenumber is observed at 3334 cm⁻¹. The peaks appeared at 2797, 2634, 2483 and 1877 cm⁻¹ correspond to the symmetry stretching due to NH⁺ salt. The N-H bending vibrations are responsible for the absorption peak at 1477 cm⁻¹ and it is in close agreement with calculated wavenumber 1480 cm⁻¹. The peak appeared at 628 cm⁻¹ corresponds to N-H wagging and it agrees with computed wavenumber 643 cm⁻¹.

O-H Vibrations

The O-H stretching vibrations of water molecules have been ascribed to a strong band detected in PBTA at 3437 cm⁻¹, while its computed wavenumber is observed at 3334 cm⁻¹.

Ring Vibrations

The C=O stretching is shown in PBTA as a very strong band at 1708 cm⁻¹. At 1625 cm⁻¹, the aromatic ring C=C stretching vibrations were found which is close agreement with computed wavenumber 1624 cm⁻¹. C-N asymmetric stretching vibration is assigned a frequency of 1310 cm⁻¹ for experimental IR, whereas 1300 cm⁻¹ for calculated spectra. The absorption peak at 1247 cm⁻¹ is C-O symmetry stretching vibration absorption peak. At 1214 cm⁻¹, the C-N stretching mode of the pyridine ring is detected. At 1012 cm⁻¹, a very strong band of the C-C in-plane bending mode may be seen.

Table 4.9. Experimental and calculated vibrational wavenumbers and fundamental bands positions assignments of PBTA

Calculated wavenumber (cm ⁻¹)	Experimental wavenumber (cm ⁻¹) ^[8]	Experimental wavenumber (cm ⁻¹) Present work	Vibrational Assignments
3334	3427	3437	O-H and N-H stretching
1795	1708	1708	C=O stretching vibration
1624	1626	1625	C=C stretching
1543	1593	1592	asymmetric vibrations of carboxylate ions COO-
1480	1478	1477	N-H bending vibrations
1453	1426	1430	symmetric vibrations of carboxylate ions COO-
1300	1310	1310	C–N asymmetric stretching
-	1275	1274	C-H deformation
1255	1243	1247	C-O symmetry stretching vibration
1219	1211	1214	C–N symmetric stretching
-	1139	1141	N-N stretching vibration of benzotriazolium salt
1120	1108	1107	C-C stretching
1030	1008	1012	C-C bending
922	974	944	C-H wagging
850	884	883	C-N deformation
751	741	743	C-H out of plane bending
-	692	697	C-H out of plane bending
643	624	628	N-H wagging
-	501	507	COO- rocking

4.3.8. Hirshfeld Surface Analysis

The Hirshfeld surface analysis is a progressive technique used for measuring intermolecular interactions by consideration of the interactions throughout the molecule [29,30]. The Hirshfeld surface of PBTA is displayed in Fig. 4.22, showing surfaces that have been mapped over a dnorm, de, di, and curvedness. The dominant

interactions such as O···H can be seen in surface plots as the bright red area. The red color spots on the surface indicate the close contacts. In the fingerprint region (Fig. 4.23), the H···H/H···H interactions (35.3%) are spotted in the middle of the plot whereas the N···H/H···N contacts contribute 20.6% represented by a pair of spikes in the bottom area. The O···H/H···O interactions contribute 15.6%. Weak interactions are identified as C-H (12.4%), C-C (7.2%), C-N (5.1%), C-O (1.9%), N-N (1.3%) and O-O (0.7%). The strong interactions occupy more space and weak ones occupy less space in the finger print region. The combination of de and di in the form of a 2D fingerprint plots provides a summary of intermolecular contacts in the crystal.

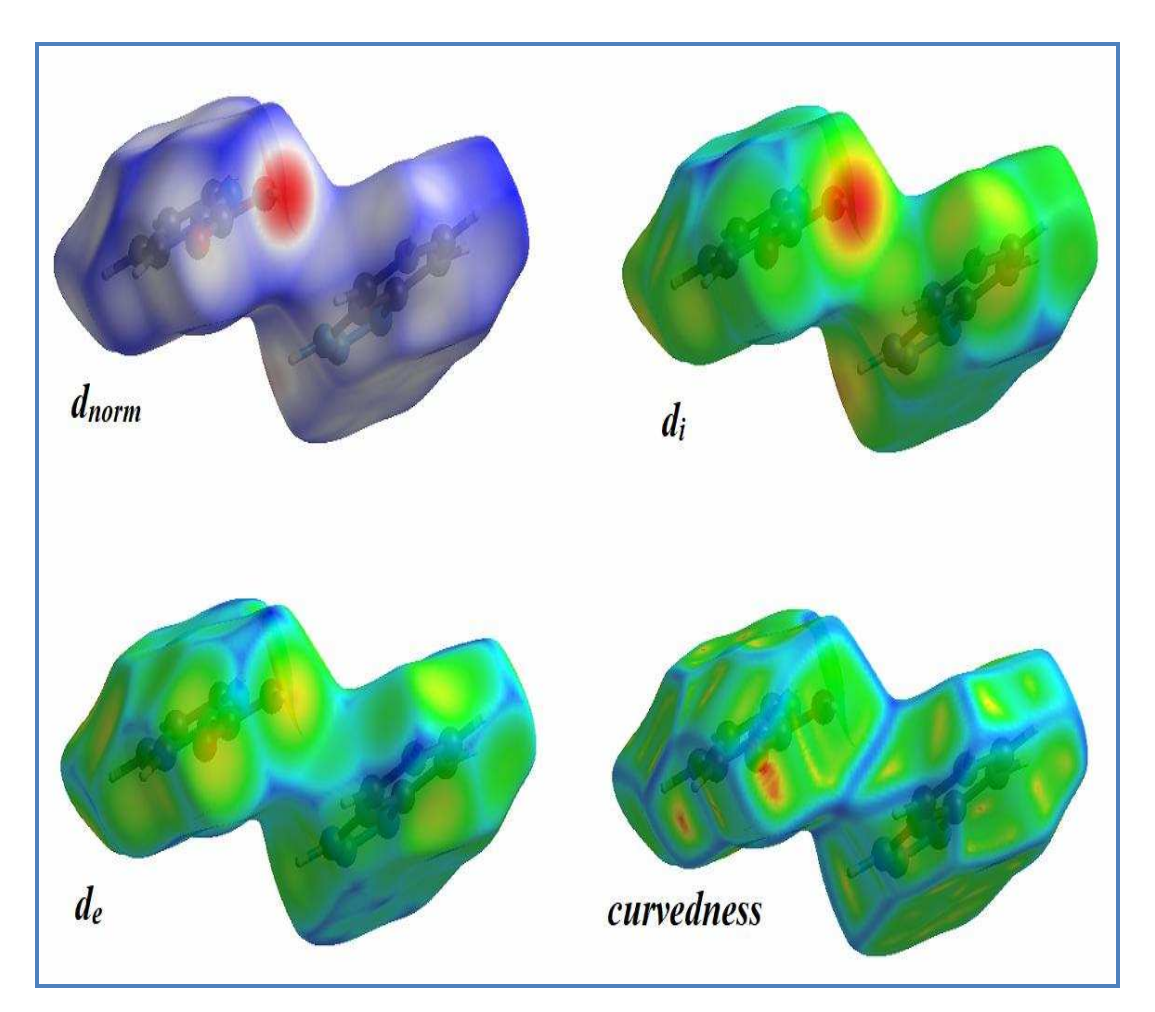


Fig. 4.22. Hirshfeld surfaces for d_{norm}, d_i, d_e and curvedness for the PBTA molecule

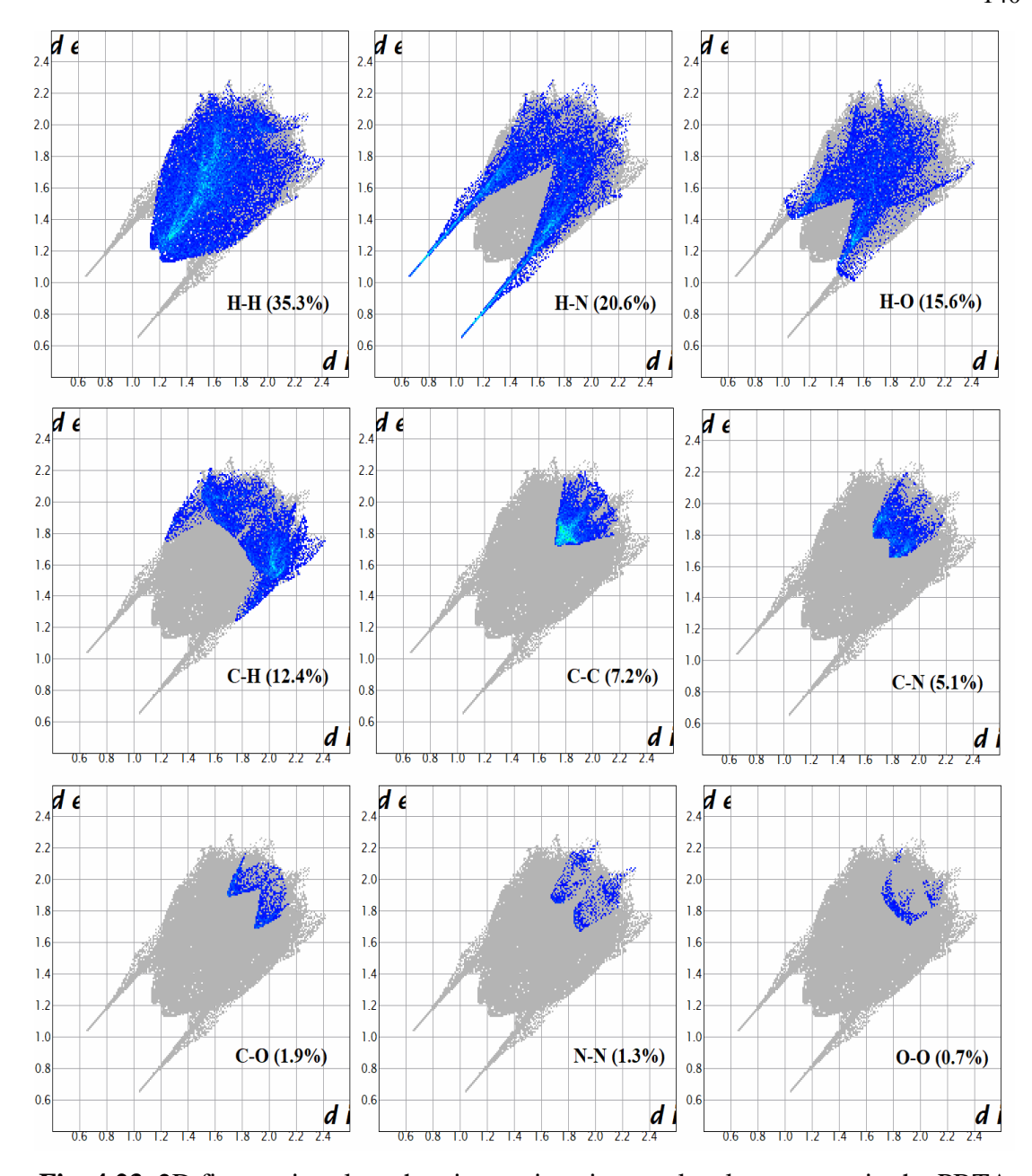


Fig. 4.23. 2D fingerprint plots showing various intermolecular contacts in the PBTA

4.4. CONCLUSIONS

The solubility studies of grown PBTA crystals indicate it has positive coefficient of solubility. Nucleation parameters of crystallization process such as interfacial energy (σ), volume of free energy (ΔG_v), critical energy barrier for nucleation (ΔG^*), radius of the critical nucleus (r^*) and nucleation rate (J) of the PBTA crystals are determined from the Classical nucleation theory. MZW can be obtained theoretically

with the help of solubility-enthalpy relation. Single crystals of PBTA were grown by adopting slow evaporation method at room temperature. The powder X-ray diffraction analysis confirmed the non-centrosymmetric space group and crystallinity of the grown crystals. Crystal size and strain due to lattice distortion were determined by the W-H approach. UV-Vis analysis exhibits the absence of absorption in the visible region. The energy band gap value determined using Tauc's plot is 3.49 eV and band gap value calculated using the DASF approach is 3.46 eV. The fluorescence spectrum indicates the crystals blue emission property. The second harmonic output power of the grown crystal is 2.2 times greater than KDP. Vickers microhardness test reveals the reverse indentation nature of the material. The DFT calculations were performed for the PBTA crystal to optimize structure and evaluate the first order hyperpolarizability, ICT interations through NBO, mulliken charges, molecular electrostatic potential, HOMO-LUMO energy gap and vibrational analysis. The calculated value of hyperpolarizability for the PBTA compound is 1.77×10^{-30} esu and energy gap of HOMO-LUMO is 4 eV. Hirshfeld surface analysis and 2-dimensional finger print plot quantify the interactions associated with PBTA molecule. From the above studies it is evident that PBTA crystals have good characteristics for fabrication and the results of optical transparency are suggesting the material with potential applications in nonlinear optics.

REFERENCES

- V. Siva Shankar, R. Sankar, R. Siddheswaran, R. Jayavel, P. Murugakoothan, Growth and characterization of tetra l-lysine alanine mono hydrochloride dihydrate (TLAMHCl), a new semiorganic nonlinear optical single crystal, Mater. Chem. Phys. 109 (2008) 119–124.
- N.Vijayan, J.Philip, D.Haranath, Brijesh Rathi, G.Bhagavannarayana, S.K. Halder,
 N.Roy, M.S.Jayalakshmy, SunilVerma, Spectrochim. Acta A Mol. Biomol.
 Spectrosc., 112 (2014) 309-314.
- 3. R. Mohan Kumar, D. RajanBabu, D. Jayaraman, R. Jayavel, K. Kitamura, J. Cryst. Growth, 275 (2005) e1935–e1939.
- 4. G. Peramaiyan, P. Pandi, N. Vijayan, G. Bhagavannarayana, R. Mohan Kumar, Crystal growth, structural, thermal, optical and laser damage threshold studies of 8-hydroxyquinolinium hydrogen maleate single crystals, J. Cryst. Growth, 375 (2013) 6-9.
- B.M. Sornamurthy, G. Peramaiyan, P. Pandi, S. Das, G. Bhagavannarayana,
 V.Manivannan, R. Mohan Kumar, Studies on the growth, thermal and optical properties of 4-aminopyridinium p-aminobenzoate dihydrate single crystals, J.
 Cryst. Growth, 397 (2014) 1-5.
- A. Silambarasan, M. Krishna Kumar, A. Thirunavukkarasu, R. MohanKumar,
 P.R. Umarani, Synthesis, crystal growth, solubility, structural, optical, dielectric and microhardness studies of Benzotriazole-4-hydroxybenzoic acid single crystals,
 J. Cryst. Growth, 420 (2015) 11–16.
- 7. T. Dhanabal, G. Amirthaganesan, M. Dhandapani, S. K. Das, Synthesis, structural, thermal and nonlinear optical characterization of benzotriazolinium picrate crystals, Optik, 124 (2013) 1966-1970.

- 8. A. Thirunavukkarsu, T. Sujatha, P.R. Umarani, M.Nizam Mohideen, A. Silambarasan, R. Mohan Kumar, Growth aspects, structural, optical, thermal and mechanical properties of benzotriazole pyridine-2-carboxylic acid single crystal, J. Cryst. Growth, 460 (2017) 42-47.
- 9. R.C. Medrud, The crystal structure of ninhydrin, Acta Cryst. B 25 (1969) 213–220.
- J. Zhang, Y. Zhang, K.W. Xu, V. Ji, General compliance transformation relation and applications for anisotropic hexagonal metals, Solid State Commun., 139 (2006) 87-91.
- 11. Sonia, N. Vijayan, Medha Bhushan, Kanika Thukral, Rishabh Raj, K. K. Maurya, D. Haranath, S. A. Martin Britto Dhas, Growth of a bulk-size single crystal of sulphamic acid by an in-house developed seed rotation solution growth technique and its characterization, J. Appl. Cryst., 50 (2017) 763–768.
- J.L.W. Warwick, N.G. Jones, K.M. Rahman, D. Dye, Lattice strain evolution during tensile and compressive loading of CP Ti, Acta Materialia, 60 (2012) 6720-6731.
- 13. Tsunekawa, Tetsuya, Tetsuya Gotoh, Masao Iwamoto, New organic non-linear optical crystals of benzylidene-aniline derivative, Chem. Phys. Lett., 166 (1990) 353-357.
- 14. Dariush Souri, Kobra Ahmadian, Ali Reza Khezripour, Optical Properties of ZnSe Nanocrystals (NCs) Prepared by Microwave Irradiation Method at Different pH and Different Irradiation Times. J. Electron. Mater., 47 (2018) 6759–6766
- 15. S. Gowri, T. Uma Devi, S. Alen, D. Sajan, C. Surendra Dilip, G. Vinitha, Synthesis, crystal structure, optical and third order nonlinear optical properties of phosphoric acid pyridine-1-ium-2-carboxylate, Mater Sci: Mater Electron 29 (2018) 19710–19723.

- 16. Anton Iurchenko, Jarosław Borc, Keshra Sangwal, Alexei Voronov, Microindentation deformation of lithium dihydrogen phosphate single crystals: Microhardness measurement and indentation size effect, Mater. Chem. Phys., 170 (2016) 276-284.
- 17. C. Ramki, R. Ezhil Vizhi, Study on the mechanical properties of potassium sodium hydroxide borate hydrate (KSB) single crystals by using Vickers microhardness tester, Mater. Lett., 215 (2018) 165-168.
- P. Jayaprakash, M. Peer Mohamed, P. Krishnan, M. Nageshwari, G. Mani,
 M. Lydia Caroline, Growth, spectral, thermal, laser damage threshold, microhardness,
 dielectric, linear and nonlinear optical properties of an organic single crystal:
 L-phenylalanine DL-mandelic acid, Phys. B: Condens. Matter, 503 (2016) 25-31.
- R. Hanumantharao, S. Kalainathan, Microhardness and SHG efficiency of pure and picric acid-added KDP crystals, Bull Mater Sci 44 (2021) 105.
- 20. Sagadevan Suresh, Growth, optical, mechanical, dielectric and theoretical properties of picolinium maleate NLO single crystal, Optik, 125 (2014) 2826–2829.
- 21. Hasan Tanak, Crystal Structure, Spectroscopy, and Quantum Chemical Studies of (E)-2-[(2-Chlorophenyl)iminomethyl]-4-trifluoromethoxyphenol, J. Phys. Chem. A, 2011, 115, 47, 13865–13876.
- S.S. Kumar, S. Athimoolam, B. Sridhar, XRD, vibrational spectra and quantum chemical studies of an anticancer drug: 6-Mercaptopurine, Spectrochim. Acta A Mol. Biomol. Spectrosc., 2015 (146) 204–213.
- 23. P.K. Devi, K. Venkatachalam, M. Poonkothai, Spectroscopic, optical, thermal, antimicrobial and density functional theory studies of 4-aminopyridinium 4-hydroxy benzoate hydrate crystal, J. Mol. Struct., 1119 (2016) 462–471.

- D. Sajan, H. Joe, V.S. Jayakumar, J. Zaleski, Structural and electronic contributions to hyperpolarizability in methyl p-hydroxy benzoate, J. Mol. Struct. 785 (2006) 43-53.
- 25. M Arivazhagan., J. Senthilkumar, Vibrational assignment, HOMO LUMO, first- hyperpolarizability and Mulliken's charge analysis of 2,7-dinitrofluorene, Ind. J. Pure Appl. Phys., 50 (2012) 363 373.
- 26. R. John Xavier, P. Dinesh, Spectroscopic (FTIR, FT-Raman, 13C and 1H NMR) investigation, molecular electrostatic potential, polarizability and first-order hyperpolarizability, FMO and NBO analysis of 1-methyl-2-imidazolethiol, Spectrochim. Acta A Mol. Biomol. Spectrosc., 118 (2014) 999-1011.
- 27. M. Prabhaharan, A.R. Prabakaran, S. Gunasekaran, S. Srinivasan, DFT studies on vibrational spectra, HOMO–LUMO, NBO and thermodynamic function analysis of cyanuric fluoride, Spectrochim. Acta A Mol. Biomol. Spectrosc., 136 (2015) 494-503.
- 28. H. Nalini, V. Charles Vincent, G. Bakiyaraj, K. Kirubavathi, K. Selvaraju, Crystal growth, structural, optical and theoretical investigations of organic nonlinear optical crystal: 2-naphthalenol, Mol. Cryst. Liq. Cryst., 712 (2020) 43-61
- 29. F. Mary Anjalin, N. Kanagathara, M.K. Marchewk, V. Mohan kumar, Crystal structure, Hirshfeld surface analysis and vibrational spectral studies on P-nitroanilinium p-toluene sulphonate single crystal, J. Mol. Struct., 1183 (2019) 78-86
- 30. M. Manikandan, P. Rajesh, P. Ramasamy, Crystal growth, structural, optical, vibrational analysis, Hirshfeld surface and quantum chemical calculations of 1, 3, 5-triphenylbenzene single crystal, J. Mol. Struct., 1195 (2019) 659-669.

Chapter-V

Experimental and Theoretical Investigations of Nonlinear Optical Crystal 2-Picolinic Hydrochloride

CHAPTER - V

EXPERIMENTAL AND THEORETICAL INVESTIGATIONS OF NONLINEAR OPTICAL CRYSTAL 2-PICOLINIC HYDROCHLORIDE

5.1. INTRODUCTION

In recent years, there has been a lot of interest in exploring NLO crystals with good suitable properties because of their numerous applications in frequency conversion, optical communications, image processing, optical computing, and data storage devices [1,2]. Third order nonlinear optical materials (NLO) with weak nonlinear absorption (NLA) but substantial nonlinear refraction (NLR) have attracted a lot of attention because of their potential usage in optical signal processing systems [3]. The Z-scan technique is a prominent approach for determining a material optical nonlinearity. It is used to measure the third order NLO characteristics and has the advantages of great sensitivity and simplicity [4]. The magnitude and sign of nonlinear refraction and nonlinear absorption, which are related with the real part $Re(\chi^3)$ and imaginary part $Im(\chi^3)$ of the third order nonlinear susceptibilities, can be measured simultaneously. To attain enhanced physical properties, new materials are created by combining organic and inorganic materials, which are referred to as semiorganic materials. Such semiorganic materials have strong mechanical strength, thermal conductivity, and nonlinear coefficient, and can be used for laser production, optical data processing, and optical limitations [5,6]. Semiorganic materials, according to the literature, exhibit substantial nonlinearity similar to organic materials while having superior mechanical and thermal durability than inorganic materials [7,8]. Though a number of compounds have been developed and reported for NLO applications, such as orthophosphoric acid, hydrochloric acid, L-tartaric acid, maleic acid, and picolinic acid (also known as pyridine-2-carboxylic acid, 2-pyridine carboxylic acid and 2-picolinic acid), there has been few research on

picolinic based compounds [9-14]. As a result, the purpose of this research work is to develop 2-picolinic hydrochloride (PHCL) single crystal and investigate its behavior using both experimental and theoretical methods. Despite the fact that the PHCL compound has been reported before [12-14], this study focuses on DFT calculations and third order nonlinear optical behavior, as well as structural, optical, and microhardness characteristics.

5.2. EXPERIMENTAL ANALYSIS

5.2.1. Solubility Study

The solubility studies were carried out for various temperatures (303 K to 318 K). Fine powder of 2-picolinic hydrochloride was dissolved in deionized water at 303 K and the solution was continuously stirred until an equilibrium concentration of the solution was obtained. After attaining saturation condition, undissolved material precipitated in the beaker. The solubility was found by gravimetric analysis (Fig. 5.1). The same method was repeated to determine the solubility for various temperatures from 303 K to 318 K. The concentration of solute increases for increasing temperature which shows that the PHCL compound has a positive temperature coefficient of solubility.

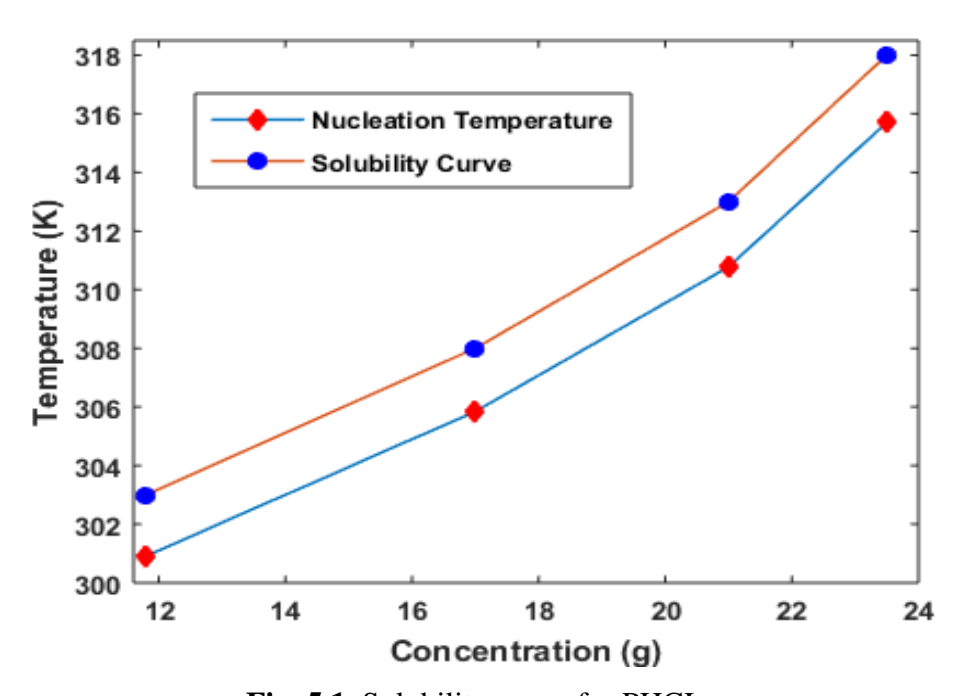


Fig. 5.1. Solubility curve for PHCL

5.2.2. Nucleation Kinetics and Metastable Zone Width (MZW)

The interfacial energy of the interface between the growing crystal and the surrounding mother phase plays an important role in the nucleation of crystals. Bennema and Sohnel [15] based on the regular solution theory have derived an expression for the relationship between the interfacial energy and solubility. The present research work outline, relation between solubility and interfacial energy is used for the calculation and its variation with temperature is tabulated. Nucleation thermodynamical parameters are calculated based on interfacial energy and are shown in Table 5.1, which provides a detailed understanding of the nucleation process of solution growth as well as the growth of optical quality crystals. With an increase in supersaturation ratio, the critical free energy barrier, the critical radius of the nucleus, and the number of molecules present in the critical nucleus of the formed crystal were decreased. Fig. 5.2 shows how the variation in energy barrier (ΔG^*) reduces as supersaturation and temperature increase.

Fig. 5.3 shows the radius of the critical nucleus as a function of supersaturation. At different supersaturation ranges (1.1-1.4) for 303K, the critical free energy barrier (ΔG^*) and critical radius (r^*) of PHCL were estimated to be 1.16×10^{-19} to 9.30×10^{-20} and (r^*) 6.23 nm to 1.77 nm, respectively. Because it is a direct measure of the stability of the solution in its supersaturated region, the metastable zone width is an important metric for the formation of excellent crystals from the solution. The current study entails providing theoretically calculated values of metastable zone width for crystallization temperatures of crystals using the slow evaporation method. The metastable zone width broadens slightly as temperature rises, according to the findings.

Table 5.1. Nucleation Tab	e from PHCL for Super	Saturation Ratio-1.1
----------------------------------	-----------------------	----------------------

T (K)	$\Delta G_{\rm v}(~{ m J/m}^3)$	$\sigma (J/m^2)$	$\Delta \mathbf{G}^{*}(\mathbf{J})$	r* (m)	i [*]	J (nuclei/m³/sec)
303	-2286473.7	0.007126	1.16E-18	6.23E-09	5817.940	1.01572E+13
308	-2324204.3	0.006443	8.29E-19	5.54E-09	4093.527	8.03516E+12
313	-2361934.9	0.006076	6.74E-19	5.15E-09	3271.979	6.92049E+12
318	-2399665.5	0.005919	6.03E-19	4.93E-09	2883.380	6.36108E+12

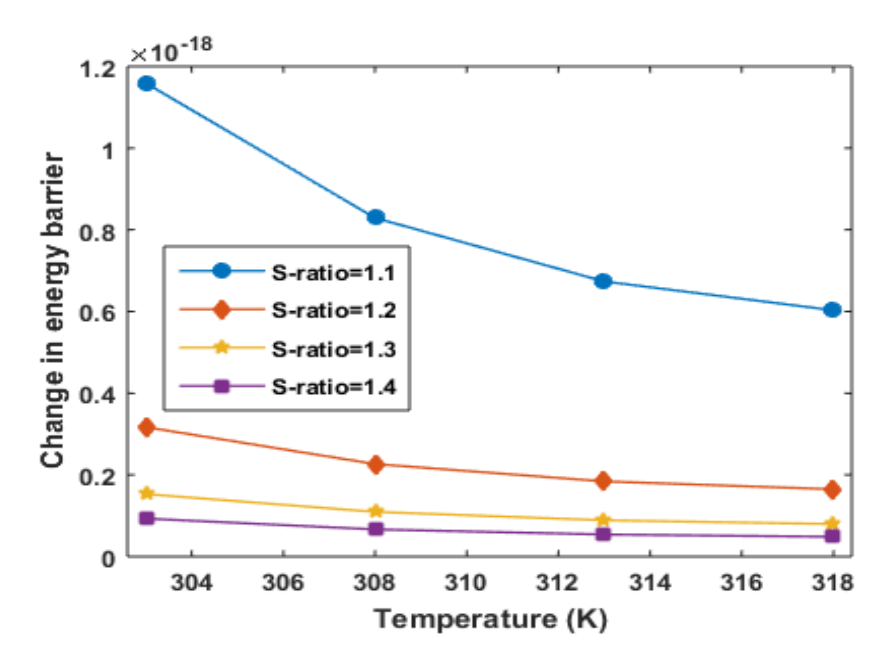


Fig. 5.2. Variation of Gibbs free energy with supersaturation and temperature for PHCL

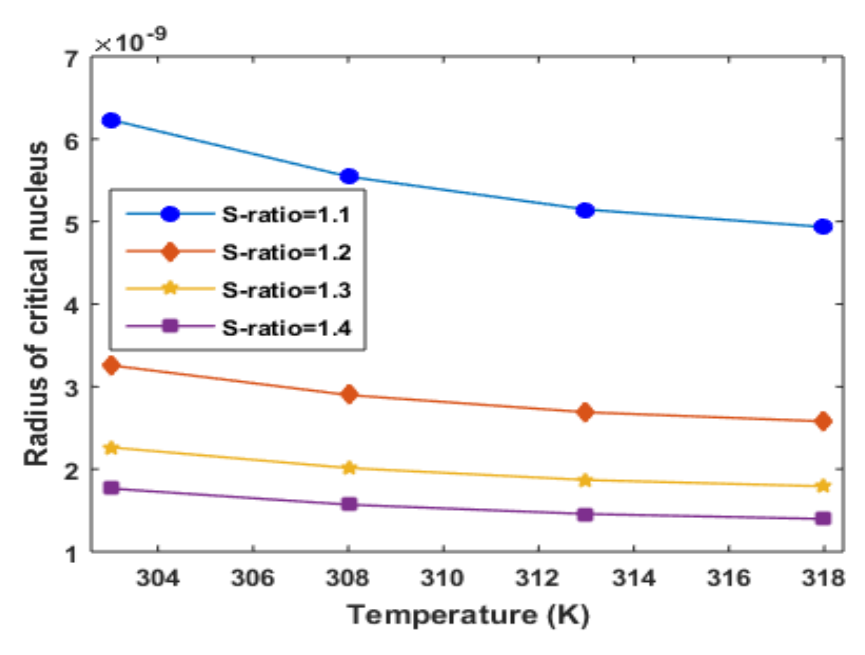


Fig. 5.3. Variation of radius of critical nucleus with temperature and supersaturation ratio of PHCL

5.2.3. Growth of PHCL Crystal

The raw materials for the growth of PHCL crystals were commercially available 2-carboxypyridine and hydrochloric acid. The raw materials were taken in an equimolar ratio and subjected to repeated crystallisation processes with distilled water as a solvent during the purification process. The solution was tightly closed after high-quality filtering to control solvent evaporation. Following the slow evaporation of the solvent, nicely shaped and transparent single crystals were harvested in 3 weeks. Fig. 5.4 depicts the single crystals that have grown.

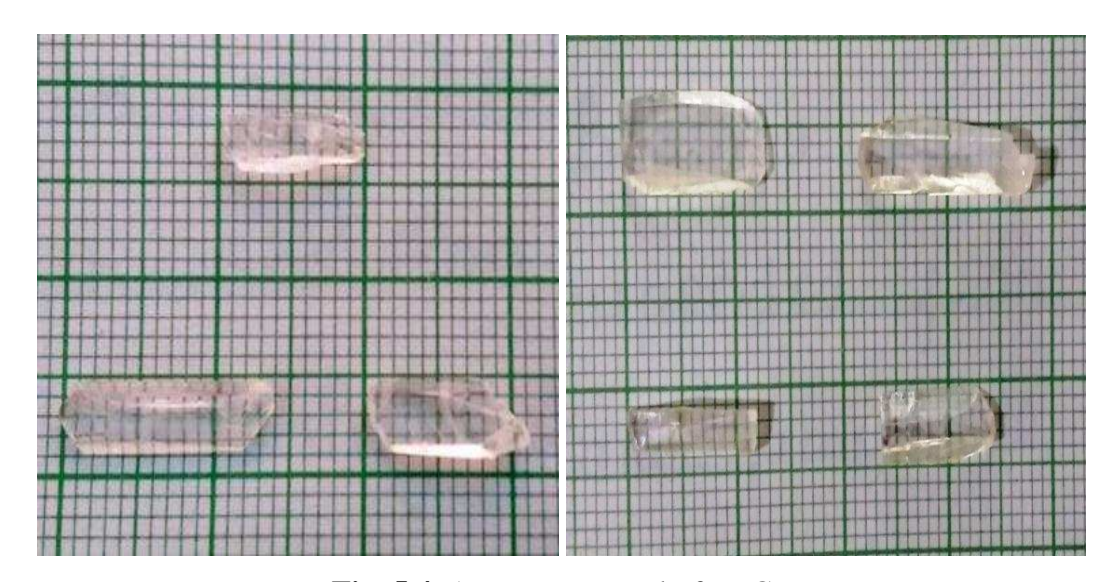


Fig. 5.4. As grown crystal of PHCL

5.2.4. Powder XRD

The powder XRD spectrum of the PHCL single crystal with discrete and pointed peaks using BRUKER X-ray diffractometer with CuK α radiation (λ = 1.5406 Å) and a step size of 0.0130 and a scanning step time of 23.97s, reveals its crystallinity and is shown in Fig.5.5. The PHCL crystal lattice parameters are a = 13.778 (32) (Å), b = 6.519 (14) (Å), c = 7.702 (19) (Å), $\alpha = \beta = \gamma = 90^{\circ}$ and volume = 691.916 (27) (Å³), orthorhombic system with space group *Pnma*, as determined using Fullprof Suite program. It agrees very much with the reported values [14].

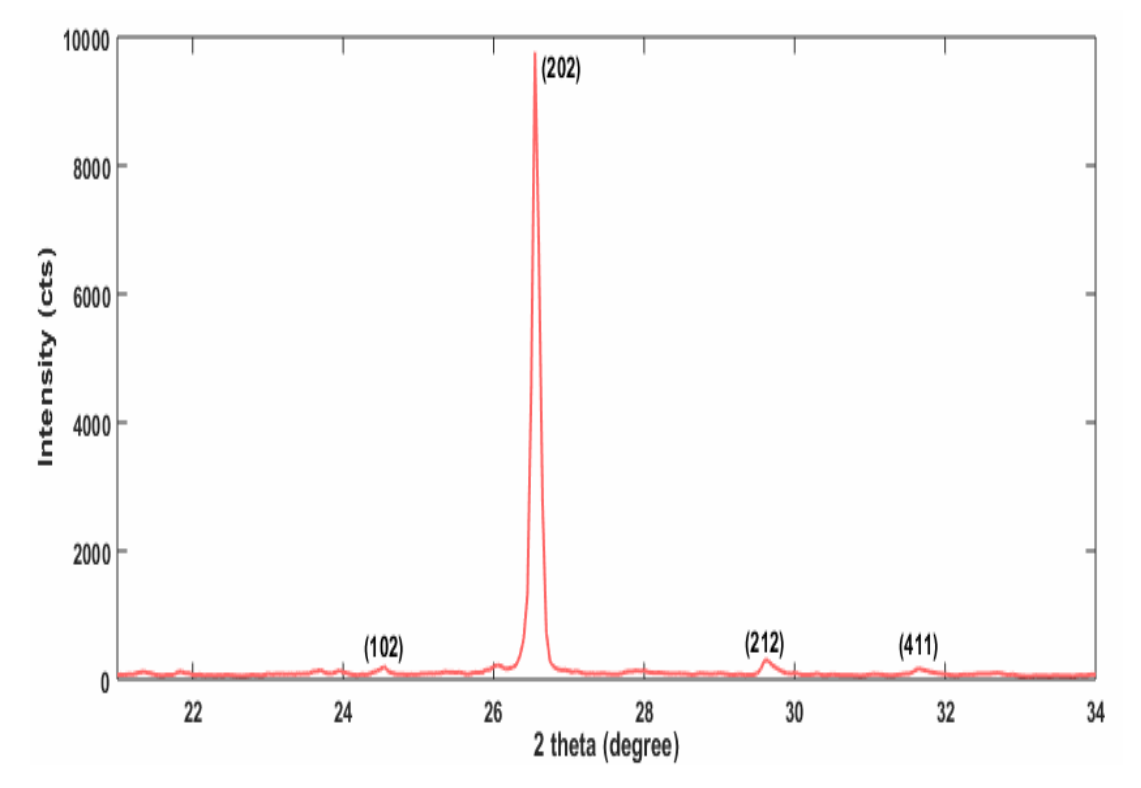


Fig. 5.5. Powder XRD pattern of PHCL crystal

The structure parameters namely; lattice strain and crystal size was obtained by Williamson–Hall equation [16]:

$$\beta \cos \theta = \frac{K\lambda}{\tau} + \eta \sin \theta \qquad ... (5.1)$$

where, β - FWHM of the diffraction peak (rad); θ - Bragg's diffraction angle (rad); K - Scherrer constant; λ - wavelength of the X-rays (Å); τ - crystallite size (μ m); η - lattice strain.

The strain and crystal size can be obtained from the slope and the intercept of the plot obtained from the relation between $\beta\cos\theta$ and $\sin\theta$ for PHCL crystal. Fig. 5.6 shows the Williamson-Hall plot for PHCL crystal. The crystallite size (τ) value is ~0.11 µm and lattice strain, $\eta = 0.0033$. Because the value of is minimum in the PHCL crystal, it has less lattice strain, implying a higher elastic stiffness constant [17].

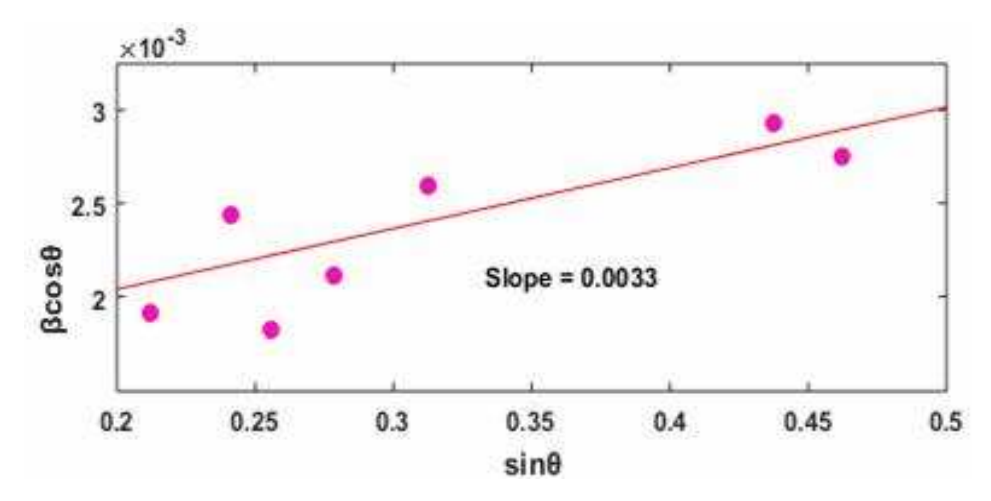


Fig. 5.6. Graph plotting $\beta\cos\theta$ versus $\sin\theta$

5.2.5. UV-vis-DRS Analysis

(a) By Tauc's Plot

The optical absorption spectrum was acquired using a SHIMADZU/ UV 2600 Spectrophotometer in the range of 220-1100 nm. For optical applications, the crystal must have a high degree of transparency and minimal absorption over a wide wavelength range. The UV spectrum is a crucial component for identifying nonlinear optical materials. Fig. 5.7 depicts the absorption spectrum of PHCL crystal. At 267 nm, it shows the greatest absorption peak. The grown crystal exhibits a low absorbance across the visible range, indicating that it is of good crystal quality. The band gap energy of the grown crystal was calculated by extrapolating the linear component near the energy axis from the plot $(\alpha h v)^2$ vs hv (Fig. 5.8a). The band gap of PHCL crystals is determined to be 3.80 eV from the x-intercept, indicating that they are suitable for immediate optoelectronic use.

When examining optical materials for optical device manufacture, the optical constants such as band gap energy, extinction coefficient, and refractive index are all important, so they are determined using equations 2.5 to 2.8 from chapter-II. At a wavelength of 800 nm, the computed values of refractive index (n), electric susceptibility (χ_C), real (ϵ_r) and imaginary (ϵ_i) dielectric constants at $\lambda = 800$ nm, are 1.03, 0.086, 1.080 and 4.900 \times 10⁻⁸, respectively, based on the optical constants.

PHCL is a good material for optoelectronic device applications because of its wide band gap, high transmittance, and low cutoff value.

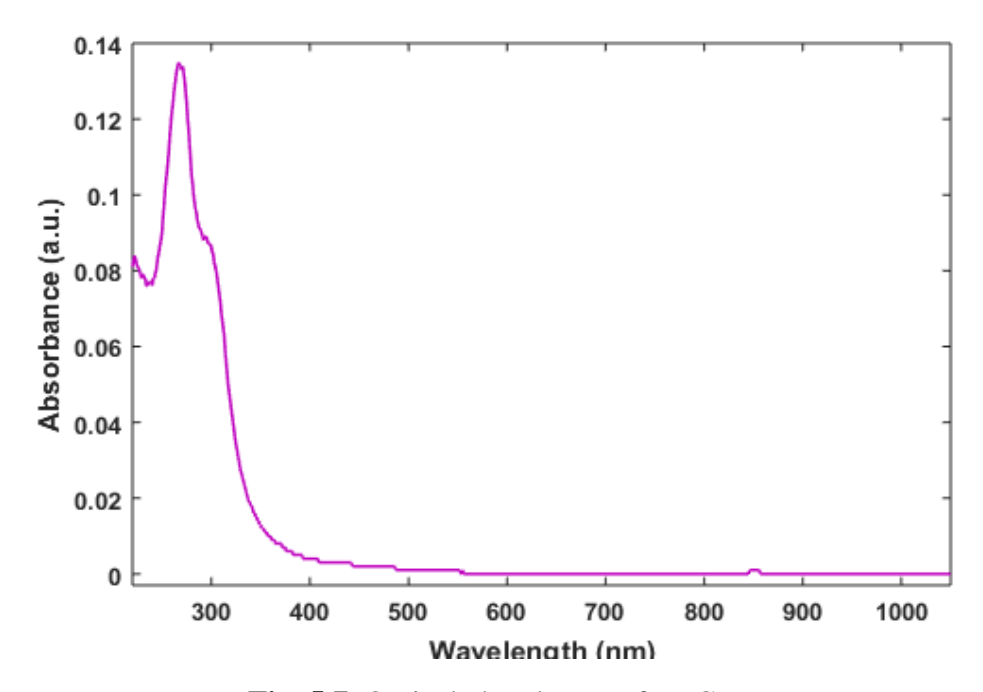


Fig. 5.7. Optical absorbance of PHCL

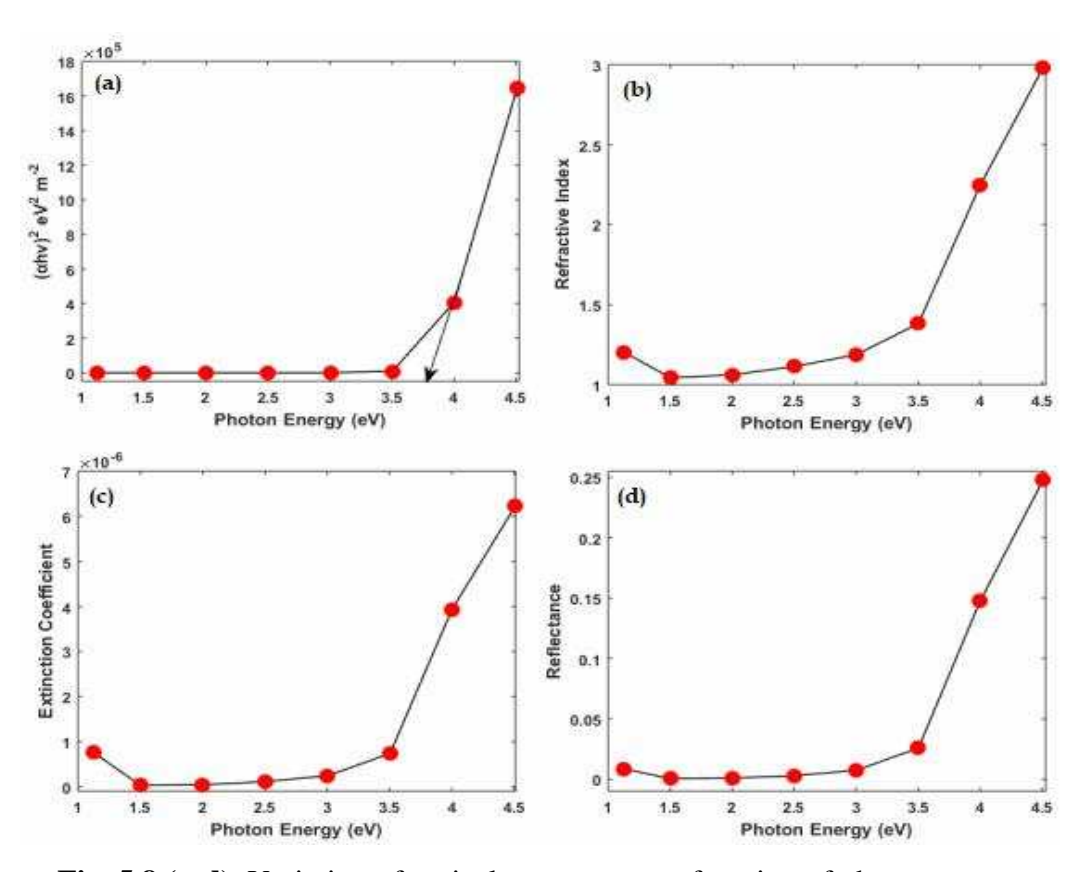


Fig. 5.8 (a-d). Variation of optical constants as a function of photon energy

(b) By Derivation of absorption spectrum fitting (DASF) method

The optical properties of PHCL are computed using the approach described in chapter-II, section 2.2.5(b). The energy band gap was obtained from the relation $E_g^{DASF} = \frac{1239.83}{\lambda_g} (eV) \text{ and its value is found to be 4.44 eV based on Fig. 5.9. The value of m is calculated using slope of Fig. 5.10. The value of m in this analysis is close to 1/2, indicating that PHCL possesses a direct band gap and allows charge carriers to transition directly. Graph of ln (A) in terms of <math>\lambda^{-1}$ (Fig. 5.11) provides the Urbach energy value of 0.27 eV. The optical study findings (Table 5.2) show that the PHCL crystal has good optical performance for NLO applications [18].

Table 5.2. Optical parameters of PHCL

Optical Parameters (DASF method)	Values
λ_g (wavelength of energy gap)	279 nm
$1/\lambda_{\rm g}$	0.00358
E _g (optical energy band gap)	4.44 eV
E _{Tail} (Urbach energy)	0.27 eV
σ (steepness parameter)	0.087
E _{e-p} (electron-phonon interaction)	7.66
n (refractive index)	1.66
ϵ_d (dielectric constant)	2.78

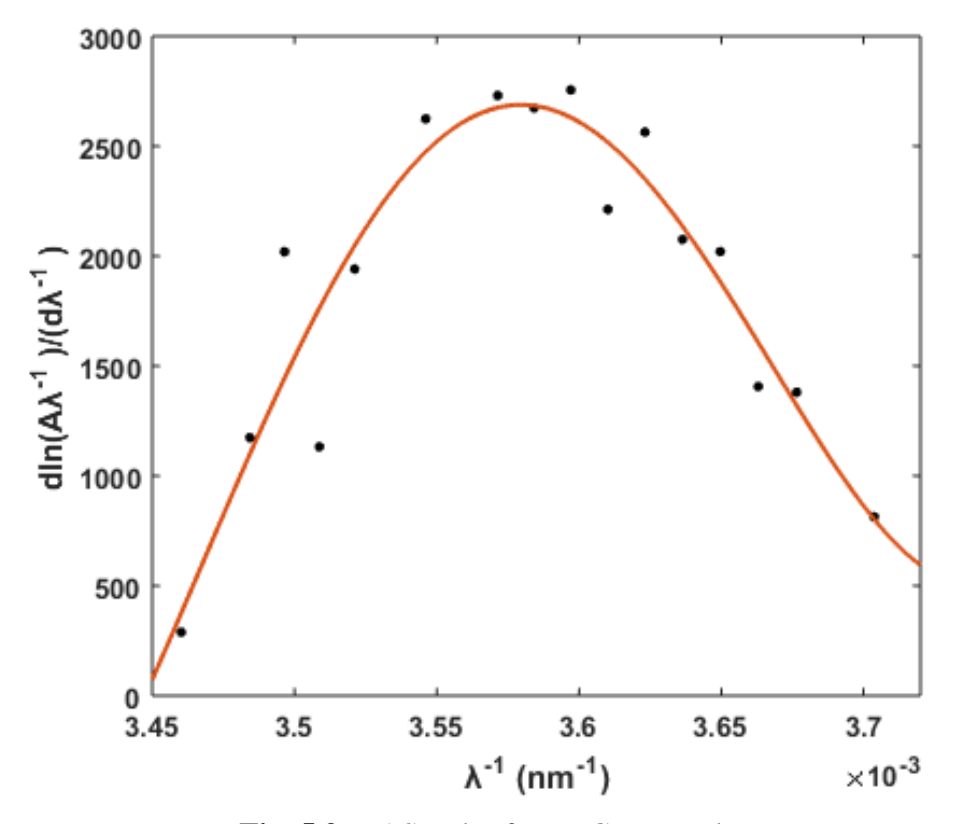


Fig. 5.9. DASF plot for PHCL crystal

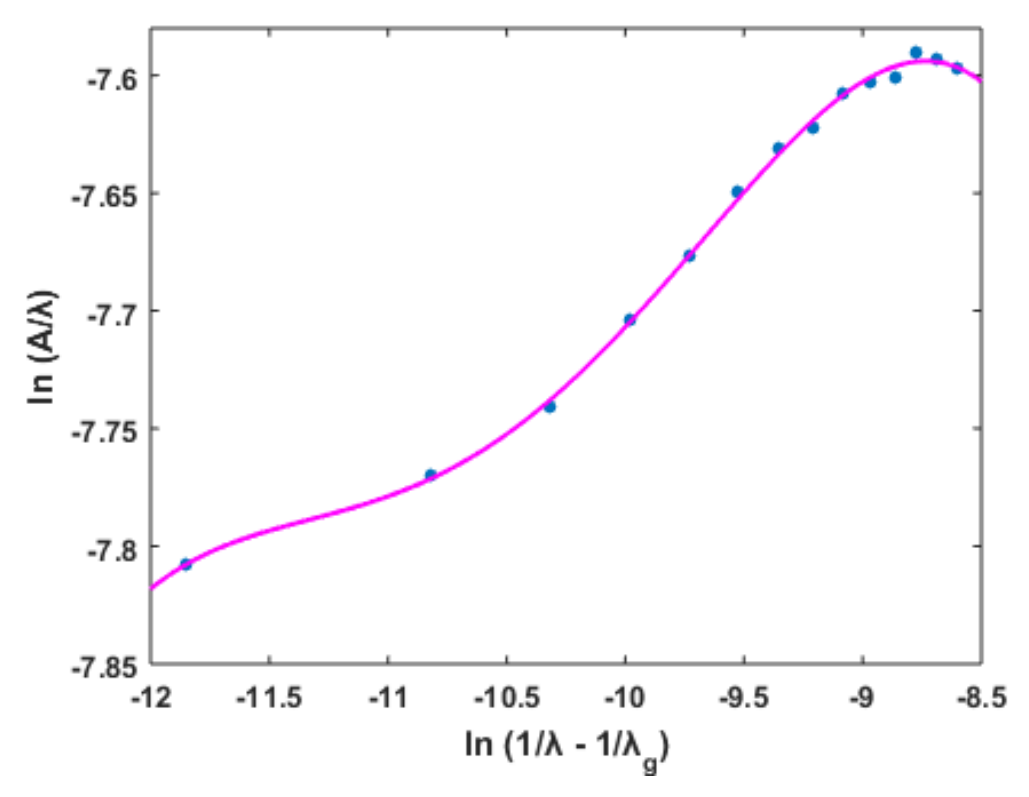


Fig. 5.10. Curves of ln (A/ λ) vs ln (1/ λ - 1/ λ_g)

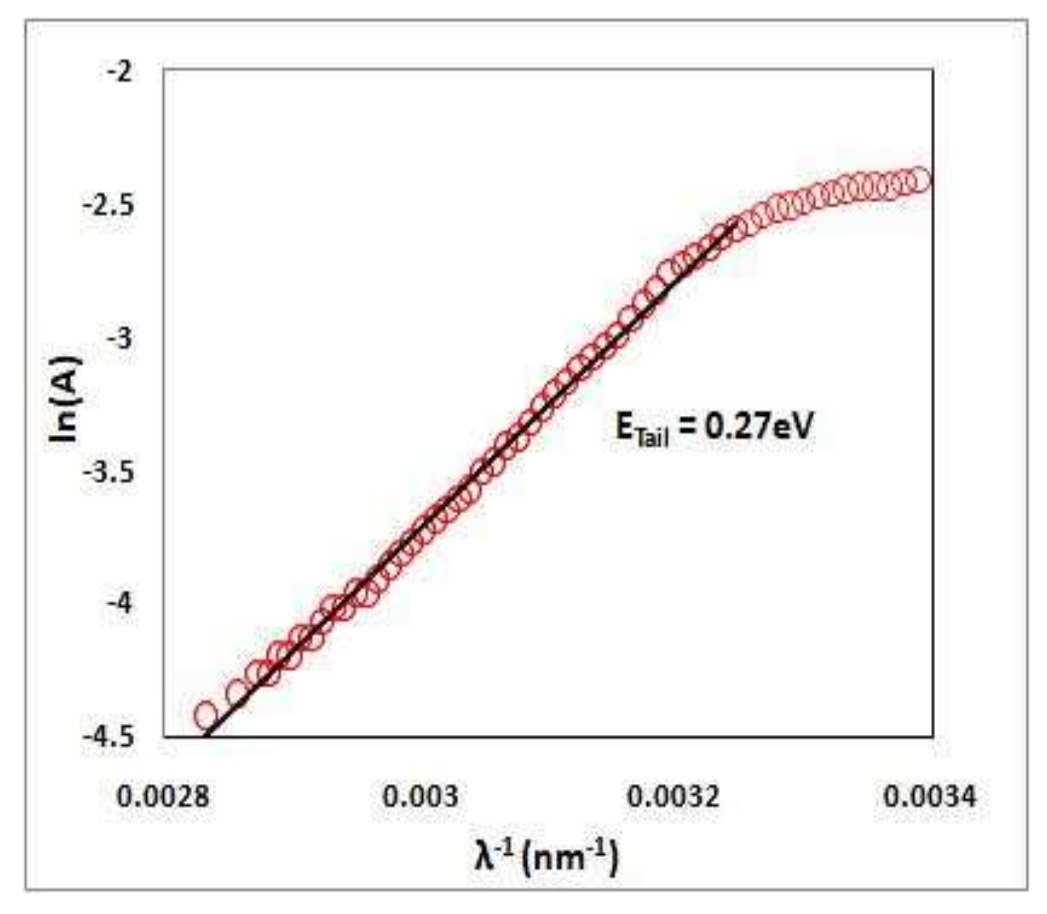


Fig. 5.11. Urbach plot for PHCL

5.2.6. Fluorescence Analysis

The emission of light which ceases after the cause of excitation in cut off is known as fluorescence and this is generally observed in those organic molecules which have rigid framework and not many loosely coupled substituent through which vibronic energy can flow out [19]. In Fig. 5.12, the fluorescence spectrum of a PHCL crystal was measured using a SHIMADZU/RF 6000 Spectro Fluorophotometer. Due to π - π * transition, emission peak is noticed at 444 and 480 nm in the spectrum, implying that PHCL crystals have a blue fluorescence emission prevalently to be useful in the OLED devices.

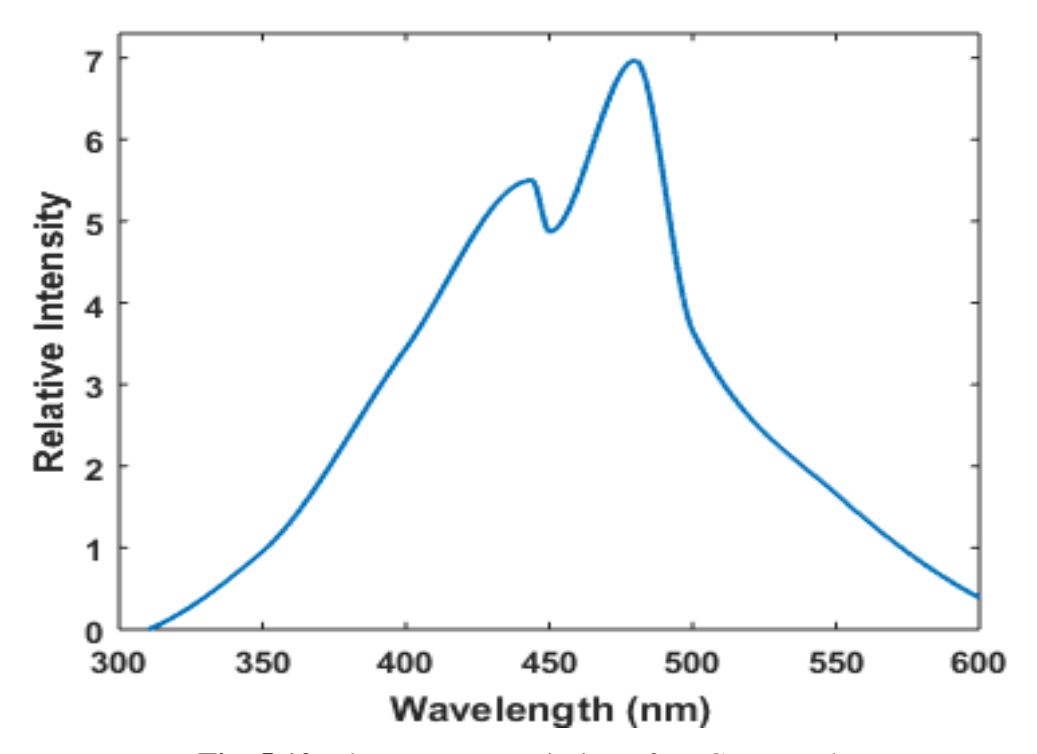


Fig. 5.12. Fluorescence emission of PHCL crystal

5.2.7. Z-scan Analysis

The usual Z-scan technique was used to explore the third order nonlinear optical characteristics of PHCL [20]. It is widely used to estimate the materials nonlinear absorption and nonlinear index (n₂), as well as the sign of nonlinearity. Fig. 5.13a and 5.13b show the PHCL crystals closed and open aperture Z-scan curves. The pre-focal valley to post-focal peak arrangement of the aperture curve in the closed aperture Z-scan curve shows that the third order nonlinear refractive index change is negative [21]. Fig. 5.13b illustrates the presence of reverse saturation absorption (RSA) with decreased transmission towards the focal point, concluding the significant reverse saturation of absorption (RSA) process in PHCL [22-24]. The experimental details and results of the Z-scan approach for PHCL crystal are tabulated in Table 5.3. As a result of the findings, the PHCL crystal appears to be a suitable candidate for third order NLO applications.

Table 5.3. Obtained nonlinear optical parameter from open- and closed-aperture
Z-scan measurement data for PHCL crystal

Parameters	Measured values for PHCL crystal
Nonlinear refractive index (n ₂)	$4.14 \times 10^{-09} (\text{cm}^2/\text{W})$
Nonlinear absorption coefficient (β)	$2.57 \times 10^{-04} (\text{cm/W})$
Real part of the third order susceptibility $[Re(\chi^3)]$	$3.74 \times 10^{-06} (\text{cm}^2/\text{W})$
Imaginary part of the third order susceptibility[Im(χ^3)]	$2.68 \times 10^{-07} (\text{cm/W})$
Third order nonlinear optical susceptibility (χ^3)	$3.75 \times 10^{-06} (esu)$

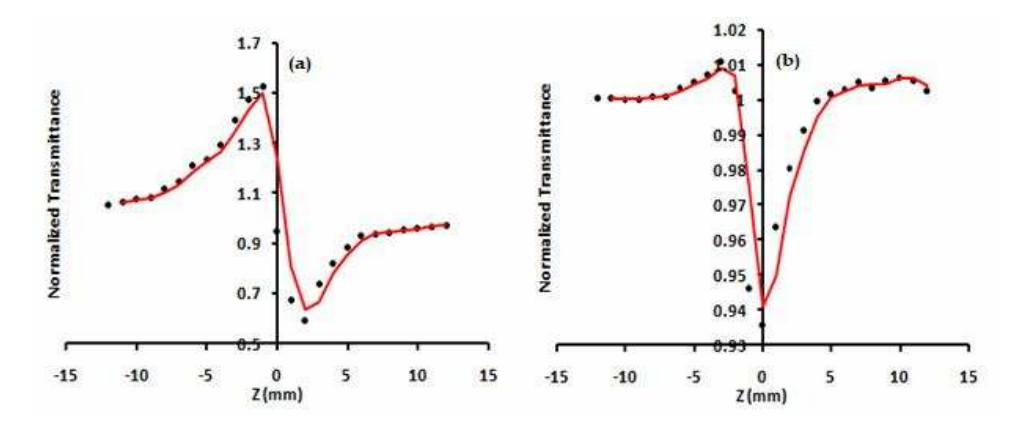


Fig. 5.13 (a). Self-focusing (closed aperture) Z-scan plot of PHCL crystal **(b)** Open aperture mode Z-scan plot of PHCL crystal

5.2.8. Microhardness Study

In order to study the mechanical properties, microhardness measurements were carried out on PHCL single crystals. Smooth surface of crystal was subjected to the Vicker's static indentation test at room temperature (303 K) using a SHIMADZU-HMV-G MicroVickers Hardness Tester. Loads of different magnitudes (25, 50 and 100 g) were applied over a fixed interval of time. The indentation time was kept as 10 sec for all the loads. The hardness was calculated using the relation H_v = (1.854 × P)/d² kg/mm² (where P is the applied load in kg and d is the diagonal length of the indentation impression in micrometer). The load above 100 g develops multiple cracks on the crystal surface due to the release of internal stresses generated locally by indentation. The hardness parameters are calculated and listed in Table 5.4.

Load P (g)	$H_v (kg/mm^2)$	d (µm)	C ₁₁ (Pa)	σ _v (MPa)
25	14.7	53.97	1.89E+14	0.48
50	23.8	42.41	4.41E+14	0.78
100	39.9	33.13	1.08E+15	1.30

Table 5.4. Hardness parameters of PHCL

Fig. 5.14a graphs the increase in hardness number for increase in load. The Meyer's index number [25] is determined from the relation $P = kd^n$ where k is the material constant and n, the "Meyer's index". By linear square fitting (Fig. 5.14b) the value of n is obtained as 3. According to Hanneman [26], the values of n read 1 to 1.6 for hard materials and more than 1.6 for the softer ones ascertaining PHCL categorized under soft material group. Fig. 5.14c reveals the PHCL compound to exhibit reverse indentation size effect (RISE) indicative of plastic deformation predominance.

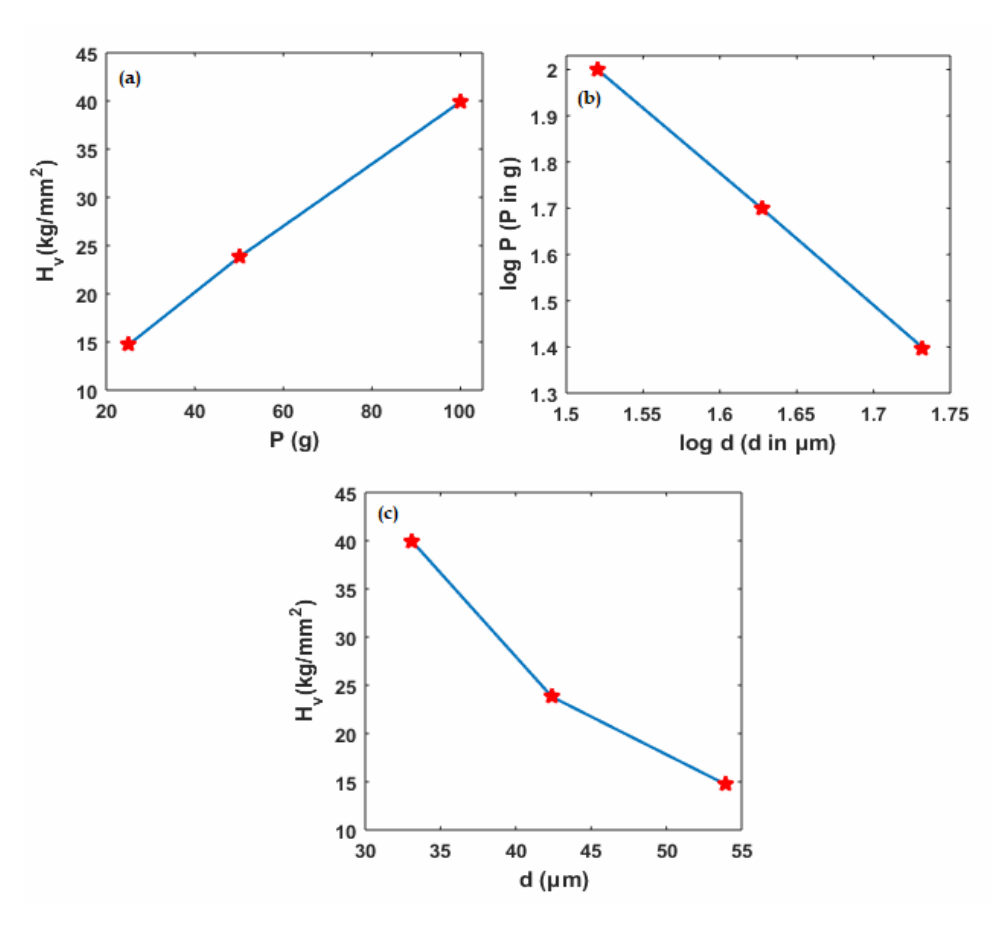


Fig. 5.14.(a) Variation of H_v against applied load P(b) log P against log d (c) H_v against d

According to Hays–Kendall's approach [27], load dependent hardness may be expressed by the relation $P = W + A_1 d^n$, where 'W' is the minimum load initiate plastic deformation, A_1 is the load independent constant and the exponent n = 2. The value of W and A_1 calculated from the plot drawn between P and d^2 are 58 g and 0.04 $(g/\mu m^2)$ respectively is shown in Fig. 5.15. The corrected hardness (H_0) calculated using the relation $H_0 = 1854.4 \times A_1$ is 74.17 (kg/mm^2) .

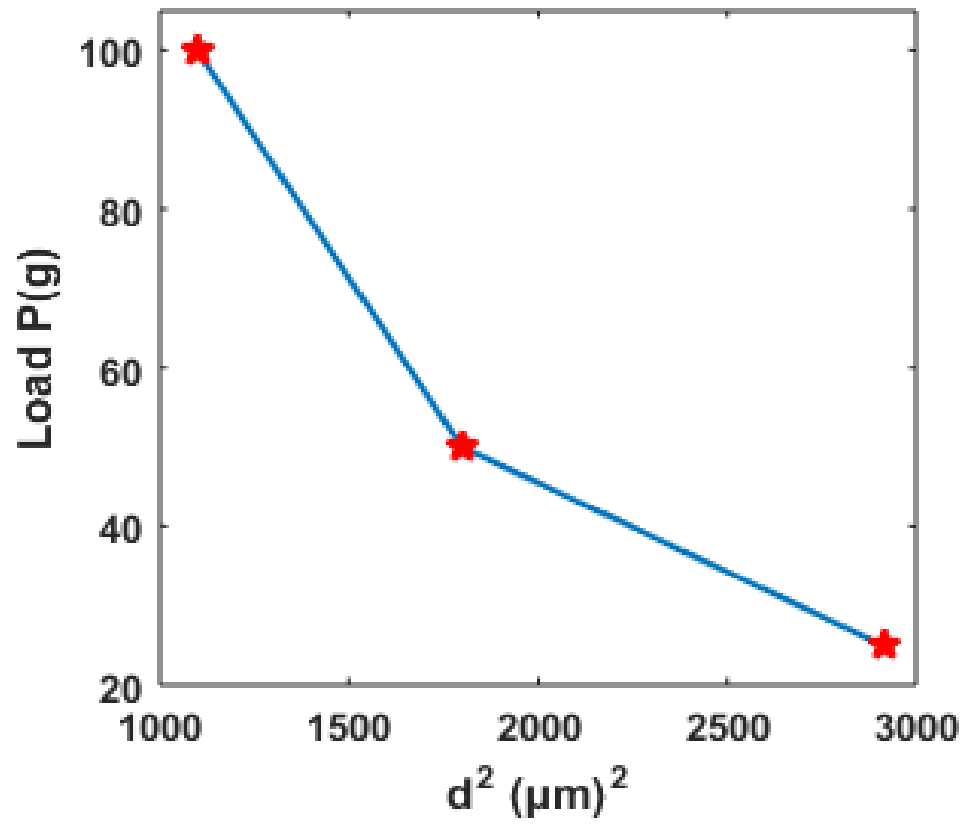


Fig. 5.15. Load P against d²

Elastic stiffness constant (C_{11}) is estimated by Wooster's empirical relation [28]. This gives an idea about the tightness of bonding between the neighboring atoms [29]. The calculated values of C_{11} are also given in Table 5.4.

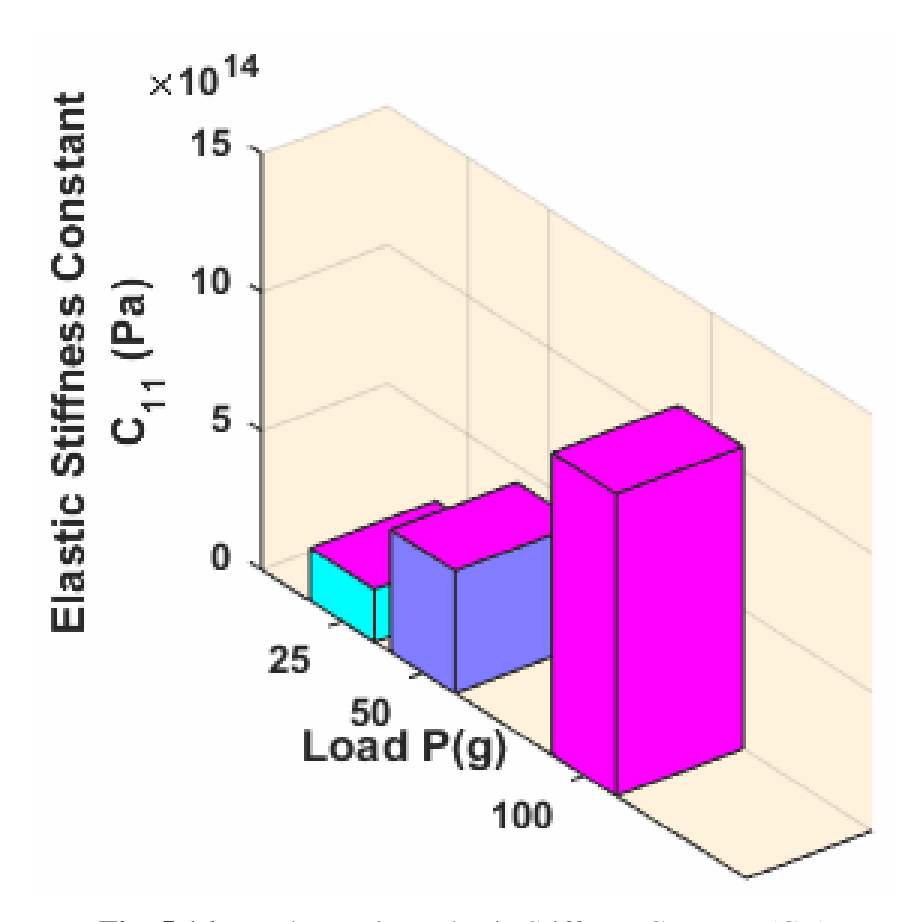


Fig. 5.16. Load P against Elastic Stiffness Constant (C₁₁)

5.3. COMPUTATIONAL ANALYSIS

5.3.1. Optimized Geometry

The optimized geometries of PHCL with symbols and numbering scheme for the atoms are computed using DFT/B3LYP/6-311++G(d,p) level (Fig. 5.17) and listed in Table 5.5. The global minimum energy value measured by the DFT structure optimization method is -2.356 × 10⁶ kJ/mol. The theoretical bond length and angles showed a slight deviation from the crystal parameters, as the theoretical values correspond to the isolated molecules in gas-phase whereas the experimental results are correlated with the molecules in solid state [30]. The optimized structure reveals two strong hydrogen bonds, O-H····Cl and N-H····Cl. The Cl⁻ ions, through their two bonds, ensure connections between molecules contained in the same symmetry plane.

In the pyridine ring, the bond length of C1-C2, C2-C3, C3-C4 and C4-C5 from the DFT method were in close agreement with the experimental length with minimal deviation (±0.018). This result shows that the C-C bond in the ring is weak and it makes the structure more stable. Earlier study [12], notes an apparently very short C=O bond length of 1.17 Å, but the current study suggests a more normal value of 1.241Å. The presence intra molecular hydrogen bond C-O···H is validated as its bond angle does not depart too much from the value 120°. All the calculated geometric parameters show a good approximation and hence can be used to calculate other parameters reported below.

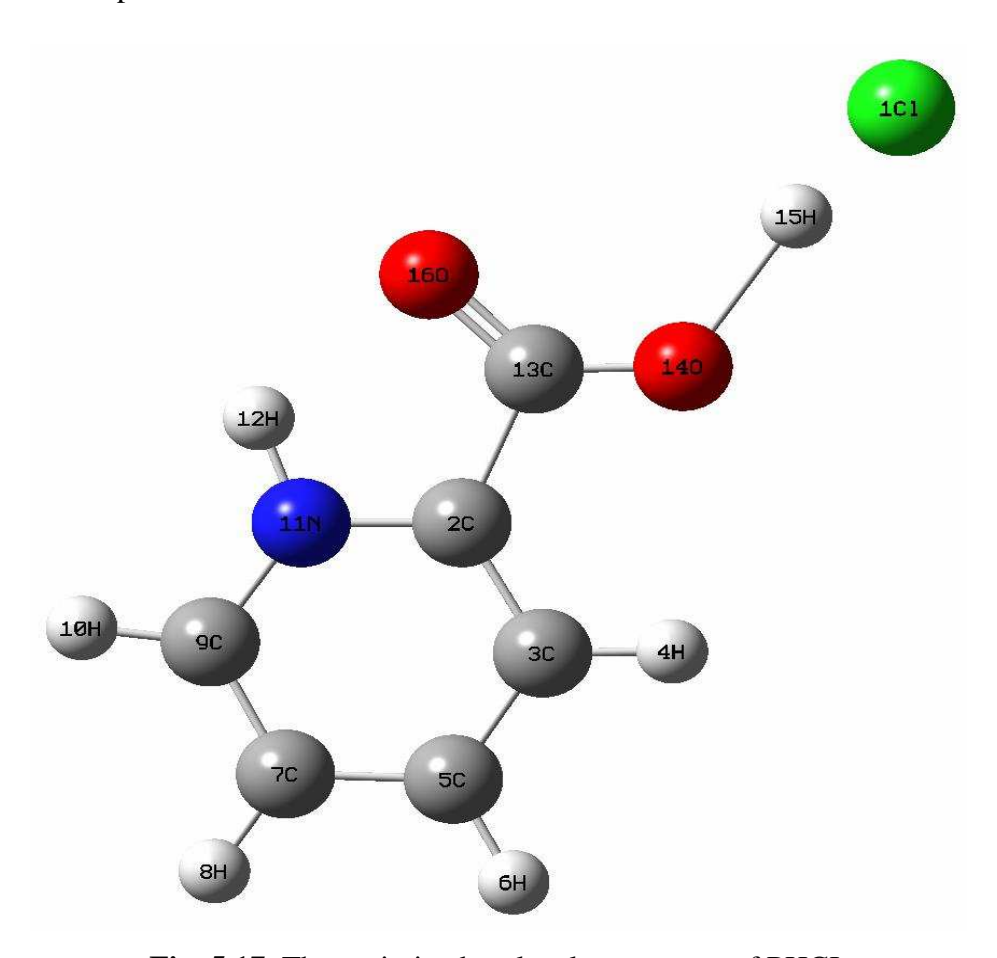


Fig. 5.17. The optimized molecular structure of PHCL

Table 5.5. Optimized parameters of PHCL by B3LYP level with 6-311++G(d,p) basis set

Bond	Valu	Values (Å)	D 14 1	Values (°)	D. 1 1 4 1	Values (°)		
Length	Calc.	Exp.[13]	Bond Angle	Calc.	Exp.[13]	Dihedral Angle	Calc.	Exp. ^[13]
C1-N1	1.342	1.340	N1-C1-C2	118.9	119.7	N1-C1-C2-C3	0.0	0.0
C1-C2	1.388	1.370	N1-C1-C6	112.8	114.9	C6-C1-C2-C3	-180.0	180.0
C1-C6	1.551	1.495	C2-C1-C6	128.3	125.5	C1-C2-C3-C4	0.0	0.0
C2-C3	1.391	1.389	C1-C2-C3	118.7	119.2	C2-C3-C4-C5	0.0	0.0
C2-H2	1.081	0.950	C1-C2-H2	118.0	120.4	C3-C4-C5-N1	0.0	0.0
C3-C4	1.401	1.383	C3-C2-H2	120.1	120.4	C4-C5-N1-C1	0.0	0.0
С3-Н3	1.084	0.950	C4-C3-C2	120.3	119.7	C2-C1-N1-C5	0.0	0.0
C4-C5	1.381	1.379	C4-C3-H3	119.5	120.1	C6-C1-N1-C5	-180.0	180.0
C4-H4	1.081	0.950	C2-C3-H3	120.1	120.1	N1-C1-C6-O2	0.0	0.0
C5-N1	1.344	1.331	C5-C4-C3	119.0	118.8	C2-C1-C6-O2	-180.0	180.0
C5-H5	1.081	0.950	C5-C4-H4	119.6	120.6	N1-C1-C6-O1	180.0	180.0
N1-H1	1.037	0.820	C3-C4-H4	121.3	120.6	C2-C1-C6-O1	0.0	0.0
C6-O2	1.241	1.200	N1-C5-C4	118.7	119.9			
C6-O1	1.243	1.312	N1-C5-H5	125.8	120.0			
O1-H1A	1.690	0.820	C4-C5-H5	124.0	120.0			
			C5-N1-C1	124.3	122.6			
			C5-N1-H1	117.3	117.5			
			C1-N1-H1	109.8	119.9			
			O2-C6-O1	133.7	126.3			
			O2-C6-C1	112.4	120.5			
			O1-C6-C1	113.7	113.1			
			C6-O1-H1A	125.1	105.0			

5.3.2. Hyperpolarizability

Theoretical hyperpolarizability determination is very useful in understanding the relationship between molecular structure and nonlinear optical characteristics. The first order hyperpolarizability (β) of this molecular system is calculated using B3LYP/6-311++G(d,p) method, based on the finite field approach. The total linear polarizability (α) can be calculated by the following equation,

$$\alpha = (\alpha_{xx} + \alpha_{yy} + \alpha_{zz})/3 \qquad \dots (5.2)$$

where, $\alpha_{xx},\,\alpha_{yy}$ and αzz are the diagonal components of polarizability tensor.

The total first-order hyperpolarizability (β) is given by the following equation,

$$\beta = [(\beta_{xxx} + \beta_{xyy} + \beta_{xzz})^2 + (\beta_{yyy} + \beta_{yzz} + \beta_{yxx})^2 + (\beta_{zzz} + \beta_{zxx} + \beta_{zyy})^2]^{\frac{1}{2}} \quad \dots (5.3)$$

where, β_{xxx} , β_{xxy} , β_{xyy} , β_{yyy} , β_{xxz} , β_{xyz} , β_{yyz} , β_{xzz} , β_{yzz} and β_{zzz} are the 10 components of the 3D matrix.

The calculated hyperpolarizability values of PHCL are given in Table 5.6. The polarizability (α) and first hyperpolarizability (β) of PHCL are 2.88×10^{-23} esu and 1.29×10^{-29} esu, respectively. Urea is one of the prototypical molecules used in the study of the NLO properties of molecular systems and frequently used as a threshold value for comparative purposes [31]. The first hyperpolarizability of the PHCL compound is greater than those of urea (β of urea is 0.3728×10^{-30} esu obtained by HF/6-311G(d,p) method).

Table 5.6. NLO properties of PHCL calculated using DFT at B3LYP/6-311++G(d,p) level

Pola	rizability	First hyper	rpolarizability
α_{xx}	220.93	eta_{xxx}	-115.37
α_{xy}	0.00	β_{xxy}	0.00
α_{yy}	54.51	β_{xyy}	-52.74
α_{xz}	-166.38	β_{yyy}	0.00
$lpha_{ m yz}$	0.00	β_{xxz}	-237.06
α_{zz}	308.59	β_{xyz}	-0.00
		$eta_{ m yyz}$	39.26
		$eta_{ ext{xzz}}$	643.57
		$eta_{ ext{yzz}}$	0.00
		β_{zzz}	-1227.67

5.3.3. Natural Bond Orbital (NBO) Analysis

In order to elucidate the inter and intramolecular charge transfer interactions and electron delocalization within the molecule, the NBO analysis is performed on PHCL at DFT/B3LYP with 6-311++G(d,p) basis set. The second order perturbation

theory analysis of Fock matrix in the NBO is presented in Table 5.7. The NBO analysis shows the stabilization energy of $n_3(Cl_1)$ to $\sigma^*(O_{14}\text{-H}_{15})$ as 11.99 kcal/mol, which quantify the intermolecular O-H···Cl hydrogen bonding. The interactions between $n_1(N_{11})$ to $\pi^*(C_2\text{-}C_3)$ and $\pi^*(C_7\text{-}C_9)$ and $\pi^*(C_2\text{-}C_3)$ to $\pi^*(C_{13}\text{-}O_{16})$ with energy values 38.38, 42.52 and 61.71, stabilize the pyridine ring system. Most important interactions in the PHCL molecule with the high E(2) values are $n_1^*(C_5)$ to $\pi^*(C_2\text{-}C_3)$ and $\pi^*(C_7\text{-}C_9)$, $n_2(O_{14})$ to $\pi^*(C_{13}\text{-}O_{16})$, $n_2(O_{16})$ to $\sigma^*(C_2\text{-}C_{13})$ and $\sigma^*(C_{13}\text{-}C_{14})$, with energy values of 55.06, 60.25, 56.15, 22.09, 29.12 kcal/mol, respectively. This high energy values leads to ICT interactions in the molecule [32]. In NBO analysis large E(2) value shows the intensive interaction between the electron donors and the electron-acceptors and greater extent of conjugation of the whole system.

Table 5.7. Second order perturbation theory analysis of Fock matrix in NBO basis including the stabilization energies using DFT at B3LYP/6-311++G(d,p) level

Donor (i)	ED (i)	Aggentan (i)	ED (j)	^a E(2)	$^{b}E(j)-E(i)$	cF(i,j)
Dollor (1)	ED (I)	Acceptor (j)		Kcal/mol	a.u.	a.u.
$n_3(Cl_1)$	1.95715	$\sigma^*(O_{14}-H_{15})$	0.03904	11.99	1.03	0.099
$\pi(C_2-C_3)$	1.98062	$n_1*(C_5)$	0.90616	54.99	0.15	0.094
$\mathcal{M}(C_2-C_3)$	1.90002	$\pi^*(C_{13}-O_{16})$	0.28098	14.15	0.33	0.063
$\sigma(C_2-N_{11})$	1.98538	$\sigma^*(N_{11}-H_{12})$	0.01560	3.76	1.76	0.073
$\sigma(C_2-C_{13})$	1.97648	$\sigma^*(C_9-N_{11})$	0.02066	4.30	1.14	0.062
$\sigma(C_3-H_4)$	1.97592	$\sigma^*(C_2-N_{11})$	0.02718	5.25	1.06	0.067
$\pi(C_7-C_9)$	1.65355	$n_1*(C_5)$	0.90616	51.94	0.16	0.096
$\sigma(C_9-H_{10})$	1.98210	$\sigma^*(C_2-N_{11})$	0.02718	4.49	1.10	0.063
n *(C)	0.90616	$\pi^*(C_2-C_3)$	0.27255	55.06	0.15	0.105
$n_1*(C_5)$		$\pi^*(C_7-C_9)$	0.25410	60.25	0.13	0.102
(NI)	1.47195	$\pi^*(C_2-C_3)$	0.27255	38.38	0.32	0.106
$n_1(N_{11})$	1.4/193	$\pi^*(C_7-C_9)$	0.25410	42.52	0.30	0.108
$n_1(O_{14})$	1.96528	$\sigma * (C_{13}-O_{16})$	0.02080	9.57	1.19	0.096
$n_2(O_{14})$	1.76724	$\pi^*(C_{13}-O_{16})$	0.28098	56.15	0.33	0.123
n ₂ (O ₁₆)	1.84569	$\sigma^*(C_2-C_{13})$	0.08091	22.09	0.64	0.108
	1.04309	$\sigma^*(C_{13}-C_{14})$	0.08201	29.12	0.67	0.127
$\pi^*(C_2-C_3)$	0.27255	$\pi^*(C_{13}-O_{16})$	0.28098	61.71	0.03	0.072

^aE(2) means the energy of hyper conjugative interactions.

^bEnergy difference between donor and acceptor i and j NBO orbitals.

^cF(i,j) is the Fock matrix element between i and j NBO orbitals.

5.3.4. Mulliken Population Analysis

The Mulliken atomic charge distribution is significant in the application of quantum chemical calculation. The atomic charge distributions determine the electron population of the individual atom of the molecule system [33]. The atomic charges affect many structural properties for instance dipole moment, and molecular polarizability. The strong negative and positive charges on the atoms of PHCL molecule demonstrate the electrostatic attraction or repulsion between the atoms (Table 5.8). The Mulliken atomic charge distribution of the PHCL compound is shown in Fig. 5.18. The charges of the molecule are ranged between -0.8 to 0.8 (Fig. 5.19). The H_{15} (0.48973) atom has high positive charge in the molecule. The carbon atoms possess both positive and negative charges, with C_{13} as the highest positive charge compared to all the other atoms in the molecule and the nitrogen atom exhibits negative charge. The sum of natural charges and atomic charges for PHCL molecule is zero and thus maintains the charge neutrality.

Table 5.8. Natural population analysis (NPA) of PHCL calculated with DFT/B3LYP/6-311++G(d,p) method

Atoms	Natural Charge	Atomic charge
Cl ₁	-0.74492	-0.60536
C_2	0.15731	0.49788
C_3	-0.13659	0.536489
H_4	0.21847	0.254765
C ₅	-0.07969	-0.47393
H_6	0.18970	0.18973
C ₇	-0.18109	0.11243
H ₈	0.19737	0.190628
C ₉	0.12195	-0.19962
H_{10}	0.18865	0.185824
N ₁₁	-0.35673	-0.02025
H_{12}	0.36989	0.330178
C_{13}	0.73468	-0.88702
O ₁₄	-0.60961	0.006661
H ₁₅	0.48973	0.085255
O ₁₆	-0.55912	-0.20366
Total	0.00000	0.00000

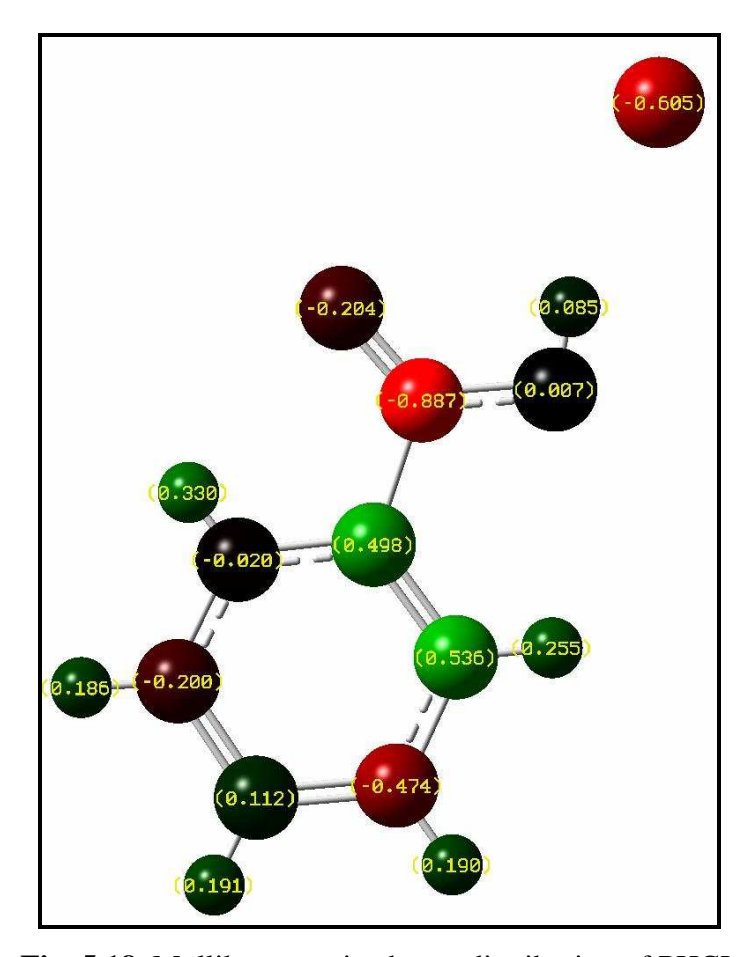


Fig. 5.18. Mulliken atomic charge distribution of PHCL

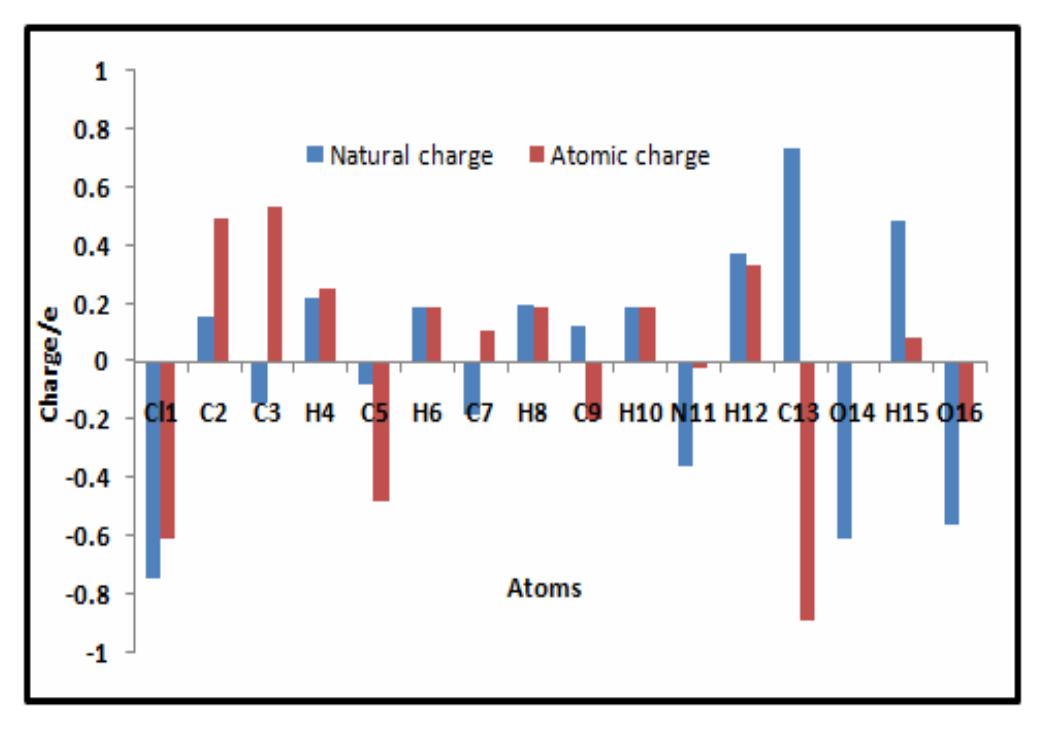


Fig. 5.19. Mulliken atomic charges of all atoms of PHCL

5.3.5. Molecular Electrostatic Potential (MEP) Analysis

MEPs are useful in molecular structure studies because they display molecular size, shape, as well as positive, negative, and neutral electrostatic potential regions in terms of colour grading [34]. The MEP at the B3LYP/6-311++G(d,p) optimized geometry was estimated to anticipate reactive sites for electrophilic and nucleophilic attack on the PHCL molecule. As illustrated in Fig. 5.20, the negative (red and yellow) areas of the MEP are associated to electrophilic reactivity, whereas the positive (blue) parts are related to nucleophilic reactivity. The color code of these maps ranges between -7.947e-2 (red) and +7.947e-2 (blue). Fig. 5.20 clearly depicts the regions having negative charges are around the C14, C15, H15 and C11 atoms.

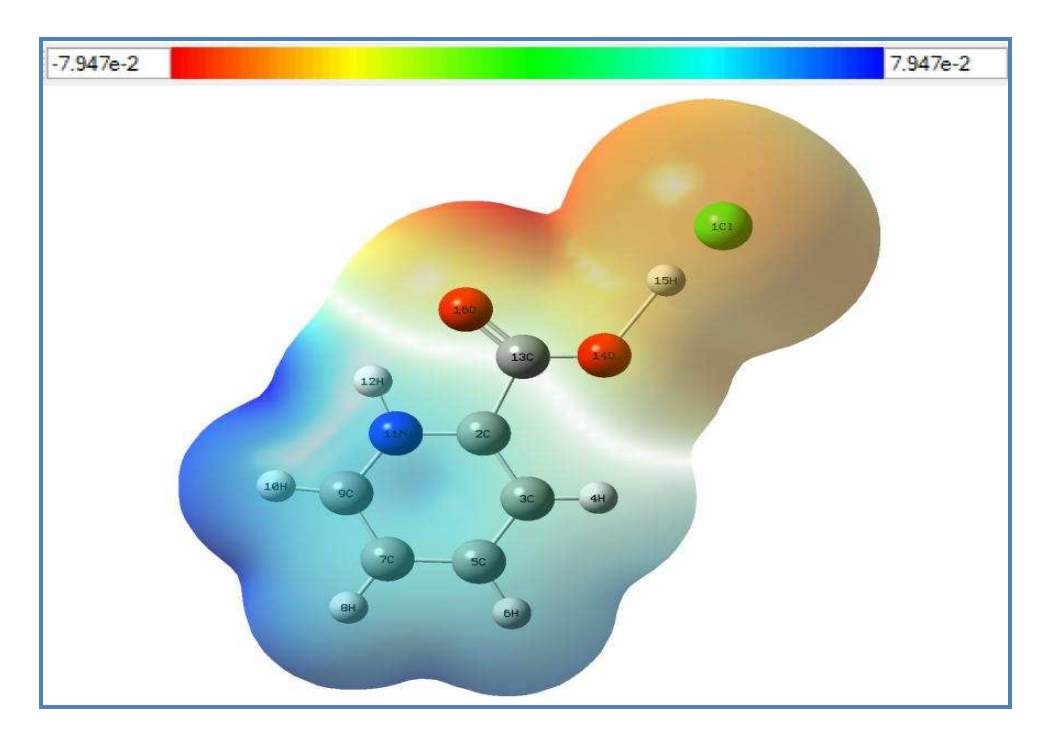


Fig. 5.20. Molecular electrostatic potential of PHCL

5.3.6. Frontier Molecular Orbital Analysis

The frontier molecular orbital analysis displays crucial function in the electric and optical properties of a material [35]. Highest occupied molecular orbital (HOMO,

acts as an electron donor) and the lowest unoccupied molecular orbital (LUMO, largely acts as an electron acceptor) energy difference influences the chemical stability and reactivity of the molecule. From the optimized structure, the energies of the HOMO and LUMO are computed as -7.16 and -3.53 eV, respectively and the HOMO–LUMO energy gap is 3.63 eV. This result clearly shows the charge transfer interactions within the conformers. The plots of HOMO and LUMO orbital computed at the B3LYP/6-311++G(d,p) level for PHCL molecule are shown in Fig. 5.21. High band gap energy of the molecule relatively has higher kinetic stability and lower chemical reactivity. The 3.63 eV gap falls within the UV region, so the molecule is colorless. The global reactivity descriptors have been calculated using the energy of HOMO and LUMO and its values are given in Table 5.9. The values suggest that the molecule is stable and also confers the proof of the NLO activity of the material [36].

Table 5.9. Calculated quantum chemical molecular orbital properties for PHCL at DFT/B3LYP/6-311++G (d, p) method

Parameters	B3LYP/6- 311++G (d, p)
HOMO energy, E _{HOMO}	-7.16 eV
LUMO energy, E _{LUMO}	-3.53 eV
HOMO-LUMO energy gap, ΔE _{GAP}	3.63 eV
Ionization potential (I)	7.16 eV
Electron affinity (A)	3.53 eV
Total energy change, ΔE_T	-0.46 eV
Overall energy balance, ΔE	-3.63 eV
Electronegativity, χ	5.35 eV
Chemical hardness (η)	1.82 eV
Chemical potential (µ)	-5.35 eV
Electrophilicityindex (ω)	7.85 eV
Softness (S)	0.55 eV ⁻¹
SCF energy	$-2.36 \times 10^6 \text{ kJ mol}^{-1}$

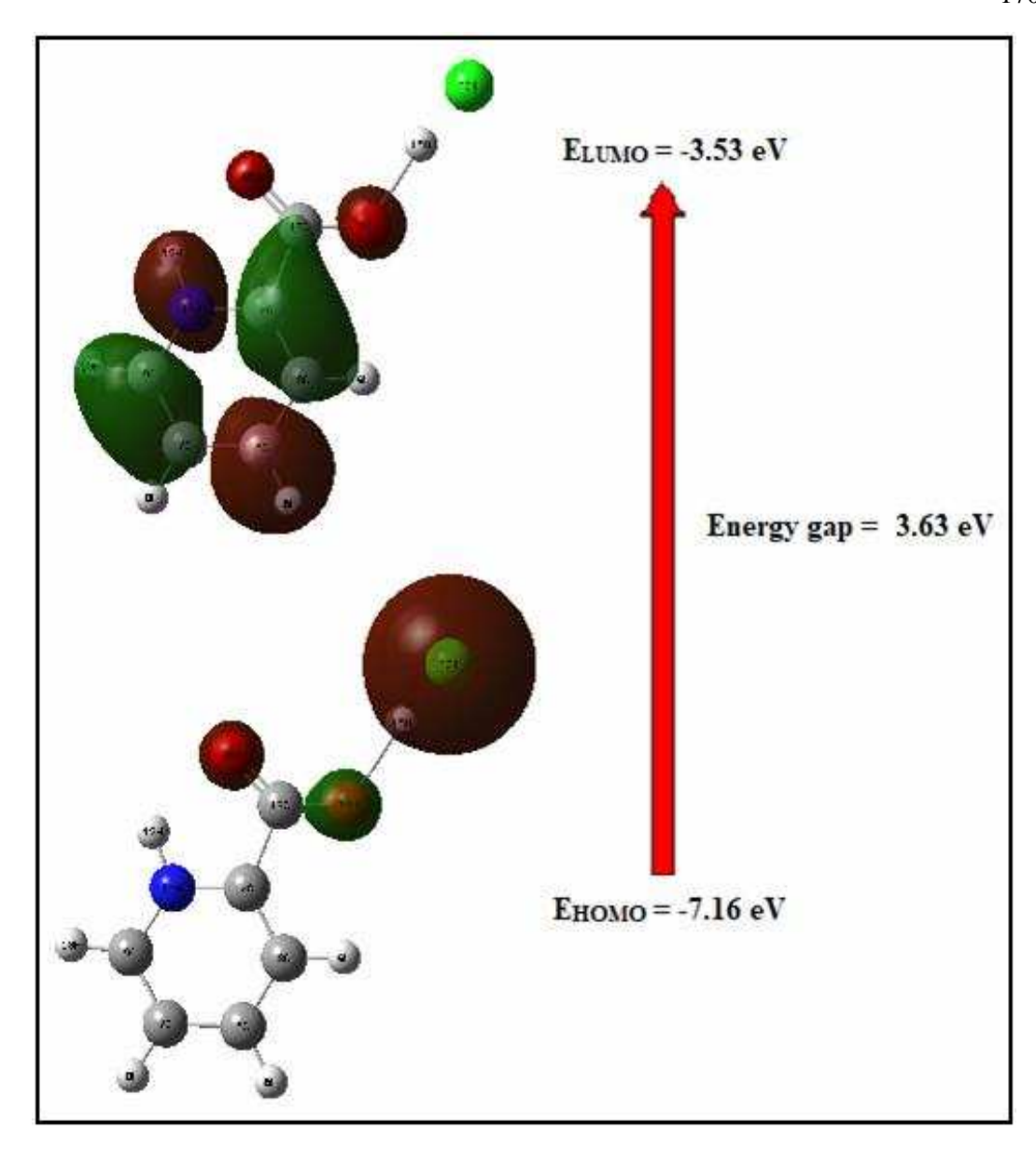


Fig. 5.21. HOMO-LUMO Plot of PHCL

5.3.7. Vibrational Spectral Analysis

The DFT with B3LYP/6-311++G(d,p) basis set is used to study various vibrations using PHCL crystal assignments. The FTIR spectrum was recorded using a Perkin Elmer Spectrum II FTIR spectrometer in the scan range 4000–400 cm⁻¹. Table 5.10 and spectra in Fig. 5.22 demonstrate the experimental frequencies of FTIR intensities and their various assignments, which were compared to theoretically computed assignments.

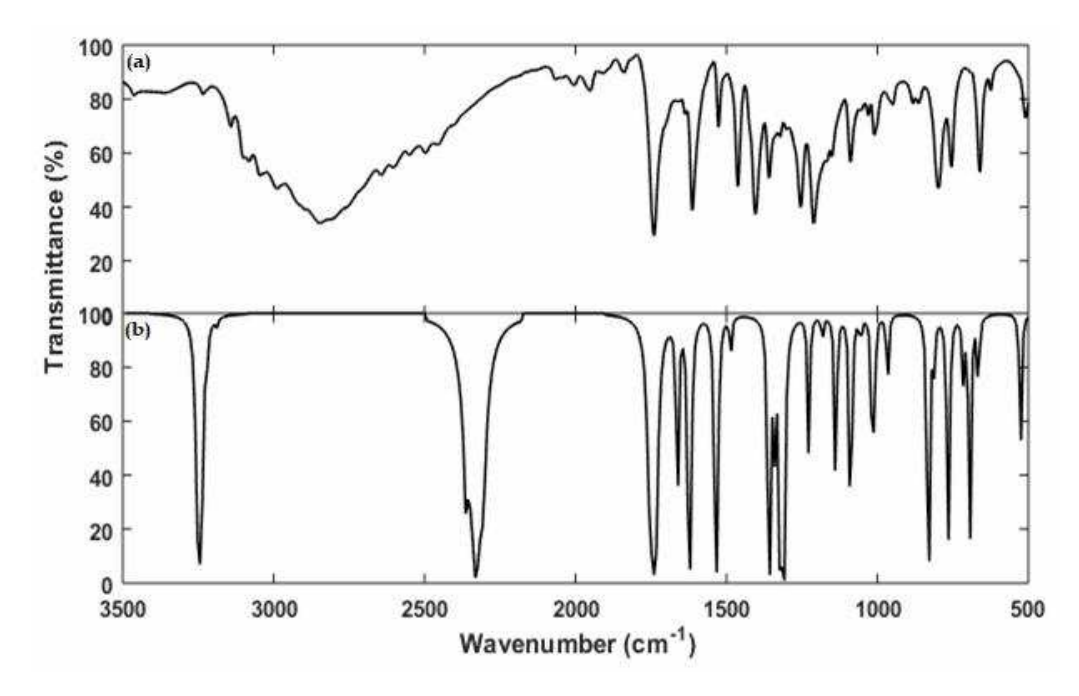


Fig. 5.22(a). Experimental FTIR spectra of PHCL (b) Computed IR spectra of PHCL

C-H Vibrations

The C-H stretching vibrations of the PHCL crystal were observed at 3141 and 2847 cm⁻¹. The out-plane deformation of C-H molecules was observed at 949 cm⁻¹ which could be attributed to strong coupled vibrations. They are in good agreement with computed wavenumbers.

N-H Vibrations

The N–H stretching modes are observed as a broad band in the FT–IR spectrum at 3462 cm⁻¹. The absorption peak appeared at 1462 cm⁻¹ is due to the N-H bending vibrations which match with calculated spectra 1484 cm⁻¹. The N-H in plane bending can be traced at 754 cm⁻¹, is in good agreement with computed wavenumber 764 cm⁻¹.

O-H Vibrations

The O-H stretching vibration appears at 3462 cm⁻¹. The COOH symmetric and asymmetric stretching vibrations were observed at 3141 cm⁻¹ at 3233 cm⁻¹ respectively. The computed and experimental FTIR are good agreement with each other.

Pyridine Ring Vibrations

In PHCL, the C=O stretching is observed as very strong band at 1739 cm⁻¹ which is in good agreement with computed spectra 1740 cm⁻¹. The aromatic ring C-C stretching vibrations observed at 1612 cm⁻¹. The bands corresponding to a strong band at 1526 cm⁻¹ is attributed to the Kekule C-C stretching mode. The band at 1462 is assigned to C-O stretching vibration. The C-N symmetric stretching was observed at 1300, 1210 and 1088 cm⁻¹ and it agrees with calculated wavenumbers 1308, 1228 and 1092 cm⁻¹. C-C-C out of plane bending vibrations was traced at 508 cm⁻¹.

Table 5.10. Experimental and calculated vibrational wavenumbers and fundamental bands positions assignments of PHCL

Calculated wavenumber (cm ⁻¹)	Experimental wavenumber (cm ⁻¹) ^[14]	Experimental wavenumber (cm ⁻¹) Present work	Vibrational Assignments
-	3410	3462	O-H Stretch & N-H stretch
3244	3300	3233	COOH asymmetric stretching vibrations
3188	3092	3141	COOH symmertric and C-H stretching vibrations
-	2857	2847	C-H stretching vibrations
1740	1725	1739	C=O stretch
1620	1609	1612	C-O stretching vibrations
1532	1536	1526	Kekuley C-C strech
1484	1455	1462	C-O stretching vibrations and N-H bending vibrations
1308	1311	1300	C-N symmertric stretching vibrations
1228	1220	1210	C-N symmertric stretching vibrations
1092	1088	1088	C-N symmertric stretching vibrations
964	960	949	Out of plane C-H deformation
764	750	754	C-O in plane deformation and N-H in plane bending
668	669	660	C-N bending vibration
524	511	508	C-C-C out of plane bending vibration

5.3.8. Hirshfeld Surface Analysis

For a greater understanding of the crystallographic force guiding the molecular configuration and packing nature of the molecule in their crystal structure, Hirshfeld surface analysis is used. The Hirshfield surfaces of PHCL are displayed in Fig. 5.23 showing the surfaces that has been mapped over dnorm, de, di, and curvedness. The deep red colored circular depressions visible on the surface are indicative of hydrogen bonding interactions O-H···Cl, N-H···Cl and C-O···H. The small range of area and light color on the surface represent a weaker and longer contact other than hydrogen bonds [37]. The dominant O...H/H...O intermolecular interactions (26.7%) is represented by a two sharp spike in the 2D fingerprint plot region (Fig. 5.24). The O...H interactions are represented by the left long sharp spike in the donor region (12.3%) and the H...O interactions are indicated by a right long spike (14.4%) in the acceptor region. 21.6% contribution from the H···H/H···H contacts are represented by a single spike in middle region and the 20.7% contribution from the Cl···H/H···Cl interactions. The relative contributions of the C...H, Cl...C, Cl...N,C...O, Cl...O, H...N and N...O contacts are 15.3, 9, 3.4, 2, 0.7, 0.5 and 0.1%, respectively.

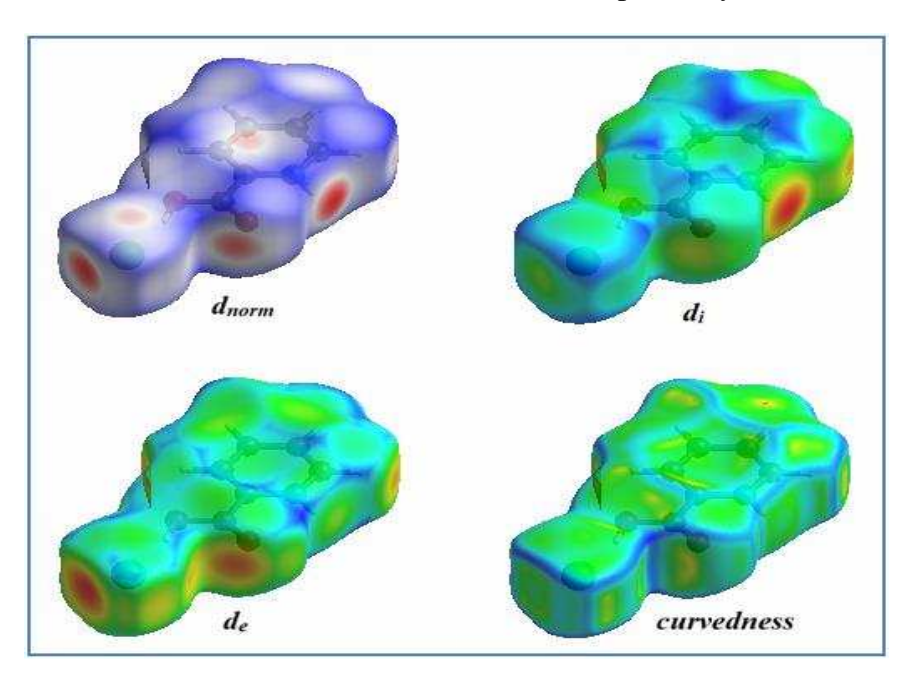


Fig. 5.23. Hirshfeld surfaces for d_{norm}, d_i, d_e and curvedness for the PHCL molecule

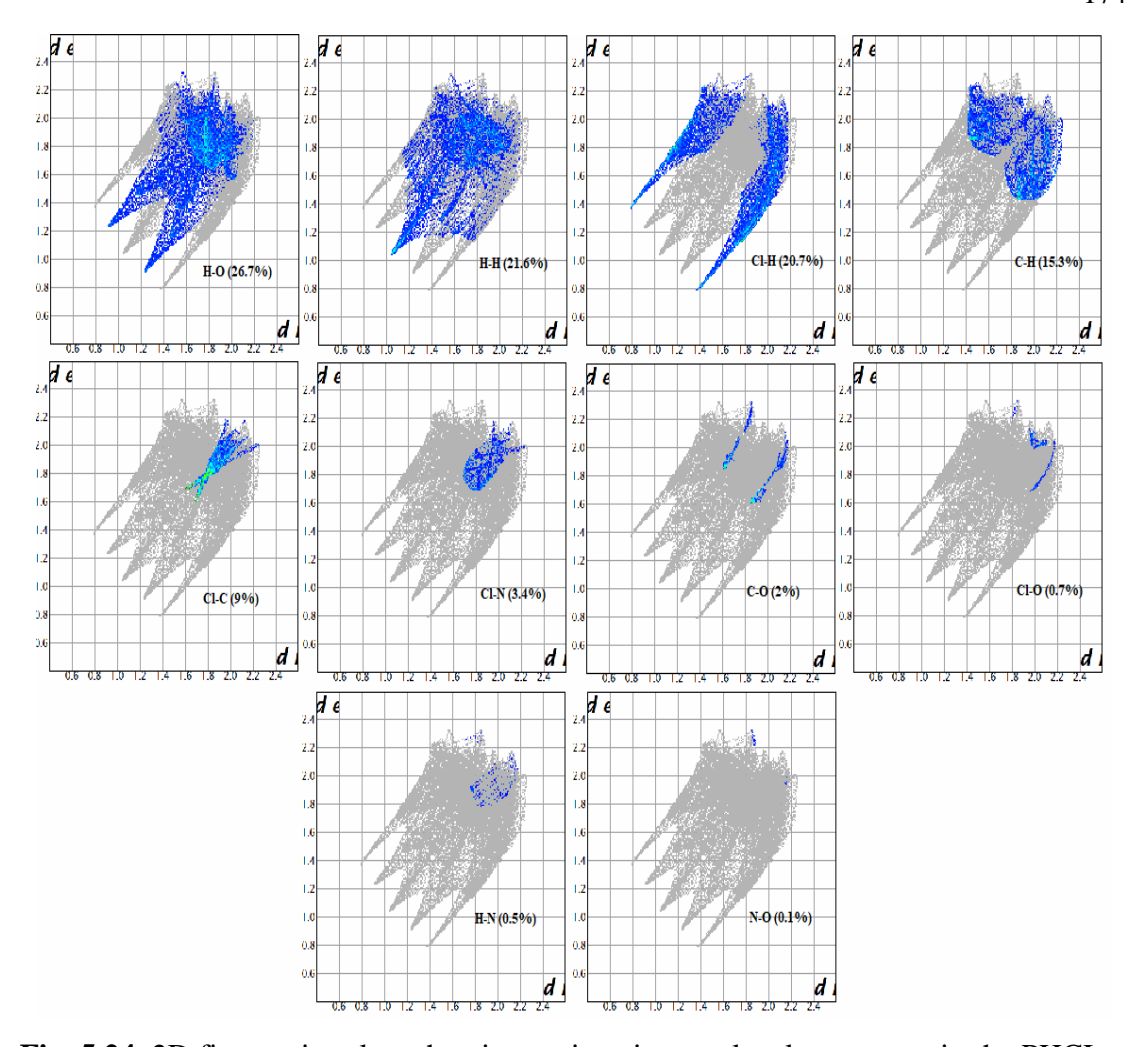


Fig. 5.24. 2D fingerprint plots showing various intermolecular contacts in the PHCL

5.4. CONCLUSIONS

Solubility studies have been carried out for PHCL and nucleation kinetics was analyzed. The nucleation parameters was assessed at various supersaturation ratios in the range of 1.1-1.4. With the increased supersaturation, critical free energy barrier and critical radius decreased. The slow evaporation approach was used to synthesize and grow single crystals of PHCL, which was characterized for its large third order NLO property. Powder XRD confirmed PHCL single crystal belongs to orthorhombic system with space group *Pnma*. The microstructural parameters such as crystal size and lattice strain were estimated using the W-H method. Optical transparency analysis

shows that the crystal is transparent in the visible region. Moreover, its lower cutoff wavelength with wide optical transparency window in the visible region makes the material suitable for its extensive investigations. Fluorescence analysis reveals a high level of blue radiation emission, which could be useful in light emitting diode (LED) applications. The PHCL compound third order non-linearity was measured using the Z-Scan technique, indicating that PHCL materials have a potential future as effective optical limiters. The reverse indentation size effect (RISE) has been discovered through mechanical studies. The yield strength (σ_v) and elastic stiffness constant (C_{11}) were computed, and the work hardening coefficient was evaluated. Optimization of the molecular structure and theoretical calculations are computed using Gaussian software using (B3LYP) level with 6-311++G(d,p) basis set. Optimized geometrical parameters are in close agreement with experimental values. The calculated β value is 1.29×10^{-29} esu. Molecular stability was successfully analyzed using NBO second order Fock matrix analysis. The intermolecular charge transfer is evidenced by Mulliken charge population analysis and packing diagram. The band gap energy value 3.63 eV is obtained from HOMO-LUMO analysis. Theoretical and experimental IR spectroscopic analyses were carried out and the presence of functional groups in PHCL molecule was qualitatively analyzed. The analysis of the Hirshfled surface and fingerprint plots is shown to be effective method to identify and quantify different types of intermolecular interactions.

REFERENCES

- M.K. Gupta, N. Sinha, B. Kumar, Growth and characterization of new semiorganicl-proline strontium chloride monohydrate single crystals, Physica B: Condens. Matter 406 (2011) 63–67.
- P. Maadeswaran, J. Chandrasekaran, S. Thirumalairajan, Synthesis, growth, spectral, thermal and photoluminescence properties of a new semiorganic NLO crystal – Thio semicarbazide lithium chloride [TSLC], Optik, 122 (2011) 259–262.
- J.M. Hales, S.J. Zheng, S. Barlow, S.R. Marder, J.W. Perry, Bisdioxaborinepolymethines with large third-order nonlinearities for all-optical signal processing, J. Am. Chem. Soc., 128 (2006) 11362–11363.
- 4. C. Gayathri, A. Ramalingam, Z-scan determination of the third-order optical nonlinearties of an azo dye using diode-pumped Nd:YAG laser, Optik, 119 (2008) 409–414.
- 5. V. Siva, S. Suresh Kumar, M. Suresh, M. Raja, S. Athimoolam, S. Asath Bahadur, N–H···O hydrogen bonded novel nonlinear optical semiorganic crystal (4- methoxyanilinium trifluoroacetate) studied through theoretical and experimental methods, J. Mol. Struct., 1133 (2017) 163-171.
- 6. D. Sajan, N. Vijayan, K. Safakath, Reji Philip, I. Hubert Joe, Intramolecular Charge Transfer and Z-Scan Studies of a Semiorganic Nonlinear Optical Material Sodium Acid Phthalate Hemihydrate: A Vibrational Spectroscopic Study, J. Phys. Chem. A, 115 (2011) 8216–8226.
- 7. P. Nagapandiselvi, C. Baby, R. Gopalakrishnan, Synthesis, growth, structure and nonlinear optical properties of a semiorganic 2-carboxy pyridinium dihydrogen phosphatesingle crystal, Optical. Mater., 47 (2015) 398-405.

- 8. N.R. Rajagopalana, P. Krishnamoorthy, K. Jayamoorthy, A strategic approach to physico-chemical analysis of bis (thiourea) lead chloride A reliable semi-organic nonlinear optical crystal, Opt Laser Technol., 89 (2017) 6-15.
- 9. K. Russel Raj, P. Murugakoothan, Studies on the optical and mechanical properties of non-linear optical 3-aminophenol orthophosphoric acid (3-amphph) single crystal, Optik, 123 (2021) 1082-1086.
- J. Mary Linet, S. Jerome Das, Optical, mechanical and transport properties of unidirectional grown l-tartaric acid bulk single crystal for non-linear optical application, Mater. Chem. Phys., 126 (2011) 886-890.
- 11. M. Lakshmipriya, R. Ezhil Vizhi, D. Rajan Babu, Growth and characterization of maleic acid single crystal, Optik, 126 (2015) 4259-4262.
- A. Laurent, Structure Cristalline du Chlorhydrate de l'Aeide Pieolique, Acta
 Cryst., 18 (1965) 799–806.
- 13. M.R.J. Elsegood, D.A. Hussain, N.M. Sanchez-Ballester, Redetermination of picolinic acid hydro-chloride at 150 K, Acta Cryst., E63 (2007) o4044.
- 14. S. Gowri, T. Uma Devi, D. Sajan, C. SurendraDilip, A. Chandramohan, N. Lawrence, Crystal growth, spectral, optical and thermal properties of semiorganic nonlinear optical material: Picolinic acid hydrochloride, Spectrochim. Acta A Mol. Biomol. Spectrosc., 110 (2013) 28-35.
- 15. P. Bennema, O. Sohnel, Interfacial surface tension for crystallization and precipitation from aqueous solutions, J. Cryst. Growth 102 (1990) 547-556.
- 16. A. Khorsand Zak, W.H. Abd. Majid, M.E. Abrishami, Ramin Yousefi, X-ray analysis of ZnO nanoparticles by Williamson–Hall and size–strain plot methods, Solid State Sci., 13 (2011) 251-256.

- 17. G. Ouyang, W. G. Zhu, C. Q. Sun, Z. M. Zhu, S. Z. Liao, Atomistic origin of lattice strain on stiffness of nanoparticles, Phys. Chem. Chem. Phys., 12 (2010) 1543-1549.
- 18. K.Aswaniya, M.B. JessieRaj, S.Gowri, G.Vinitha, Promising computational, structural, vibrational and optical properties of piperazinium bis(2-carboxypyridine) monohydrate (PBCPM) crystal for NLO device applications, Optik, 246 (2021) 167836.
- F. Hammer, Inorganic Photochemistry, Sarup Book Publishers Pvt. Ltd., New Delhi, 2009.
- 20. S.R. Maidur, J.R. Jahagirdar, P.S. Patil, T.S. Chia, C.K. Quah, Structural characterizations, Hirshfeld surface analyses, and third order nonlinear optical properties of two novel chalcone derivatives. Opt. Mater. 75 (2018) 580–594.
- 21. R.O. Paavai Eraa, M.U. Jauhar, P. Murugakoothan, Optimization of growth parameters and investigations on the physico-chemical properties of an organometallic guanidinium chromate single crystal for nonlinear optical and optical limiting applications, Opt. Mater., 99 (2020) 109558.
- 22. T. Hannah Clara, R.Ragu, D. Reuben Jonathan, Johanan Christian Prasana, Structural, optical, thermal, dielectric and Z-scan study on novel (2E)-1-(4-aminophenyl)-3-(4-benzyloxyphenyl)-prop-2-en-1-one (APBPP) chalcone crystal for nonlinear optical applications, Opt. Mater., 109 (2020) 110331.
- 23. H.J. Ravindra, A. John Kiran, K. Chandrasekharan, H.D. Shashikala, S.M. Dharmaprakash, Third order nonlinear optical properties and optical limiting in donor/acceptor substituted 4'-methoxy chalcone derivatives, Appl. Phys. B, 88 (2007) 105–110.

- 24. MohdAnis, D.A. Hakeem, G.G. Muley, Optical and dielectric studies of KH₂PO₄ crystal influenced by organic ligand of citric acid and L-valine: A single crystal growth and comparative study, Results Phys., 6 (2016) 645-650.
- 25. A. Silambarasan, M. Krishna Kumar, A. Thirunavukkarasu, R. Mohan Kumar, P.R. Umarani, Synthesis, crystal growth, solubility, structural, optical, dielectric and microhardness studies of Benzotriazole-4-hydroxybenzoic acid single crystals, J. Mol. Struct., 420 (2015) 11-16.
- 26. M. Lakshmipriya, D. Rajan Babu, R. Ezhil Vizhi, Vickers microhardness studies on solution-grown single crystals of potassium boro-succinate, IOP Conf. Ser.: Mater. Sci. Eng., 73 (2015) 012091.
- 27. T. Sivanandan, S. Kalainathan, Vickers microhardness studies on Cobalt Mercury Thiocyanate single crystals grown in silica gel, Mater. Lett., 162 (2016) 211-213.
- 28. K.Mahendra, N.K.Udayashankar, Investigation on mechanical and temperature dependent electrical properties of potassium hydrogen oxalate oxalic acid dihydrate single crystal, Phys. Lett. A, 384 (2020) 126475.
- 29. Neelam Rani, N. Vijayan, M.A. Wahab, G. Bhagavannarayana, B. Riscob, K.K. Maurya, Growth and characterization analyses of pure and p-nitroaniline doped L-lysine monohydrochloride single crystal for nonlinear optical applications, Optik, 124 (2013) 1550-1554.
- 30. N. Sundaraganesan, C. Meganathan, Mustafa Kurt, Molecular structure and vibrational spectra of 2-amino-5-methyl pyridine and 2-amino-6-methyl pyridine by density functional methods, J. Mol. Struct., 891 (2008) 284-291.
- K. Ramachandran, Arumugam Raja, V. Mohankumar, Muthu Senthil Pandian,
 P. Ramasamy, Experimental and theoretical approach of organic 4,4'-

- dimethylbenzophenone (DMBP) single crystal for NLO application, Opt Laser Technol., 119 (2019) 105640.
- 32. P. Karuppasamy, V. Sivasubramani, M. Senthil Pandian, P. Ramasamy, Growth and characterization of semi-organic third order nonlinear optical (NLO) potassium 3,5-dinitrobenzoate (KDNB) single crystals, RSC Adv., 6 (2016) 109105-109123.
- 33. R.S. Mulliken, Electronic population analysis on LCAO–MO molecular wave functions, I. J. Chem. Phys. 23 (1955) 1833-1840.
- 34. R. Meenakshi, L. Jaganathan, S. Gunasekaran, S. Srinivasan, Density functional theory, restricted Hartree–Fock simulations and vibrational spectroscopic studies of nicorandil, Mol Simul., 36 (2010) 425-433.
- 35. V. Sasikala, D. Sajan, N. Vijayan, K. Chaitanya, M. S. Babu Raj, B.H. Selin Joy, Growth, molecular structure, NBO analysis and vibrational spectral analysis of 1-tartaric acid single crystal, Spectrochim Acta A Mol Biomol Spectrosc. 123 (2014) 127-141.
- 36. V. Charles Vincent, G.Bakiyaraj, K.Kirubavathi, K.Selvaraju, Synthesis, growth and theoretical investigations of L-methionine L-methioninium perchlorate monohydrate a nonlinear optical crystal, Chem. Data Collect., 22 (2019) 100247.
- 37. Mohd Faizan, Mohammad Jane Alam, Ziya Afroz, Vítor Hugo Nunes Rodrigues, ShabbirAhmad, Growth, structure, Hirshfeld surface and spectroscopic properties of 2-amino-4-hydroxy-6-methylpyrimidinium-2,3-pyrazinedicorboxylate single crystal, J. Mol. Struct., 1155 (2018) 695-710.

Chapter-VI

CHAPTER - VI

SUMMARY AND SUGGESTIONS FOR FUTURE WORK

6.1. SUMMARY

The "Experimental and Theoretical Investigations of Picolinic Acid Based Single Crystals" research are summarized and concluded in this chapter. The future research scopes are also highlighted. Single crystals of 2-picolinic acid (2PA) (also known as pyridine-2-carboxylic acid, 2-pyridine carboxylic acid and picolinic acid), 2-picolinic trichloro acetate (PTCA), 2-picolinic benzotriazole (PBTA), and 2-picolinic hydrochloride (PHCL) are grown and their properties are discussed in detail. The present investigation is divided into six chapters.

Fundamentals of crystal growth, nucleation theories, various crystal growth methods, computational approaches and instrumentation techniques were reviewed in the first chapter.

The second chapter discusses the nucleation kinetics, growth, W-H analysis, spectroscopic, and optical properties of organic single crystal 2-picolinic acid (2PA). At 304, 308, 316, and 321K, the nucleation characteristics were evaluated at various supersaturation ratios (1.1 to 1.4). The metastable zone width is narrow at lower temperatures and broader at higher temperatures. The slow evaporation process was used to grow the single crystals. The grown crystal belongs to the monoclinic system with space group C2c, according to powder X-ray diffraction. As per Williamson–Hall method, the 2PA crystal with the minimum lattice strain has a lower dislocation density. The synthesized crystal has high transmittance throughout the visible spectrum. Using Tauc's method, the optical band gap is determined to be 3.5 eV and 3.47 eV

using the DASF method. The emission of 2PA is in the blue range, according to fluorescence emission analysis. The Z-scan analysis of 2PA shows that it can be used as a good third order NLO material, with applications in optical limiting devices. The DFT/B3LYP/6-311++G(d,p) basis set was used to calculate the optimized structure, first hyperpolarizability parameters, NBO and Milliken population analysis. The computed spectroscopic parameters are in good agreement with the experimental data results. The molecular energy gap was discovered via HOMO-LUMO studies. Three-dimensional Hirshfeld surfaces were used to investigate intermolecular interactions. It shows that H····H/H····H interactions contribute 44.4% Hirshfeld surface, whereas O····H/H····O interactions contribute 28.1%. The 2-picolinic acid crystal has good quality, with increased crystalline perfection and optical transparency nature.

Experimental and theoretical investigations of nonlinear optical crystal 2-picolinic trichloro acetate (PTCA) are discussed in chapter-III. The solubility studies reveal PTCA has a positive coefficient of solubility. The critical radius, metastable zone width, interfacial surface energy, critical free energy, and free energy change parameters obtained by the application of different equations are in good agreement with each other. Single crystal of PTCA has been grown by slow evaporation technique. Powder XRD spectrum revealed the crystalline nature of the sample. The crystal has monoclinic structure with space group $P2_I$. According to UV-Vis-DRS investigations, PTCA has a low absorption, which is a fundamental need for materials with NLO applications. At 260 nm, it shows the maximum absorption peak, which corresponds to the π - π * transition. The reverse saturation absorption optical phenomenon found in the PTCA crystal is highlighted using the Z-scan technique. The fluorescence test reveals that PTCA emits a blue tint. The PTCA crystal mechanical behavior indicates that it is in

the soft category. The optimized structure of the PTCA molecule was computed using DFT (B3LYP) level using 6-311++G(d,p) basis set. Experimental bond lengths and bond angles are in good agreement to those calculated theoretically. NBO analysis reveals the intramolecular charge transfer interactions and stability in PTCA molecule. The MEP analysis proves that PTCA is an electron-rich species and explains why it is electrophilic. The hardness value and negative chemical potential of the PTCA molecule from HOMO-LUMO imply that it is stable. The existence of functional groups in the PTCA molecule is qualitatively examined using theoretical and experimental IR spectroscopy analyses. The percentage of strong and weak intermolecular interactions in the crystalline form is determined by the Hirshfeld surface analysis of PTCA.

The chapter-IV shows the solubility studies of 2-picolinic benzotriazole (PBTA) with methanol as solvent. The nucleation parameters of PBTA crystal are determined from classical nucleation theory. Powder XRD examination confirmed the orthorhombic crystal structure with the space group $Pna2_1$. According to the optical absorption spectra, PBTA has the lowest absorption between 200 and 1100 nm. The optical band gap of the material is 3.49 eV as per Tauc's plot and 3.46 eV from the DASF method. The optical properties of the PBTA crystal are determined and related to incident photon energy. The NLO efficiency of the grown crystal is analyzed by Kurtz-Perry method. Vickers microhardness test reveals the reverse indentation nature of the material and work hardening coefficient value was found to be 2.4. The DFT calculations were performed for the PBTA crystal to optimize structure and evaluate the first order hyperpolarizability, ICT interactions through NBO, Milliken charges, molecular electrostatic potential, HOMO-LUMO energy gap and vibrational analysis.

and energy gap of HOMO-LUMO is 4 eV. Hirshfeld surface analysis and 2-dimensional finger print plot specify the interactions associated with PBTA molecule.

In chapter-V solubility studies and nucleation kinetics have been carried out for 2-picolinic hydochloride (PHCL) crystal. The nucleation parameters was assessed at various supersaturation ratios in the range of 1.1-1.4. With the increased supersaturation, critical free energy barrier and critical radius decreased. The PHCL single crystals are grown by slow evaporation solution growth technique. Powder XRD confirmed PHCL single crystal belongs to orthorhombic system with space group *Pnma*. The optical absorption analysis demonstrates that grown crystals have a high degree of transparency over the whole visible spectral range, making them potentially useful materials for device applications. The third order nonlinearity of PHCL crystal was determined using Z-scan technique. Hardness studies reveal that PHCL crystal belongs to soft material category. The elastic stiffness constant (C_{11}) was determined, and it confirms that the bonding between nearby atoms is quite stiff. Theoretical computations and molecular structure optimization are performed using Gaussian software at the (B3LYP) level with the 6-311++G(d,p) basis set. Geometrical parameters that have been optimized are in close accord with experimental results. The NBO second order Fock matrix technique was used to successfully investigate molecular stability. Mulliken population analysis and packing diagram reveal intermolecular charge transfer. HOMO-LUMO analysis yielded the band gap energy value of 3.63 eV. The existence of functional groups in the PHCL molecule was qualitatively examined using theoretical and experimental IR spectroscopy investigations. The Hirshfled surface analysis and fingerprint plots has been found to be a useful tool for identifying and quantifying various forms of intermolecular interactions.

Table 6.1. Summary of present work

S. No.	Description	2PA	PTCA	PBTA	PHCL	
1.	Molecular formula	C ₆ H ₅ NO ₂	$C_8H_6C_{13}NO_4$	$C_{12}H_{10}N_4O_2$	C ₆ H ₆ NO ₂ ⁺ Cl ⁻	
2.	Method / Solvent	Slow evaporation / Deionized water	Slow evaporation / Deionized water	Slow evaporation / Methanol	Slow evaporation / Deionized water	
3.	Crystal system	Monoclinic	Monoclinic	Orthorhombic	Orthorhombic	
4.	Space group	C2/c	$P2_{I}/n$	$Pna2_1$	Pnma	
5.	Structural determination	Centrosymmetric	Centrosymmetric	Non- Centrosymmetric	Centrosymmetric	
6.	UV cut-off wavelength (nm)	263	260	254	267	
7.	$\begin{array}{c} \textbf{Optical Band gap} \\ \textbf{(E}_g) \ \textbf{eV-Tauc's} \\ \textbf{plot} \end{array}$	3.5	4.25	3.49	3.80	
8.	$\begin{array}{c} \textbf{Optical Band gap} \\ \textbf{(E_g) eV-DASF} \\ \textbf{method} \end{array}$	3.47	3.83	3.46	4.44	
9.	Urbach energy (E _{Tail}) eV	0.01	0.19	0.11	0.27	
10.	SHG	-	-	2.2 times KDP	-	
11.	Third order Nonlinearity $\chi^{(3)}$ (esu)	2.95×10^{-6}	5.06×10^{-7}	-	3.75×10^{-6}	
12.	Theoretical basis set	B3LYP / 6-311++G(d,p)				
13.	Polarizability (esu)	1.316×10^{-23}	3.759×10^{-25}	2.58×10^{-23}	2.88×10^{-23}	
14.	First Hyperpolarizability (esu)	8.730×10^{-30}	2.796×10^{-28}	1.77×10^{-30}	1.29×10^{-29}	
15.	HOMO-LUMO gap (eV)	5.38	3.14	4	3.63	

6.2. SUGGESTIONS FOR FUTURE WORK

The crystals were grown using a slow evaporation solution growth approach,
and the results are presented in this dissertation. These crystals nucleation
kinetics have been studied, and these results could be exploited to create largescale crystals using the Sankaranarayanan – Ramasamy (SR) method and seed
rotation method for possible potential applications.

- Different studies, such as phase matching, optical limiting, and laser damage threshold, can be applied to the grown crystals, which can lead to fascinating results.
- Different organic solvents can be used to analyze the etching behavior of different crystallographic faces in order to discover dislocations and lattice inhomogenties, and then to compute crystallinity.
- Appropriate dopants can be used to change the NLO behavior of the grown crystals.
- Simulation theories based on classical nucleation and density functional theories with different basis sets could be used.



LIST OF PUBLICATIONS

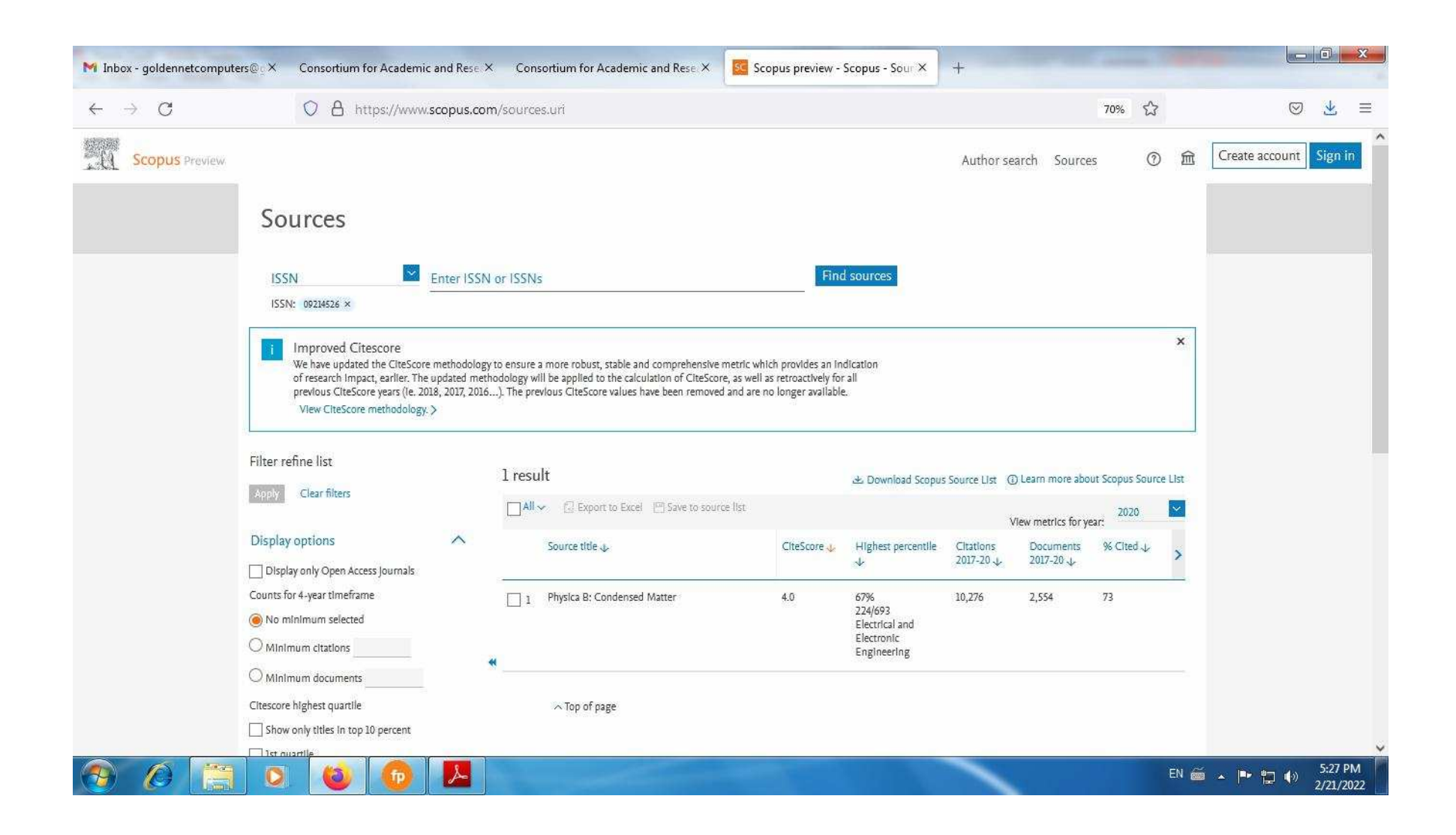
- 1. Theoretical investigation on growth kinetics and thermodynamic properties of pyridine-2- carboxylic acid crystals,
 - N Manopradha, S Rama, S Gowri, K Kirubavathi, K Selvaraju, Mechanics and Mechanical Engineering, 23 (2019) 23-27.
- 2. Spectroscopic and third order nonlinear optical properties of organic singlecrystal 2-picolinictrichloroacetate: an overview,
 - **N Manopradha**, S Gowri, S Rama, K Selvaraju, K Kirubavathi, G Vinitha, Bulletin of Materials Science, 43 (2020) 272.
- 3. Nucleation kinetics, Williamson-Hall analysis, hardness and dielectric properties of pyridine-2-carboxylictrichloroacetate single crystals,
 - N Manopradha, S Gowri, S Rama, K Selvaraju, K Kirubavathi,
 - Physica B: Physics of Condensed Matter, 624 (2021) 413397.
- 4. Experimental and theoretical investigation on nucleation kinetics, spectroscopic and third order nonlinear optical properties of 2-picolinic benzotriazole single crystals,
 - **N Manopradha**, S Gowri, S Rama, K Selvaraju, K Kirubavathi, G Vinitha, Optik (Under Review)
- 5. Nucleation kinetics, growth, spectroscopic and third order nonlinear optical properties of 2-picolinic hydochloride single crystals,
 - N Manopradha, S Gowri, S Rama, K Selvaraju, K Kirubavathi, G Vinitha, Journal of Molecular Structure (Under Review)

Paper Presented / Participated in Seminar, Conferences and Workshops

PAPER PRESENTED / PARTICIPATED IN SEMINAR, CONFERENCES AND WORKSHOPS

- Synthesis and growth mechanism of an organic single crystal: L-Alanine picolinate. Presented at National Seminar on Advanced Materials conducted by Department of Physics, Jamal Mohamed College, Trichy on 23rd January 2020.
- 2. Crystal Growth and Third-Order Nonlinear Optical Properties of Organic Single-Crystal 2-Picolinictrichloroacetate: An Overview. Presented at 4th International Conference on Recent Trends in Applied Science and Technology (ICRTAST-2020) conducted by Department of Physics, Bharathidasan University, Trichy on 26th December 2020 to 29th December 2020.
- 3. **Participated** in webinar on Quantum Mechanical Picture of Periodic Table conducted by Division of Chemistry, School of Advanced Sciences, Vellore Institute of Technology, Chennai on 06th June 2020.
- Participated in AICTE sponsored National level online Conference on Advances in Functional Materials organized by Department of Physics, Thanthai Periyar Government Institute of Technology, Vellore during 08th – 09th October 2020.
- 5. **Participated** in State Level Online Workshop on Fundamental Aspects of Quantum Mechanics organized by the Department of Physics, B.S. Abdur Rahman Crescent Institute of Science and Technology, Chennai in collaboration with Chennai Mathematical Institute, Chennai and The National Academy of Sciences, Allahabad during 29th October 2021 to 2nd November 2021.







Contents lists available at ScienceDirect

Physica B: Physics of Condensed Matter

journal homepage: www.elsevier.com/locate/physb





Nucleation kinetics, Williamson-Hall analysis, hardness and dielectric properties of pyridine-2-carboxylictrichloroacetate single crystals

N. Manopradha ^{a,c}, S. Gowri ^a, S. Rama ^b, K. Selvaraju ^c, K. Kirubavathi ^{c,*}

- ^a Department of Physics, Cauvery College for Women (Autonomous), Tiruchirappalli, 620 018, India
- ^b Department of Physics, St. Joseph's College of Engineering, Chennai, 600 119, India
- c PG & Research Department of Physics, Government Arts College (affiliated to Bharathidasan University), Ariyalur, 621 713, India

ARTICLE INFO

Keywords: Nucleation kinetics Williamson-Hall approach Optical band gap

ABSTRACT

The single crystals of pyridine-2-carboxylictrichloroacetate (P2CT) were synthesized using standard method at room temperature. Nucleation parameters such as, radius of critical nucleus, nucleation rate, and interfacial and volume free energy has been estimated. The solubility of the crystal at different temperatures is analyzed. Thermodynamic parameters from vibration analysis are compared with the enthalpy obtained from solubility to predict the stability of the crystal. X-ray diffraction investigating the structural aspects establishes the crystal structure belonging to crystal system as monoclinic nature. Williamson–Hall approach assesses the structural characteristics of the grown crystal: average crystallite size along with lattice strain. In between 220 and 1000 nm wavelength range, the optical absorption spectra of P2CT are recorded. Based on derivation of absorption spectrum fitting method, optical energy band gap and nature of optical transitions in the crystal is determined. Vickers microhardness test estimates the hardness parameters and elastic stiffness is evaluated through Wooster's empirical relation.

1. Introduction

Researchers recently are drawn appreciably to growing organic single crystals for their utility in band gap materials to direct and organize the course of light [1,2]. The crystalline organic materials enable calibration of their optical properties through molecular engineering and chemical synthesis [3,4]. Carboxylic acids are the fascinating organic materials in the optical applications because of their potential to form H – bonding interactions. 2-carboxypyridine is one such carboxylic acid that likely creates stable compound such as Pyridine-1-ium-2-carboxylatehydrogenbromide and phosphoric acid pyridine-1-ium-2-carboxylate [5,6]. The material synthesis, structure and spectroscopic properties of P2CT crystals have earlier been reported [7]. The present investigations are novel in reporting the nucleation kinetics and its parameters. The study also involves the growth, optical, mechanical and dielectric characterization of P2CT single crystals. The obtained results are discussed.

Nucleation kinetics bestows details of optimal growth conditions, nucleation rate and solution supersaturation, which characterize the growth of flawless bulk crystals [8]. The nucleation parameters like interfacial energy (σ) , volume free energy (ΔG_v) , critical energy barrier

for nucleation (ΔG^*) , radius of the critical nucleus (r^*) and nucleation rate (J) were evaluated [9,10]. The thermodynamic parameters from the vibration analysis were compared to the enthalpy obtained from solubility to predict the stability of the crystal. The lattice strain was evaluated by means of Williamson–Hall analysis. The optical band gap and other optical parameters were estimated by using Derivation of absorption spectrum fitting (DASF) method [11]. This method determines the type of optical transition more precisely and more directly in contrast to Tauc's method [12]. Mechanical and dielectric studies of P2CT have also been conducted alongside, and its results are conveyed.

2. Experimental

2.1. Preparation of the crystal

Commercially available 2-carboxypyridine and tricholoroacetic acid were separately dissolved in demineralized water and the raw materials for crystal growth were synthesized. Tricholoroacetic acid solution was then added slowly to the 2-picolinic acid solution and stirred well using a magnetic stirrer to get a homogeneous mixture. The filtered solution was allowed to evaporate at room temperature and transparent crystals

^{*} Corresponding author. Post Graduate & Research Department of Physics, Government Arts College, Ariyalur, 621 713, Tamilnadu, India. E-mail address: kkirubaphysics@gmail.com (K. Kirubavathi).

were harvested in three weeks time [7].

3. Results and discussion

3.1. Powder XRD

Powder X-Ray diffraction study at the grown crystal was done by employing BRUKER X-ray diffractometer with 1.5406 Å CuK $_{\alpha}$ radiation using step size: 0.0130° and scanning step time: 23.97s. The process was carried out on room temperature with the aim of checking the phase purity. In the obtained diffraction pattern, well-defined peaks at specific 20 angle can be seen, which corresponds to excellent quality of the crystalline material [Fig. 1]. The lattice parameters of the P2CT crystal obtained from FullProf Suite software [13] are a = 6.134 (7) (Å), b = 22.140 (30) (Å), c = 8.049 (9) (Å), $\alpha = \gamma = 90^{\circ}$, $\beta = 95.755$ (8) and volume = 1087.8 (2), monoclinic system with space group $P2_1$. It is consistent with the reported values [7]. Further, using Williamson–Hall equation the strain present in the grown crystal is evaluated [14]:

$$\beta cos\theta = \frac{K\lambda}{\tau} + \eta sin\theta \tag{1}$$

where, β - FWHM of the diffraction peak, θ - Bragg's diffraction angle, K-Scherrer constant, λ -wavelength of the X-rays, τ -crystallite size, η -lattice strain. Plotting the $\beta cos\theta$ versus $sin\theta$ [Fig. 2] and fitting the data linearly, the crystallite size (τ) is obtained by Williamson-Hall method

$$\tau = \frac{k\lambda}{y - axis\ intercept} \tag{2}$$

whose value is \sim 0.1 µm and lattice strain (slope of the fitted line), is 0.006 which alludes P2CT crystal has less lattice strain. It suggests larger elastic stiffness constant, which is discussed in microhardness section [15].

3.2. Solubility studies

The solubility studies of P2CT were pursued through a constant temperature bath with temperature accuracy $\pm 0.01^{\circ}\text{C}$. The solute was added to double distilled water until the saturation condition was reached. The equilibrium concentration of the solute was analyzed gravimetrically. The experiment was done again at different temperatures [Fig. 3]. It is observed that the solubility of material increases with an increase in temperature and nucleation temperature increases with the increase in concentration. Thus the grown crystal has a positive temperature coefficient of solubility.

3.3. Nucleation kinetics and metastable zone width (MZW)

Interfacial energy of the solid and liquid inter phase plays a key role in the nucleation process. Based on the solution theory, Bennema and Sohnel [16] have derived an expression that explains the linear dependence of interfacial energy (σ) on solubility

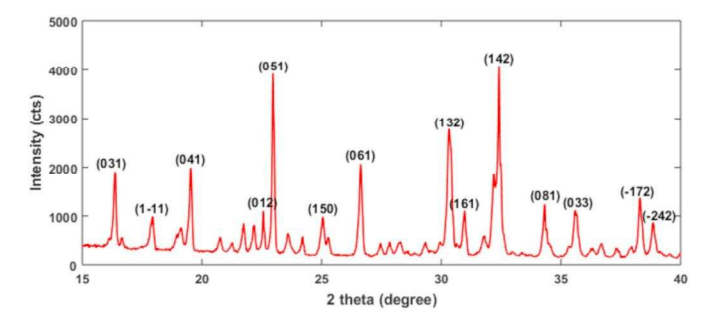


Fig. 1. Powder XRD pattern of P2CT crystal.

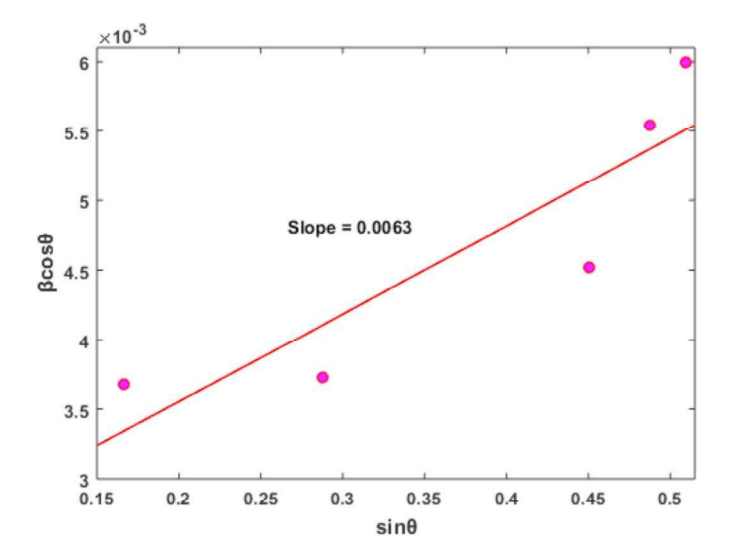


Fig. 2. Graph plotting $\beta\cos\theta$ versus $\sin\theta$.

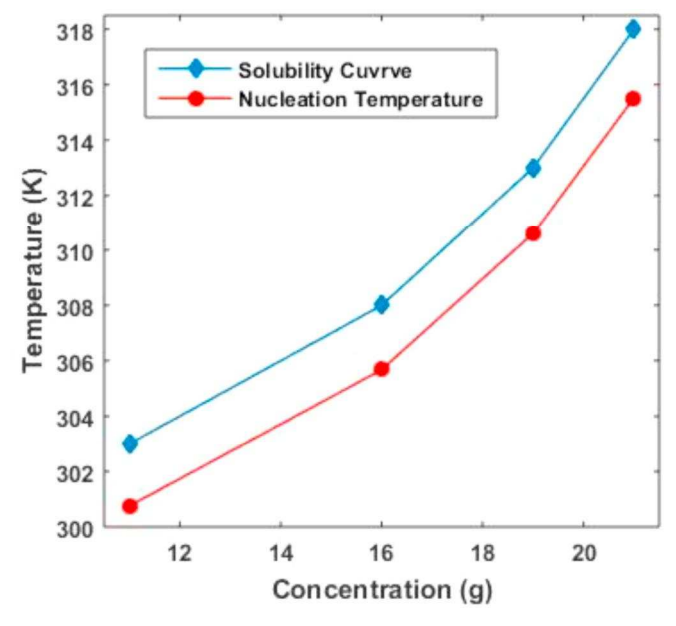


Fig. 3. Solubility curve for P2CT.

$$\sigma = (KT/d^2)[0.173 - 0.248 \ln \chi_m] \quad (J/m^2)$$
(3)

Where, K - Boltzmann constant (JK^{-1}) , T - Temperature (K), d - mean molar ionic diameter $[d = \{(6/\pi)v\}^{1/3}]$, χ_m - mole fraction of solute in solution.

The correlation of solubility and the enthalpy is [17]:

$$ln \chi_m = (-\Delta H s / RT) + (\Delta S_E / R)$$
(4)

Where ΔHs - Enthalpy of fusion (Jmol⁻¹), R - Gas constant (J K⁻¹mol), ΔS_E - Excess entropy of mixing.

Change in entropy per unit volume is given as

$$\Delta G_{v} = -\left\{\frac{KTlnS}{V}\right\} \tag{5}$$

Where, V - specific volume of the solute molecule. Critical radius is expressed as,

$$r^* = -\frac{2\sigma}{\Delta G_c} \tag{6}$$

Critical energy barrier of the critical nucleation is derived from

$$\Delta G^* = \frac{16\pi\sigma^3}{3\Delta G_v^2} \tag{7}$$

The number of molecules in the critical nucleus is stated by

$$i^* = \frac{4\pi (r^*)^3}{3V} \tag{8}$$

The rate of nucleation (J) is calculated from the equation:

$$J = Aexp\left(\frac{-\Delta G^*}{KT}\right) \tag{9}$$

The estimated nucleation parameters of P2CT crystal at various super saturation values from the above formulas are tabulated in Table 1.

The change in free energy per unit volume (ΔG_v) decreases with increasing the supersaturation which drives the crystallization process. Fig. 4 shows the variation in energy barrier (ΔG^*) with respect to temperature. Fig. 5 shows the change in critical radius (r^*) as a function of temperature as well as the supersaturation. A decrease in interfacial energy (σ) (as shown in Table 1) with higher value of temperature leads to decrease in radius of critical nuclei, causing the diminished free energy in the system. The classical nucleation theory diagram implies that when volume free energy decreases and surface free energy increases the crystal growth initiates.

The knowledge of MZW will help in the selection of optimum rate of supersaturation generation to avoid the exercise of secondary nucleation. MZW (ΔT_{max}) for each saturation temperature is obtained from the relation

$$\Delta T_{max} = \frac{RT^2}{\Delta H_s} (S - 1) \tag{10}$$

Where, the value of enthalpy is obtained from eq (4) by plotting $\ln \chi_m$ vs 1/T which gives a straight line, the slope of which is equal to $\Delta H_s/R$. The present study involves reporting theoretically calculated values of metastable zone width for the crystallization temperatures of crystals by slow evaporation method. From the results it is observed that zone width slightly broadens as temperature rises.

3.4. Equilibrium concentration of P2CT crystal

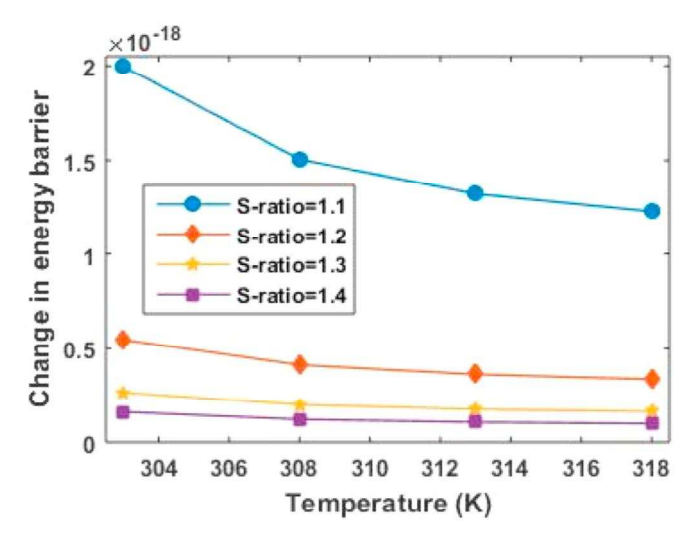
The solubility data of P2CT crystal are fitted to a second order polynomial equation form for all the equilibrium temperatures [18].

$$C_{\text{sat}} = -0.03T^2 + 19.29T - 3080 \tag{11}$$

Correlative equation (11) is used to obtain the saturation concentration of any temperature for P2CT crystal. Table 2 shows thermodynamic values obtained from NIST thermo.pl program [19]. The procured results reveal that Gibbs free energy decreases as the temperature increases. This enhances the growth of the crystal.

3.5. UV-Vis-DRS (Diffuse Reflection Spectroscopy) analysis

The absorption spectra of the P2CT crystal are depicted in Fig. 6. In the current work, precise DASF method is made use of to find the band $\frac{1}{2}$



 $\begin{tabular}{ll} {\bf Fig.~4.~Variation~of~energy~barrier~with~supersaturation~and~temperature~for~P2CT.} \end{tabular}$

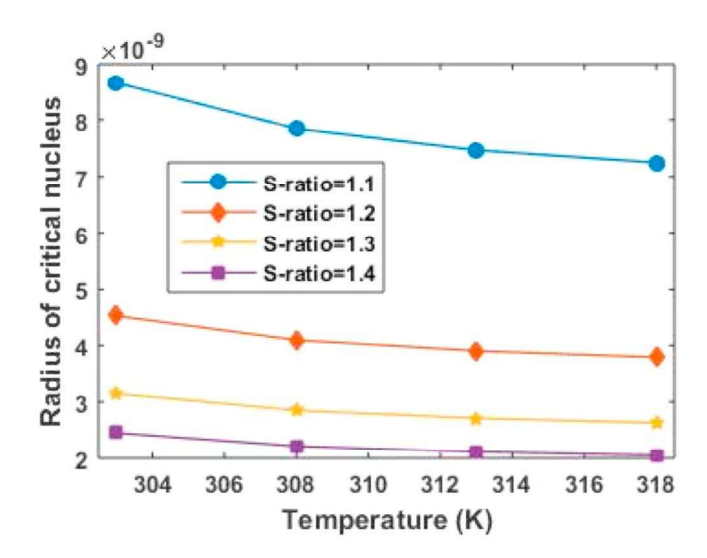


Fig. 5. Variation of radius of critical nucleus with temperature and supersaturation ratio of P2CT.

Table 2
Thermodynamics values.

T (K)	S (J/mol.K)	Cp (J/mol.K)	ddH (kJ/mol)	Gibbs free energy (j)
303	586.360	246.917	46.408	-177620.672
308	590.423	249.619	47.649	-181802.635
313	594.465	252.298	48.904	-186018.641
318	598.484	254.954	50.172	-190267.740

gap energy.

The ratio of the optical absorbance (A) and the wavelength of the radiation (λ) is given by Refs. [11,20].

 Table 1

 Nucleation table from P2CT for super saturation Ratio-1.1

T (K)	$\Delta G_{\rm v}({\rm J/m}^3)$	$\sigma (J/m^2)$	ΔG* (J)	r* (m)	i*	J (nuclei/m³/sec)
303	-1466231.2	0.006351	1.99E-18	8.66E-09	10015.636	1.45898E+13
308	-1490426.4	0.005845	1.51E-18	7.84E-09	7431.595	1.19578E+13
313	-1514621.6	0.005655	1.32E-18	7.47E-09	6412.663	1.08382E+13
318	-1538816.9	0.005577	1.23E-18	7.25E-09	5864.569	1.02114E+13

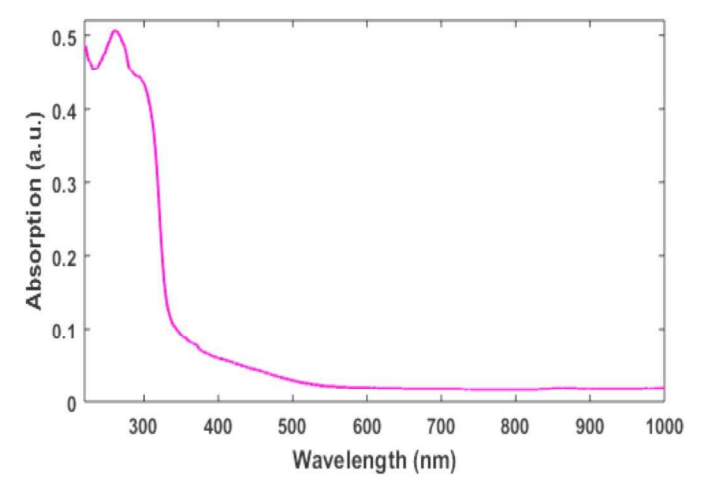


Fig. 6. Optical absorbance of P2CT.

$$\frac{d\left(\ln\frac{\Delta}{\lambda}\right)}{d\left(\frac{1}{\lambda}\right)} = \frac{m}{\frac{1}{\lambda} - \frac{1}{\lambda_{\varepsilon}}} \tag{12}$$

In the above equation,

 λ_{g} - wavelength attributed to the energy gap, m - optical transition index of charge carriers.

From Fig. 7, optical energy band gap is acquired by using λ_g ,

$$E_g^{DASF} = \frac{1239.83}{\lambda_g} \ (eV) \tag{13}$$

This is done devoid of any assumption about the nature of charge carrier transition.

From the slope of Fig. 8, the value of m is acquired. Present analysis expose the value of m near to 1/2, which indicates P2CT has the direct band gap and direct allowed transition of charge carriers [15].

An exponential part called Urbach tail is present near the optical band edge in the absorption coefficient curve. This exponential tail appears to be more for poor crystalline materials which are disordered in lattices and for amorphous materials. If this tail appears to be minimum, this indicates good crystalline nature and also good perfection in lattice sites [21]. Urbach equation is expressed as,

$$A(\lambda) = kexp\left(\frac{hc}{E_{Toil}\lambda}\right) \tag{14}$$

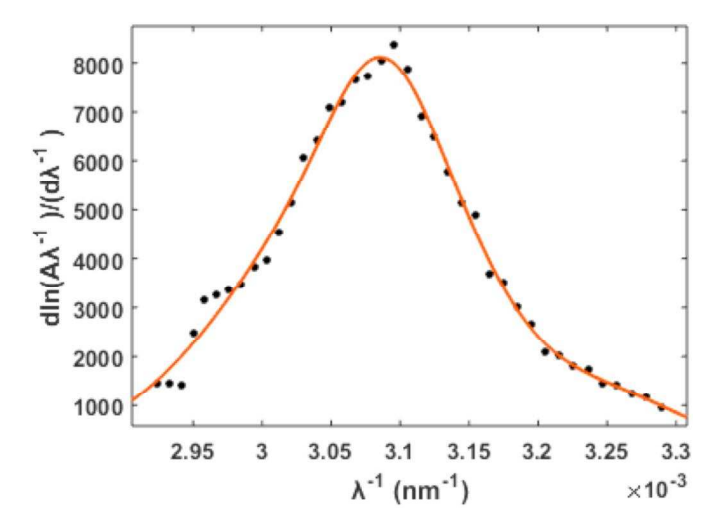


Fig. 7. DASF plot for P2CT crystal.

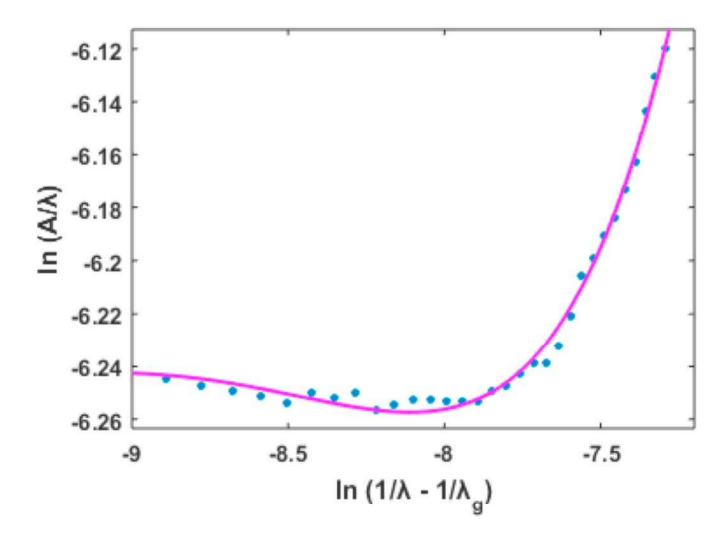


Fig. 8. Curves of ln (A/ λ) vs ln (1/ λ - 1/ λ_g).

where h - Planck's constant, c - light speed, k - constant, E_{Tail} - width of the tail of the localized states adjacent to bands.

The Urbach energy value is obtained from equation $E_{Tail} = \frac{1239.83}{Slope}$ (eV), where the slope is acquire from linear fit established in the straight-line segment of the graph of ln (A) in terms of λ^{-1} (Fig. 9) [22]. The obtained value of E_{Tail} is 0.19 eV. The minimal value of E_{Tail} , imparts the P2CT crystal has less disorder in near band edge in addition to perfect crystalline quality [23,24].

Steepness parameter σ is derived from the equation:

$$\sigma = \frac{K_B T}{E_{Tail}} \tag{15}$$

The electron-phonon interaction $(E_{\text{e-p}})$ is measured through the relation:

$$E_{e-p} = \frac{2}{3\sigma} \tag{16}$$

Apart from these, refractive index (n) and dielectric constant (ε_d) at the absorption edge were estimated by applying the disclosed energy gap values in the equation below [25]:

$$\frac{n^2 - 1}{n^2 + 1} = \left(1 - \frac{E_g^{DASF}}{20}\right)^{\frac{1}{2}} \tag{17}$$

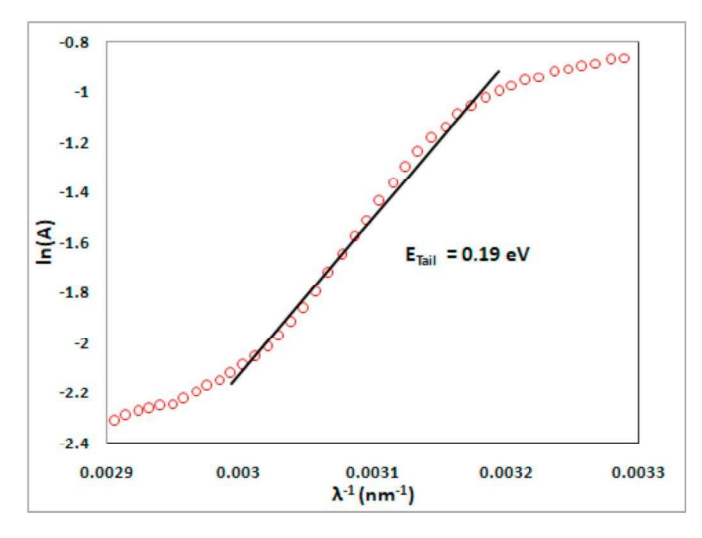


Fig. 9. Urbach plot for P2CT.

$$\varepsilon_d = n^2 \tag{18}$$

The results obtained (Table 3) from the optical studies reveal that the P2CT crystal holds good optical behavior for NLO applications [26].

3.6. Microhardness study

The mechanical strength of P2CT crystal is assessed using Vickers micro hardness tester, fitted with a Vickers diamond pyramidal intender. The indentation is measured for various loads from 2g to 100g. The hardness parameters are calculated and listed in Table 4, using the relation [27].

$$H_{v} = 1.854 \ P/d^{2}kg/mm^{2} \tag{19}$$

Where, H_v - Vickers micro hardness number (kg/mm^2) , P- applied load (kg), d - average diagonal length of the impression (mm). Fig. 10a graphs the increase in hardness number for increase in load. The Meyer's index number [28] is determined from the relation $P = kd^n$ where k is the material constant and n, the "Meyer's index". By linear square fitting (Fig. 10b) the value of n is obtained as 3.8. According to Hanneman [29], the value of n is around 1–1·6 for hard materials and beyond 1·6 for the softer ones ascertaining P2CT categorized under soft material group. Fig. 10c reveals the title compound to exhibit reverse indentation size effect (RISE) indicative of plastic deformation predominance.

On the basis of Hays-Kendall's model, load dependent hardness is measured employing the following equation [30]:

$$P = W + A_1 d^n (20)$$

Where 'W' - minimum load initiate plastic deformation, A_1 - load independent constant, n=2. The value of W and A_1 are calculated from the graph drawn between P and d^2 . These two values from Fig. 11 are -135.7g and $0.065~(g/\mu m^2)$ respectively. The corrected hardness (H_0) calculated using the relation $H_0=1854.4~x~A_1$ is 97.08 (kg/mm²). Elastic stiffness constant (C_{11}) is estimated by Wooster's empirical relation [31]. From Fig. 12 it is evident that the elastic stiffness constant increases with increase in load, which authenticates the tightness of bonding between the neighboring atoms [32].

3.7. Dielectric studies

With the assistance of Digital LCRZ meter with frequency region ranging between 50 Hz and 200 KHz, dielectric studies of the P2CT crystals have been conducted at variant temperatures. Fig. 13a and b depicts the graph of the dielectric constant and the dielectric loss of P2CT as a function of frequency at temperatures viz. 308, 313, 318 and 323 K, respectively. Fig. 13a portrays the dielectric constant of the grown crystal has larger value at low frequencies. This is probably due to the existence of ionic, electronic, dipole orientation and space charge polarizations. Furthermore the decrease in dielectric constant at higher frequency is caused by drop in net polarization of the material. As a result of space charge polarization owing to charged lattice defect, dielectric loss is reduced at high frequencies (Fig. 13b) [33,34]. The AC conductivity (σ_{ac}) of P2CT crystals in Fig. 13c limelights conductivity to

Table 3 Optical parameters of P2CT.

Optical parameters (DASF method)	Values
λ_{g} (wavelength of energy gap)	323 nm
$1/\lambda_{\rm g}$	0.0031
E _g (optical energy band gap)	3.83 eV
E _{Tail} (Urbach energy)	0.19 eV
σ (steepness parameter)	0.12
E _{e-p} (electron-phonon interaction)	5.56
n (refractive index)	1.88
$\varepsilon_{ m d}$ (dielectric constant)	3.56

Table 4Hardness parameters of P2CT.

Load P (g)	H_v (kg/mm ²)	d (μm)	C ₁₁ x 10 ¹⁵ (Pa)	σ _v (MPa)
2	3.65	31.88	0.016574227	0.005845755
5	4.46	45.61	0.023537307	0.007143032
10	8.09	47.87	0.066731468	0.012956756
25	18.1	50.62	0.273122997	0.028988539
50	33.8	52.38	0.814751162	0.054133294
100	50.1	60.82	1.622320975	0.080238995

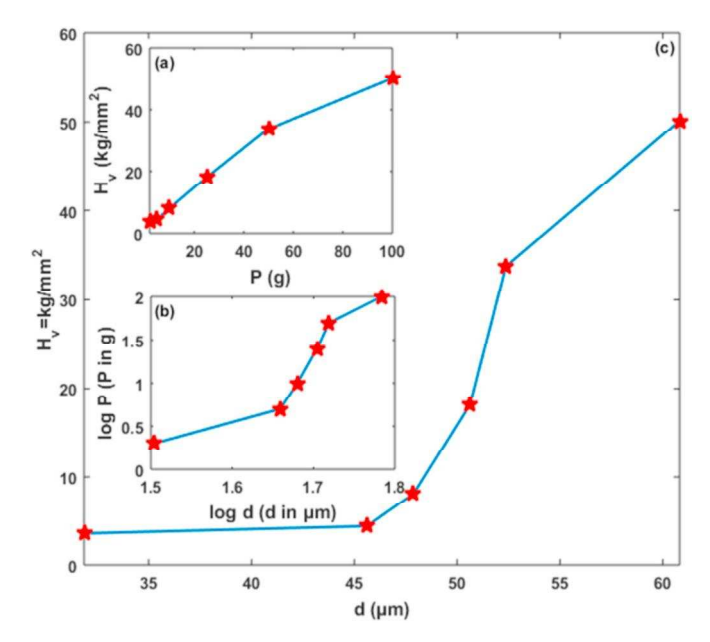


Fig. 10. (a) variation of H_v against the applied load P (b) log P against log d (c) H_v against d.

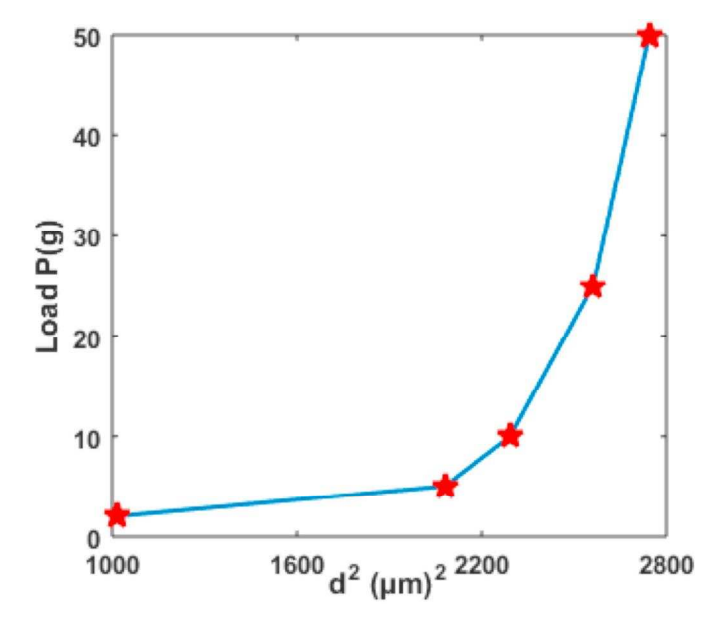


Fig. 11. Load P against d.².

be frequency dependent as it increases rapidly at higher frequencies. Based on the above results, the title compound proves to be right component for device fabrication in electro-optic devices and photonics industries [35].

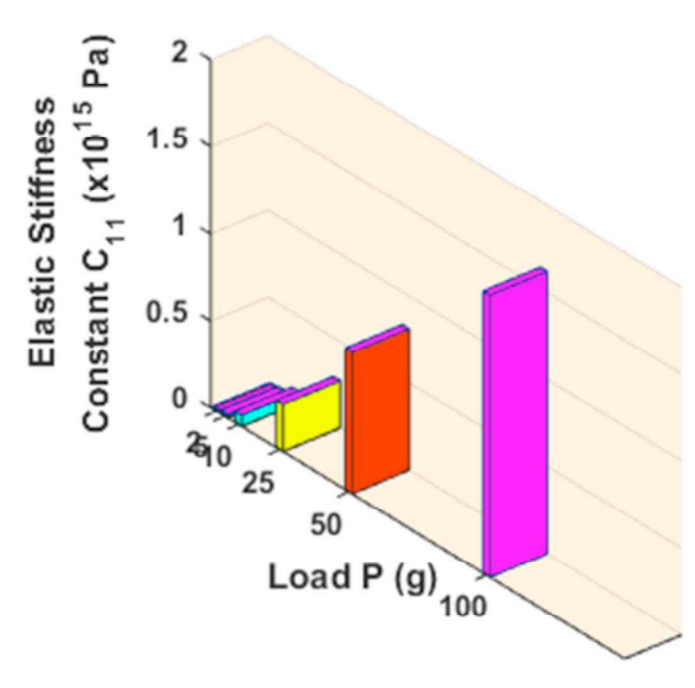


Fig. 12. Load P against elastic stiffness constant (C_{11}) .

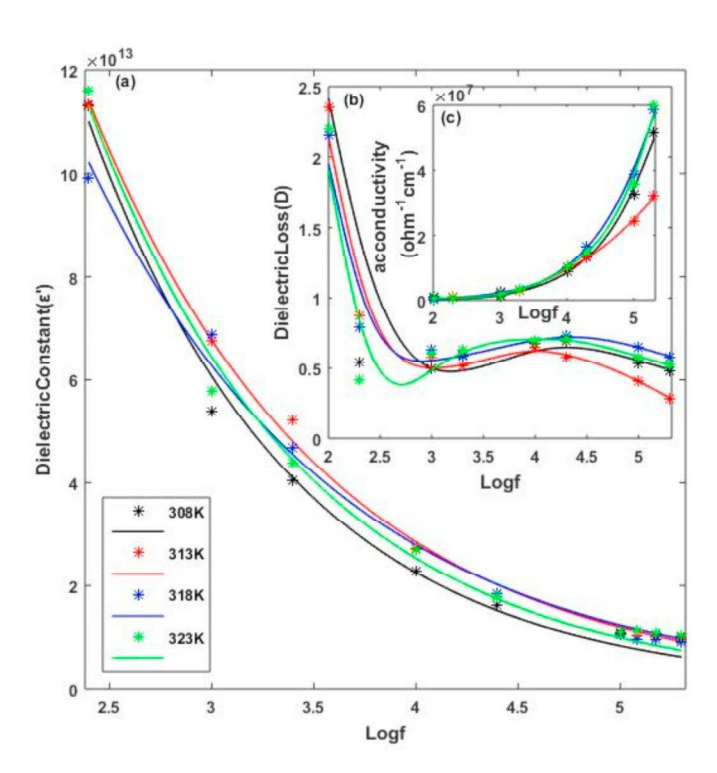


Fig. 13. (a) Variation of dielectric constant with frequency at various temperatures. (b) Variation of dielectric loss with frequency at various temperatures. (c) AC conductivity of P2CT crystals as a function of Log f.

4. Conclusion

Nucleation kinetics of grown crystal is studied. The estimated values of nucleation parameters are in agreement to one another. The minimum value of lattice strain on the grown crystal suggests lower dislocation density. DASF method used to acquire the optical band gap and other optical parameters interpret the optical band gap of title crystal equal to 3.83eV. On the basis of mechanical studies, P2CT crystal turns out be soft category. The value of C_{11} points out stiffness of bonding between

neighboring atoms. The electrical properties of the title crystal at different temperatures viz., 308K, 313K, 318K and 323K confirms reduced dielectric loss at higher frequencies, which in turn establishes P2CT to be of good quality crystal with minimum defects.

Credit author statement

N. Manopradha: Experimentation, Methodology and writing. S. Gowri: review editing and Writing. S. Rama: Resources, Data curation and software. K. Selvaraju: Critical revision and drafting. K. Kirubavathi: Conceptualization, Supervision and editing

Declaration of competing interest

The authors declare that they have no known competing financial interests or personal relationships that could have appeared to influence the work reported in this paper.

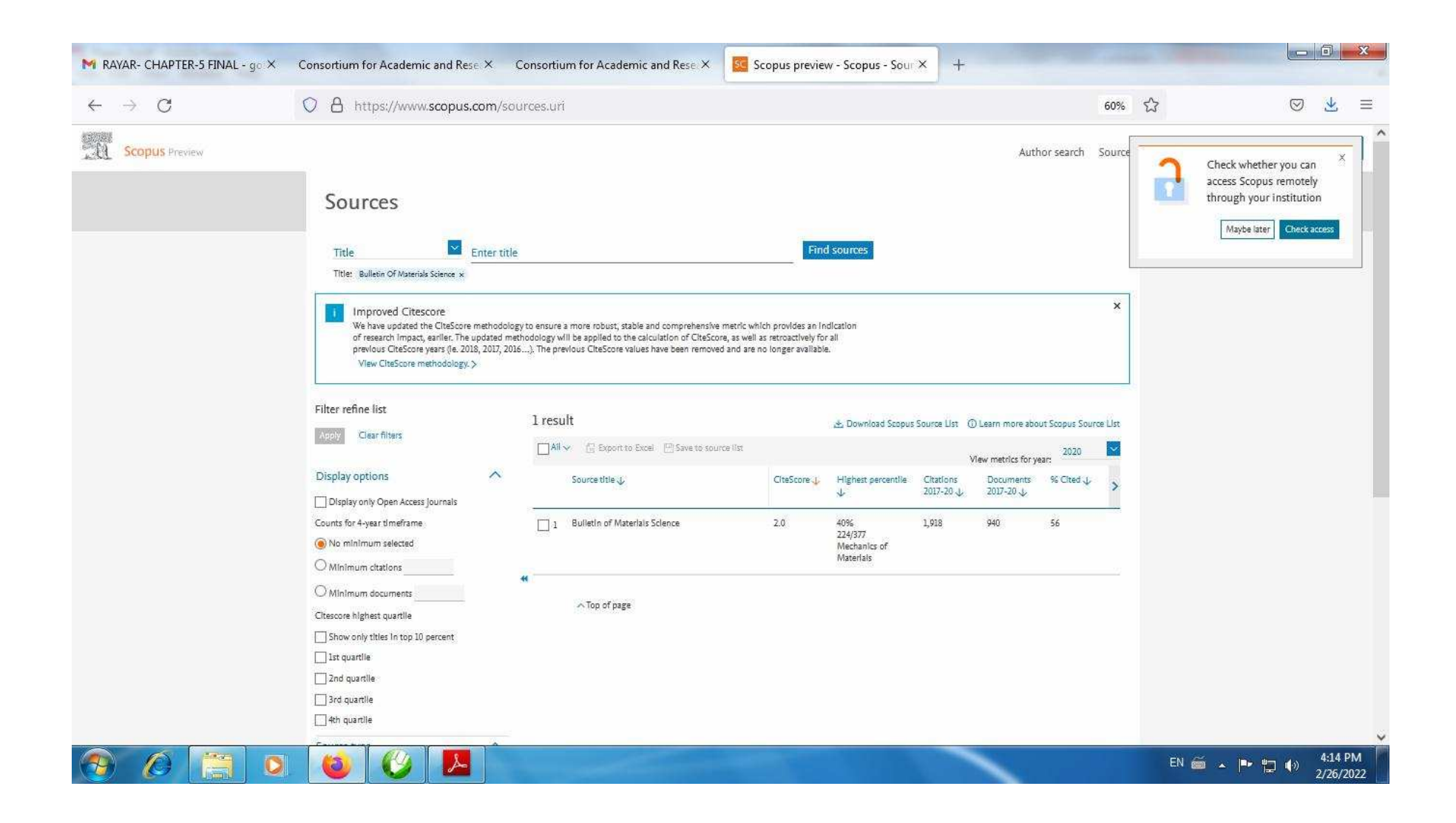
Acknowledgement

The authors thank Cauvery College for Women (Autonomous), Tiruchirappalli, for providing instrument facility under the support of DST-FIST-Level'0' program (Ref.No.SR/FST/College-246/2015(c)).

References

- [1] Yuri S. Kivshar, Opt Express 16 (2008) 22126-22128.
- 2] Mao-Liang Xu, Ming-Tao Li, Zi-Ruo Hong, Wen-Lian Li, An Zhong-Wei, Qun Zhou, Opt. Mater. 28 (2006) 1025–1028.
- [3] T. Jayanalina, G. Rajarajan, K. Boopathi, Dig. J. Nanomater. Biostructures 10 (2015) 1139–1151.
- [4] T. Chen, Z. Sun, L. Li, S. Wang, Y. Wang, J. Luo, M. Hong, J. Cryst. Growth 338 (2012) 157–161.
- [5] S. Gowri, T. Uma Devi, S. Priya, C. Surendra Dilip, S. Selvanayagam, N. Lawrence, Spectrochim. Acta 143 (2015) 192–199.
- [6] S. Gowri, T. Uma Devi, S. Alen, D. Sajan, C. Surendra Dilip, G. Vinitha, J. Mater. Sci. Mater. Electron. 29 (2018) 19710–19723.
- [7] S. Gowri, K. Anitha, A. Suresh, T. Uma Devi, S. Selvanayagam, D. Sajan, A. Chandramohan, N. Lawrence, Spectrochim. Acta 95 (2012) 73–79.
- [8] Senthilkumar Chandran, Rajesh Paulraj, P. Ramasamy, J. Cryst. Growth 468 (2016) 68–72.
- S. Rama, C. Surendra Dilip, Rajesh Narayana Perumal, J. Cryst. Growth 409 (2015) 32–38.
 J. N. Narayana the G. Rama, G. Cavrei, V. Kimbayanthi, V. Calvaraita, Mach. Mach. Pag.
- [10] N. Manopradha, S. Rama, S. Gowri, K. Kirubavathi, K. Selvaraju, Mech. Mech. Eng. 23 (2019) 23–27.
- [11] Dariush Souri, Zahra Esmaeili Tahan, Appl. Phys. B 119 (2015) 273–279.
- [12] S. Terny, M.A. Frechero, Physica B 583 (2020) 1–29.
- [13] I.Md Zahid, C. Amirtha Kumar, A. Malarkodi, K.S. Joseph Wilson, R. Mohan Kumar, Mater. Lett. 209 (2017) 167–170.
- [14] N. Vijayan Sonia, Medha Bhushan, Kanika Thukral, Rishabh Raj, K.K. Maurya, D. Haranath, S.A. Martin Britto Dhas, J. Appl. Crystallogr. 50 (2017) 763–768.
- [15] Yazdan Shahmoradi, Dariush Souri, Ceram. Int. 45 (2019) 7857-7864.
- [16] P. Bennema, O. Sohnel, J. Cryst. Growth 102 (1990) 547–556.
- [17] S. Rama, C. Surendra Dilip, Rajesh Narayana Perumal, Comput. Phys. Commun. 185 (2014) 661–669.
- [18] N. Tagmatarchis, E. Aslanis, K. Prassides, H. Shinohara, Chem. Mater. 13 (2001) 2374–2379.
- [19] K.K. Irikura, THERMO.PL, National Institute of Standards and Technology, 2002.
- [20] D. Souri, A.R. Khezripour, M. Molaei, M. Karimipour, Curr. Appl. Phys. 17 (2017) 41–46.
- [21] G. Iyappan, Rajesh Raulraj, Ramasamy Perumalsamy, Kamalesh Kumar Maurya, Soma Venugopal Rao, Ferroelectrics 550 (2019) 151–172.
- [22] D.S. Arteev, A.V. Sakharov, E.E. Zavarin, W.V. Lundin, A.N. Smirnov, V Yu Davydov, M.A. Yagovkina, S.O. Usov, A.F. Tsatsulnikov, J. Phys. Conf. Ser. 1135 (2018), 012050.
- [23] F. Urbach, Phys. Rev. 92 (1953) 1324.
- [24] S.J. Ikhmayies, R.N. Ahmad-Bitar, J. Mater. Res. Technol. 2 (2013) 221-227.
- [25] V. Dimitrov, S. Sakka, J. Appl. Phys. 79 (1996) 1736–1740.
- [26] Rejeena V. Rajan, S. Gowri, N. Manopradha, D.R. Leenaraj, Lija K. Joy, D. Sajan, Opt Laser. Technol. 119 (2019) 105664.
- [27] T. Pal, T. Kar, Mater. Lett. 59 (2005) 1400-1404.
- [28] Min Jin, Jiayue Xu, Xinhua Li, Hui Shen, Qingbo He, Mater. Sci. Eng., A 472 (2008) 353–357.
- [29] P. Karuppasamy, Muthu Senthil Pandian, P. Ramasamy, S.K. Das, Optik 156 (2018) 707–719.
- [30] J. Mary Linet, S. Dinakaran, S. Jerome Das, J. Alloys Compd. 509 (2011) 3832–3836.
- [31]] W.A. Wooster, Rep. Prog. Phys. 16 (1953) 62-82.

- [32]] P. Nisha Santha kumari, S. Kalainathan, N. Arunai Nambi Raj, Mater. Lett. 62 (2008) 305–308.
 [33] N. Goel, N. Sinha, B. Kumar, Opt. Mater. 35 (2013) 479–486.
- [34] J. Balaji, P. Srinivasan, S. Prabu, Merin George, D. Sajan, J. Mol. Struct. 1207 (2020) 1–27.
 [35] C. Balarew, R. Duhlev, J. Solid State Chem. 55 (1984) 1–6.





Spectroscopic and third-order nonlinear optical properties of organic single-crystal 2-picolinictrichloroacetate: an overview

N MANOPRADHA^{1,2}, S GOWRI¹, S RAMA³, K SELVARAJU², K KIRUBAVATHI^{2,*} o and G VINITHA⁴

- ¹Department of Physics, Cauvery College for Women (Autonomous), Tiruchirappalli 620 018, India
- ²PG and Research Department of Physics, Government Arts College (Affiliated to Bharathidasan University), Ariyalur 621 713, India
- ³Department of Physics, St. Joseph's College of Engineering, Chennai 600 119, India
- ⁴Department of Physics, School of Advanced Sciences, VIT, Chennai 600 127, India

MS received 3 April 2020; accepted 23 June 2020

Abstract. Organic single crystals of 2-picolinictrichloroacetate (PTCA) have been successfully grown by slow evaporation technique. The structural and optical characterization of the PTCA is analysed experimentally by Fourier transform infrared and UV-visible spectroscopic technique and theoretical studies, by density functional theory method. The charge transfer interactions leading to nonlinear properties taking place in the molecule have been studied by highest energy occupied molecular orbital and lowest energy unoccupied molecular orbital analysis and natural bond orbital analysis. Open-aperture Z-scan results on evaluating the nonlinear optical properties experimentally, confirm these materials as good optical limiters. In addition, the PTCA exhibits a blue luminescence emission which shows that it is a potential material for OLED device applications.

Keywords. Vibrational analysis; Hirshfeld surface; fluorescence; Z-scan studies.

1. Introduction

Demand for nonlinear optical (NLO) materials are skyscraping in the area of laser applications, which include second-harmonic generation (SHG), mode-locking and Q-switching [1]. Organic NLO crystals fulfill those needs with their quick response, high NLO productivity and high laser damage threshold compared to inorganic NLO materials [2,3]. Consequently, organic single-crystal compound, 2-picolinictrichloroacetate (PTCA), is chosen for study. Titular compound is preferred as recent researches on pyridine and pyridine derivatives exposed their excellent optical, magnetic, medicinal and biological properties [4].

The material synthesis, structural, spectral and thermal properties of PTCA crystals have been reported earlier [5]. The present work focuses on experimental study and quantum chemical calculations of PTCA crystal. The study is bent upon to elucidating the correlation between the molecular structure and the NLO property together with the theoretical spectral simulations using the density functional theoretical (DFT) computations. The natural bond orbital (NBO) analysis explores the interaction between inter- and

intra-molecular charge transfers. The quantum chemical molecular orbital parameters have been evaluated from Frontier molecular orbitals analysis. Hirshfeld surface maps and fingerprint graphs are plotted to understand the various types of intermolecular interactions in the molecular crystal package. The third-order non-linear absorption behaviour of PTCA has been experimentally studied using open-aperture Z-scan technique and theoretically by hyperpolarizabilities.

2. Procedure

2.1 Preparation of the crystal

Commercially available 2-carboxypyridine and trichloroacetic acid are combined in equimolar ratio and dissolved in double distilled water. The solution is stirred well using a temperature controlled magnetic stirrer to yield a homogeneous mixture. Then as a result of evaporation of the filtered solution at room temperature, transparent single crystals have been harvested in 3 weeks time. Successive recrystallization and filtration account for the purity of the crystal (figure 1).

Published online: 09 October 2020

^{*}Author for correspondence (kkirubaphysics@gmail.com)



Figure 1. As-grown crystal of PTCA.

2.2 Computational details

All the theoretical calculations have been performed using the GAUSSIAN 09W [6] program of DFT with B3LYP method 6-311++G(d,p) as the basis set [7]. With the help of the GAUSSVIEW 5.0 molecular visualization program [8], the results of the molecule have been visualized.

3. Results

3.1 Optimized geometry

The optimized geometries of PTCA with symbols and numbering scheme for the atoms are shown in figure 2. Table 1 lists main structural parameters of PTCA maximized at DFT/B3LYP/6-311++G(d,p) level. The global minimum energy value measured by the DFT structure optimization method is -5.372×10^6 kJ mol⁻¹. The computed bond lengths show slightly higher readings than the X-ray data, as the theoretical values correspond to the isolated molecules in gas-phase, whereas the experimental results are correlated with the molecules in solid state [9]. The optimized structure reveals intermolecular hydrogen bonding of the type N10-H22^{...}O4 (2.941 Å), taken place due to linkage of cations to anions forming ion pairs through the H22N10 atom. Protonation effected between COO atoms and NH+ group of hydrogen bonding is confirmed by the increase in C11-N10 (1.361 Å) and C15-N10 (1.340 Å) and C15-N10-C11 (123.0 $^{\circ}$) bond angle. The increase in N10-H22 (1.017 A) reveals strong intramolecular hydrogen bonding N10-H22^{...}O5 (2.964 Å). Despite the differences, calculated geometric parameters show a

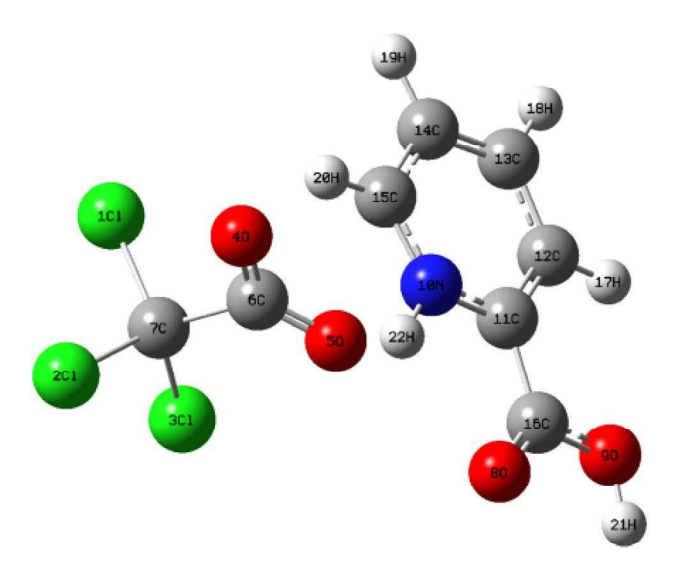


Figure 2. The optimized molecular structure of PTCA.

good approximation and hence can be used to calculate other parameters reported below.

3.2 Vibrational spectral analysis

The structural units of the PTCA are confirmed by Fourier transform infrared (FTIR) spectroscopy through the KBr pellet technique. The FTIR spectrum of the grown PTCA crystals records the frequency region to be 4000–400 cm⁻¹ using Perkin-Elmer spectrometer. The vibrational analysis is performed using DFT method B3LYP/6-311++G(d,p)level basis set. The calculated and measured wavenumbers and their assignments are tabulated in table 2. The simulated and observed FTIR spectra are presented in figure 3. Broad N-H stretch is visible in the region 3300-2500 cm⁻¹. C-H stretch at 3056 cm⁻¹ is superimposed upon N-H stretch, which is calculated at 3195 cm⁻¹. The fine structure on the lower frequency side of the broad N-H band suggests the overtone and combination of bands at longer wavelength. The normal C=O stretch around 1709 cm⁻¹ of the carboxylic acid is recorded at 1698 cm⁻¹. The C-O-H in plane bend observed at 1449 cm⁻¹ agrees with the calculated wavenumber 1423 cm⁻¹. Also, aromatic C–H in plane bending at 1130 cm⁻¹ and N-H out of plane bending at 670 cm⁻¹ are in good agreement with the computed results.

3.3 Natural bond orbital analysis

In order to elucidate the inter- and intra-molecular charge transfer interactions and electron delocalization within the molecule, the NBO analysis is performed on PTCA at DFT/B3LYP with 6-311++G(d,p) basis set. The NBO analysis shows hydrogen bond interaction between oxygen lone pairs and (C-H) and (N-H) σ^* anti-bonding orbitals. The stabilization energies coupled with the

Table 1. Optimized parameters of PTCA by B3LYP level with 6-311++G(d,p) basis set.

	Value	es (Å)		Value	es (°)		Valu	es (°)
Bond length	Calc.	Exp.a	Bond angle	Calc.	Exp.a	Dihedral angle	Calc.	Exp.a
H17-C12	1.079	0.975	C6-C7-C13	112.2	112.8	H17-C12-C13-H18	-1.9386	0.2699
C13-C7	1.791	1.752	C6-C7-C12	109.1	111.3	H17-C12-C13-C14	176.618	-179.755
C12-C13	1.408	1.383	C6-C7-C11	108.7	108.8	C11-C12-C13-H18	179.184	-178.432
C12-C11	1.369	1.373	C11-C7-C13	108.7	108.3	C11-C12-C13-C14	-2.2587	1.5422
C13-C14	1.376	1.379	C13-C7-C13	112.2	112.8	H17-C12-C11-C16	0.0205	-0.4100
O9-H21	0.969	0.953	C12-C7-C13	108.7	108.8	H17-C12-C11-N10	179.6756	-179.458
O9-C16	1.338	1.306	C11-C7-C12	109.1	108.7	C13-C12-C11-C16	179.9237	178.335
C11-C7	1.808	1.775	C12-C7-C13	109.1	108.6	C13-C12-C11-N10	-1.4212	-0.7131
C7-C6	1.594	1.564	C16-O9-H21	108.04	111.2	H18-C13-C14-H19	1.3026	-1.6947
C12-C7	1.807	1.770	C11-N10-C15	123.0	109.5	H18-C13-C14-C15	178.3029	179.113
C14-C15	1.405	1.371	C11-N10-H22	115.8	122.8	C12-C13-C14-H19	-177.246	178.329
C11-C16	1.488	1.500	C15-N10-H22	120.2	117.3	C12-C13-C14-C15	-0.2466	-0.8627
C11-N10	1.361	1.348	C12-C11-C16	126.4	119.5	H21-O9-C16-C11	-177.871	179.196
O4-C6	1.258	1.249	N10-C11-C12	119.8	125.7	H21-O9-C16-O8	2.5905	-1.6142
C16-O8	1.207	1.203	N10-C11-C16	113.7	119.3	C13-C7-C13-O5	1.4662	20.1208
N10-C15	1.340	1.328	C13-C12-H17	121.8	114.9	Cl3-C7-C13-O9	-178.751	-162.327
N10-H22	1.017	0.855	C13-C12-H17	119.6	122.1	C11-C7-C13-O5	-118.885	-98.7592
C15-H20	1.076	0.937	C11-C12-C13	118.5	118.9	Cl1-C7-C13-O9	60.8961	78.7929
O5-C6	1.231	1.226	C12-C13-H18	119.5	188.8	C12-C7-C13-O5	122.1532	142.8358
			C14-C13-H18	120.1	120.8	C12-C7-C13-O9	-58.0648	-39.6121
			C12-C13-C14	120.2	117.9	C13-C14-C15-N10	6.4420	-0.6669
			C13-C14-H19	121.8	120.1	C13-C14-C15-H20	-174.588	178.2775
			C13-C14-C15	119.4	119.3	H19-C14-C15-N10	-176.459	-179.841
			C15-C14-H19	118.6	119.1	H19-C14-C15-H20	-8.3128	-0.8973
			N10-C15-C14	118.2	121.4	C12-C11-C16-O9	-2.0120	0.3159
			C14-C15-H20	123.3	119.6	C12-C11-C16-O8	177.540	-178.930
			N10-C15-H20	117.3	124.2	N10-C11-C16-O9	178.314	-179.400
			O9-C16-C11	112.8	116.0	N10-C11-C16-O8	-2.1331	0.1547
			O8-C16-O9	124.8	112.1	C12-C11-N10-C15	8.1167	-0.8495
			O8-C16-C11	122.2	126.9	C12-C11-N10-H22	177.2117	173.046
					120.8	C16-C11-N10-C15	-172.186	-179.997
						C16-C11-N10-H22	-3.0913	-6.1015
						C11-N10-C15-C14	-10.5471	1.5527
						C11-N10-C15-H20	-179.416	-177.475
						H22-N10-C15-C14	-179.175	-172.220
						H22-N10-C15-H20	11.9549	8.7509

^aValues taken from ref. [9].

Table 2. Computed vibrational wavenumbers and fundamental band position assignments of PTCA.

Calculated wavenumber (cm ⁻¹)	Experimental wavenumber ^a (cm ⁻¹)	Vibrational assignments
	(0)	
3525	3449	N-H stretching vibration
3195	3056	C-H stretching vibration
1698	1709	C=O stretching vibration
1632	1610	C-C in-ring stretching vibration
1423	1449	C-O-H bending
1326	1307	
1203	1209	C-H in-plane bending
1150	1130	
919	911	C-H out-of-plane bending
836	823	
733	725	
680	670	N-H out-of-plane bending
501	512	C-C-C bending

^aValues taken from ref. [9].

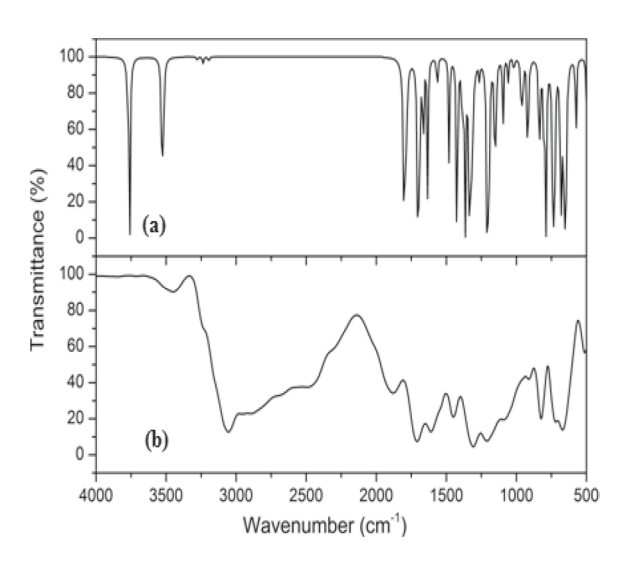


Figure 3. (a) Simulated IR spectra and (b) FTIR spectra of PTCA.

Table 3. Second-order perturbation theory analysis of Fock matrix in NBO basis, including the stabilization energies using DFT at B3LYP/6-311++G(d,p) level.

Donor (i)	$\mathrm{ED}\left(i\right)$	Acceptor (j)	ED(j)	$E(2)^{a}$, kcal mol ⁻¹	$E(j)-E(i)^{b}$, a.u.	$F(i,j)^{c}$, a.u.
n ₂ (O ₄)	1.76589	$\sigma^*(C_6-C_7)$	0.16071	20.79	0.56	0.018
2. "		$\pi^*(N_{10}-C_{15})$	1.76589	27.15	0.19	0.069
$n_3(O_4)$	1.63936	$\pi^*(O_5-C_6)$	0.35315	95.01	0.27	0.144
$n_2(O_5)$	1.82100	$\sigma^*(O_4-C_6)$	0.05485	18.56	0.79	0.111
		$\sigma^*(C_6-C_7)$	0.35315	26.43	0.52	0.105
$\pi(N_{10}-C_{15})$	1.83345	$\pi^*(C_{11}-C_{12})$	0.25128	20.44	0.39	0.081
$\pi(C_{11}-C_{12})$	1.67927	$\pi^*(O_8-C_{16})$	0.24683	18.05	0.28	0.065
		$\pi^*(N_{10}-C_{15})$	0.46254	11.72	0.24	0.049
		$\pi^*(C_{11}-C_{12})$	0.25128	17.28	0.31	0.067
$\pi(C_{13}-C_{14})$	1.65861	$\sigma^*(O_9-C_{16})$	0.08837	33.97	0.23	0.081
		$\sigma^*(C_{11}-C_{16})$	0.07068	16.56	0.29	0.063
$n_2(O_8)$	1.84616	$\sigma^*(O_9-C_{16})$	0.08837	31.53	0.63	0.128
		$\sigma^*(C_{11}-C_{16})$	0.07068	18.31	0.68	0.101
$n_2(O_9)$	1.81254	$\pi^*(O_8-C_{16})$	0.24683	49.92	0.34	0.115
$\pi^*(O_8-C_{16})$	0.24683	$\pi^*(C_{11}-C_{12})$	0.25128	85.48	0.02	0.073
$\pi*(N_{10}-C_{15})$	0.46254	$\pi^*(C_{11}-C_{12})$	0.25128	29.55	0.06	0.062
		$\pi^*(C_{13}-C_{14})$	0.20932	50.45	0.06	0.088

^aE(2) means energy of hyperconjugative interactions.

hyperconjugative interactions for $n2(O4) \rightarrow \sigma^*(C15-H20)$, $n2(O8) \rightarrow \sigma^*(N10\text{-H}22)$ are obtained as 0.63 and 0.99 kcal mol⁻¹, respectively (table 3), which quantify the extent of intramolecular N-H...O and intermolecular C-H...O hydrogen bonding. The most important intramolecular interaction $(n-\pi^*)$ energy related to the resonance in the molecules are electron donating from n2(O4) atom to anti-bonding acceptor $\pi^*(N10\text{-}C15)$ atom, whose energy is 95.01 kcal mol⁻¹ resulting in hyperconjugation interactions from n(O) to N-C bond. The second-order perturbation energies of $\pi^*(O8-C16)$ to $\pi^*(C11-C12)$, $\pi^*(N10\text{-}C15)$ to $\pi^*(C11\text{-}C12)$ and $\pi^*(N10\text{-}C15)$ to $\pi^*(C13-C14)$ are 85.48, 29.55 and 50.45 kcal mol⁻¹, respectively. These interactions make the pyridine ring of PTCA stable. The strong negative and positive charges on the atoms of PTCA molecule demonstrate the electrostatic attraction or repulsion between the atoms (table 4). It results in significant contribution to the inter- and intramolecular charge transfer interactions, leading to the stabilization of the molecule [10] (figure 4).

3.4 Molecular electrostatic potential

The electrostatic potential values at the surface are represented in different colours. The colour code of these maps ranges between -8.081e-2 (deepest red) and +8.081e-2 (deepest blue) (figure 5). The light blue indicates the slight electron-deficient region, while the yellow portion shows the slight electron-rich region. As depicted in figure 5 on PTCA, the regions having negative charges are around the C11, C12, C13, O4 and O5 atoms. The absence of maximum

negative potential region in molecular electrostatic potential (MEP) plot confirms the low chemical reactivity of the molecule and the presence of partial negative potential region (yellow colour) indicates the electron-rich region, which is the favourable site for electrophilic reactivity.

3.5 Frontier molecular orbital analysis

The energy gap of highest energy occupied molecular orbital and lowest energy unoccupied molecular orbital (HOMO–LUMO) explains the charge transfer interactions within the conformers. The HOMO and LUMO energies of PTCA, as calculated by DFT/B3LYP/6-311++G(d,p) method, are as follows:

HOMO energy,
$$E_{\rm HOMO} = -6.59 \, {\rm eV}$$

LUMO energy, $E_{\rm LUMO} = -3.45 \, {\rm eV}$
HOMO-LUMO energy gap [11],

$$\Delta E_{\rm GAP} = E_{\rm LUMO} - E_{\rm HOMO} = 3.14 \, \rm eV.$$

The plots of HOMO and LUMO are shown in figure 6. The computed larger value of HOMO-LUMO energy gap (3.14 eV) in PTCA confirms higher kinetic stability and lower chemical reactivity of the molecule. The 3.14 eV gap falls within the UV region, so the molecule is colourless. The global reactivity descriptors, such as ionization potential (I), electron affinity (A), electrophilicity index (ω), chemical hardness (η), softness (S), chemical potential (μ) and charge transfer ($\Delta N_{\rm max}$), have been calculated using the energy of HOMO and LUMO (table 5). The hardness value

^bEnergy difference between donor and acceptor *i* and *j* NBO orbitals.

 $^{{}^{}c}F(i,j)$ is the Fock matrix element between i and j NBO orbitals.

Table 4. Natural population analysis of PTCA calculated with DFT/B3LYP/6-311++G(d,p) method.

Atoms	Natural charge
Cl1	0.01743
Cl2	0.01981
Cl3	0.03812
O4	-0.70406
O5	-0.70172
C6	0.74571
C7	-0.23762
O8	-0.58049
O9	-0.65983
N10	-0.45967
C11	0.14429
C12	-0.17075
C13	-0.11541
C14	-0.19154
C15	0.18254
C16	0.77685
H17	0.24599
H18	0.22463
H19	0.23760
H20	0.24721
H21	0.49777
H22	0.44314
Total	0.00000

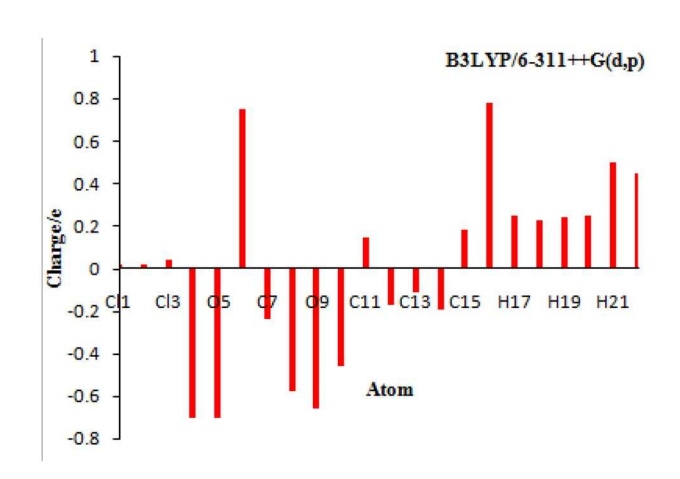


Figure 4. Mulliken atomic charges and plots of PTCA.

and negative chemical potential indicate that the molecule is stable [12].

3.6 Hirshfeld surface analysis

The 3D image in Hirshfeld surface analysis depicts internuclear distances and angles, whereas 2D fingerprint plot shows the existence of different types of intermolecular interactions [13,14]. The Hirshfild surfaces of the PTCA are given in figure 7 and it explains the

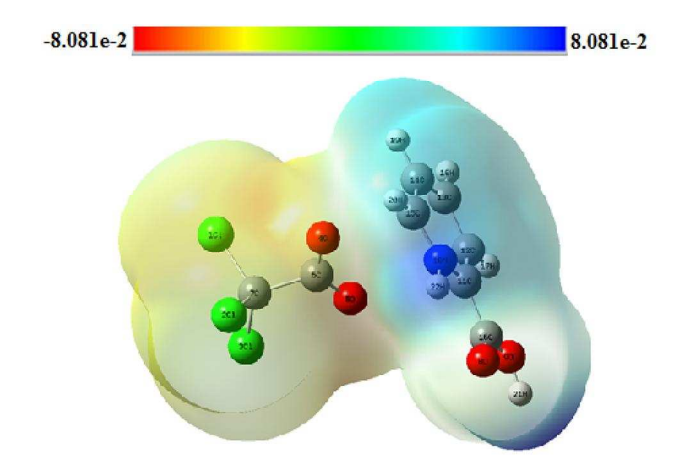


Figure 5. Molecular electrostatic potential of PTCA.

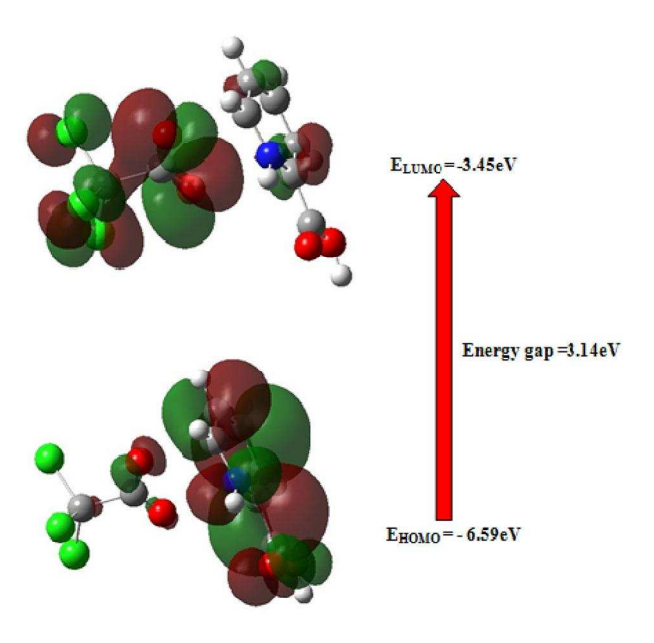


Figure 6. HOMO-LUMO plot of PTCA.

Table 5. Calculated quantum chemical molecular orbital properties for PTCA at DFT/B3LYP/6-311++G(d,p) method.

Parameters	B3LYP/6-311++G(d,p)
Ionization potential (I)	−6.59 eV
Electron affinity (A)	-3.45 eV
Chemical hardness (η)	1.57 eV
Chemical potential (μ)	-1.57eV
Electrophilicity index (ω)	0.785 eV
Softness (S)	0.6369 eV^{-1}
Charge transfer (ΔN_{max})	1

surfaces that has been mapped over d_{norm} , d_{e} , d_{i} and curvedness (3D plots). The surface representing the deep red coloured circular depressions indicates hydrogen

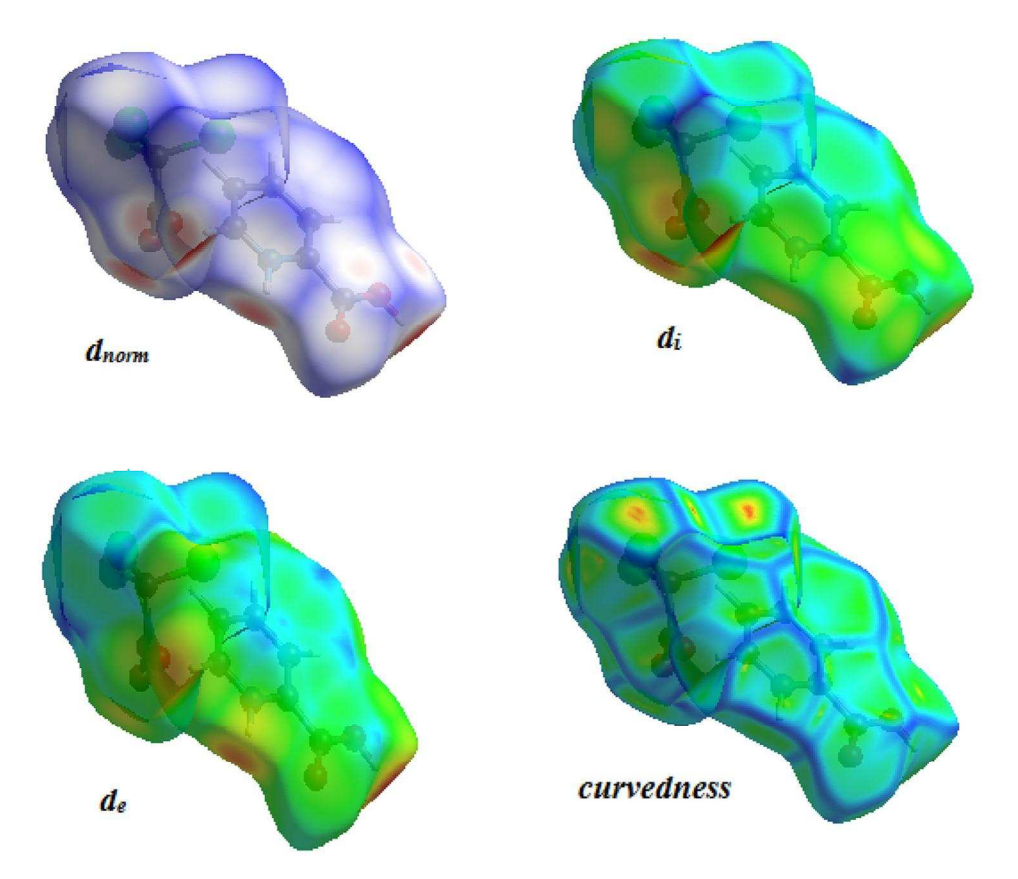


Figure 7. Hirshfeld surfaces for d_{norm} , d_{i} , d_{e} and curvedness for the PTCA molecule.

bonding contacts (figure 7). O"H/H"O intermolecular interactions (30.4%) are represented by a two sharp spike in the 2D fingerprint plot region (figure 8). The O"H interactions represented by the left long sharp spike in the donor region (16.5%) shows the hydrogen atom interacting with carboxylate groups of two compounds. The H"O interactions are indicated by a right long spike (13.9%) in the acceptor region. It specifies carboxyl oxygen atom acts as an acceptor to the hydrogen atom of the NH⁺ group [15,16]. The relative contributions of the H"H, C"H, H"Cl, Cl"Cl and C"C contacts are 5, 3.8, 25, 13 and 1%, respectively.

3.7 NLO studies first-order hyperpolarizability

The values of α_o and β components of Gaussian 09 output are reported in atomic units (a.u.), the calculated values should be converted into electrostatic units (e.s.u.). The polarizability and first hyperpolarizability of PTCA are 3.759×10^{-25} and 2.7965×10^{-28} esu, respectively. The first hyperpolarizability of the PTCA is greater than that of urea (β of urea is 0.3728×10^{-30} esu obtained by HF/6-311G(d,p) method), which confirm PTCA as best material for NLO applications.

3.8 UV-Vis-NIR spectral analysis

The absorption spectrum of PTCA crystal is displayed in figure 9. It shows the maximum absorption peak at 260 nm, which corresponds to π - π * transition. Using the recorded absorption spectra, the linear optical constants of PTCA are calculated and the variation in optical constants as a function of photon energy is plotted (figure 10a-d). From figure 10a the bandgap of PTCA crystal is jotted down to be 4.25 eV, which indicates the grown crystal possessing large transmittance and permits it to be a suitable candidate for optoelectronic applications.

From the optical constants, the calculated values of refractive index (n), electric susceptibility (χ_C) , real (ε_r) and imaginary (ε_i) dielectric constants at $\lambda = 800$ nm are 1.48, 0.175, 2.198 and 7.275×10^{-6} , respectively. These values suggest that the PTCA material has profound NLO efficiency.

3.9 Fluorescence studies

The optical application of PTCA has been validated by the fluorescence studies. The fluorescence spectrum is captured using PERKIN ELMER/LS 45 Fluorescence spectrophotometer in the range of 320–800 nm and is depicted in

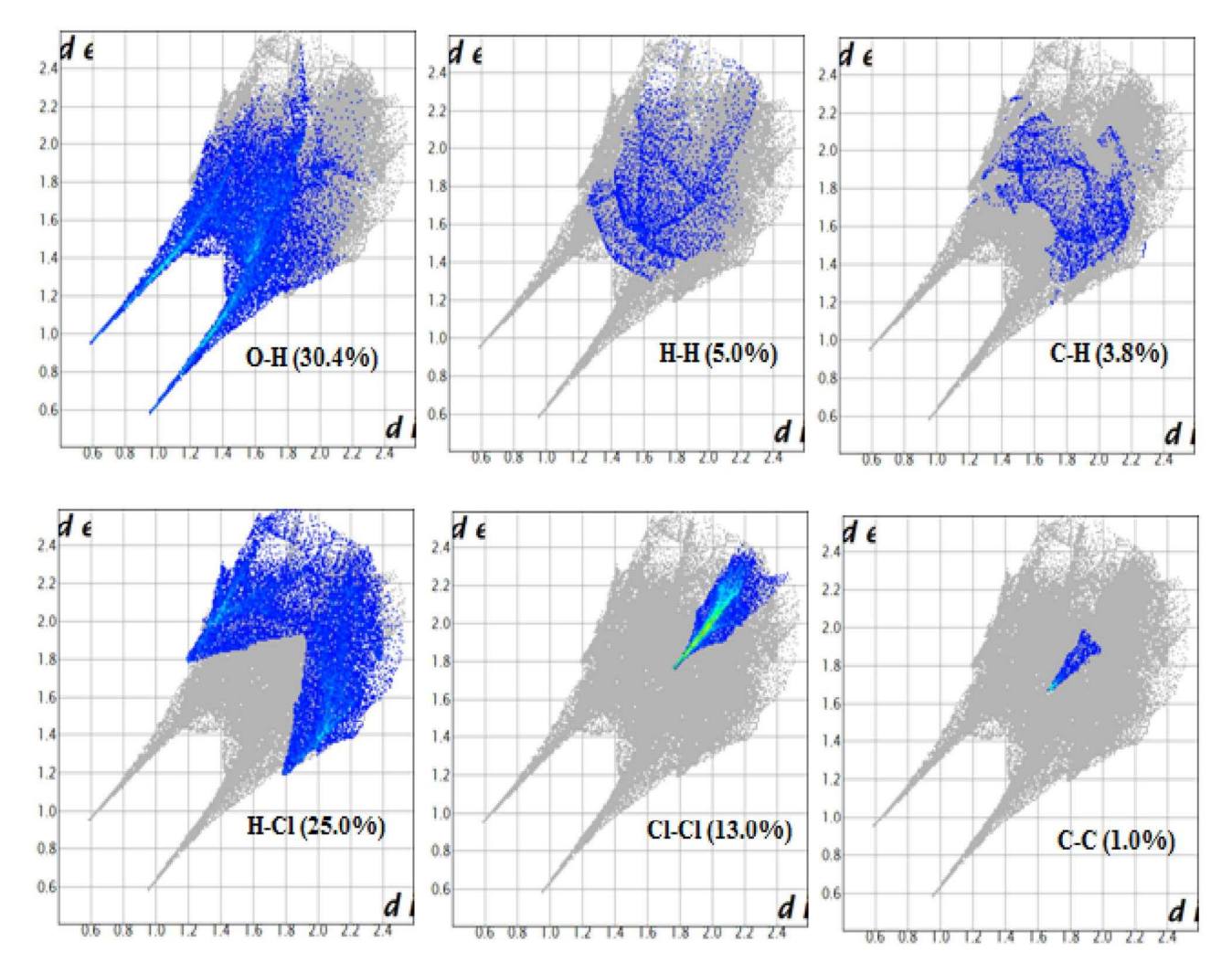


Figure 8. 2D fingerprint plots showing various intermolecular contacts in the PTCA.

figure 11. Due to π - π * transition, emission peak is noticed at 513 nm in the spectrum, implying that PTCA crystals have a blue fluorescence emission prevalently to be useful in the OLED devices.

3.10 Z-scan measurements

The Z-scan is a widely accepted technique for characterization of NLO by the scientific community. The third-order NLO properties of the PTCA crystal are investigated using a He–Ne laser (5 mW) of wavelength at 633 nm as a source. It is very simple and highly sensitive, but relatively the most accurate method to determine nonlinear index of refraction (n_0) , nonlinear absorption coefficient (β) and third-order NLO susceptibility $(\chi^{(3)})$ by closed- and open-aperture mode, respectively [17]. The closed- and open-aperture normalized transmittance as a function of sample position Z have been measured for PTCA crystal and are exemplified in figure 12a and b. In closed-aperture pattern (figure 12a), the peak followed by the valley intensity is vividly visible,

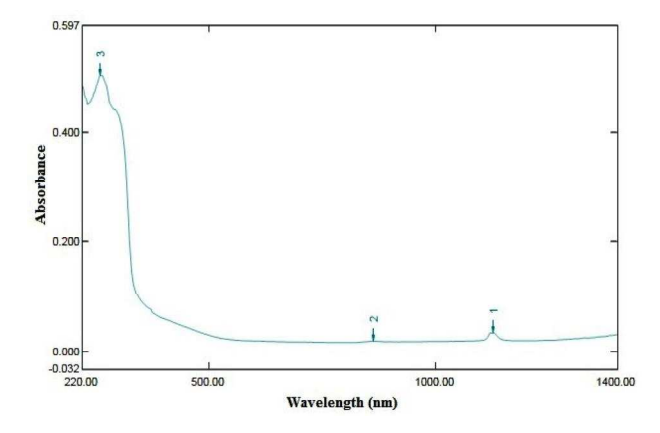


Figure 9. The optical absorption spectrum of PTCA crystal.

signifying that the sign of the refraction nonlinearity is negative, i.e., the feasibility of self-defocusing effect [18]. Figure 12b exhibits a decrease in transmission with increase in the input intensity, illustrative of the presence of reverse saturable absorption (excited state absorption) with a

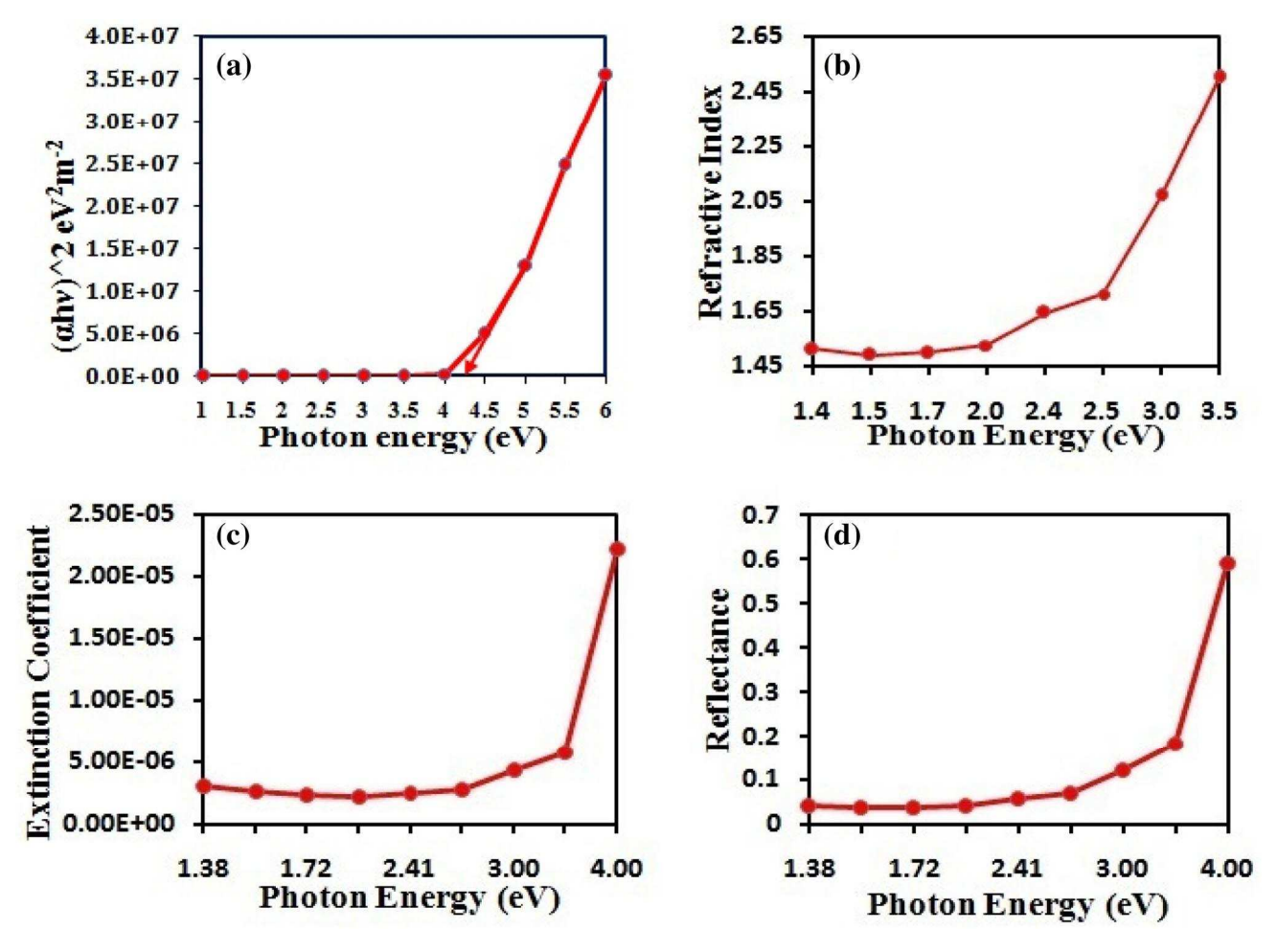


Figure 10. (a-d) Variation of optical constants as a function of photon energy.

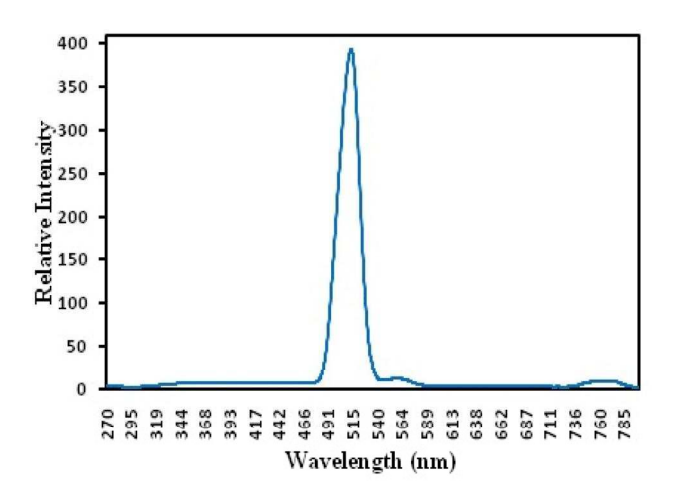


Figure 11. Fluorescence emission of PTCA crystal.

positive nonlinear absorption coefficient enabling the material for optical limiting applications [19–21]. Table 6 tabularizes the experimental details and the results of the Z-scan technique for PTCA crystal. The excellent NLO

properties of the grown crystal testify it a promising material for optical-limiting applications.

4. Conclusions

Single crystal of PTCA has been grown by slow evaporation technique. The computed spectroscopic parameters are in good agreement with the experimental data results. The NBO analysis reveals the possible intramolecular charge transfer interactions and stability in PTCA. The MEP study confirms PTCA as an electron-rich species and explains its electrophilic nature. The hardness value and negative chemical potential from HOMO-LUMO indicates that the title molecule is stable. The Hirshfeld surface analysis of PTCA interprets the percentage of strong and weak intermolecular interactions in the crystalline state. UV-visible studies disclose that the title compound is transparent in the entire visible region. Also, optical constants like bandgap $(E_g = 4.25 \text{ eV})$, refractive index (n = 1.48), reflectance and extinction coefficient are evaluated from UV-Vis-NIR spectrum. Z-scan technique points out reverse saturated absorption optical process observed in the titular crystal.

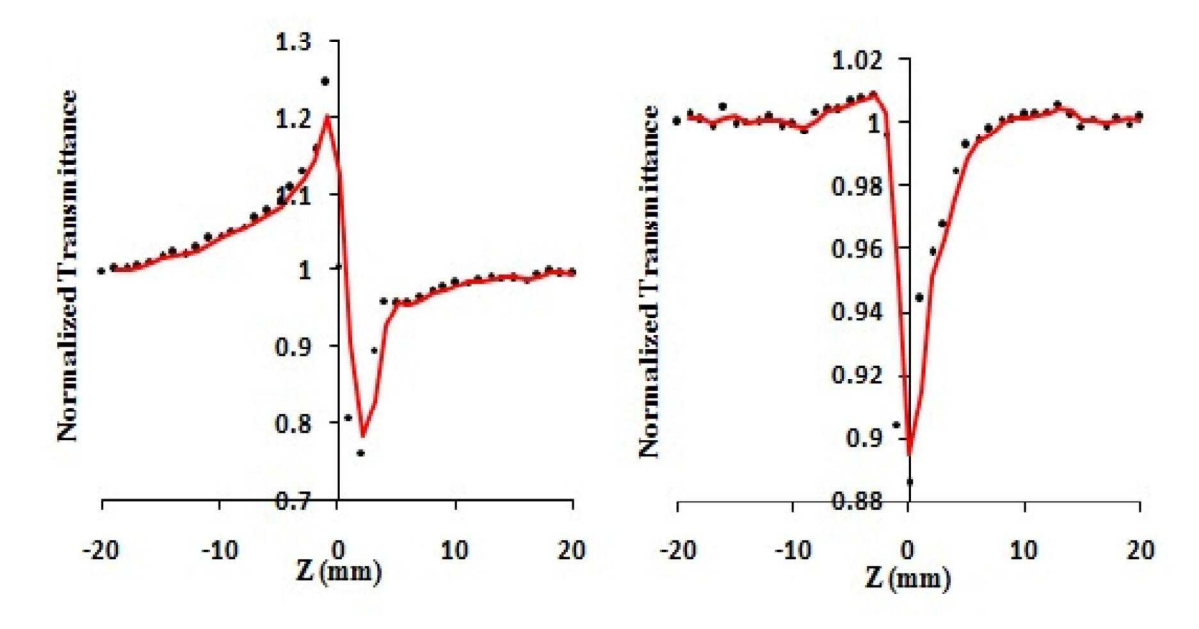


Figure 12. (a) Self-focusing (closed-aperture) and (b) open-aperture mode Z-scan plot of PTCA crystal.

Table 6. Obtained NLO parameter from open- and closed-aperture Z-scan measurement data for PTCA crystal.

Parameters	Measured values for PTCA crystal
Nonlinear refractive index (n_2)	$3.03 \times 10^{-10} (\text{cm}^2 \text{W}^{-1})$
Nonlinear absorption coefficient (β)	$8.47 \times 10^{-06} \text{ (cm W}^{-1}\text{)}$
Real part of the third-order susceptibility $[Re(\chi^3)]$	$6.05 \times 10^{-08} \text{ (cm}^2 \text{ W}^{-1}\text{)}$
Imaginary part of the third-order susceptibility $[Im(\chi^3)]$	$5.03 \times 10^{-07} \text{ (cm W}^{-1})$
Third-order NLO susceptibility (χ^3)	$5.06275 \times 10^{-07} \text{ (esu)}$

The fluorescence emission analysis confirms the emission of PTCA is in the blue region. The vibrational, UV-visible absorption, NBO and Z-scan studies suggest PTCA as an attractive material for optical-limiting applications.

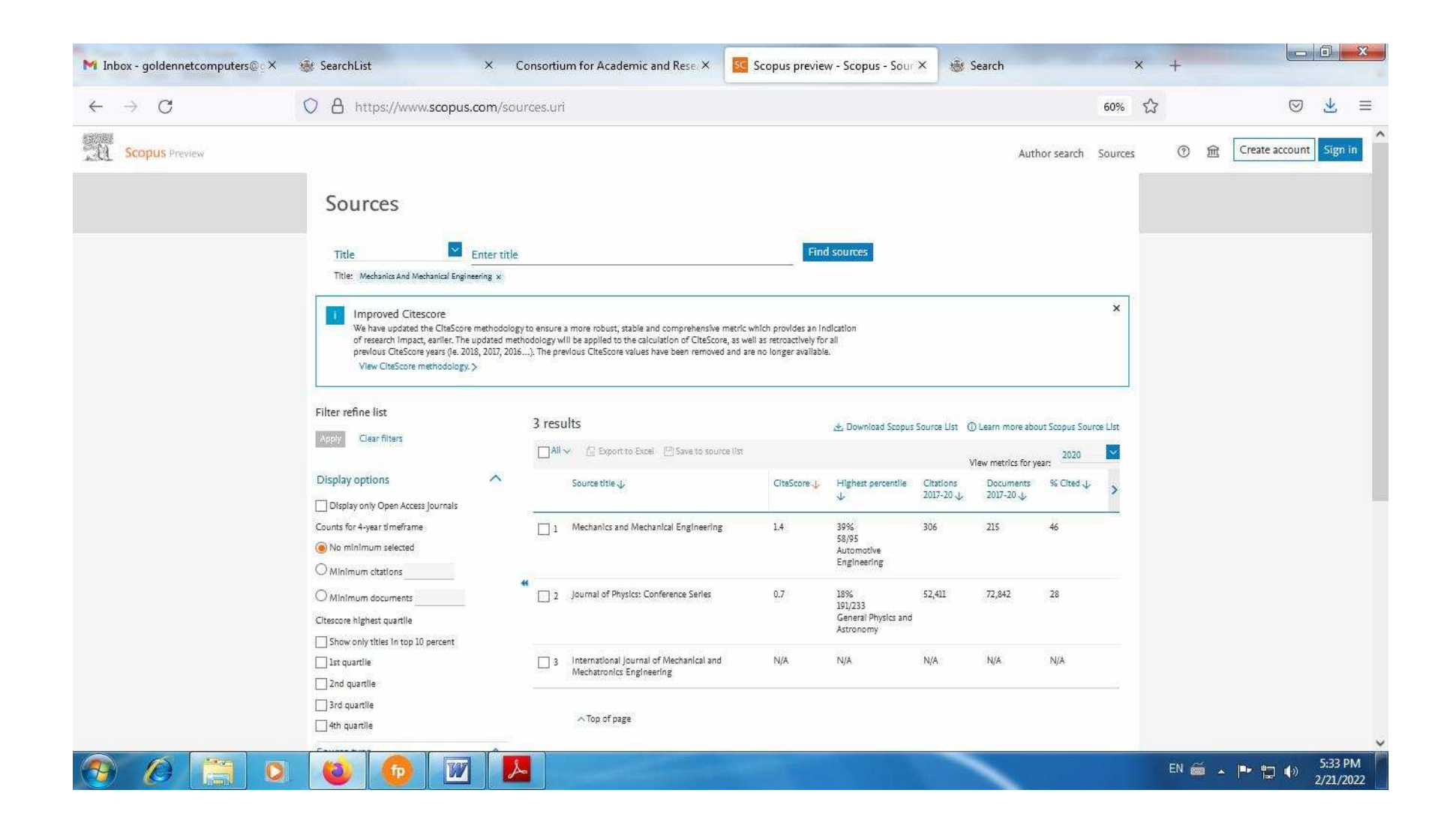
Acknowledgements

We thank Cauvery College for Women (Autonomous), Tiruchirappalli, for providing instrument facility under the support of DST-FIST-Level 0 program (Ref. No. SR/FST/College-246/2015(c)). We also thank VIT University, Chennai, for providing Z-scan facility.

References

- [1] Gao S, Chen W, Wang G and Chen J 2006 J. Cryst. Growth 297 361
- [2] Uma Devi T, Lawrence N, Ramesh Babu R, Ramamurthi K and Bhagavannarayana G 2009 Spectrochim. Acta A Mol. Biomol. Spectrosc. 71 1667
- [3] Jagannathan K, Kalainathan S, Gnanasekaran T, Vijayan N and Bhagavannarayana G 2007 Cryst. Res. Technol. 42 471
- [4] Gowri S, Uma Devi T, Alen S, Sajan D, Surendra Dilip C and Vinitha G 2018 J. Mater. Sci.: Mater. Electron. 29 19710
- [5] Gowri S, Anitha K, Suresh A, Uma Devi T, Selvanayagam S, Sajan D et al 2012 Spectrochim. Acta A Mol. Biomol. Spectrosc. 95 73
- [6] Frisch M J, Trucks G W, Schlegel H B, Scuseria G E, Robb M A, Cheeseman J R et al 2009 Gaussian 09 revision A. Wallingford, CT: 02 Gaussian Inc.
- [7] Schlegel B 1982 J. Comp. Chem. 3 214
- [8] Dennington R, Keith T and Millam J 2009 *GaussView* Version 5 Semichem Inc., Shawnee Mission, KS
- [9] Matsuzawa N, Ata M and Dixon D A 1995 J. Phys. Chem. 99 7698
- [10] Sasikala V, Sajan D, Vijayan N, Chaitanya K, Babu Raj M S and Selin Joy B H 2014 Spectrochim. Acta A Mol. Biomol. Spectrosc. 123 127
- [11] Gilman J 1977 Mater. Res. Innov. 1 71
- [12] Chitrambalam S, Manimaran D, Joe I H, Rastogi V K and Hassan I U 2018 *Opt. Mater.* **75** 285
- [13] Spackman M A and Byrom P G 1977 Chem. Phys. Lett. 267 215
- [14] Spackman M A and McKinnon J J 2004 CrystEngComm 4 378
- [15] Hirshfeld F L 1977 Theor. Chim. Acta 44 129

- [16] Spackman M A and Jayatilaka D 2009 CrystEngComm. 11 19
- [17] Senthil K, Kalainathan S, Ruban Kumar A and Aravindan P G 2014 RSC Adv. 4 56112
- [18] Nivetha K, Kalainathan S, Yamada M, Kondo Y and Hamada F 2016 RSC Adv. 6 35977
- [19] Wang J and Blau W J 2011 J. Opt. A: Pure Appl. Opt. 11 024001
- [20] Henari F Z, Balu W J, Milgrom L R, Yahyoglu G, Philips D and Lacey J A 1977 Chem. Phys. Lett. 267 229
- [21] Henari F Z 2001 J. Opt. A: Pure Appl. Opt. 3 188



Research Article

N. Manopradha*, S. Rama, S. Gowri, K. Kirubavathi, and K. Selvaraju

Theoretical Investigation on Growth Kinetics and **Thermodynamic Properties of Pyridine-2-Carboxylic Acid Crystals**

https://doi.org/10.2478/mme-2019-0004 Received Apr 21, 2018; revised Oct 1, 2018; accepted Nov 20, 2018

Abstract: This work illustrates the significance of kinetic parameters of nucleation and thermal decomposition for Pyridine-2-carboxylic acid crystals. In the interest of maximizing the growth condition for the production of single crystals, nucleation parameters such as interfacial energy (σ) , volume free energy (ΔG_{ν}) , critical energy barrier for nucleation (ΔG^*), radius of the critical nucleus (r^*) and nucleation rate (J) were determined from the classical nucleation theory of solubility-enthalpy relation. The optimized geometry of the compound was computed from the DFT-B3LYP gradient calculations employing 6-31G(d,p) basis set and its vibrational frequencies were evaluated. Based on the vibrational analysis, the thermodynamic parameters were obtained and the correlative equations between these thermodynamic properties and variation in temperatures were also reported.

Keywords: Nucleation kinetics, growth from solution, DFT

a proton donor depending on the deprotonated groups. [2] The growth aspects of pyridine-2-carboxylic crystals have been studied in the past, but there are no reports on the nucleation kinetics and DFT study of this organic material. In the present work, the nucleation parameters such as interfacial energy (σ), volume free energy (ΔG_{ν}), critical energy barrier for nucleation (ΔG^*) , radius of the critical nucleus (r*) and nucleation rate (J) were evaluated. [3] The thermodynamic parameters from the vibration analysis were compared to the enthalpy obtained from solubility to predict the stability of the crystal.

DFT methods were performed to acquire the vibration information on the optimized geometry, relationships between molecular structure, hydrogen bonding and hyperpolarizability, and thus, non-linear response of the title compound was obtained. This can be used to support the effort towards the discovery of new efficient materials for technological applications by the design strategy for engineering of crystals with predesigned architecture, especially, in the field of nonlinear optics. [4]

1 Introduction

Pyridine-2-carboxylic acid (2PA) are used as building blocks in crystal engineering and many coordination polymers. These are beneficial compounds for human organism and are also involved in several essential biochemical processes. 2PA has been used as a valuable chelating agent. [1] It is not only a potential proton acceptor but also

2 Nucleation Kinetics

Nucleation study is useful to interpret proper supersaturation to provide controlled nucleation rate to obtain good quality single crystals. [5] The concept of nucleation kinetics was introduced by Gibbs. Nucleation is the initial process that occurs in the formation of a crystal from a solution, in which a small number of ions become arranged in a pattern, forming a site on which additional particles are deposited as the crystal grows. To generate a new nucleus from the parent phase, the nucleation process must overcome the potential barrier; this is done using the process of super saturation, which results in the formation of seed nuclei. The process of nucleation is controlled by nucleation rate parameter, which plays a key role in new phase formation.

At the solution- crystal interface, the interfacial energy is formed, which is a crucial parameter in the theo-

^{*}Corresponding Author: N. Manopradha: Department of Physics, Cauvery College for Women, Tiruchirappalli - 620 018, India; Email: mano.pradha@gmail.com

S. Rama: Department of Physics, Agni College of Technology, Chennai - 600 130, India

S. Gowri: Department of Physics, Cauvery College for Women, Tiruchirappalli - 620 018, India

K. Kirubavathi, K. Selvaraju: PG & Research Department of Physics, Govt. Arts College, Ariyalur - 621 713, India

ries of nucleation and crystal growth. However, certain difficulties were encountered in the nucleation experiments such as the requirement of a solution free from foreign particles, volume of the solution and so on. Theoretical attempts have been made by several researchers to estimate the interfacial energy using solubility data.

Interfacial energy of the solid and liquid interface is an important phenomenon in the nucleation process. Based on the solution kinetics theory, Bennema and Sohnel [6] have derived an expression that explains the linear dependence of interfacial energy (σ) on solubility:

$$\sigma = (kT/d^2)[0.173 - 0.248 \ln \chi_m] \tag{1}$$

where, σ - interfacial energy (J/m²); k - Boltzmann constant (J K⁻¹); T - Temperature in (K); d - mean molar ionic diameter in crystal = $\{(6/\pi)v\}^{1/3}$; χ_m - mole fraction of solute in solution.

The relation between solubility and enthalpy of a real solution is given as: [7]

$$\ln \chi_m = (-\Delta H_S/RT) + (\Delta S_E/R) \tag{2}$$

 ΔH_s - Enthalpy of fusion (J mol⁻¹)

R - Gas constant (J K⁻¹mol)

 ΔS_E - Excess entropy of mixing.

From the reported nucleation kinetics equations, nucleation parameters such as interfacial energy (σ) , volume free energy (ΔG_v) , critical energy barrier for nucleation (ΔG^*) , radius of the critical nucleus (r^*) and nucleation rate (J) of 2PA crystal was calculated for various temperatures with constant variation in the super saturation ratio and vice versa.

3 Experimental

3.1 Materials and methods

The chemical used in this experiment was an analytical reagent as received from the commercial sources without further purification. Pyridine-2-carboxylic acid was purchased from Alfa Aesar. The solubility studies of 2PA were carried out in a constant temperature bath with temperature accuracy $\pm~0.01^{\circ}$ C. The solute was added to double distilled water until the saturation condition was reached. The equilibrium concentration of the solute was analyzed gravimetrically. The experiment was repeated at different temperatures.

3.2 Computational Methods

GAUSSIAN 09 quantum chemical software [8] was used for all the calculations. The molecular structure of pyridine-2-carboxylic acid was optimized by Berny's optimization algorithm using redundant internal co-ordinates at the DFT level, using the closed-shell Becke-Lee-Yang-Parr hybrid exchange-correlation three-parameter functional (B3LYP) in combination with 6-31G(d,p) basis set to derive the complete geometry optimizations and normal mode analysis on isolated entities. [9-11] The frontier molecular orbitals (HOMO and LUMO) are generated at DFT/B3LYP/6-31G(d,p) level to explain the electronic and optical properties. The important quantum chemical molecular properties, that is, the global reactivity descriptors have been calculated using the highest occupied molecular orbital (HOMO) and lowest unoccupied molecular orbital (LUMO). [12–17]

The first hyperpolarizability (β) and the static polarizability (α) of 2PA have been predicted using the DFT/B3LYP/6-31G(d,p) method. Using the third rank tensor, the 27 components of 3D matrix can be reduced to 10 components due to the Kleinmann symmetry. [18, 19] The output from Gaussian 09 provides ten components of this matrix as β_{XXX} , β_{YXX} , β_{XYY} , β_{YYY} , β_{YYY} , β_{ZXX} , β_{XYZ} , β_{ZYY} , β_{ZZZ} , respectively. The following equation renders the results of components of first hyperpolarizability:

$$\beta = (\beta_x^2 + \beta_y^2 + \beta_z^2)^{1/2} \tag{3}$$

where,

$$\beta_X = \beta_{XXX} + \beta_{XYY} + \beta_{XZZ}; \ \beta_Y = \beta_{YYY} + \beta_{YXX} + \beta_{YZZ}; \ \beta_Z = \beta_{ZZZ} + \beta_{ZXX} + \beta_{ZYY}$$

The equations for calculating the magnitude of static polarizability is defined as follows:

$$\alpha_O = (\alpha_{xx} + \alpha_{yy} + \alpha_{zz})/3 \tag{4}$$

4 Results and Discussion

4.1 Metastable zone width (MZW)

The knowledge of MZW will help us in the selection of an optimum rate of supersaturation generation to avoid the exercise for secondary nucleation. The difference between the equilibrium temperature and nucleation temperature in the nucleation curve is called the metastable zone width. The nucleation temperature for each saturation temperature can be calculated using the data represented in Figure 1.

Table 1: Nucleation Table from Picolinic Acid for Super Saturation Ratio-1.1

Т	$\Delta G_{ m v}$	σ	∆G *	r*	i*	J
(K)	(J/m³)	(J/m^2)	(J)	(m)		(nuclei/m³/sec)
304	-2.543050e+006	0.006923	8.592447e-019	5.444707e-009	4.297886e+003	8.300411e+012
308	-2.576511e+006	0.003852	1.442422e-019	2.990478e-009	7.121199e+002	2.503985e+012
316	-2.643433e+006	0.002345	3.090731e-020	1.774264e-009	1.487256e+002	8.814279e+011
321	-2.685260e+006	0.001556	8.754144e-021	1.159123e-009	4.146868e+001	3.761922e+011

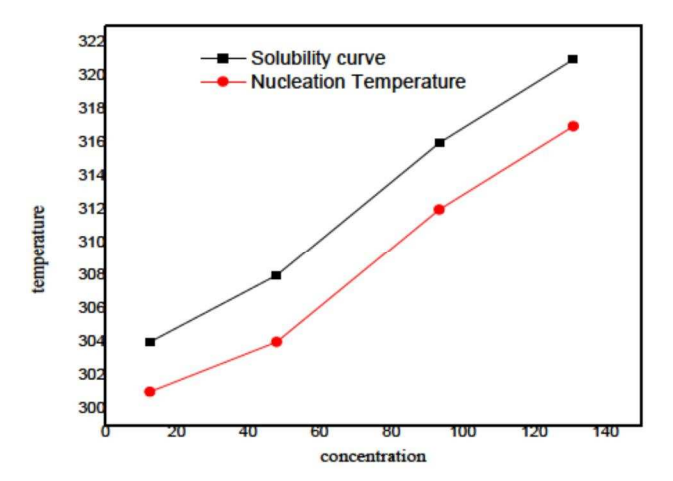


Figure 1: Solubility curve for 2PC

In this work, the theoretically calculated values of metastable zone width for the crystallization temperatures of crystals using the slow evaporation method have been reported for the first time. From the results, it is observed that the zone width is narrow at lower temperatures and broader at higher temperatures. Table 1 enlists the estimated nucleation parameters of 2PA with different temperatures. The change in free energy per unit volume (ΔG_{ν}) decreases with an increase in the supersaturation, which drives the crystallization process. Figure 2 shows the variation of energy barrier (ΔG^*) with respect to temperature. Figure 3 shows the change in critical radius (r^*) as a function of temperature as well as the supersaturation. Decrease in interfacial energy (σ) (as shown in Table 1) with higher values of temperature leads to a decrease in the radius of the critical nuclei and causes the decreases in the free energy of the system. From the classical nucleation theory diagram, this implies that volume free energy decreases and surface free energy increases, which starts the growth of the crystal.

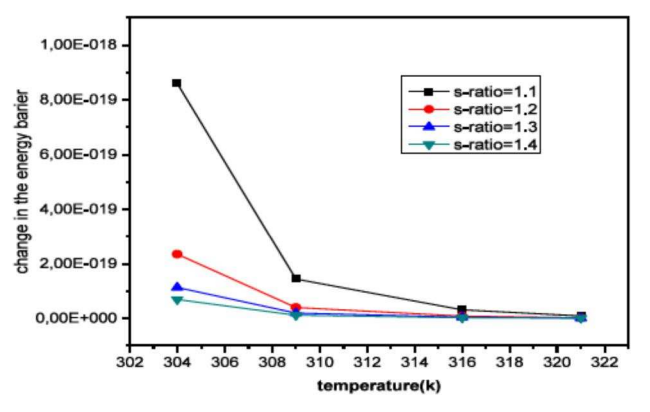


Figure 2: Variation of Gibbs free energy with supersaturation and temperature for 2PA

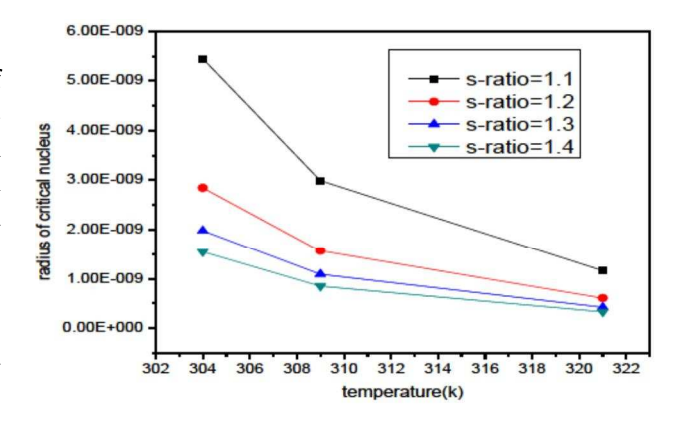


Figure 3: Variation of radius of critical nucleus with temperature and supersaturation ratio of 2PA

4.2 Equilibrium Concentration of Pyridine-2-carboxylic acid crystals

The solubility data of Pyridine-2-carboxylic acid crystal is fitted to a second order polynomial equation form for all the equilibrium temperatures. [20]

$$C_{sat} = -0.0312746T^2 + 26.2771T - 5083.14$$
 (5)

Correlative equation (5) is used to obtain the saturation concentration of any temperature for Pyridine-2carboxylic acid crystals. Table 2 shows that there is a de-

Table 2: Thermodynamics values

T (K)	S (I/mol K)	Cp (J/mol.K)	ddH (kl/mol)	Gibbs free energy (j)
304	355.16	120.69	21.64	-107947
308	357.33	122.12	22.12	-110035.52
316	360.5	124.96	23.11	-113894.89
321	362.48	126.73	23.74	-116332.34

cline in the Gibbs free energy with an increase in the temperature. This enhances the growth of the crystal.

4.3 Frontier molecular orbital analysis

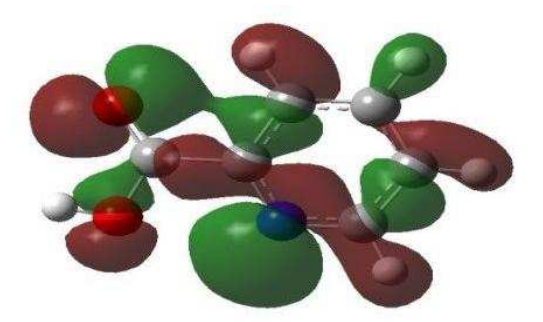
The energy gap of HOMO-LUMO explains the eventual charge transfer interactions within the conformers. The HOMO and LUMO energies of 2PA, as calculated by DFT/B3LYP/6-31G(d,p) method, are as follows:

HOMO energy, $E_{HOMO}=-7.092 {\rm eV}$ LUMO energy, $E_{LUMO}=-1.630 {\rm eV}$ HOMO-LUMO energy gap, [22] $\Delta E_{GAP}=E_{LUMO}-E_{HOMO}=5.46118 {\rm eV}$

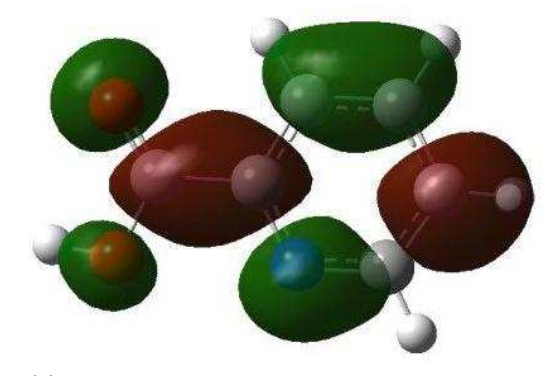
The gap between HOMO and LUMO has been used to prove the bioactivity from intramolecular charge transfer. The plots of HOMO and LUMO are shown in Figure 4. The computed high value of HOMO-LUMO energy gap (5.46118 eV) in 2PA confirms the chemical stability of the molecule. [21? -25] The global reactivity descriptors, such as ionization potential (I), electron affinity (A), electrophilicity index (ω), chemical hardness (η), softness (S) and chemical potential (μ), have been calculated using the energy of HOMO and LUMO. The values are listed in Table 3.

Table 3: Calculated quantum chemical molecular orbital properties for 2PA using the DFT/B3LYP/6-31G(d,p) method

Parameters	B3LYP/6-31G(d,p)
ionization potential (I)	7.092eV
electron affinity (A)	1.630eV
chemical hardness (η)	2.730eV
chemical potential (μ)	-4.361eV
electrophilicity index (ω)	3.483eV
softness (S)	$0.366 \mathrm{eV}^{-1}$



(a) HOMO



(b) LUMO

Figure 4

4.4 NLO studies – First order hyperpolarizability

The values of α_0 and β components of the Gaussian 09w output are reported in atomic units (a.u.); and the calculated values should be converted into electrostatic units (esu). The polarizability and the first hyperpolarizability of 2PA are 1.0405 x 10^{-23} esu and 4.1027 x 10^{-31} esu, respectively. The first hyperpolarizability of the title compound is 1.1 times greater than those of urea (β of urea is 0.3728 x 10^{-30} esu obtained by HF/6-311G(d,p) method).

5 Conclusion

The study evaluates the nucleation parameters of the title compound. The interfacial energy and the energy barrier for nucleation decreases with an increase in temperature. The values of kinetic parameters obtained by the application of different equations are in good agreement with each other. This confirms that the evaluated nucleation parameters are feasible for the growth of 2PA crystals. The first-order hyperpolarizability, polarizability and quantum chemical molecular orbital properties of 2PA are computed at the DFT level and the results are discussed.

References

- [1] S. Gowri, T. Uma Devi, D. Sajan, C. Surendra Dilip, A. Chandramohan, N. Lawrence, Crystal growth, spectral, optical and thermal properties of semiorganic nonlinear optical material: Picolinic acid hydrochloride Spectrochimica Acta, Part A: Molecular and Bi molecular Spectroscopy, 110, 28–35, 2013.
- [2] Di Li and Guo-Qing Zhong, Synthesis, Crystal Structure, and Thermal Decomposition of the Cobalt(II) Complex with 2-Picolinic Acid, Hindawi Publishing Corporation, The Scientific World Journal, 7 pages, 2014.
- [3] S. Rama, C.Surendra Dilip, Rajesh Narayana Perumal, Evaluation of kinetic parameters for water soluble crystals by thermo gravimetric analysis, Journal of Crystal Growth, 409, 32–38, 2015.
- [4] V. Sasikala, D. Sajan, N. Vijayan, K. Chaitanya, M. S. Babu Raj, B.H. Selin Joy, Electronic structure, vibrational spectral and intervening orbital interaction studies of NLO material: Guanidium 4-nitrobenzoate, Spectrochimica Acta, Part A: Molecular and Biomolecular Spectroscopy, 123, 127–141, 2014.
- [5] K. Selvaraju, K. Kirubavathi, N. Vijayan, S. Kumararaman, Investigations on the nucleation kinetics of bis glycine sodium nitrate, Journal of Crystal Growth, 310, 2859–2862, 2008.
- [6] P. Bennema, O. Sohnel, Interfacial surface tension for crystallization and precipitation from aqueous solutions, Journal of Crystal Growth, 102, 547–556, 1990.
- [7] U. Rychlewska, Chiral recognition in salts of trans-1,2-diaminocyclohexane and optically active tartaric acids: crystal structure of 1:2 salt of (S,S)-diaminocyclohexane with (R,R)-tartaric acid, Journal of Molecular Structure, 474, 235–243, 1999.
- [8] A.D. Becke, Density-functional thermochemistry. I. The effect of the exchange-only gradient correction, Journal of Chemical Physics, 98 (7), 5648-5652, 1993.
- [9] C. Lee, W. Yang, R. G. Parr, Development of the Colle-Salvetti correlation-energy formula into a functional of the electron density, Physics Review B, 37, 785–789, 1988.
- [10] P. Perdew, Y. Wang, Accurate and simple analytic representation of the electron-gas correlation energy, Physics Review B, 45, 13244–13249, 1992.
- [11] R.G. Parr, W. Yang, Density Functional Theory for Atoms and Molecules, Oxford University Press, New York, 1989.
- [12] T.A. Koopmans, Über die Zuordnung von Wellenfunktionen und Eigenwerten zu den Einzelnen Elektronen Eines Atoms, Physica, 1, 104–113, 1933.

- [13] Jane S. Murray, Fakhr Abu-Awwad and Peter Politzer, Prediction of Aqueous Solvation Free Energies from Properties of Solute Molecular Surface Electrostatic Potentials, Journal of Physical Chemistry A, 103 (12), 1853–1856, 1999.
- [14] R.S. Mulliken, A new electroaffinity scale; together with data on valence states and on valence ionization potentials and electron affinities, Journal of Chemical Physics, 2, 782–793, 1934.
- [15] R.G. Pearson, Absolute electronegativity and hardness: applications to organic chemistry Journal of Organic Chemistry 54, 1423–1430, 1989.
- [16] V. Balachandran, A. Nataraj, T. Karthick, Comparative vibrational spectroscopic studies, HOMO-LUMO, NBO analyses and thermodynamic functions of p-cresol and 2-methyl-p-cresol based on DFT calculations Spectrochimica Acta, Part A: Molecular and Bi molecular Spectroscopy, 104, 114–129, 2013.
- [17] D.A. Kleinman, Nonlinear Dielectric Polarization in Optical Media, Physical Review, 126, 1977–1979, 1962.
- [18] H. Tanak, Y. Koysal, S_. Is_ık, H. Yaman, V. Ahsen, Experimental and Computational Approaches to the Molecular Structure of 3-(2-Mercaptopyridine)phthalonitrile, Bull. Korean Chem. Soc., 32 (2), 673–680, 2011.
- [19] S. Rama, C. Surendra Dilip, Rajesh Narayana Perumala, A software program to investigate the nucleation kinetics of solution grown crystals using MATLAB platform, Computer Physics Communications 185, 661–669, 2014.
- [20] N. Tagmatarchis, E. Aslanis, K. Prassides, H. Shinohara, Mono-, Di- and Trierbium Endohedral Metallofullerenes: Production, Separation, Isolation, and Spectroscopic Study, Chemistry of Materials, 13, 2374–2379, 2001.
- [21] Z. Zhou, R.G. Parr, Activation hardness: new index for describing the orientation of electrophilic aromatic substitution, Journal of the American Chemical Society, 112, 5720-5724, 1990.
- [22] J. Gilman, Chemical and physical "hardness", Materials Research Innovations, 1, 71–76, 1997.
- [23] J. Aihara, Reduced HOMO-LUMO Gap as an Index of Kinetic Stability for Polycyclic Aromatic Hydrocarbons, Journal of Physical Chemistry A, 103, 7487–7495, 1999.
- [24] J. Aihara, Why are some polycyclic aromatic hydrocarbons extremely reactive?, Physical Chemistry Chemical Physics, 1, 3193-3197, 1999.
- [25] J. Aihara, Weighted HOMO-LUMO energy separation as an index of kinetic stability for fullerenes, Theoretical Chemistry Accounts, 102, 134-138, 1999.